UMONS
Université de Mons

Faculté Polytechnique

Modeling and optimal command of resonant wireless power transfer systems

PhD thesis

Alexis DESMOORT

POLYTECH MONS

Supervisor: Prof. Olivier DEBLECKER
Co-supervisor: Dr Zacharie DE GRÈVE

September 2019

ACADÉMIE UNIVERSITAIRE WALLONIE-BRUXELLES

CONTENTS

CHAPTER

ONE

INTRODUCTORY ASPECTS

1.1 Need for wireless power transfer solutions

Wireless power transfer (WPT) refers to the remote transfer of electrical supply power between systems separated in space, without resorting to any wired connection. Among the different technologies enabling WPT, the resonant inductive power transfer (RIPT) [1–5] is the most popular. Based on the mutual electromagnetic induction between electromagnetic oscillators, the RIPT requires to convert a significant amount of power at an intermediate frequency (from 1 kHz to 10 MHz, which is *intermediate* between the well-known 50/60 Hz and the very high frequencies involved in telecommunications). Therefore, its development has been dependent on the contemporary technological limitations and restricted to low-power applications, essentially pertaining to mobile electronic devices. The progressive advances in the field of power electronics have paved the way for the implementation of RIPT to increasingly energy-greedy applications, with always better performances over the years. High-power WPT is nowadays a popular and always more trending topic in the electrical power engineering community, principally in the field of electric vehicles (EVs) battery charging (see Figure 1.1). Furthermore, the upcoming change in paradigm for transportation could be fostered by the implementation of wireless EVs battery charging.

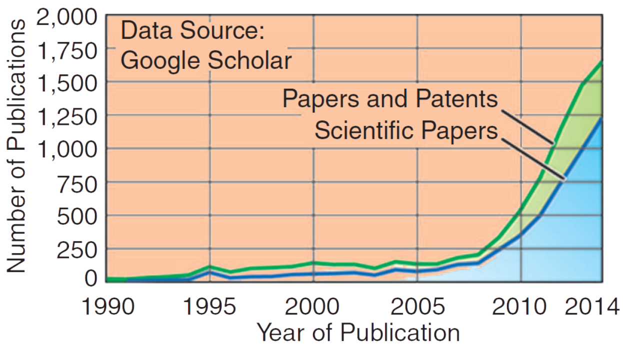

Figure 1.1: Number of publications on Google Scholar about *power inductive electric vehicle* or *power contactless electric vehicle* (excluding electrical machine research) [6]

1.1.1 From more convenience for electronic mobile devices ...

In the last thirty years, the combined evolutions in the fields of wireless communication and electronics have fostered the development and the commercialization of manifold mobile devices. Nowadays, mobile devices such as the laptop computer and the mobile phone have become two major devices impacting our daily life. This advance has been made possible thanks to the discover and the development of the wireless transmission of data, whereas data is the essential raw material to the exploitation of those communication tools. Alongside the invention of the wireless internet (via the *Wi-Fi* technology and via the *3G/4G/5G* networks) and of the wireless phone network, the number of wires around us has also decreased with the implementation of communication protocols for pairing devices together or with accessories (notably via the *Bluetooth* technology). In this journey towards more convenience and freedom, it has quickly seemed obvious to the scientific and industrial communities that the next step would consist in cutting the last chord, which is the supply cable. Moreover, this initiative becomes even more interesting as the size of the batteries equipping those devices are more and more lessened for reducing their cost and their impact on the device aesthetics.

Hence, WPT applied to small electronic devices could release the user from the charging chore as a phone or a computer battery could charge while staying in its owner pocket or in its carrying bag, respectively. Beyond those convenience purposes which fall within comfort considerations, WPT can have a real practical purpose for revolutionising the implementation of given electronic devices. For instance, non-exhaustively, WPT enables the transmission of energy to implanted medical electronic prostheses without resorting to surgery [7–9] or the uninterrupted wireless energy supply for sensors networks, paving the way for a significant step forward in the monitoring sector [10, 11].

1.1.2 ... to a major challenge for the current transportation revolution

The automobile industry is currently confronted to the major challenge of adopting a viable alternative to the use of fossil fuels. As a matter of act, those combustibles cause an important pollution in terms of fine particles and greenhouse gas emission, whereas the global petroleum reserves are receding drastically. For illustration purposes, transportation was responsible for 33.7 % of the world greenhouse gas emissions and 27 % of the world total petroleum consumption in 2012 [12]. At this rhythm, the end of the classic gasoline automobile is commonly estimated by the horizon 2050. In this context, one of the most sustainable alternatives consists in resorting to the electrical energy to power our vehicles. Basically, an EV does not produce any local pollution and does not consume any kind of fossil fuels. The real environmental challenges are deported on the primary energy employed for the generation of the electricity powering the EVs and on the technology and the fabrication process of the batteries equipping EVs (deemed highly contaminant). However, those considerations lie beyond the scope of this work.

Electricity has already a significant role in the modern transportation sector with the electrification of the railway systems which started in the beginning of the 20th century. Nevertheless, the significantly larger mobility and flexibility pertaining to the automobile prevent the use of electrified overhead lines like those supplying locomotives. Consequently, modern electric vehicles embed a battery pack. However, the latter hinders the EV expansion on the consumer market for two main reasons.On the one hand, the cost of the battery is currently high so that an electric vehicle is more expensive to purchase than its classic counterpart. However, one can note that this cost issue progressively vanishes as the average battery cost has drastically fallen from 1,000 $/kWh in 2010 to 227 $/kWh in 2016 and is expected to decrease under 100 $/kWh by the year 2030 (see Figure 1.2). On the other hand, the energy density of batteries is very low with only 100 Wh/kg typically, whereas gasoline presents an energy density of 12,000 Wh/kg [14]. Hence, an EV presents currently a limited autonomy. Although the electrical energy is available almost everywhere (in contrast with the gasoline), the charging frequency inconveniences the user, especially because the charging process lasts from a half-hour (with a 22-kW power rate) to several hours (with a 3.3-kW power rate).

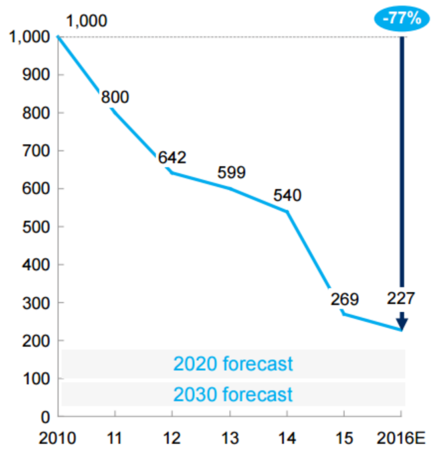

Figure 1.2: Average battery price forecast (in \$ per kWh) [13]

Presently, only a few plug-in charging stations are available. In essence, the connection of a cable is a procedure which is not more flexible than a gasoline filling, and lasts 10 times more in the best case. For those reasons, the charging procedures and facilities must be improved, notably by taking profit of mechanisms which are typically pertaining to electricity for defining innovative and clever replenishment processes. Hence, the development of infrastructures is one of the four main keys to enhance the EVs deployment, aside with its cost, its range and the multiplication of EVs models [15]. The resort to wireless EVs battery charging is precisely an infrastructural revolution with great potential.

Among the manifold mechanisms for achieving WPT, the RIPT is unanimously recognized as the most suitable solution for fulfilling the requirements associated with a wireless EVs battery charging application [4, 14, 16–21]. Those requirements consist in ensuring

- a high power transfer capability (at least 3.3 kW, corresponding to a wired charger) ;
- a range compatible with the typical height of a car underseal (tens of cm) ;
- a high efficiency (above 90 %), regarding the prominence of the concerned power level.

Envisioned by Tesla [5, 22–24] in the end of the 19$^{\text{th}}$ century, the resonant inductive coupling (which is the core principle for achieving RIPT) is a technique consisting in enhancing the performances of the classic inductive coupling, negatively affected by a large air gap. To this end, a capacitor is connected to each winding of an air transformer for building LC oscillators designed to resonate at the same frequency. Hence, driving the system at the latter frequency improves the interaction between the coupled circuits. Combined with the recent progress in modern power electronics, it provides performances comparable to those of wired connections, as shown in Table 1.1.

Wireless charging brings convenience and high flexibility to the replenishment process. The user just needs to park on a dedicated parking space (for stationary charging) or to drive on a specifically equipped roadway (for dynamic charging). The adequate combination of stationary and dynamic charging (consisting in equipping only restricted road portions with a wireless charger and called the opportunistic charging) is notably interesting for buses, which have a fixed route with multiple stops (with a charger in each stop). Opportunistic charging may also be used for charging the vehicles stopped at a road toll or in well-known road segments subject to traffic jam. In this thesis, the attention is drawn on stationary charging.

Type	Source	Power rate (kW)	Efficiency (%)
Conductive	Nissan Leaf 2013 [25]	3.3	85.0
	Chevrolet Volt [26]	3.3	89.6
	m-pec [27]	6.6	96.0
Wireless	WiTricity WiT3300 [28]	3.3	89.0
	Chinthavali *et al.* [26]	6.6	85.0
	Goeldi *et al.* [29]	22	97.0
	Bosshard *et al.* [30]	50	95.8
	Primove 200 [31]	200	90.0

Table 1.1: Comparison of most significant references for conductive and wireless EVs battery chargers [6]

Technologically speaking, the lack of cable and connector avoids the related deterioration and maintenance, whereas fostering the charger universality. Without any galvanic connection, the charging process is safer for the user and becomes practicable outside regardless of the weather conditions. Moreover, the galvanic insulation of the embedded electronics is achieved naturally. The RIPT presents very simple transmission terminals which can be integrated easily in our daily environment without depreciating the urban aestheticism. With an interoperability improved by standards such as those published by the Society for Automobile Engineers [32] (fixing notably a universal operating frequency at 85 kHz), the charging stations should proliferate and be integrated in the user's daily life. The deployment of wireless charging stations may also improve the EVs access to the grid for serving as domestic storage units for vehicle-to-home (V2H) interactions, or as distribute storage units dear to the modern distribution network operators for performing vehicle-to-grid (V2G) interactions [33].

However, the implementation of RIPT to high-power applications such as EVs battery charging raises several challenges pertaining to electrical power engineering, explaining the University of Mons Electrical Power Engineering Unit interest for this topic. The current ongoing PhD thesis proposes to tackle those challenges, whereas pioneering this new field of research in the Unit.

1.2 Wireless power transfer techniques

This thesis focuses on the resonant inductive coupling for achieving wireless power transfer. As it pioneers the research activities in the Electrical Power Engineering Unit of the University of Mons on this subject, it seems appropriate to clarify the reasons behind the resonant inductive coupling supremacy in the current landscape of wireless power transfer, which is reported by a numerous reviews [16–18, 20, 34, 35]. Except from some marginal techniques with a very specific range of applications such as those using acoustic waves [36] or light beams [37], the wireless power transfer is mainly achieved by using the remote effects of electrical charges, pertaining to electromagnetics. Depending on the field region and on the type of interacting systems, different electromagnetic effects prevail and enable as much WPT mechanisms. In the far-field region, the electric and magnetic fields are strongly coupled and are consequently assimilated to a self-propagating electromagnetic wave. Wave phenomena occur and lead to a power transmission. In the near-field region, the electric and magnetic fields are weakly bound and one is dominating the other depending mainly on the shape of the interacting conductors. Flat plane conductors tend to generate a strong electric field, yielding electric interaction opportunities, while wound conductors tends to generate a strong magnetic field, yielding magnetic interaction opportunities. In both cases, those interaction opportunities enable a transfer of power.

1.2.1 Microwave power transfer

Electromagnetic waves are capable to carry energy even in the total vacuum, as demonstrated by J. H. Poynting [38]. Consequently, they have been - and still are - widely employed for the wireless transmission of information. However, the significant decrease of the power density arising from the conventional omnidirectional emissions of electromagnetic waves is irrelevant in the framework of WPT. Though, the technological advances have fostered the rise of the achievable wave frequency, reaching the microwaves range (presenting a frequency from 300 MHz to 300 GHz). With wavelength falling within the order of the meter, microwaves allow the conception of practicable wave concentration facilities. Once concentrated in a beam, the microwaves are almost preserved from power density decrease and can be used for performing microwave power transfer (MPT) [39–43]. Fostered by the flourishing researches in radar and telecommunications during the World War II and the Cold War in the 1960s, Brown *et al.* have first proceeded to successful experiments for a progressively high-power transfer (from a few W to tens of kW) with an interesting efficiency (above 50 %) on distances of several km (see Figure 1.3). Still, the interacting systems (*i.e.* a magnetron on the transmission side and a rectifying antenna, or rectenna, array on the receiving side) display a high complexity which hinders the MPT implementation for domestic and industrial applications. Moreover, the latter implementation is complicated by the quasi-perfect and clear line-of-sight alignment required between the transmitting and the receiving devices. These devices are not interchangeable and bidirectional power transfer is thus not possible. Finally, the hazardous nature of such high-power microwaves emissions is not compatible with a wide public application. Therefore, the MPT has mainly been limited to very specific (essentially military) applications.

Figure 1.3: MPT demonstration over 1.54 km (largest ground-to-ground transmission) at the Venus Site of the JPL Goldstone Facility [40]

1.2.2 Capacitive power transfer

Two nearby conducting plates form a capacitor and can interact via a common time-varying electric field for establishing a displacement current which can lead to a power transfer. When the plates are submitted to a potential difference (*i.e.* a voltage), electric influence occurs so that the plate with the highest potential is positively charged and the other is negatively charged. Though, the total amount of charge remains constant. When the plates are submitted to an alternative voltage, the charge are moving back and forth, yielding a *displacement* current from one plate to the other without any galvanic connection. This is the fundamental principle of the capacitive power transfer (CPT) [44–51]. A typical CPT system (see Figure1.4) comprises two pairs of plates forming two capacitors, one coupling the positive terminals of the power supply and of the load and the other coupling their negative terminals. The CPT principle has been envisioned by Tesla [22] and has been reconsidered in the mid-2000s for high-frequency (several MHz), low-power (from a few to tens of W) and low-range (a few cm) power transfer destined to small electronic devices [44–46]. The CPT has been gaining popularity since then, notably thanks to improvements in its implementation. Hence, impedance compensation techniques (consisting in the establishment of a resonant operation by connecting inductances to the interacting plates) recently permitted to perform high-power transfer (from 1 kW to 2 kW) with an efficiency up to 90 % for ranges circa 15 cm [47–49]. In comparison with MPT, the CPT resorts to relatively simple facilities (*i.e.*, a power supply, well-designed plates and a rectifier) and is based on elementary electrical principles. Nevertheless, efficient CPT systems require operating frequencies belonging to the MHz-range, which limit the attainable power range due to the consecutive constraints peculiar to the electronic power supply. However, since the electric field is naturally confined between the coupling plates, the CPT systems produce low electromagnetic interferences (EMI) in comparison with the inductive techniques, where the magnetic field spreads in the surrounding air in absence of magnetic shielding.

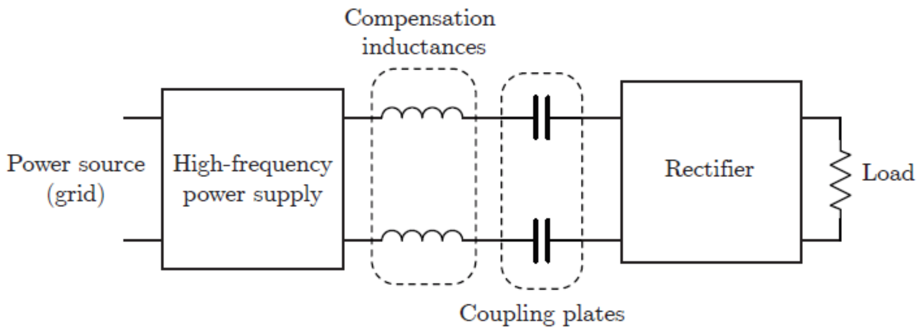

Figure 1.4: Schematic of a typical compensated capacitive power transfer system

1.2.3 Inductive power transfer

Two wound conductors placed nearby (called the primary and the secondary, respectively) and crossed by alternative currents (i_p and i_s, respectively) tend to interact via the magnetic field. According to the Ampère's law, each winding generates a time-varying contribution to the ambient magnetic field. Based on the electromagnetic induction phenomenon described by Faraday, a changing magnetic field induces in any closed conductor (or turn) an electromotive force, equal to the variation rate of the magnetic flux the latter conductor embraces. Hence, each conductor proceeds to self-induction, but also to mutual induction in the other conductor. As a result, the circuits comprising the windings are remotely coupled and energy can be transferred from one side to the other, without any galvanic connection. In absence of magnetic saturation (*e.g.* in the air), the magnetic flux generated by each conductor is directly proportional to their respective current via the primary and the secondary self-inductance coefficient L_p and L_s. The resulting mutual magnetic flux is associated with a mutual inductance coefficient M relating the induced electromotive force in each conductor to the variation in current in the other. The voltage v_p and v_s across the primary and the secondary windings, respectively, are given by

$$v_p = R_p i_p + L_p \frac{di_p}{dt} + M \frac{di_s}{dt} \tag{1.1}$$

$$v_s = R_s i_s + L_s \frac{di_s}{dt} + M \frac{di_p}{dt} \tag{1.2}$$

$$\tag{1.3}$$

where R_p and R_s are the equivalent parasitic resistances of the primary and the secondary windings, respectively. In the frequency domain, one has

$$\underline{V}_p = R_p\underline{I}_p + j\omega L_p\underline{I}_p + j\omega M\underline{I}_s \tag{1.4}$$

$$\underline{V}_s = R_s\underline{I}_s + j\omega L_s\underline{I}_s + j\omega M\underline{I}_p \tag{1.5}$$

where j is the imaginary unit (*i.e.*, $j = \sqrt{-1}$), ω is the operating angular frequency and each quantity marked with an underbar represents the phasor of the related time-domain quantity. Consequently, the equivalent circuit of two inductively coupled windings is represented in Figure 1.5a, which is commonly simplified in the circuit presented in Figure 1.5b.

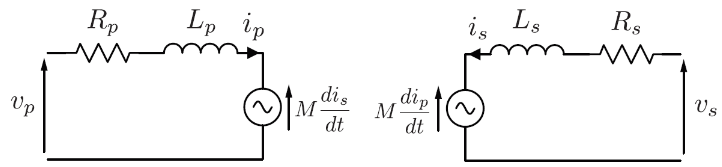

(a)

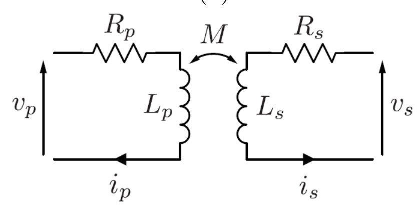

(b)

Figure 1.5: Equivalent circuits for inductively coupled conductors

Well-known and widely employed in electrical engineering, the inductive coupling is a simple mechanism, naturally bidirectional, tolerant to movement, with interesting performances for frequencies starting from 10 kHz and particularly efficient when the coupling between the windings (quantified by the mutual inductance) is tight. As a consequence, the magnetic coupling has been envisioned for transferring power between two circuits without any galvanic connection, yielding inductive power transfer (IPT). A typical IPT system is represented in Figure 1.6. For guaranteeing a tight coupling between the transmitter and the receiver coils, the IPT is implemented for supply power without a galvanic connection (*i.e.*, without wire), but with a contact between the transmitting and the receiving devices. Hence, IPT has been applied for the charging of EVs battery by considering a receiving coil that can be inserted in a splitable transformer [52] or by using inductive pads [17]. A purely inductive standard destined to the in-contact charging of small electronic devices (called the *Qi* standard) has also been published and is currently extremely popular for the transmission of 5 W at frequencies ranging from 110 to 205 kHz [53]. For wireless and contactless power transfer, the consecutive loose coupling rises drastic limitations in the performances of the inductive link. These limitations are discussed hereafter.

Highlight of the limitations impacting loosely coupled windings

The dynamics of inductively coupled windings is not trivial. However, a global and physical approach of the energy exchanges in and between inductively coupled circuits permits to understand the limitations on the performances (in terms of power transfer capability and transfer efficiency) impacting loosely coupled windings.

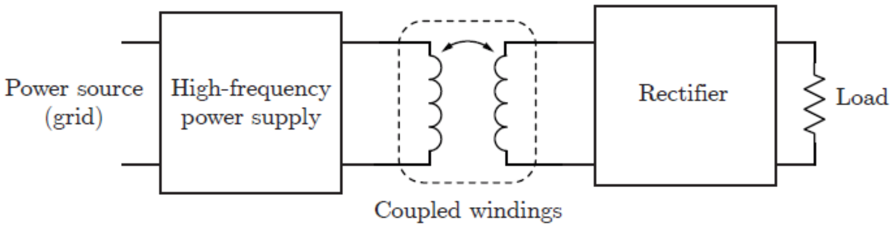

Figure 1.6: Schematic of a typical inductive power transfer system

The windings self-inductance coefficients L_p and L_s are the circuital representations of the energy storages that occur in the coupled windings system and are crucial in the concept of resonant inductive coupling, as discussed hereafter. These energy storages can be segregated in two different complementary contributions, namely the magnetizing contribution and the leakage contribution. The magnetizing energy consists in the energy which is stored by the windings in the magnetic field for establishing the mutual magnetic flux at the origin of the inductive coupling. The leakage energy corresponds to the energy which is stored by the windings in the magnetic field which does not contribute to the inductive coupling.

In an ideal transformer, these energy storages are cancelled by canalizing the entire magnetic flux from one winding to the other with a magnetic core (*i.e.*, a physical channel made of a material highly permeable to the magnetic flux) presented an infinite permeability. Since the entire flux links both windings, the leakage phenomenon and the related energy storage are non-existent and since the magnetic core is infinitely permeable to the magnetic flux, the magnetizing energy is null. In usual transformers, these energy storages are minimized by using a magnetic core presenting a sufficiently high magnetic permeability in comparison with the ambient air. Therefore, the usual transformers are tightly coupled and the power transfer capability is high as the instantaneous power furnished to the primary winding is directly transmitted to the secondary and vice versa. Nevertheless, such implementation is not relevant with a convenient and effective framework for wireless power transfer, where the windings must be necessarily separated by free-space.

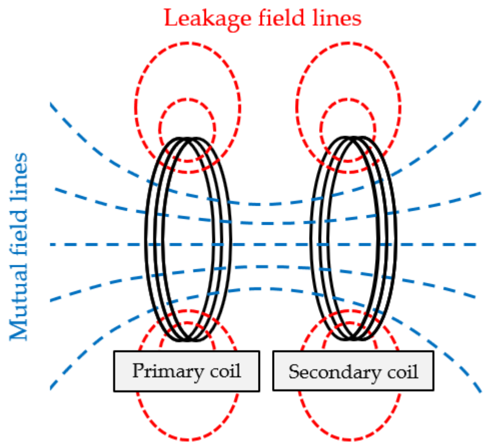

Figure 1.7: Schematic fields lines associated with inductively coupled inductors

When the free-space between the primary and the secondary windings increases, more and more field lines are closing on each winding without interlinking with the other (as schematized on Figure 1.7), yielding a significant leakage phenomenon. The related magnetic fluxes (called leakage fluxes) do not contribute to the coupling and the energy related to these fluxes is alternatively invested in the field by each side and recovered by the same side by self-induction. As a consequence, the leakage phenomenon delays the flow of an increasing portion of the energy transiting through the system as the coupling decreases, yielding an increasing reactive loading on each side of the circuit, and thus to a surging reactive power consumption. Concomitantly, the magnetizing energy is decreasing and progressively invested in the leakage fluxes. Without constituting *per se* an actual loss, the leakage phenomenon and the related energy storages are restraining drastically the power transfer capability of loosely coupled windings. In practice, the windings (and the component connected to the latter) present a parasitic resistance dissipating a portion of the transferred power, but also a portion of the energy exchanged with the magnetic field without participating to the power transmission. As a result, a loose coupling causes also a degradation of the transfer efficiency. For achieving practicable power transfer capability, either the current in the windings or the operating frequency could be increased, but both solutions lead to a consequent rise of the resistive losses, with an even lower efficiency.

By defining the fictive leakage inductances l_p and l_s associated respectively with the primary and the secondary leakage fluxes, the mutual inductance can be expressed as [54]

$$M = \sqrt{(L_p - l_p)(L_s - l_s)} \tag{1.6}$$

Conventionally, the strength of the coupling between two windings is evaluated by the normalized coupling coefficient k, which is the ratio between the effective mutual inductance M and its theoretical value in absence of leakage phenomenon. One has

$$k = \frac{M}{\sqrt{L_p L_s}} \tag{1.7}$$

For wireless power transfer applications, the coupling coefficient is typically smaller than 20 %. The simplicity of the principle behind inductive coupling as well as its easy practical implementation plead for its usage as an interesting option for achieving wireless power transfer. Therefore, the scientific and industrial communities have focused on improving the inductive transfer performances by resorting to the concept of electrical resonance for laying the foundation of resonant inductive power transfer.

1.2.4 Resonant inductive power transfer

The idea behind the resonant inductive coupling is attributed to Nikola Tesla [23, 24, 55] and consists in associating the self-inductance of two coupled windings with adequate capacitances for enabling a resonant operation. Presenting unique physical and circuital features, such an operation allows to achieve high-performance inductive wireless power transfer despite loosely coupled windings.

Concept of electrical resonance

A pure inductive component is characterized by a voltage which is proportional to the time variation of the current passing through it. Such component is capable to store in the magnetic field an energy which is proportional to the square of the current. In contrast, a pure capacitive component is characterized by a current proportional to the time variation of the voltage across it. Such a component is capable to store in the electric field an energy which is proportional to the square of the voltage. As a consequence, an arrangement of two or more reactive components (with at least one inductor and one capacitor) manifests an oscillatory behavior due to the complementarity in the energy storages between inductive and capacitive components. In the frequency domain, an oscillatory circuit is associated to one (or more, depending on the number of the interconnected reactive components) specific angular frequency at which the energy exchanges in the latter circuit are perfectly synchronized so that its reactance is zero. Operating at this specific frequency, the oscillatory circuit demonstrates an exceptional behavior pertaining to electrical resonance. Hereafter, we consider the two most basic configurations for establishing an electrical resonance, namely the series and the parallel connections of an inductance L and a capacitance C (see Figure 1.8).

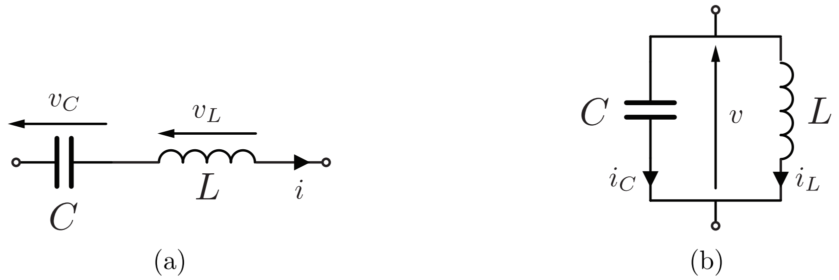

Figure 1.8: Equivalent circuit for an (a) LC-series oscillator and (b) LC-parallel oscillator

LC-series resonance The series connection of an inductance L and a capacitance C implies that both are crossed by the same current. Considering a common sinusoidal current (denoted i), the inductance voltage v_L and the capacitance voltage v_c are in phase-opposition. As a result, when the inductance stores energy in its magnetic field (*i.e.* when the product of v_L and i is positive), the capacitance recovers energy from its electric field (since the product of v_C and i is negative) and vice versa. The corresponding circuit branch presents therefore an oscillatory behavior as the energy can flow back and forth between the electric field, the magnetic field and the source. As the inductance and capacitance voltages are related to the current via a time-variation rate, one can define a particular angular frequency ω_0 at which the exact energy recovered from the electric field is directly invested in the magnetic field and vice versa, corresponding to a resonant operation. In the frequency domain, the energies E_L and E_C alternatively stored in each field are given respectively by

$$E_L = \frac{1}{2}LI^2 \quad \text{and} \quad E_C = \frac{1}{2}CV_c^2 = \frac{1}{2}\frac{I^2}{\omega^2 C} \tag{1.8}$$

where I is the root-mean-square (RMS) value of the current crossing both the inductance and the capacitance, ω is the angular operating frequency and V_c is the RMS value of the capacitance voltage. Accordingly, these quantities are identical when the operating angular frequency ω of the circuit is equal to

$$\omega = \frac{1}{\sqrt{LC}} = \omega_0 \tag{1.9}$$

At this resonant frequency, the reactive energy flows between the inductance and the capacitance are perfectly synchronized and are therefore confined within the LC-series branch.

From a physical point of view, such a circuit is a resonating oscillator analogous to a pendulum in mechanics, storing energy alternatively in kinetic and potential forms. Theoretically, exciting an LC-series branch at its self-resonant frequency results in infinite current oscillations which are in practice damped by the inherent parasitic resistances in the circuit.

From a circuital point of view, one can verify that the reactances associated with the inductance X_L and with the capacitance X_C - representing the components tendency to store energy - are logically equal but from opposite sign, and cancel logically each other out as follows

$$X_L = \omega_0 L = \frac{1}{\omega_0 C} = X_C \tag{1.10}$$

Leaving the parasitic resistances aside, the branch presents a null impedance and behaves as a short-circuit. The reactive power consumed by the LC-series branch is null and the inductance and the capacitance are said to compensate each other.

LC-parallel resonance The parallel connection of an inductance L and a capacitance C implies that both are submitted to the same voltage. Considering a sinusoidal voltage (denoted v), the inductance current i_L and the capacitance current i_c are in phase-opposition. Therefore and similarly to the LC-series case, the respective energy storages are complementary. In the frequency domain, the energies E_L and E_C alternatively stored in each field are given respectively by

$$E_L = \frac{1}{2} L I_L^2 = \frac{1}{2} \frac{V^2}{\omega^2 L} \quad \text{and} \quad E_C = \frac{1}{2} C V^2 \tag{1.11}$$

where I_L is the RMS value of the inductance current and V is the RMS value of the voltage across both the inductance and the capacitance. One can observe that the parallel self-resonant frequency is equal to the series resonant frequency. At the self-resonant frequency, the reactive energy flows between the inductance and the capacitance are also perfectly synchronized and confined in the LC-parallel mesh.

From a physical point of view, such a circuit is also a resonating oscillator. Supplied at its self-resonant frequency, the LC-parallel mesh produces virtually infinite voltage oscillations which are anew damped in practice by the parasitic resistances in the circuit.

From a circuital point of view, the susceptances associated with the inductance B_L and with the capacitance B_C are equal but opposite from sign and cancel each other out, as

$$Y_L = \frac{1}{\omega_0 L} = \omega_0 C = Y_C \tag{1.12}$$

In this case, leaving the parasitic resistances aside, the mesh presents a null admittance and behaves as an open-circuit. The reactive power consumed by the LC-parallel mesh is also null and the inductance and the capacitance are here also compensating each other.

Implementation to inductively coupled windings

In the light of the foregoing, one can envision a potential solution to mitigate the detrimental energy storages occurring in coupled windings. By connecting an adequate capacitance to each coupled circuit, the latter can resonate with the corresponding winding at the operating frequency of the system. The local energy storages and the consecutive reactance are hence compensated by the capacitance and the power transfer capability of the system is theoretically infinite, despite the loose magnetic coupling. This type of operation leads to an original way to implement the inductive power transfer, namely RIPT. A typical RIPT system is represented schematically on Figure 1.9.

One has to note that the aforementioned physical and circuital points of view are two different but equivalent manners to describe the same phenomena and principles. As a consequence, each vision has been employed for pioneering the development of different descriptions of the RIPT. The physical vision has led to the proposition of the strongly coupled magnetic

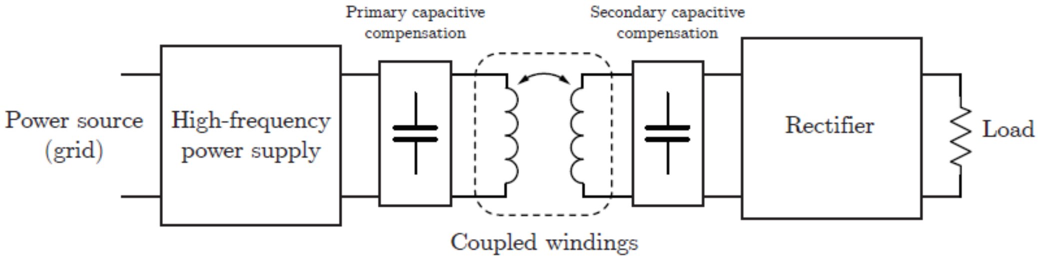

Figure 1.9: Schematic of a typical resonant inductive power transfer system

resonance technique, whereas the circuital vision has led to the proposition of the inductively coupled power transfer technique. These approaches and their respective purposes are described hereafter.

Strongly coupled magnetic resonance

Kurs *et al.* from the Massachusetts Institute of Technology have generated the current RIPT popularity by publishing an article in *Science* in 2007, on a technology called *strongly coupled magnetic resonance* (SCMR) [2]. The tremendous impact of this paper (it records currently 5000 citations[1], including more than 300 from patents) has hidden the previous works and a common misconception in the academia consists in assigning to its authors the paternity of the resonant inductive concept. Actually, this contribution presented an alternative approach for addressing RIPT. Focused on a relatively low-power application (which is adapted for the supply of electronic devices), the proposed system can operate at a frequency level in the order of the MHz. At such high frequencies, the oscillatory behavior of the LC circuits primes on the circuital aspects. By ignoring the circuital concerns and assimilating the interacting circuits to coupled oscillators (described physically in terms of energy exchanges), Kurs *et al.* employed the coupled-mode theory [56] to demonstrate that the interaction between those oscillators is enhanced by a common resonant state of operation. Moreover, they stipulate that, as an oscillatory phenomenon, the SCMR is not affected by the surrounding materials, which are not excited at the circuit frequency. As a consequence, in contrast with conventional radiating mechanisms, the SCMR seems to channel the energy from the source to the load. Finally and more practically, an experimental validation of the proposed methodology has been conducted and resulted in the transfer of 60 W to 2 m (more than three times the diameter of the employed windings) with an efficiency around 40 %. A picture of the latter prototype is presented in Figure 1.10.

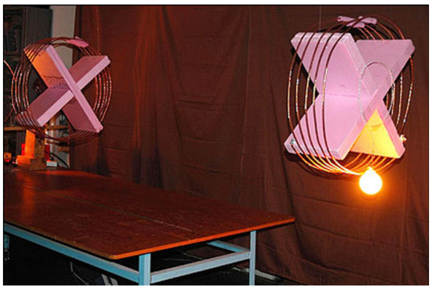

Figure 1.10: Picture of the SCMR prototype built by Kurs *et al.* [57]

[1]According to *Google Scholar*

Inductively coupled power transfer

A team from the University of Auckland has pioneered in the mid-1990s the development of the resonant inductive coupling destined to energy-greedy applications, with a specific focus on EVs [1, 19, 58–61]. Given the contemporary power electronics state of the art and since the transfer of several kW is considered, the investigated operating frequencies are in the kHz-range. This research team designated this technology as the *inductively coupled power transfer* (ICPT). From their electrical engineer's point of view, the resonant inductive coupling answers to power conversion concerns, as the inclusion of a capacitor on each side of a loosely coupled transformer ensures the compensation of the reactive power

- on the secondary for eliminating the secondary winding reactance and enabling hence an ideal and virtual infinite power transfer capability ;
- on the primary for eliminating the primary winding reactance and eventually the reactive load reflected from the secondary (despite of its own compensation) for decreasing the volt-ampere rating of the power converter supplying the system.

These features permit to mitigate the detrimental effects of a loose inductive coupling and enable transfer performances which are comparable to classical wired connections, as depicted in Table 1.1. Moreover, the resonant inductive circuit is employed as a resonant tank network transforming the supply power converter into a resonant converter. Such converters are characterized by an oscillating output current (in the case of a voltage-source converter) or output voltage (in the case of a current-source converter) which enables the possibility to decrease the switching losses by performing soft switching. A synergy exists therefore between the resonant inductive circuit and the surrounding power converter, as the former requires the latter to convert high-power with a high switching frequency for ensuring an effective transfer and the latter requires the former for achieving soft switching and allowing such a conversion. The soft-switching possibilities offered by a RIPT system employed as a resonant tank network are briefly discussed in Chapter 5 of this thesis. One can note that earlier or concomitantly to the first developments of ICPT, some contributions had already considered to establish a resonant operation in an inductive EV charger for achieving soft switching in the supply converter, without referring to the RIPT and its particular features as a wireless power transfer mechanisms [62–64].

Although addressed differently, Kiani *et al.* have demonstrated that the features highlighted by both the ICPT and the SCMR approaches are two visions of the same operating mode, pertaining to RIPT [65]. Different effects prevail in each case, depending notably on the operating frequency level and therefore on the targeted applications, since the power level must comply with the switching frequencies afforded by the contemporary semiconductors components. The study pursued in this thesis, with a focus on energy-greedy applications, will be based on the ICPT vision. Nevertheless, the different tools and methodologies developed in the following can be applied as well to high-frequency/low-power applications, falling more within the SCMR vision of the resonant inductive technology.

1.3 Circuit analysis of the resonant inductive power transfer

Before clarifying the objectives of this thesis in the light of the concepts raised in this chapter, a circuit analysis of the RIPT is proposed in this section. For simplicity purposes, the frequency-domain equivalent circuits of the different RIPT topologies are employed, where the power supply is replaced by an ideal AC voltage source $\underline{V}_{ac}$, and the cascade of the secondary rectifier (with an eventual additional DC-DC converter) and the load is replaced by an equivalent load resistance R_L.

1.3.1 Compensation topologies

As mentioned previously, the self-inductance of a winding can be compensated by connecting a capacitor to the latter, either in series or in parallel. Considering two coupled windings, the different arrangement possibilities define the four basic compensation topologies represented on Figure 1.11, which are the series-series (SS), the series-parallel (SP), the parallel-series (PS) and the parallel-parallel (PP) topologies. More sophisticated topologies have been proposed in the literature, but these four are the most commonly employed.

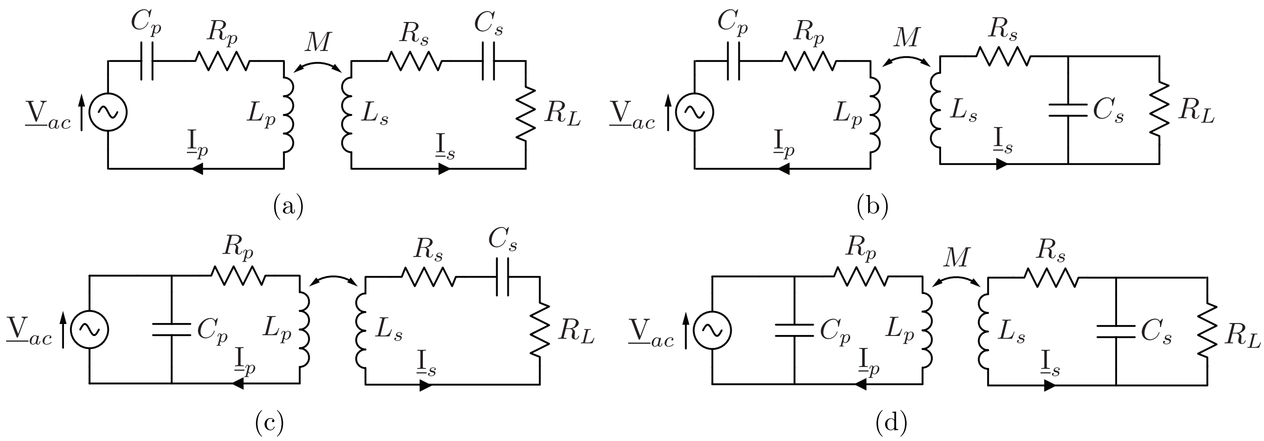

Figure 1.11: Four elementary compensation topologies

Going from the load to the power supply, the circuital analysis of the secondary and the primary compensations are successively considered hereunder. For emphasizing on the reactive feature of each compensation in an easily readable way, the parasitic resistances are neglected in this compensations analysis.

Secondary compensation The compensation of the secondary winding transforms the resonant WPT device in a voltage source (in the case of a series compensation) or in a current source (in the case of a parallel compensation) driven by the primary current. For demonstrating this feature, one can consider the Thevenin's equivalent circuit of a series-compensated secondary and the Norton's equivalent circuit of a parallel-compensated secondary (see Figure 1.12).

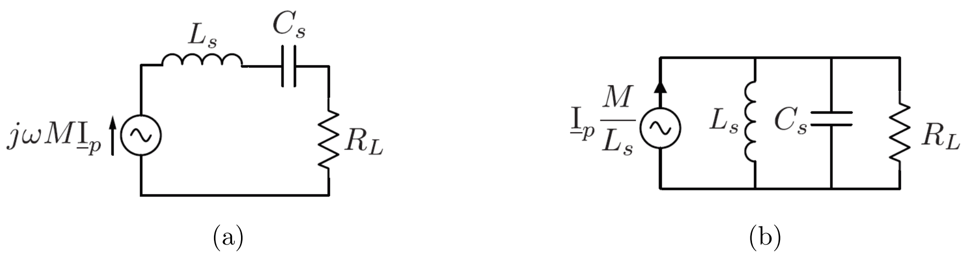

Figure 1.12: Equivalent circuit of a (a) series- and a (b) parallel-compensated secondary

At the secondary self-resonant frequency (*i.e.*, when $\omega = 1/\sqrt{L_s C_s}$), the LC-series branch in the series-compensated secondary behaves as a short-circuit and the load is directly connected to a voltage source delivering the secondary open-circuit voltage. In similar conditions, the LC-parallel mesh in the parallel-compensated secondary behaves as an open-circuit and the load is directly connected to a current source delivering the secondary short-circuit current. Theoretically, the corresponding power transfer capability is therefore infinite. In practice, the circuit components parasitic resistances limit the power transfer capability to a finite, but high value depending on the primary current. Tackled further in this section, the analysis of the transmission efficiency demonstrates moreover that the secondary compensation allows to maximize the efficiency of the resonant inductive system.

Primary compensation The primary compensation aims to minimize the volt-ampere rating of the supply power converter by cancelling the reactance and hence the reactive power consumed by the entire system, while the latter is operated at the secondary self-resonant frequency $\omega_0 = 1/\sqrt{L_s C_s}$. This is achieved by cancelling the imaginary part of the whole circuit input impedance for ensuring a zero phase angle (ZPA) between the voltage and the current delivered by the supply power converter. Therefore, the primary capacitor must not only compensate the primary winding self-inductance, but also the eventual reactance reflected from the secondary. Even operated at its self-resonant frequency, a parallel-compensated secondary produces a non-zero reflected reactance in the primary circuit. A simple way for investigating the primary compensation is the resort to the reflected impedance $\underline{Z}_r$ from the secondary to the primary (see Figure 1.13) [60].

(a) (b)

Figure 1.13: Equivalent circuit of a (a) series- and a (b) parallel-compensated primary

The reflected impedance $\underline{Z}_r$ from the secondary to the primary, coupled via a mutual inductance M is given by

$$\underline{Z}_r = \frac{\omega^2 M^2}{\underline{Z}_s} \tag{1.13}$$

where $\underline{Z}_s$ is the equivalent secondary impedance seen from the terminals of the induced electromotive force, expressed by

$$\underline{Z}_s = j\omega L_s + \frac{1}{j\omega C_s} + R_L \quad \text{for a series-compensated secondary} \tag{1.14}$$

$$\underline{Z}_s = j\omega L_s + \frac{R_L}{1 + j\omega C_s R_L} \quad \text{for a parallel-compensated secondary} \tag{1.15}$$

One can note in (1.14) the reflected reactance $\mathbf{Im}(\underline{Z}_r)$ is zero for $\omega = \omega_0 = 1/\sqrt{L_s C_s}$, but not for parallel-compensated secondary (see expression (1.15)). The mathematical development of the expressions for the primary capacitance C_p ensuring the ZPA-operation of the supply power converter has been conducted in [60] for the four conventional topologies, which are

$$C_p = \frac{1}{\omega^2 L_p} \quad \text{for a the SS topology} \tag{1.16}$$

$$C_p = \frac{1}{\omega_0^2 (L_p - M^2/L_s)} \quad \text{for the SP topology} \tag{1.17}$$

$$C_p = \frac{L_p}{\left(\omega_0^2 M^2/R_L\right)^2 + \omega_0^2 L_p} \quad \text{for the PS topology} \tag{1.18}$$

$$C_p = \frac{\left(L_p - M^2/L_s\right)}{\left(R_L M^2/L_s^2\right)^2 + \omega_0^2 \left(L_p - M^2/L_s\right)^2} \quad \text{for the PP topology} \tag{1.19}$$

One can observe that the primary capacitance C_p is

- independent from the coupling and from the load for an SS topology ;
- dependent from the coupling and independent from the load for an SP topology ;
- dependent from the coupling and from the load for PS and PP topologies.

Except for the SS topology, the primary capacitance C_p should vary according to possible changes in the coupling (impacting M), and/or in the loading conditions (impacting R_L). However, the terms which represent this (these) dependence(s) are proportional to the square of the coupling coefficient k. Consequently, the variability of the required primary capacitance is a necessary concern in practice only for coupling coefficient higher than 0.2 [61]. For weaker coupling coefficient values, the constant primary capacitance C_p designed for the primary to share a common self-resonant frequency with the secondary (*i.e.*, such that $1/\sqrt{L_pC_p} = \omega_0 = 1/\sqrt{L_sC_s}$) ensures an efficient compensation and the ZPA-operation at the output of the supply converter.

1.3.2 Frequency-splitting phenomenon

Both the inductive coupling and the resonance mechanisms are strongly associated with the alternative nature of the current and consecutively to the frequency. As a consequence, some unique effects in relation with the windings coupling occur in the frequency domain. Notably, the *frequency-splitting* (also called bifurcation) phenomenon is a specific characteristic displayed by resonant coupled windings. Here, the latter is firstly addressed qualitatively based on an intuitive physical description and is further analyzed mathematically in the case of an SS-compensated resonant inductive system.

Let us consider two coupled windings, each compensated by a capacitance such that both coupled circuits share a common self-resonant frequency. When the inductive link is weak, each circuit is operating almost independently from the other. The entire system operation can be considered as the simple superposition of each oscillator self-operation. As a consequence, the global resonant effects appear at their common self-resonant frequency and the resonant inductive system is said to be *under-coupled*. However, when the coupling strengthens, both circuits are becoming less independent from each other, and tend to form a full-fledged system of a higher order, with thus its own specific functioning. Such a system is said to be *over-coupled*. Its operation in the frequency domain is characterized by the combination of several elementary oscillators (similarly to two pendulums attached by a stiff spring in mechanics) and presents therefore multiple eigenmodes. As a result, the effective resonant frequency is duplicated in two modes, corresponding respectively to a frequency smaller and a frequency greater than the self-resonant. The more the inductive coupling increases, the more these additional frequencies distance themselves from the self-resonant one, explaining the origin of the phenomenon name (as the new resonant frequencies seem to split from the self-resonant one).

The latter qualitative interpretation is based on the physical vision of the coupled-resonance phenomenon, which is more intuitive. The quantitative analysis of the bifurcation phenomenon - keeping this physical point of view - would require to employ coupled-mode theory, which is nonetheless cumbersome. However, as demonstrated repeatedly in this chapter, each phenomenon can be observed with an equivalent circuital point of view. Notably, the frequency splitting phenomenon can be analyzed quantitatively by determining the frequencies at which the imaginary part of the resonant inductive system input impedance $\underline{Z}_i$ (as seen from the supply power converter) is cancelled, with respect to the circuit parameters. Hagiwara has achieved such analysis for the SS topology, of which the conclusions are presented hereafter for illustration purpose [66]. One can notice that a similar development for topologies involving at least one parallel compensation becomes highly cumbersome and requires numerical techniques for computing the resonant frequencies. Leaving out of the context of this thesis, such developments are not pursued here, but one has to keep in mind that the frequency splitting phenomenon affects any compensation topology.

The imaginary part of the input reactance of the SS-compensated RIPT system represented in Figure 1.11a is given by [66]

$$\mathbf{Im}(\underline{Z}_i) = \left(\frac{\omega^2}{\omega_0^2} - 1\right) \cdot \left(\frac{1-k^2}{\omega_0^4}\omega^4 + \left[C_s^2(R_s+R_L)^2 - \frac{2}{\omega_0}\right]\omega^2 + 1\right) \tag{1.20}$$

where $\omega_0 = 1/\sqrt{L_p C_p} = 1/\sqrt{L_s C_s}$. This expression is potentially cancelled for six different values of ω, but only the three positive values are realistic given the physical sense of ω. The first factor in (1.20) is cancelled systematically for $\omega = \omega_0$. The second factor presents two positive solutions (leading to a frequency splitting) when

$$\left[C_s^2(R_s+R_L)^2 - \frac{2}{\omega_0}\right] < 0 \text{ and } \left[C_s^2(R_s+R_L)^2 - \frac{2}{\omega_0}\right]^2 - 4\left(\frac{1-k^2}{\omega_0^4}\right) > 0 \tag{1.21}$$

which corresponds to two conditions relative respectively to the load R_L and the coupling coefficient k, with

$$R_L < \sqrt{\frac{2L_s}{C_s}} - R_s \quad \text{and} \quad k > \sqrt{1 - \left(\frac{C_s(R_s+R_L)^2}{2L_s} - 1\right)^2} \tag{1.22}$$

In this situation, the solution $\omega = \omega_0$ is an anti-resonance and the solutions yielded by the second factor of (1.20) are the additional resonances pertaining to the frequency splitting phenomenon. One may notice from conditions (1.22) that the load is also impacting the splitting phenomenon. As a matter of fact, a high load causes a small reflected load on the primary side and participates to the decoupling of the oscillators operations. Nevertheless, the load is fixed by the application in most cases so that the frequency splitting is essentially considered as dependent of the coupling. When the system is over-coupled, the two additional resonant frequencies are respectively given by

$$\omega_1 = \sqrt{\frac{-\left[C_s^2(R_s+R_L)^2 - \frac{2}{\omega_0}\right] + \sqrt{\left[C_s^2(R_s+R_L)^2 - \frac{2}{\omega_0}\right]^2 - 4\left(\frac{1-k^2}{\omega_0^4}\right)}}{2\left[C_s^2(R_s+R_L)^2 - \frac{2}{\omega_0}\right]^2 - 8\left(\frac{1-k^2}{\omega_0^4}\right)}} \tag{1.23}$$

$$\omega_2 = \sqrt{\frac{-\left[C_s^2(R_s+R_L)^2 - \frac{2}{\omega_0}\right] - \sqrt{\left[C_s^2(R_s+R_L)^2 - \frac{2}{\omega_0}\right]^2 - 4\left(\frac{1-k^2}{\omega_0^4}\right)}}{2\left[C_s^2(R_s+R_L)^2 - \frac{2}{\omega_0}\right]^2 - 8\left(\frac{1-k^2}{\omega_0^4}\right)}} \tag{1.24}$$

As an illustration example, the phenomenon is demonstrated on a test-case from [5] (presenting a self-resonant frequency $f_0 = \omega_0/2\pi = 1$ MHz) by depicting on Figure 1.14a the ratio between the voltage across the load and the voltage supplied by the source power converter, as a function of the coupling coefficient and the operating frequency $f = \omega/2\pi$. The solutions (1.23) and (1.24) are superposed on the figure and the evolution of the phase of the system input impedance is shown in Figure 1.14b for various values of the coupling coefficient k.

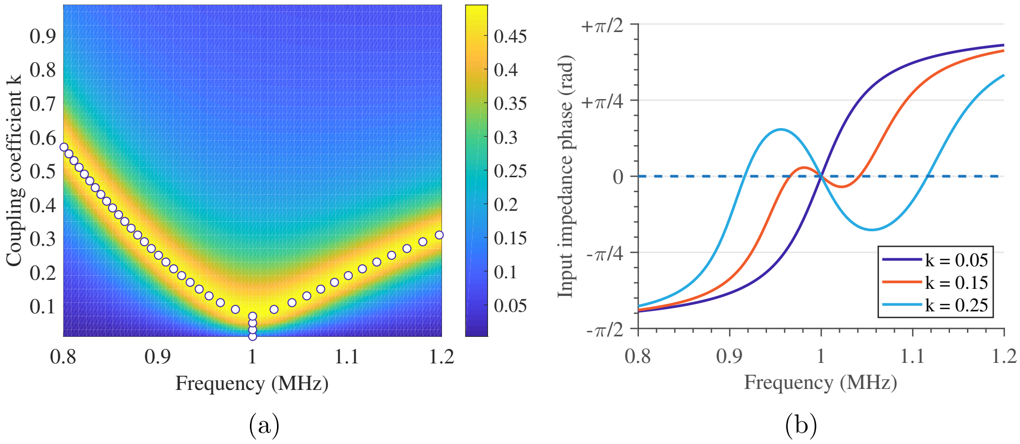

Figure 1.14: Frequency splitting in (a) the ratio between the load and the source voltages and (b) the input impedance phase

One can notice that the allure displayed by the voltage ratio in Figure 1.14a is also the allure of the output power (which is proportional to the square of the load voltage). The frequency splitting is therefore a key-phenomenon for applications seeking to maximize the transferred power, which are mainly low-power applications prioritizing the output power against the efficiency (given the smallness of the absolute losses). The adaptation of the operating frequency is accordingly required for fulfilling the power maximization objective. As the applicative framework of this thesis is focused on energy-greedy applications, our attention is drawn on the maximization of the power efficiency rather than the maximization of the output power. As evinced by Figure 1.15 for the same test-case, the power efficiency is not impacted by the splitting phenomenon and is always maximal for an operating frequency corresponding to the oscillators self-resonant frequency (as shown in the next section). As a result, an operation of the RIPT systems at the oscillators self-resonant frequency is considered in the following.

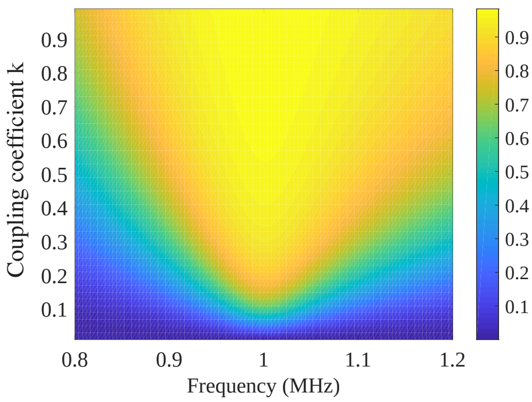

Figure 1.15: Evolution of the efficiency as a function of the operating frequency and of the coupling coefficient

1.3.3 Analysis of the transfer efficiency

The power efficiency can be defined as the ratio between the power consumed by the load on the latter power to which one adds the Joules losses occurring in the primary and secondary parasitic resistances. One has

$$\eta = \frac{R_L I_s^2}{R_p I_p^2 + R_s I_s^2 + R_L I_s^2} \tag{1.25}$$

where I_p and I_s are the RMS value of the primary and the secondary current, respectively. By applying the Kirchhoff's voltage law to the secondary circuit, the respective currents can be eliminated from the power efficiency expression since

$$\begin{aligned} j\omega M \underline{I}_p &= -(R_s + j\omega L_s + 1/j\omega C_s + R_L)\ \underline{I}_s & (1.26)\\ &= -(R_s + R_L + jX_s)\ \underline{I}_s \quad \text{with } X_s = \omega L_s - 1/\omega C_s & (1.27)\end{aligned}$$

and the RMS value of the primary and the secondary current can be related as

$$I_p = \frac{\sqrt{(R_s + R_L)^2 + X_s^2}}{\omega M}\ I_s \tag{1.28}$$

By introducing (1.28) in the expression (1.25), the power efficiency becomes independent from the currents and is expressed as

$$\eta = \frac{R_L}{R_p \frac{(R_s+R_L)^2+X_s^2}{\omega^2 M^2} + R_s + R_L} \tag{1.29}$$

From expression (1.29), the beneficial effect of the secondary compensation on the transfer efficiency is proven as the cancellation of the secondary reactance X_s ensures the maximization of the efficiency for a given set of circuit parameters. Assuming the resonant operation of the secondary (*i.e.* $X_s = 0$), the efficiency is given by

$$\eta = \frac{R_L}{R_p \frac{(R_s+R_L)^2}{\omega^2 M^2} + R_s + R_L} \tag{1.30}$$

One can observe that the efficiency depends on parameters which can be segregated in two categories, which are the lumped parameters of the transmission circuit (*i.e.* the parasitic resistances R_p and R_s as well as the mutual inductance M) intrinsically imposed by the design of the windings and the apparent load resistance R_L potentially scalable via the adequate control of the power converter interfacing the secondary circuit with the actual load. For its part, the operating angular frequency ω is not an intrinsic parameter describing the windings, but the variation of the operating frequency as a control parameter is discussed and overruled in Chapter 6, dedicated to the optimal control of RIPT system. As a consequence, the operating frequency is supposed to be imposed by the targeted application.

The maximization of the efficiency requires therefore two types of efforts from the designer of a RIPT system, namely

- the establishment of an optimal control of the power transfer corresponding to the imposition of an optimal apparent load resistance R_L using the power converters surrounding the transmission system ;

- the optimal design of the inductively coupled windings.

Optimal apparent load resistance and maximum achievable efficiency

Since the apparent load resistance R_L is an adjustable parameter during the system operation whereas the windings lumped parameters are imposed by the design, the optimal value of the apparent load R_L^{opt} is determined and assumed to be achieved prior to address the optimal design of the coupled windings. Hence, for obtaining the maximum power efficiency from a given transmission system, the apparent load resistance must meet its optimal value R_L^{opt}, defined so that

$$\frac{\partial \eta}{\partial R_L}(R_L^{opt}) = 0 \text{ and } \frac{\partial^2 \eta}{\partial R_L^2}(R_L^{opt}) < 0 \tag{1.31}$$

Solving analytically the problem (1.31) leads to

$$R_L^{opt} = R_s\sqrt{1 + \frac{\omega^2 M^2}{R_p R_s}} \tag{1.32}$$

By operating the system in order to ensure an optimal apparent load resistance R_L^{opt}, the power efficiency depends only on the lumped parameters of the windings, which are imposed physically by their respective geometries and their relative position. The corresponding efficiency is accordingly designated in this thesis as the system maximum achievable efficiency, denoted η_{max} and obtained by introducing (1.32) in (1.30), yielding

$$\eta_{max} = \frac{\omega^2 M^2}{R_p R_s \left(1 + \sqrt{1 + \frac{\omega^2 M^2}{R_p R_s}}\right)^2} \tag{1.33}$$

The expression (1.33) is valid regardless of the primary compensation and demonstrated here for a series-compensated secondary. The same but more cumbersome development has been realized for a parallel-compensated secondary in [3], leading to the same expression as (1.33) for the maximum efficiency which is thus valid regardless of the compensation topologies. As a consequence, **the maximization of the expression (1.33) can serve as a guideline for the design of the windings.**

Figure-of-merit and optimal design

The observation of the expression (1.33) reveals a figure-of-merit (FOM) on which the maximum achievable efficiency depends and with which it increases. This FOM is defined as

$$\text{FOM} = \frac{\omega M}{\sqrt{R_p R_s}} \tag{1.34}$$

so that the maximum power efficiency η_{max} can be expressed as

$$\eta_{max} = \frac{FOM^2}{\left(1 + \sqrt{1 + FOM^2}\right)^2} \tag{1.35}$$

One can notice that the expression of the FOM (by its form and the term it involves) reminds the expression of a coil quality factor. Actually, the FOM can be interpreted as a sort of quality factor not relevant for one winding only, but for a pair of coupled windings. For that matter, the FOM is equal to the geometric mean of the primary winding quality factor Q_p and of the secondary winding quality factor Q_s weighted by coupling coefficient k, with

$$\text{FOM} = \frac{\omega M}{\sqrt{R_p R_s}} = \frac{\omega k\sqrt{L_p L_s}}{\sqrt{R_p R_s}} = k\sqrt{\left(\frac{\omega L_p}{R_p}\right)\left(\frac{\omega L_s}{R_s}\right)} = k\sqrt{Q_p Q_s} \tag{1.36}$$

The maximum achievable efficiency η_{max} is strictly increasing with the FOM. The design of the windings must be driven by the maximization of the FOM under the practical constraints fixed by the targeted application. As evinced in Figure 1.16, the evolution of the maximum efficiency with respect to the FOM exhibits a saturated shape so that a further increasing of the FOM produces only a slight rise of the efficiency. This observation could be useful for establishing compromises or stop criteria in the design optimization process. The representation of the derivative of the efficiency with respect to the FOM in Figure 1.16 highlights the aforementioned saturation for FOMs higher than 20.

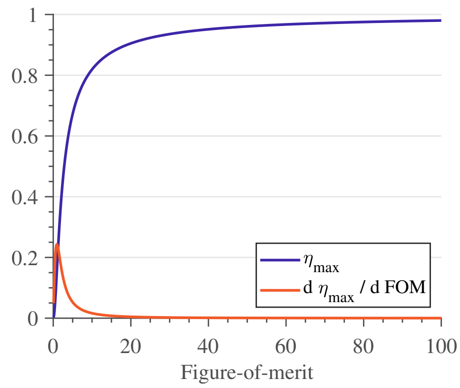

Figure 1.16: Evolution of the maximum achievable efficiency and of its derivative with respect to the figure-of-merit

1.4 Objectives of this thesis

As evinced by the analysis performed in the previous section, the maximization of the power efficiency in RIPT systems requires two types of efforts for the designer, namely

- the optimal design of the inductively coupled windings, corresponding to the maximization of the related FOM ;
- the establishment of an optimal control strategy of the power transfer operating conditions via the adequate command of the power electronic converters inherent to the exploitation of the RIPT for energy-greedy applications.

In this context, this thesis pursues a double objective, each pertaining to a different field of expertise from the Electrical Power Engineering Unit of the University of Mons.

1.4.1 First objective

The first objective pertains to the development of a flexible, accurate and fast electromagnetic model of the windings involved in RIPT. The idea is to employ the developed models in a virtual design procedure, thereby avoiding the time and money of costly experimental prototyping.

Challenges The transfer performances achievable by a given couple of windings are highly sensitive to their corresponding equivalent circuit parameters, which depend on their shape, on their relative position and can be influenced by the surrounding environment (*e.g.* the presence of a car chassis or magnetic shielding materials). Considering the limited accuracy and the restricted flexibility of the existing analytical models, as will be demonstrated in the upcoming chapters, the use of computational electromagnetics appears as mandatory for achieving this objective. Besides displaying a large flexibility in geometries and materials, the numerical modeling of the windings allows to assess accurately magnetic field distribution in the system environment so that the sanitary impact of the system (*i.e.* regarding human health issues [67, 68]) or even the possible EMI with the mobile devices of the EVs on-board electronics, can be quantified.

Nevertheless, the fine numerical modeling of the windings is subject to a significant computational burden, due to the well-known skin and proximity effects, and leads to computation times which would be not compatible with the inclusion of the resulting model in a sufficiently fast design procedure. As a matter of fact, the windings employed for RIPT are submitted to intermediate frequencies (around 100 kHz) and incur eddy-current effects (*i.e.* skin and proximity effects) which are responsible for non-negligible losses (especially regarding the high-power level envisioned for EV battery charging applications). As these effects result in localized high variations of the fields, their proper numerical modeling requires a drastic refinement of the conductors mesh and is therefore associated with important computational burden. Beyond the scope of RIPT, the modeling of eddy-current effects constitutes a topical scientific challenge by the multiplicity of disciplines in which the eddy currents modeling turns out to be necessary. Moreover, in absence of magnetic core, the accurate determination of the windings self-inductances (which are key factors in the resonant frequency tuning) and of their mutual inductance (which is as preponderant as the resistive losses in the determination of transfer performances) requires to integrate a large portion of the surrounding air in the model, with a consecutive increase of the computational burden.

Contributions In that context, the contributions of this thesis are the following.

1. The computational burden associated to the brute-force application of two-dimensional (2-D) and three-dimensional (3-D) magnetodynamic finite-element models to RIPT systems has been precisely quantified. A formulation allowing the strong coupling of the windings finite-element models circuit equations [69] has been employed, considering the importance of the external circuits in RIPT operation ;

2. An original procedure for addressing the 2-D meshing of winding conductors subject to eddy currents has been proposed, which provides results at least as accurate than traditional meshing strategies, based on a best-practice approach ;

3. The potential of the 3-D generalized partial element equivalent circuit method (PEEC) in magnetodynamics [70] has been quantified with respect to the modeling of RIPT systems. Indeed, the PEEC method is an integral method which does not require to mesh the air volume surrounding the windings, and appears therefore as an interesting candidate for the modeling of RIPT coils ;

4. Aware of the importance of 3-D models of the windings (*e.g.* for considering misaligned windings or for the integration of surrounding objects) despite their proven heaviness, a 3-D finite-element model with surface impedance boundary condition [71–73] and strong circuit coupling has been developed. The proposed model permits to avoid the volume meshing of the conductor windings, thereby decreasing the computational burden ;

5. An experimental validation of all the proposed numerical models has been pursued, as well as a comparison with the most accurate analytical formulae available in the literature as for today ;

6. A fully parametrized virtual laboratory which gathers all the numerical models developed in this thesis has been developed in the ONELAB environment [74, 75]. The proposed tool is particularly well-adapted to an integration in an optimization process for *e.g.* the sizing of the windings.

The publications relative to these contributions are (in chronological order)

- A. Desmoort, Z. De Grève and O. Deblecker, "A virtual laboratory for the modeling of Wireless Power Transfer systems," *2015 International Conference on Electromagnetics in Advanced Applications (ICEAA)*, Turin, Italy, 2015, pp. 1353-1356.

- A. Desmoort, Z. De Grève and O. Deblecker, "Analytical, Numerical and Experimental Modeling of Resonant Wireless Power Transfer Devices (Research & Development Award)," in *SRBE/KBVE Revue E Tijdschrift*, 132nd year, no. 1-4, 2016.

- A. Desmoort, J. Siau, G. Meunier, J.-M. Guichon, O. Chadebec, O. Deblecker, "Comparing partial element equivalent circuit and finite element methods for the resonant wireless power transfer 3D modeling," *2016 IEEE Conference on Electromagnetic Field Computation (CEFC)*, Miami, United States, 2016, pp. 1-1.

- A. Desmoort, Z. De Grève, P. Dular, C. Geuzaine and O. Deblecker, "Surface impedance boundary condition with circuit coupling for the 3D finite element modeling of wireless power transfer," *2016 IEEE Conference on Electromagnetic Field Computation (CEFC)*, Miami, United States, 2016, pp. 1-1.

- A. Desmoort, Z. De Grève, P. Dular, C. Geuzaine and O. Deblecker, "Surface Impedance Boundary Condition With Circuit Coupling for the 3-D Finite-Element Modeling of Wireless Power Transfer," in *IEEE Transactions on Magnetics*, vol. 53, no. 6, pp. 1-4, June 2017, Art no. 7402104.

- A. Desmoort, Z. De Grève and O. Deblecker, "Modeling and Optimal Control of Resonant Wireless Power Transfer," *2018 IEEE Young Researcher Symposium Benelux (YRS2018)*, Brussels, Belgium, 2018.

1.4.2 Second objective

The second objective pertains to the elaboration of an optimal control strategy for the power converters surrounding the transmission coils, in order to ensure the wireless transfer of energy with a maximum coil-to-coil efficiency, despite non-idealities related to real operating conditions.

Challenges Considering the implementation of RIPT to energy-greedy applications requires to pay a particular attention on the system optimal operation, since each percent of its power efficiency represents a non-negligible amount of power. Maintaining a constant output power is also capital for complying with standards fixing a specific rated power. Therefore, an adequate control is mandatory for practicable domestic and industrial WPT applications.

Moreover, non-idealities pertaining to real operating conditions can have a significant impact on the WPT coils circuit parameters. A simple misalignment between the windings, which can occur frequently in practice, modifies for instance the value of the coils mutual inductance. Furthermore, ageing or defaults in electrical circuit components such as the resonant capacitors may alter the resonant state of operation of the system. These parameters deviations have a strong impact on the power efficiency of the WPT system.

Contributions In that regard, the contributions of this thesis are the following.

1. An original optimal command strategy for bidirectional series-series compensated WPT systems has been proposed. The command is based on a resonant dual active bridge (RDAB) topology, which enables (via the adequate command of the active rectifier) the control of the active as well as the reactive power flows in the system in order to operate at the maximum achievable efficiency, despite the deviations in the circuit parameters values (*e.g.* the windings mutual inductance, the resonant capacitances or the load) which may occur in practice ;

2. The consideration of voltage step-up solutions (namely the insertion of current-reversible two-quadrant choppers and the transition to Z-source converters) has been investigated for improving the proposed RDAB topology, in order to increase the operating range where the proposed command strategy can be achieved, thereby ensuring the robustness to larger circuit parameters deviations ;

3. The proposed optimal command strategy has been generalized to parallel-parallel, series-parallel and parallel-series compensated bidirectional WPT systems, through the use of an original approach via appropriate equivalent circuit transformations ;

4. A successful low-power 20-W experimental proof-of-concept of the proposed optimal command strategy has been realized in laboratory, based on a series-series compensated system. Time domain simulations were in that way validated experimentally, and the robustness of the proposed command strategy with respect to various types of circuit parameters deviations (mutual inductance and resonant capacitance) has been demonstrated.

As highlighted previously, the concept of RIPT can be employed in a wide range of applications, from low to high power, as discussed previously. Nevertheless, for consistency with the usual research activities of our Unit, this thesis focuses on wireless electric vehicle charging applications, so that the tools and models developed in this work will systematically be illustrated and discussed on EV charging case studies. More particularly, an operating frequency of 85 kHz and a rated output power of 3.7 kW will be assumed, in accordance to the recent standard SAE J2954 in EV charging [32]. A particular attention has however been paid to provide generic tools and models, in the sense that these could be applied to other RIPT applications with minor modifications.

The publications relative to these contributions are (in chronological order)

- A. Desmoort, O. Deblecker and Z. De Grève, "Active Rectification for the Optimal Control of Bidirectional Resonant Wireless Power Transfer," *2018 International Symposium on Power Electronics, Electrical Drives, Automation and Motion (SPEEDAM)*, Amalfi, 2018, pp. 756-761.

- A. Desmoort, O. Deblecker and Z. De Grève, "Active Rectification for the Optimal Command of Bidirectional Resonant Wireless Power Transfer Robust to Severe Circuit Parameters Deviations," in reviewing process in *IEEE Transactions in Industry Applications*

1.5 Structure of this report

This thesis report is organized in two distinctive parts, each part being dedicated to one of the aforementioned objectives.

Chapter 2 opens the first part, dedicated to the electromagnetic modeling of RIPT windings, and proposes the related state of the art. Chapter 3 presents the theoretical aspects relative to the computational electromagnetic methods employed in this thesis. Chapter 4 gathers the presentation of the different computational models employed and developed in the framework of this thesis, associated with discussions based on topical numerical results, destined to mark out our investigations concerning the windings electromagnetic modeling.

As an introduction to the second part of this thesis (dedicated to an optimal command strategy for RIPT systems), Chapter 5 describes the power converter topology and command which will be employed in the following, through the prism of the resonant converter concept. In Chapter 6, after an analysis of the related state of the art and the clarification of the positioning of this thesis, the original optimal command methodology for series-series compensated RIPT systems proposed in this thesis is developed, illustrated and discussed via frequency- and time-domain simulations of an EV test-case. For extending the controllability range associated with the latter method, the two aforementioned voltage step-up solutions are presented and compared in Chapter 7. Further, Chapter 8 exposes the extension of the applicability scope of the proposed methodology to parallel-parallel, series-parallel and parallel-series compensated systems. Frequency- and time-domain simulations for the EV test-case employed previously are presented and discussed for a parallel-parallel compensated system commanded via the extended methodology. The proof-of-concept destined to the experimental validation of the proposed methodology is presented in Chapter 9. Finally, Chapter 10 gathers the general conclusions and exposes the perspectives of this thesis.

Part I

Electromagnetic modeling of resonant inductive power transfer windings

CHAPTER

TWO

STATE OF THE ART

Usually, transformers are peripheral and utilitarian components destined to achieve a well-defined function (*e.g.* voltage transformations or galvanic insulation). For holistic approaches, the transformers are assumed ideal, or impacted by limited non-idealities with abstraction for their actual material and geometric design. Only transformers manufacturers have to address the latter. However, in the case of WPT, the windings are the key components of the system and their design has an important impact on the whole system performances. The diversity in WPT applications goes hand in hand with the diversity on the windings design. Therefore, an accurate and flexible model of the windings is mandatory for adopting a general approach of the system, while integrating directly its disparate non-idealities in the study.

An accurate mathematical model is a powerful tool, dear to the engineer. By representing as precisely as possible the behaviour of a system, the model obviates the time and the cost of experimental prototyping and allows quick and free testing procedures. During the modeling step, mathematical trends may appear and highlight particular dependencies between intrinsic properties and resulting quantities of interest. The design and the analysis of the modeled system can consequently be more adapted and efficient. Besides traditional analytical modeling techniques, the evolution of the computational tool has fostered the resort to numerical modeling techniques, which are precisely addressed in this thesis.

In this chapter, the electromagnetic modeling of windings for WPT is introduced in three steps. Since a system electromagnetic modeling is tightly associated with its geometry and its material properties, the description of a typical WPT winding is firstly proposed. As the most popular approach for the characterization of WPT windings, analytical modeling techniques are reviewed and a best-effort analytical model is proposed, based on a literature review. Then, a general overview of computational electromagnetics applied to WPT windings is presented. Finally, the positioning of this work in the state of the art is described, and the modeling objectives are clarified in consequence.

2.1 Description of typical wireless power transfer coils

The description of the main characteristics of the WPT windings is mandatory for their efficient modeling. Hence, in this section, a literature review permits to establish the template of a typical WPT winding for decreasing as best as possible the complexity of the future model. Also, the parameters of the design are clarified for a clear identification of the inputs of the model.

Shape of a WPT winding

Generally, a WPT winding is flat-shaped in order to ease its integration in a device or a vehicle external panel. As a consequence, it is either a single-layer solenoidal coil with a limited number of turns, a planar spiral coil or a combination of both (*i.e.*, a multiple-layer solenoidal with a limited number of turns). The planar coil presents a better coupling robustness in case of misalignment in comparison with the single-layer solenoidal coil, and requires less conducting material than the multiple-layer coil, so that it is usually preferred by the scientific and industrial communities. Such a circular planar spiral coil is also called a *pancake* coil (see Figure 2.1). Since pancake coils are very specific to the WPT application, the modeling efforts carried out within the WPT framework are mainly concentrated on them. In this thesis, we decided to follow this trend. A pancake coil is described by four parameters which are its inner radius R, the wire radius r, the number of turns N and the spiral pitch p. Browsing the literature, numerous pancake-derivative designs emerge, but the model can be restricted to the pancake coils for granting a sufficient generality while providing particularization possibilities.

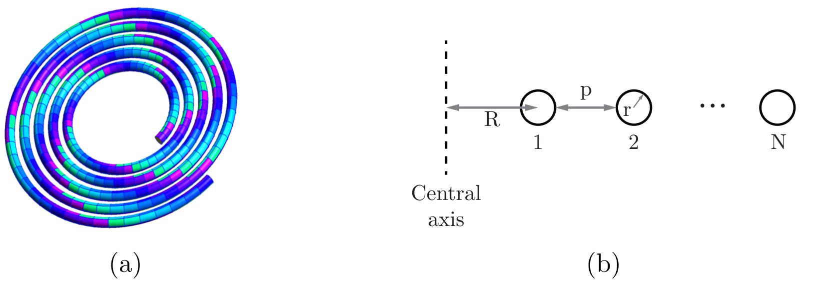

Figure 2.1: (a) Schematic and (b) sectional view of a pancake winding

Solid and Litz wires

The wire forming a WPT coil can be either a solid wire or a Litz wire. As a reminder, a Litz wire consists in a bundle of multiple smaller strands which aims at reducing the effects of eddy currents on the AC resistance of the wires. More precisely, the strands are typically designed to have a radius significantly smaller than the skin depth at the operating frequency, so that the current in each strand is uniform and the AC resistance is small. By twisting adequately the bundle, each strand incurs in average the same electromagnetic influence than the others, which prevents from the circulation of eddy current loops between parallel strands, with a beneficial lowering effect on the AC resistance. Depending on the envisioned application, Litz wire may provide substantial improvements on the system performances, but can also lead to additional losses in case of improper usage. The efficiency of Litz wire is therefore pertaining to the wire manufacturer and user as well. Moreover, and as discussed in Section 2.3, efficient modeling techniques for Litz wire are already available in the literature so that our contribution will focus on the challenging modeling of solid wire submitted to intermediate frequencies. From an applicative point of view, solid-wire windings are not devoid of interest. In the operating conditions targeted by this work, solid-wire windings still present interesting figure-of-merits in the saturation range of the maximum achievable efficiency. Whereas the Litz wire is designed for a specific frequency range, the solid wire is more accessible, more simple and cheaper, and is therefore more adapted to the windings elaboration for the establishment of multiple experimental validations setup in our laboratory.

Couplers

For completeness purposes, one can mention that a WPT coil can be associated with a piece of magnetic material (usually ferrite) called a *coupler* and placed on the side of the coil which is opposite to the transfer direction [19, 76, 77]. The latter material acts as a shield stopping the development of useless magnetic flux lines outside the WPT system, and redirecting the magnetic flux in the power transfer direction. For pancake coils, the typical coupler is a circular plate. An alternative for saving ferrite materials consists in placing uniformly distributed radial ferrite bars instead of an entire plate (see Figure 2.2). Improving the coupling between the coils, the coupler must be cleverly designed and placed for avoiding additional losses. As a matter of fact, the couplers support local rises in the magnetic flux density and an eventual misplacing could lead to increased eddy-current effects and subsequent losses in the related coil. This work focuses on totally coreless windings, as it aims at implementing a progressive approach. Nevertheless, the developed virtual laboratory is sufficiently flexible to include couplers as well, provided that an accurate model of ferrite losses at high frequencies is available.

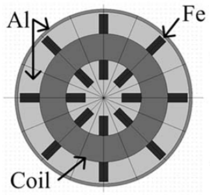

Figure 2.2: Upper view of an example of a coupler made of radial ferrite bars

2.2 Analytical techniques

The use of analytical approaches is the most common method for modeling solid-wire WPT windings, widely available and investigated in the literature [66, 78–83]. Except for some empirical laws, these approaches are for most based on the analytical development of the Maxwell's equations, made possible by approximations and/or by the realization of simplifying hypotheses on the conductors shape or on their operating conditions. The analytical approaches main advantages rely in the implementation simplicity and the computation speed (as the modeling comes down to the evaluation of a few formulae). The analytical approaches main drawbacks are the poor adaptability and the restricted range of applicability (as the hypotheses limit the number of input parameters), which can lead to a questionable accuracy for specific cases and which does not comply with the targeted virtual laboratory approach.

One can note that analytical models for usual transformers [84–87] (which are accurate due to the averaging effect of the high number of turns) are not applicable to the pancake coils due to the predominance of the edge effects, since the coils are made of one flat layer of turns. For making the analytical modeling possible, the pancake coils are approached by a combination of concentric tori, for which analytical developments exist. However, in the existing works, two typical shortcomings have been identified in the analytical modeling of WPT windings, namely

- the evaluation of the coils parasitic resistance in DC conditions only, whereas the skin and proximity effects can generate significant power losses
- the evaluation of the coils mutual inductance with approximate formulae, only applicable when the coils axes are aligned, whereas the inductive coupling is a key factor and should be evaluated even in misaligned configurations.

A thorough literature review has been conducted for gathering the most accurate analytical approaches, which are reported here with three purposes, which are (by order of importance)

1. the illustrated description of the different effects to render in the windings modeling (with the analytical, as well as with numerical approaches) ;
2. the constitution of a reference model for the validation of the numerical tool developed further in this thesis (with testing conditions within the analytical model validity domain) ;
3. the argued highlight of the analytical approaches limitations.

2.2.1 Series resistance

The series resistance of windings is described using three different contributions.

Direct-current resistance The first contribution is associated with the inherent property of any conductor to physically oppose a resilience to a current flow. This contribution is usually called the direct-current (DC) resistance in opposition with the others contributions, which are due to the alternative nature of the current. The conductor DC resistance R_{DC} is evaluated via the Pouillet's law, which yields

$$R_{DC} = \frac{l}{\sigma S} \tag{2.1}$$

with l the length of the conductor, σ the conductivity of the conductor and S the cross-section of the conductor. The conductor length being often fixed by the targeted application, the reduction of this first contribution to the series resistance is achieved by the increase of the conducting cross-section or by the choice of a high-conductivity material.

Skin effect The second contribution is associated with the alternative nature of the current crossing the windings and is called the *skin effect* resistance. An alternative current flowing in a conductor can be decomposed in elementary currents crossing elementary sections in the conductor. Each elementary current generates a local magnetic field which induces in turn an eddy current tending to decrease the current density locally by Lenz's law. Completely surrounded by those elementary currents, the center of the conductor is logically more impacted than the conductor boundary by this local effect. The total current is therefore concentrated in a more or less thin portion nearby the conductor boundary which is called the conductor *skin* (lending its name to the related effect). More precisely, well-known developments have demonstrated that the current density is decreasing exponentially from the conductor boundary to its center. The strength of the skin effect is described by a spatial quantity called the skin depth δ and corresponding to the distance from the conductor surface where the current reaches 37 % of its value at the conductor surface. The skin depth δ is rigorously given by

$$\delta = \sqrt{\frac{2}{\omega \mu \sigma}} \tag{2.2}$$

where ω is the angular frequency (or the pulsation) of the current and μ is the magnetic permeability. The frequency is the key-parameter for addressing the skin effect impact. The higher the frequency is, the thinner the current skin is and the higher the effective resistance of the conductor is. Mathematically, the contribution of the skin effect can be factored in with a coefficient F_S which multiplies the DC resistance. Hence, the alternative current (AC) resistance of a conductor submitted to the skin effect is [87]

$$R_{AC} = F_S \; R_{DC} \tag{2.3}$$

where F_S depends on the skin depth δ and on the conductor shape. For the round conductors addressed in this work, the skin effect factor F_S is rigorously equal to

$$F_S = \frac{\alpha}{2} \frac{ber\,(\alpha)\,bei'\,(\alpha) - bei\,(\alpha)\,ber'\,(\alpha)}{\left[ber'\,(\alpha)\right]^2 + \left[ber'\,(\alpha)\right]^2} \tag{2.4}$$

where $\alpha = \sqrt{2}\,r_c/\delta$ (with r_c the conductor section radius), ber and bei are the Kelvin functions and ber' and bei' are their respective derivatives.

Proximity effect The third and last contribution is associated on the one hand with the alternative nature of the current and on the other hand with the presence of nearby conductors. It is called the *proximity effect* resistance. Windings are inherently impacted by proximity effect as two adjacent turns are locally seen as two nearby conductors. As mentioned above, the alternative nature of the current generates a local magnetic field resulting in the appearance of eddy currents. When two or more conductors are sufficiently close, mutual magnetic influences occur and reshape the current distribution in each conductor. The disparate current density in the impacted conductors leads ineluctably to a raise of their effective resistance. The very essence of the proximity effect highlights the complexity of its mathematical analytical modeling, which is still an open problem. As a matter of fact, the impact on each conductor depends not only on its own properties, but also on the nearby conductor(s) properties and positions and on external electromagnetic conditions.

Instead of ignoring the proximity effect impact, a best-effort approach is implemented by using a proximity factor G_p proposed and tabulated by Smith [88], so that the total AC resistance of the windings can be expressed as

$$R_{AC} = (1 + G_p)\ F_S\ R_{DC} \tag{2.5}$$

One have to note that this approach is employed as a last resort, but leads to a relative error between 10 % and 25 % on the total resistance according to the comparison with experimental measurements and with the numerical results furnished by to the virtual laboratory developed in the following.

2.2.2 Self- and mutual inductances

Accurate approaches exist for the determination of the self- and the mutual inductances of single loops, so that the coils inductances are obtained by combining adequately the individual loops parameters.

The self-inductance L_i of a loop i is evaluated in the air and in DC conditions (since it is assumed to be slightly affected by the frequency [89])

$$L_i = \mu_0 R_i \left[\ln\left(\frac{8R_i}{r}\right) - 2\right] \tag{2.6}$$

where μ_0 is the vacuum magnetic permeability, R_i is the loop radius and r is the wire radius.

Babic *et al.* have developed an accurate analytical form for the mutual inductance between two single loops arbitrarily positioned in the air and in DC conditions (like the self-inductance, the mutual inductance is supposed to be slightly affected by the frequency) [90]. The main advantage of this approach is the free positioning of the loop, which can be misaligned or angularly shifted. The exact formula depends on no more than eleven parameters which are functions of the loops radii and relative position. Highly cumbersome, it is note reported here. By consulting the work proposed by Babic *et al.*, the interested reader will ascertain the approach sophistication, which allows to seize the effort (or even the impossibility) for extending such development to more complex cases, *e.g.* including magnetic materials (such as couplers).

Now that the formulae for single loops have been clarified, the inductances relative to entire coils are obtained by combining adequately the constituting loops parameters. A coil self-inductance is the combination of each loop self-inductance with the mutual inductance between each loops couple, *i.e.*

$$L = \sum_{i=1}^{N} L_i + \sum_{i=1}^{N} \sum_{\substack{j=1 \\ j \neq i}}^{N} M_{ij} \tag{2.7}$$

where M_{ij} is the mutual inductance between a loop i and a loop j. The mutual inductance between two coils is the combination of the mutual inductance between each loop from the first coil and each loop from the second coil, with

$$M = \sum_{i=1}^{N_1} \sum_{j=1}^{N_2} M_{ij} \tag{2.8}$$

where N_1 and N_2 are the number of turns in the first and in the second coil, respectively.

2.3 Computational techniques

The electromagnetic modeling of WPT windings falls within the wider field of study related to the modeling of wound components solicited by intermediate-frequency currents. Although this makes the methods proposed in the following applicable to wider problems, it complicates the exhaustivity of the literature review. Therefore, the following state of the art focuses on typical contributions, and summarizes the main trends in WPT windings numerical modeling.

2.3.1 Finite-element method

The finite-element method is a well-known and proven computational approach, with an inherent flexibility in geometries and materials. Most contributions employ the finite-element method for the modeling of WPT windings. Among these, a substantial share is using the finite-element method for characterizing specific test-cases, as a validation step in a more global process. Usually, in the literature, the information about the modeling methodology is deficient and the authors rely on flourishing finite-element software solutions, employed as black boxes [91, 92]. However, other contributions illustrate substantively the current state of the art for the finite-element modeling of WPT windings. Different approximation levels have been investigated by the academia in that context.

WPT windings are mostly modeled as **stranded conductors**, immune to the appearance of eddy currents. In such formulations, the winding windows are replaced by a homogeneous conductor in which the current density distribution is uniform. Intrinsically inappropriate for solid-wire windings, the stranded conductor assumption is however relatively relevant for the Litz-wire windings. Notably, Hariri *et al.* have implemented this technique for the virtual prototyping of Litz-wire windings [93]. In another publication, the same authors have employed their tool for training a neural network driven by a genetic algorithm destined to the Litz-wire coil design [94]. Bosshard *et al.* have implemented a similar approach complemented by an analytical evaluation of the skin-and proximity-effect losses in the Litz-wire bundle [95].

Homogenization techniques have been applied to Litz-wire and to solid-wire WPT windings. These techniques can be interpreted as advanced stranded-conductor formulations, where the proximity effect is considered locally by using a complex magnetic reluctivity and where the skin effect is included globally by the determination of an adequate skin-effect series impedance [96]. The latter reluctivity and impedance are previously determined via a normalized fine modeling (using a massive-conductor formulation) of the conductors forming the micro-structure pattern. Klis *et al.* have implemented such a technique on Litz-wire windings, by homogenizing the entire winding windows, with a complex reluctivity and a skin-impedance based on the micro-structure at the level of the Litz-wire strands [97]. Ferreira *et al.* have contributed to the characterization of solid-wire WPT windings by homogenizing the entire winding windows, based on a micro-structure considering a single solid wire [98]. Presenting interesting results for the input impedance of complete WPT systems with windings including more than twenty turns, the latter method is supposed to deliver less accurate results for the self-parameters determination applied to windings with less than fifteen turns, as investigated in this work. Indeed, homogenization models are based on the assumption that an elementary pattern is repeated periodically over the entire winding window. The low resolution of the micro-structure (consisting in a single wire, as a reminder) in the homogenized region can be problematic.

Hence, in the literature, the contributions proposing to model finely the eddy currents occurring in solid-wire windings via **massive conductor formulations** are either weakly documented or inexistent, due to the expected computational burden entailed by the mesh refinement for rendering accurately the skin and proximity effects. Nevertheless, the majority of contributions are considering operating frequencies within the 1-to-10 MHz range, while the targeted frequency level in this thesis is around 100 kHz, so that the massive conductors modeling cumbersomeness could be mitigated.

2.3.2 Integral methods

Given the large share of free-space in a WPT system, integral methods have logically been considered for the WPT coils electromagnetic modeling. As a matter of fact, these methods are based on an integral formulation of the electromagnetic fields, so that the spatial integral bond accounts "remotely" for the interaction between two distant parts of the discretized geometry. The direct consequence is the exclusion of the ambient medium (*i.e.* the air) from the discretized model, with a significant decrease in the number of numerical unknowns when it is applied to free-space systems. However, the numerical integrations for assembling the system of equations, as well as numerical difficulties when solving the resulting system of equations (coefficient matrices are full with integral methods, whereas there are sparse with finite-element method), mitigate the consecutive computational gain. Also, most integral formulations require to discretize the system geometry in a structured mesh for ensuring their validity, limiting their scope of application.

In the framework of WPT and due to their intrinsic application constraints, the integral methods have been employed for characterizing the electromagnetic influence on the outside environment of a WPT system, or the inductive coupling only (without resistive losses), in the 1-to-100 MHz range. For characterizing the electromagnetic influences of a WPT system, a method of moment (MoM) has been used for representing the electric field of a coil approached as a filament, whereas the scattered field is computed on neighboring objects via the finite-element method [99]. In another contribution, the coils are considered as perfect conductors and assimilated to infinitely thin conducting tubes for evaluating the inductive coupling and the associated performances of a WPT system [100]. The contribution matching the most the scope of this thesis is proposed by Huang *et al.* [101]. They have proposed a volume integral method for the characterization of WPT windings, represented as a homogeneous stranded domain with a simple shape. Such an implementation demonstrates the computational gain offered by an integral method in comparison with the finite-element method. However, as for finite-element contributions, the detailed modeling of solid-wire coils impacted by eddy-current effects is not addressed currently in the literature.

2.4 Positioning of this thesis

In the light of the foregoing, we propose to investigate the solid-wire WPT windings modeling as massive conductors for the fine determination of the eddy currents impact on the system, under intermediate frequency-levels (around 100 kHz). **The latter investigation concerns the identification of the actual computational burden associated with the application of the finite-element method based on a massive conductor formulation, as a brute-force approach. Discussions on this burden will drive the research for improvements via the development and/or the application of original methods for the WPT windings computational electromagnetic modeling.**

With the increasing power of the computational tool, integral methods become gradually adapted to an implementation on complex geometries operated at low frequencies, targeting electrical engineering industrial systems. Notably, the Grenoble Electrical Engineering Laboratory (G2ELab) in France (which whom we collaborate) is currently developing a generalized implementation of the partial element equivalent circuit (PEEC) method, based on the transformation of the electromagnetic problem expressed on a structured mesh in a circuit problem via integral formulations. The main feature of this generalization is the inclusion of unstructured meshes, more adapted for curved geometries through the use of facet elements, borrowed from the finite-element community, for approximating the current density in conductors. Using simple windings and working at intermediate frequency, WPT represents an interesting test-case, as an intermediate step in this transition effort. In return, the generalized PEEC appears to be an elegant alternative to the finite-element method, due to the absence of any need to mesh the air (which represent the most important part of the system) and to its circuit interpretation. Our collaboration with the G2ELab has granted us a direct access to an under-development version of the generalized PEEC method, as part of the MIPSE (*Modeling of Interconnected Power SystEms*) project. **As a consequence, we propose to take advantage of this opportunity for assessing the potential of the generalized PEEC method for the fine modeling of solid-wire WPT coils**.

As a scientific as well as an engineering contribution, **the different modeling techniques developed in this part of the thesis will be using flexible and adequate software materials for implementing a virtual laboratory approach**. In other words, our computational electromagnetic tool will be built as a fully parametrized tool for easily considering any set of parameters. A modularity effort will guarantee the embedding of different formulations. Once validated, such a tool will act as a virtual laboratory for the WPT windings design and characterization, saving the precious time and money associated with experimental prototyping. Since the modeling of the sole conductors is expected to be sufficiently challenging, the inclusion of couplers or surrounding components (*e.g.* a car chassis) is not addressed here. However, the virtual laboratory will be built with a particular attention to its modularity capabilities and provide input for the future inclusion of such components.

CHAPTER

THREE

COMPUTATIONAL ELECTROMAGNETICS

The study of electromagnetic systems implies to understand complex phenomena which require a precise knowledge of the electric and magnetic field space-time distributions. Such a precision necessitates to solve the most fundamental equations in the field of electricity, *i.e.* the Maxwell's equations. However, these consist in a set of vector partial differential equations which are coupled, so that an analytical resolution is not practicable (except for very simple systems). Computational electromagnetics develops numerical methods for solving such problems, at the expense of adequate hypotheses and discretizations from various natures. Fostered by the development of the computer tool, their use has spread quickly during the last decades.

This chapter presents the theoretical aspects associated with the numerical methods employed in this work, based on references [102–105]. Two different methods are used, namely the finite-element method and the generalized inductive partial element equivalent circuit method. Since the generalized PEEC partially benefits from the finite-element concept, the approach associated with the finite-element method is addressed first, and the theory is thereafter extended to the PEEC method. In the following, the bold lower case letters are referring to vectors and bold upper case in brackets are referring to matrices.

3.1 Maxwell's equations

Maxwell's equations are a set of vector and partial differential equations which constitutes the most advanced and the most complete mathematical model for the description of electromagnetic phenomena in classic physics. The local forms of the Maxwell's equations in a continuous space are

$$\text{curl } \mathbf{h} = \mathbf{j} + \frac{\partial \mathbf{d}}{\partial t} \tag{3.1}$$

$$\text{curl } \mathbf{e} = -\frac{\partial \mathbf{b}}{\partial t} \tag{3.2}$$

$$\text{div } \mathbf{b} = 0 \tag{3.3}$$

$$\text{div } \mathbf{d} = \rho \tag{3.4}$$

where $\mathbf{h}$ is the magnetic field (in A/m), $\mathbf{j}$ is the current density (in A/m^2), $\mathbf{d}$ is the electric displacement or electric flux density (in C/m^2), t is the time (in s), $\mathbf{e}$ is the electric field (in V/m), $\mathbf{b}$ is the magnetic flux density (in T) and ρ is the volume charge density (in C/m^3).

Those equations are coupled via three constitutive laws describing the behavior of the matter when it is solicited by the different fields, which are

$$\mathbf{b} = \mu \cdot \mathbf{h} \tag{3.5}$$

$$\mathbf{d} = \epsilon \cdot \mathbf{e} \tag{3.6}$$

$$\mathbf{j} = \sigma \cdot \mathbf{e} \tag{3.7}$$

where μ is the magnetic permeability (in H/m), ϵ is the electric permittivity (in F/m) and σ is the electric conductivity (in S/m) of the considered medium. Usually, the permeability and permittivity are respectively defined with respect to the constant vacuum permeability $\mu_0 = 4\pi \cdot 10^{-7}$ H/m and vacuum permittivity $\epsilon_0 = 8.85 \cdot 10^{-12}$ F/m, so that

$$\mu = \mu_0 \cdot \mu_r \tag{3.8}$$

$$\epsilon = \epsilon_0 \cdot \epsilon_r \tag{3.9}$$

with μ_r and ϵ_r the relative permeability and the relative permittivity of the considered medium, respectively. The permeability, the permittivity and the conductivity can take the form of a tensor (*e.g.* for an anisotropic medium), and can depend on the fields intensity (*e.g.* for a non-linear medium) and history (*e.g.* for an hysteretic medium).

3.2 Formulation of the magnetodynamic problem

The constitutive laws entail a strong mathematical coupling between the Maxwell's equations that prevents a direct resolution of electromagnetic problems (except for the most elementary systems). Depending on the nature of the addressed problem, adequate hypotheses can however decouple and simplify the equations set. The identification of the prevailing phenomena is therefore essential for the simplification of the problem with a limited impact on the solution accuracy. Also, the formalism of the simplified problem is alleviated by the introduction of intermediary variables, called *potentials*. The combined choices of a simplified model and of the potentials to express the problem yields the *formulation* of the problem.

3.2.1 Electromagnetic models

The choice of an adequate electromagnetic model depends on the prevailing phenomena, which can be identified by considering the fields frequency and the size of the investigated system. As a matter of fact, the electromagnetic field presents two regions, which are the far- and the near-field regions. In the far-field region (*i.e.* when the size of the system is comparable to the field wavelength), the evolutions of the electric and magnetic fields are interdependent and inseparable, leading to the concept of the electromagnetic wave. The electromagnetic models corresponding to this kind of problem are labelled as *full-wave* models and outreach the context of this thesis. In the near-field region (*i.e.* when the size of the system is very small in comparison with the field wavelength), the evolutions of the electric and magnetic fields are independent, so that each field can be treated separately. In this thesis, the frequency range is delimited by the upper bound of 1 MHz corresponding to a minimum wavelength of 300 meters, whereas the WPT system size will not exceed 1 meter. The investigated problems are clearly situated in the near-field region. Beside the fields decoupling, an efficient modeling requires to assume further hypotheses leading to different near-field electric and near-field magnetic models. Those models are detailed here with their corresponding assumptions, and the choice of the suitable model for the WPT windings modeling is discussed.

Near-field electric models

The near-field electric models are relevant for the description of the electric field distribution and of the related effect(s) on the matter. The corresponding equations ensue from the decoupling of equations (3.1) and (3.2), by the negligence of the time-variation of $\mathbf{b}$ in the equation (3.2). Hence, the most complete electric model pertains to *electrodynamics*, described by

$$\text{curl } \mathbf{h} = \mathbf{j} + \frac{\partial \mathbf{d}}{\partial t} \quad (3.1) \qquad\qquad \text{curl } \mathbf{e} = 0 \quad (3.10)$$

which accounts for the electric field and the electric current distributions in insulating and conducting materials. Depending on the problem, further simplification can be applied within the scope of the electric field study. Hence, *electrostatics* focuses on the electric field distribution in insulating materials due to static charges and constant levels of electric potential, based on equations (3.4) and (3.10) solely. Finally, *electrokinetics* focuses on the static current distribution in conducting regions submitted to a constant electric potential difference, by neglecting the time-variation of $\mathbf{d}$ in front of $\mathbf{j}$ in (3.1). Those models are essentially appropriate for evaluating the system capacitive and dissipative properties when it incurs constant (or null) currents.

Near-field magnetic models

The near-field magnetic models are relevant for the description of the magnetic field distribution and the related effect(s) on the matter. The corresponding equations ensue from the decoupling of $\mathbf{d}$, by the negligence of its time-variation in front of $\mathbf{j}$ in the equation (3.2). Hence, the most complete magnetic model pertains to *magnetodynamics*, described by

$$\text{curl } \mathbf{h} = \mathbf{j} \quad (3.11) \qquad \text{curl } \mathbf{e} = -\frac{\partial \mathbf{b}}{\partial t} \quad (3.2) \qquad \text{div } \mathbf{b} = 0 \quad (3.3)$$

which accounts for the magnetic field and the eddy current distributions due to moving magnet and space- or time-variable currents. *Magnetostatics* focuses on the static magnetic field distribution due to stationary magnets and static currents, based on equations (3.3) and (3.11) solely. Those models are essentially appropriate for evaluating the system inductive and total dissipative properties when it incurs alternative currents.

Choice of a model for the modeling of WPT windings

Destined to perform an inductive coupling based on a time-variable magnetic field, the modeling of the resistive and inductive behaviours of WPT windings must be addressed in the **magnetodynamics** framework. Given the shape and dimensions of the windings, the capacitive effect are supposed to be negligible in the frequency-range investigated in this work, avoiding the need for an electric modeling.

3.2.2 Introduction of intermediary variables (potentials)

Gathering the different equations describing magnetodynamics in a compact formulation requires to introduce intermediary variables. The latter are employed for eliminating variables in the problem. Depending on the choice of intermediary variables (or potentials), different formulations are available for expressing a magnetodynamic problem. Futile at first sight, the selection of potentials is crucial as the latter are the unknowns to solve for reaching the problem solution. Moreover, choosing potentials conditions the mathematical treatment and the physical interpretation of the formulation.

The three most popular magnetodynamic formulations are the **h** - ϕ (with ϕ the magnetic scalar potential), the **t** - ϕ (with **t** the electric vector potential) and the **a** - v (with **a** the magnetic vector potential and v the electric scalar potential) formulations. Even if it leads to more unknowns than its **h** - ϕ counterpart in three-dimensional models, the **a** - v formulation is usually preferred in the context of electrical engineering, notably for the modeling of electromechanical machines and transformers. On the one hand, the physical interpretation of the potentials **a** (the circulation of **a** on a closed path is equal to the magnetic flux it embraces) and v (a difference of v is equal to a voltage) are more adapted. On the other hand, the potential ϕ is intrinsically multivalued in multi-connected domains (such as windings) and requires to define a cut (*i.e.* a discontinuity in ϕ) alongside each conductor in the system for ensuring that curl $\mathbf{h} = 0$ in the non-conducting domains. The practical implementation of these cuts for the modeling of wound components is cumbersome and curtails the resort to ϕ. In contrast, the potential **a** presents another type of ambiguity due to its equivocal definition, which can be cleared by a simple additional mathematical condition (called a *gauge* condition). **Considering the previous analysis, the a - v magnetodynamic formulation is chosen for the modeling of the WPT windings.**

3.2.3 Development of the a - v magnetodynamics formulation

A general magnetodynamic problem is defined on a bounded domain Ω delimited by the boundary Γ and segmented in different sub-domains (see Figure 3.1), which are

- the sub-domain Ω_s gathering the source regions where a source current density $\mathbf{j}_s$ is imposed and where no eddy current are induced ($\sigma = 0$) ;
- the sub-domain Ω_c gathering the massive conducting regions where eddy current can be induced ($\sigma \neq 0$) ;
- the sub-domain Ω_0 gathering the ambiant, non-magnetic ($\mu_r \approx 1$) and non-conducting ($\sigma = 0$) regions, such as air or vacuum.

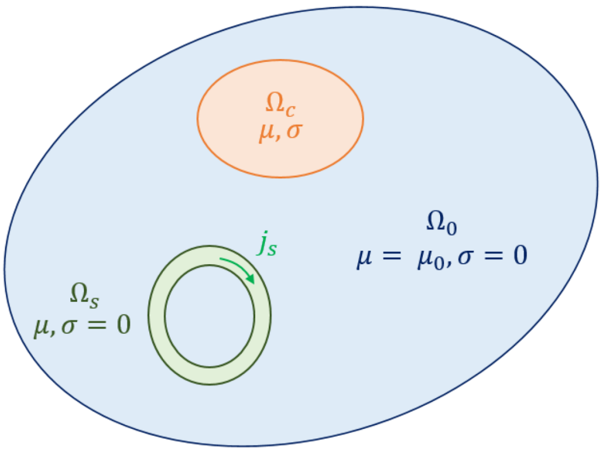

Figure 3.1: Typical definition domain of a magnetodynamic problem

Definition of the magnetic vector potential a

In accordance with the properties of vector analysis (div curl $\mathbf{x} = 0$, $\forall \mathbf{x} \in R^n$), the Gauss' law for magnetism (3.3) can be strongly verified by introducing the magnetic vector potential **a** such that

$$\mathbf{b} = \text{curl } \mathbf{a} \tag{3.12}$$

The definition (3.12) of the vector field **a** is equivocal since another vector field **a'** = **a** + grad φ (with $\varphi \in R$) also fulfills expression (3.12), as

$$\text{curl grad } x = 0 \qquad \forall x \in R$$

For ensuring the uniqueness of the vector field **a** and consequently the uniqueness of the **a** - v magnetodynamic problem solution, an additional condition is required. This condition is called a *gauge* condition. The most common gauge condition is the Coulomb's gauge (div **a** = 0), notably due to its implicit verification in the case of two-dimensional (2-D) problems. For the three-dimensional (3-D) problems addressed in this work, another gauge condition is employed. Detailed in [106], this specific gauge condition ensures numerically that $\mathbf{a} \cdot \mathbf{w} = 0$ with **w** a vector field of which the field lines are not closed, thanks to a tree/co-tree technique.

Definition of the electric scalar potential v

The introduction of **a** in Faraday's law (3.2) results in

$$\text{curl } \mathbf{e} = -\frac{\partial(\text{curl } \mathbf{a})}{\partial t} = \text{curl } \left(-\frac{\partial \mathbf{a}}{\partial t}\right) \tag{3.13}$$

so that

$$\text{curl } \left(\mathbf{e} + \frac{\partial \mathbf{a}}{\partial t}\right) = 0 \tag{3.14}$$

In accordance with the properties of vector analysis (curl grad $\mathbf{x} = 0$, $\forall \mathbf{x} \in R^n$), the Faraday's law is strongly verified by introducing the electric scalar potential v such that

$$\mathbf{e} + \frac{\partial \mathbf{a}}{\partial t} = -\text{grad } v \tag{3.15}$$

Remark. *Due to the decoupling of the electric displacement* ***d*** *from the magnetodynamic equations, the electric scalar potential v does not render the capacitive effects in the system, but serves for the determination of the electric field distribution in the conducting domain.*

The definitions of the potentials **a** and v ensure the respective verification of equations (3.3) and (3.2), respectively. Hence, the resolution of a magnetodynamic problem is confined to solving the remaining equation of the model, *i.e.* the simplified Ampère's law (3.11), expressed in terms of potentials. By eliminating expressions (3.5) and (3.12) in equation (3.11), one has

$$\text{curl } \mathbf{h} = \text{curl } \left(\frac{\text{curl } \mathbf{a}}{\mu}\right) = \mathbf{j} \tag{3.16}$$

The total current density **j** is decomposed in two contributions, which are the source current density $\mathbf{j}_s$ imposed in Ω_s and the eddy current density $\sigma \cdot \mathbf{e}$ induced in Ω_c. By introducing the magnetic reluctivity $\nu = \mu^{-1}$, one has

$$\text{curl } (\nu \text{ curl } \mathbf{a}) = \mathbf{j}_s + \sigma \cdot \mathbf{e} \tag{3.17}$$

Finally, the electric field **e** is eliminated by employing the definition (3.15) of the electric scalar potential v, yielding the final **a** - v magnetodynamic formulation, which is

$$\text{curl } (\nu \text{ curl } \mathbf{a}) + \sigma \cdot \frac{\partial \mathbf{a}}{\partial t} + \sigma \cdot \text{grad } v = \mathbf{j}_s \tag{3.18}$$

Transposition in the frequency domain

Assuming a sinusoidal excitation of the system with an angular frequency ω, the generated fields present a sinusoidal evolution, with

$$\mathbf{j}_s(t) = \mathbf{j}_{s,m} \cdot \cos(\omega t + \theta_{j_s}) \tag{3.19}$$

$$\mathbf{a}(t) = \mathbf{a}_m \cdot \cos(\omega t + \theta_a) \tag{3.20}$$

$$v(t) = v_m \cdot \cos(\omega t + \theta_v) \tag{3.21}$$

where $\mathbf{j}_{s,m}$, $\mathbf{a}_m$ and v_m are the amplitude and θ_{j_s}, θ_a and θ_v are the phase of the related fields. In this context, the formulation (3.18) can be transposed in the frequency domain by using phasors for representing the fields. One has

$$\text{curl } (\nu \text{ curl } \underline{\mathbf{a}}) + \sigma \cdot j\omega \cdot \underline{\mathbf{a}} + \sigma \cdot \text{grad } \underline{v} = \underline{\mathbf{j}}_s \tag{3.22}$$

where j is the imaginary unit (*i.e.* $j = \sqrt{-1}$) and where

$$\underline{\mathbf{j}}_s = \left(\mathbf{j}_{s,m}/\sqrt{2}\right) \cdot e^{-j\theta_{j_s}} \tag{3.23}$$

$$\underline{\mathbf{a}} = \left(\mathbf{a}_m/\sqrt{2}\right) \cdot e^{-j\theta_a} \tag{3.24}$$

$$\underline{v} = \left(v_m/\sqrt{2}\right) \cdot e^{-j\theta_v} \tag{3.25}$$

3.2.4 Integration of geometric symmetry in the system structure

In some cases, the studied system presents a geometric symmetry implying the invariance of the fields in a certain space direction. The numerical model can henceforth be limited to the investigation of a 2-D geometry, contained in a plane which is perpendicular to the latter direction. There are two types of symmetry leading to a 2-D study: the translation symmetry (see Figure 3.2a) and the axial symmetry (see Figure 3.2b). In the first case, the modeled geometry remains unchanged along an axis perpendicular to the study plan (corresponding to $x-y$ on the figure). In the second case, this geometry remains unchanged during a revolution around an axis belonging to the study plan (corresponding to z on the figure).

(a) (b)

Figure 3.2: (a) Translation and (b) axial symmetries [103]

When such a simplification occurs, the formulation is reduced to a scalar equation. As a matter of fact, the magnetic vector potential $\mathbf{a}$ and the source current density $\mathbf{j}_s$ are systematically oriented in a direction perpendicular to the study plan. The only unknowns are their respective modules a and j_s and the formulation becomes

$$\text{div } (\nu \text{ grad } a) - \sigma\frac{\partial a}{\partial t} - \sigma \text{grad } v = -j_s \tag{3.26}$$

Beside reducing the computational complexity of the problem and increasing the easiness of the geometry conception, a 2-D model provides numerous advantages for observing and interpreting the results, since the vector **b** and **h** are contained in the study plan. Moreover, in general (*i.e.* in 3-D), the magnetic vector potential has no direct physical meaning. In a 2-D system, one can demonstrate that the iso-value contours of the module a (for a translation symmetry) or of the product $r \cdot a$ (for an axial symmetry, with r the distance from the revolution axis) correspond to the fields lines (*i.e.* the path of the magnetic flux). Also, the Coulomb's gauge is always verified in 2-D, ensuring the uniqueness of the solution.

Finally, in 2-D as well as in 3-D, one can take a clever profit from other types of symmetry (*e.g.* orthogonal or central symmetries) for modeling only a portion of the 2-D or the 3-D system, the latter portion corresponding to the sole geometry of the symmetry pattern. In this instance, the adequacy of the solution is guaranteed by the imposition of appropriate boundary conditions.

3.2.5 Boundary conditions

As for any problem defined by partial differential equations on a bounded domain Ω, the uniqueness of the solution must be guaranteed by the application of conditions on the its boundary Γ, in addition to the aforementioned gauge condition. There are no less than three types of boundary conditions

- the Dirichlet (or first-type) boundary conditions, which fix the tangential component of the magnetic vector potential $\mathbf{n} \times \mathbf{a}$ and thus the normal component of the magnetic flux density $\mathbf{n} \cdot \mathbf{b}$ on a boundary portion $\Gamma_e \subset \Gamma$;
- the Neumann (or second-type) boundary conditions, which fix the tangential component of the magnetic field $\mathbf{n} \times \mathbf{h}$ on a boundary portion $\Gamma_h \subset \Gamma$;
- the Robin (or third-type) boundary conditions, which are a relation between a first- and a second-type boundary conditions and are not employed in this thesis (so that $\Gamma_e \cup \Gamma_h = \Gamma$).

One can note that the boundary portions which are subject to concomitant Dirichlet and Neumann boundary conditions are said to be subject to mixed boundary conditions. Since Dirichlet conditions are strongly verified, the boundary portions associated with a mixed boundary conditions are included in Γ_h.

A homogeneous Dirichlet boundary condition $\mathbf{n} \times \mathbf{a} = 0$ accounts for a magnetic insulation as the normal component of **b** is cancelled on the related boundary (and the corresponding magnetic flux is zero across the boundary). The latter condition is imposed on the external limits of the studied domain and on lines of symmetry[1] (*e.g.* the axis of an axial symmetry). A homogeneous Neumann boundary condition $\mathbf{n} \times \mathbf{h} = 0$ (called a natural condition) imposes the perfect perpendicularity between the magnetic field **h** and the related boundary. The latter condition is imposed on lines of anti-symmetry. The development of the finite-element method applied to **a** - v magnetodynamics will further show that natural conditions are implicitly verified.

In this thesis, non-homogeneous Neumann boundary conditions are used for imposing an external source magnetic field $\mathbf{h}_s$ acting on certain portions of Γ_h. For generality purposes, the notation $\mathbf{n} \times \mathbf{h} = \mathbf{n} \times \mathbf{h}_s$ is employed with $\mathbf{n} \times \mathbf{h}_s$ equal to zero when a natural condition is required.

[1] The type of symmetry must be chosen in accordance with the geometric symmetry, but also with the direction of the source current density in the problem since the latter are influencing the distribution of the fields.

3.3 Mathematical structure of the Maxwell's equations

The finite-element method aims to propose a discrete mathematical structure destined to enable the numerical resolution of electromagnetic problems. Witnessing the adequacy of such a discrete structure requires to highlight the main properties of the Maxwell's equations mathematical structure in the continuous domain. A brief analysis of the main characteristics of the latter structure is proposed in this section, as a precise analysis is out of the scope of this applicative thesis.

The Maxwell's equations are naturally hosted by a continuous mathematical structure called the De Rham's complex. Let $L^2(\Omega)$, respectively $\boldsymbol{L}^2(\Omega)$, be the space of square-integrable scalar, respectively vector, fields on the domain Ω. The complex (relative to the boundary[2]) is composed by two sub-spaces $F^0(\Omega)$ and $F^3(\Omega)$ of $L^2(\Omega)$, by two sub-spaces $F^1(\Omega)$ and $F^2(\Omega)$ of $\boldsymbol{L}^2(\Omega)$ and by three differential operators (grad, curl and div) defined on Ω.

In the De Rham's structure, each operator is defined on a sub-space, with

$$\mathrm{Dom(grad)} = F^0(\Omega) \qquad \mathrm{Dom(curl)} = F^1(\Omega) \qquad \mathrm{Dom(div)} = F^2(\Omega)$$

so that the image of each sub-space by each operator is included in another subspace, *i.e.*

$$\mathrm{grad}\ F^0(\Omega) \subset F^1(\Omega) \qquad \mathrm{curl}\ F^1(\Omega) \subset F^2(\Omega) \qquad \mathrm{div}\ F^2(\Omega) \subset F^3(\Omega)$$

Consequently, the complex forms a sequence formalized by

$$F^0(\Omega) \xrightarrow{grad} F^1(\Omega) \xrightarrow{curl} F^2(\Omega) \xrightarrow{div} F^3(\Omega) \tag{3.27}$$

The electromagnetic fields and potentials as described and coupled by the Maxwell's equations fit perfectly in this structure. As a matter of fact, one can validate the coherence of the following sequence

$$v \in F^0 \xrightarrow[cf.\ (3.15)]{grad} \mathbf{e} \text{ and } \mathbf{a} \in F^1(\Omega) \xrightarrow[cf.\ (3.2)\ \&\ (3.12)]{curl} \mathbf{b} \in F^2(\Omega) \xrightarrow[cf.\ (3.3)]{div} 0 \tag{3.28}$$

The uniqueness of the solution to the Maxwell's equations is guaranteed by the exactness properties of the complex of De Rham. The objective of the finite-element method is the definition of a discrete mathematical structure mimicking the De Rham's complex for transposing those properties in the discrete domain.

Remark. *The electromagnetic fields and potentials sequence presenting above is particularly focused on the $\boldsymbol{a}$ - v magnetodynamics formulation. However, the complex of De Rham homes actually the complete set of Maxwell's equations, leading to enriched inclusions of the different vector field spaces. However, the sole sequence (3.28) is sufficient for the understanding of the following developments, focused on magnetodynamics.*

[2]The operators as well as the complete complex are relative to the boundary Γ in order to comply with the problem boundary conditions. The rigorous notation requiring to index the spaces and operators with the boundary Γ is however dropped here for simplicity purposes.

3.4 Finite-element method

The finite-element method enables the numerical resolution of vector and partial differential equations for advanced problems. Polyvalent, this method is widely employed in applied sciences, notably for the numerical modeling of mechanic, thermic and electromagnetic problems. Based on advanced concepts from the differential geometry theory, the finite-element method is broadly outlined here in its practical essence, for a sharper understanding of the modeling challenges and for the appraisal of the adequacy of the original contributions proposed in this thesis.

The finite-element method is based on a double discretization of the partial derivative problem, involving synergistically

- a spatial discretization, via a meshing process which decomposes the geometry of the investigated system in a finite set of geometrical elements ;
- a mathematical discretization, via the definition of discrete function spaces allowing the natural expression of the fields and potentials on the discretized geometry, thanks notably to a structure analogous to the De Rham's complex called the Whitney's complex.

The method takes its name from the finite elements, each one being both geometric and mathematical entity described by three fundamental features, namely

- a domain of space K corresponding to an elementary portion of the system obtained from the spatial discretization ;
- a function space P_K of finite dimension n_K defined on the domain K ;
- a set Σ_K of n_k degrees of freedom represented by n_k linear functionals ϕ_i (with $1 \leq i \leq n_k$) defined in P_K.

Therefore, the discrete approximation $\mathbf{u}_k$ of any function $\mathbf{u} \in P_K$ is uniquely defined by the related degrees of freedom $\phi_i(u)$ via an interpolation of the type

$$\mathbf{u}_k = \sum_{i=1}^{n_k} \phi_i(u) \cdot \mathbf{p}_i \tag{3.29}$$

with $\mathbf{p}_i$ for $1 \leq i \leq n_k$, the basis function of the function space P_K. The finite-element space is the union of all the system finite elements, ensuring that the union of their respective domains are filling the system geometry and that continuity conditions are respected on the elements boundaries.

3.4.1 Spatial discretization of the geometry

For complying with the finite size of the computational memories, the geometry of the studied system requires to be discretized. Hence, the domain Ω is partitioned in a finite set of geometrical sub-domains Ω_e presenting an elementary shape (defined by a few vertices only), called *elements*. Some of the common elements shapes are presented on Figure 3.3. The entire set of elements is called the *mesh* and its creation process based on the system geometry is called the *meshing*. Depending on the elements shapes, the mesh can be *structured* (with an orderly arrangement of prisms or hexahedrons in 3-D or quadrangles in 2-D) or *unstructured* (with a disorderly arrangement of elements, often tetrahedrons in 3-D or triangles in 2-D). More arduous to control, the unstructured meshes are nevertheless extremely popular due to the larger fields of applications provided by their better fitting to curved geometries.

Contemporarily, numerous meshing algorithms have been proposed and implemented. In this thesis, all the meshes have been generated using the Delaunay's algorithm included in the computer-assisted-design (CAD) software GMSH [74].

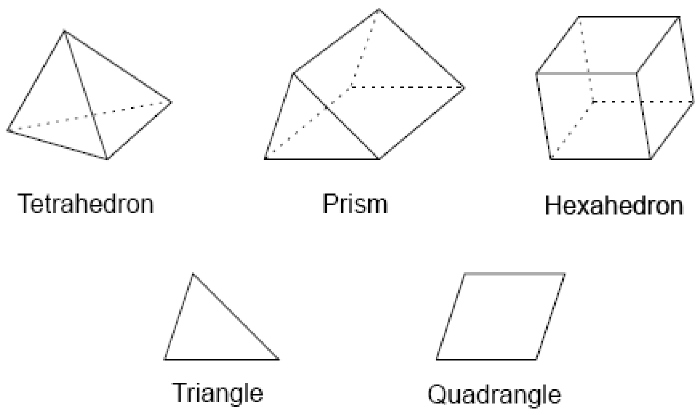

Figure 3.3: Common elements shapes in 3-D (up) and 2-D (down) [103]

3.4.2 Mathematical discretization of the fields

As electromagnetic quantities are scalar fields or vector fields defined in space, the discretization of the system geometry implies the necessity to express those fields on the discretized domain. The sophistication of the mathematical structure hosting the Maxwell's equations in the continuous domain (*i.e.* the complex of De Rham) has been outlined in the previous section. Reproducing such a complex structure in the discrete domain by using conventional projection techniques (such as the projection in an orthonormal basis) would lead to a complex reformulation of the problem. Therefore, Hassler Whitney has proposed to use geometrical entities from the mesh (*i.e.* nodes, edges, facets and volumes) to build discrete function spaces forming a sequence replicating the complex of De Rham and thereby able to host the Maxwell's equations in the discrete domain. The fields and potentials properties are hence naturally conserved during the transition from the continuous level to the discrete level.

For clarity purposes, the description of the Whitney's elements requires a clear formalism for identifying the nodes, edges, facets and volumes from the mesh. The set of nodes $\mathcal{N}$ contains $N_{\mathcal{N}}$ nodes n_i with $1 \leq i \leq N_{\mathcal{N}}$. The set of edges $\mathcal{E}$ contains $N_{\mathcal{E}}$ edges e_{ij} linking the nodes i and j with $1 \leq i, j \leq N_{\mathcal{N}}$ and $i \neq j$. The set of facets $\mathcal{F}$ contains $N_{\mathcal{F}}$ facets $f_{ijk(l)}$ formed by the nodes i, j and k (for triangle) and eventually l (for quadrangles) with $1 \leq i, j, k(, l) \leq N_{\mathcal{N}}$ and $i \neq j \neq k$ $(\neq l)$. The set of volume $\mathcal{V}$ contains $N_{\mathcal{V}}$ volumes v with $1 \leq v \leq N_{\mathcal{V}}$, each one being associated with a finite element.

Nodal elements

The description of Whitney's nodal elements is based on the definition of continuous and scalar basis functions s_{n_i} (associated with each node $n_i \in \mathcal{N}$) such that

$$\begin{aligned} s_{n_i} &= 1 \text{ at node } n_i \\ s_{n_i} &= 0 \text{ at node } n_j \text{ with } j \neq i \end{aligned} \tag{3.30}$$

Between two nodes, on the elements involving n_i, the function s_{n_i} presents a linear evolution (for first order nodal elements) or a quadratic evolution (for second order nodal elements), etc. One can note that s_{n_i} is different from zero only on the elements including the node

i. Considering the totality of the nodes, the functions s_{n_i} employed as basis functions generate a scalar function space $S^0(\Omega)$ of finite dimension $N_{\mathcal{N}}$ in which a scalar field u can be approximated by $\hat{u}$ with

$$\hat{u} = \sum_{i \in \mathcal{N}} s_{n_i} u_{n_i} \tag{3.31}$$

where the u_{n_i} are the $N_{\mathcal{N}}$ degrees of freedom associated with the Whitney's nodal elements, corresponding to the value of u on the node n_i.

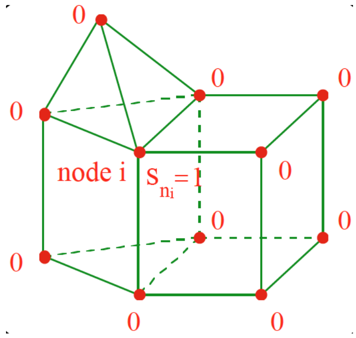

Figure 3.4: Representation of the s_{n_i} scalar field for nodal elements [104]

Edge elements

The description of the Whitney's edge elements is based on the definition of continuous and vector basis functions $\mathbf{s}_{e_{ij}}$ (associated with each edge e_{ij} in $\mathcal{E}$) such that

$$\mathbf{s}_{e_{ij}} = s_{n_j} \text{ grad} \sum_{r \in \mathcal{N}_{F,j\bar{i}}} s_{n_r} - s_{n_i} \text{ grad} \sum_{r \in \mathcal{N}_{F,i\bar{j}}} s_{n_r} \tag{3.32}$$

with $\mathcal{N}_{F,m\bar{n}}$ the set of nodes forming the facet including m but not n. One can note that $\mathbf{s}_{e_{ij}}$ is different from zero only on the elements including the edge e_{ij}. Moreover, the circulation of $\mathbf{s}_{e_{ij}}$ is unitary on e_{ij} and equal to zero on the other edges. Considering the totality of the edges, the functions $\mathbf{s}_{e_{ij}}$ employed as basis functions generate a vector function space $S^1(\Omega)$ of finite dimension $N_{\mathcal{E}}$ in which a vector field $\mathbf{u}$ can be approximated by $\hat{\mathbf{u}}$ with

$$\hat{\mathbf{u}} = \sum_{e_{ij} \in \mathcal{E}} \mathbf{s}_{e_{ij}} u_{e_{ij}} \tag{3.33}$$

where the $u_{e_{ij}}$ are the $N_{\mathcal{E}}$ degrees of freedom associated with the Whitney's edge elements corresponding to the circulation of $\mathbf{u}$ on the edges e_{ij}.

Facet elements

The description of the Whitney's facet elements is based on the definition of continuous and vector basis functions $\mathbf{s}_{f_{ijk(l)}}$ (associated with each facet $f_{ijk(l)}$ in $\mathcal{F}$) such that

$$\mathbf{s}_{f_{ijk(l)}} = a_f \sum_{c=1}^{n_f} s_{n_{q_c}} \left(\text{grad} \sum_{r \in \mathcal{N}_{\mathcal{F},q_c\bar{q}_{c+1}}} s_{n_r} \right) \wedge \left(\text{grad} \sum_{r \in \mathcal{N}_{\mathcal{F},q_c\bar{q}_{c-1}}} s_{n_r} \right) \tag{3.34}$$

where $a_f = 2$ for a triangular facets or $a_f = 1$ for a quadrangular facet, n_f is the number of the facet $f_{ijk(l)}$ vertices and the set of index $\{q_1, q_2, q_3\} = \{i, j, k\}$ for a triangular facet and $\{q_1, q_2, q_3, q_4\} = \{i, j, k, l\}$ for a quadrangular facet. The latter sequence of indexes q_c are

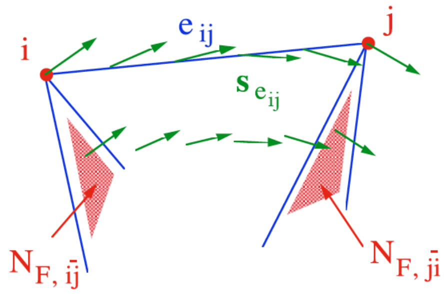

Figure 3.5: Representation of the $\mathbf{s}_{e_{ij}}$ vector field for edge elements [104]

circular, with $q_0 = q_{n_f}$ and $q_{n_f+1} = q_1$. One can note that $\mathbf{s}_{f_{ijk(l)}}$ is different from zero only on the elements including the facet $f_{ijk(l)}$. Moreover, the flux of $\mathbf{s}_{f_{ijk(l)}}$ is unitary through $f_{ijk(l)}$ and equal to zero through any other facet. Considering the totality of the facets, the functions $\mathbf{s}_{f_{ijk(l)}}$ employed as basis functions generate a vector function space $S^2(\Omega)$ of finite dimension $N_{\mathcal{F}}$ in which a vector field $\mathbf{u}$ can be approximated by $\hat{\mathbf{u}}$ with

$$\hat{\mathbf{u}} = \sum_{f_{ijk(l)} \in \mathcal{F}} \mathbf{s}_{f_{ijk(l)}} u_{f_{ijk(l)}} \tag{3.35}$$

where the $\mathrm{u}_{f_{ijk(l)}}$ are the $N_{\mathcal{F}}$ degrees of freedom associated with the Whitney's facet elements, corresponding to the flux of $\mathbf{u}$ trough the facets $f_{ijk(l)}$.

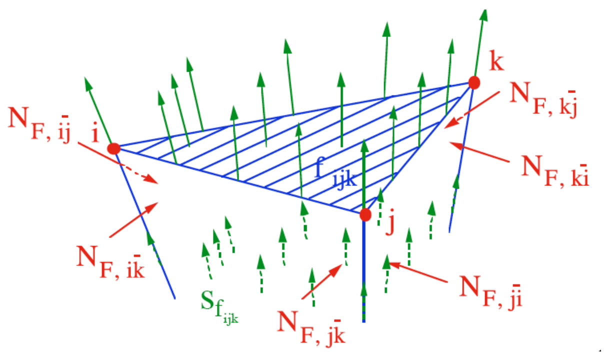

Figure 3.6: Representation of the $\mathbf{s}_{f_{ijk}}$ vector field for facet elements [104]

Volume elements

The description of the Whitney's volume elements is based on the definition of discontinuous and scalar basis function s_v (associated with each volume v in $\mathcal{V}$) such that

$$s_v = 1/\mathrm{vol}(v) \tag{3.36}$$

where $\mathrm{vol}(v)$ is the volume of the considered element. Considering the totality of the volumes, the functions s_v employed as basis functions generate a scalar function space $S^3(\Omega)$ of finite dimension $N_{\mathcal{V}}$ in which a scalar field u can be approximated by $\hat{u}$ with

$$\hat{u} = \sum_{v \in \mathcal{V}} s_v u_v \tag{3.37}$$

where the u_v are the $N_{\mathcal{V}}$ degrees of freedom associated with the Whitney's volume elements.

Analogy with the De Rham's complex

An advanced analysis of the basis functions (3.30), (3.32), (3.34) and (3.36) demonstrates the underlying cleverness behind the Whitney's elements.

On the one hand, one can prove that the discrete function spaces $S^0(\Omega)$, $S^1(\Omega)$, $S^2(\Omega)$ and $S^3(\Omega)$ are embedded one in the other following

$$\text{grad } S^0(\Omega) \subset S^1(\Omega) \qquad \text{curl } S^1(\Omega) \subset S^2(\Omega) \qquad \text{div } S^2(\Omega) \subset S^3(\Omega)$$

The Whitney's elements function spaces can therefore be arranged in a mathematical sequence analogous to the De Rham's complex (called the Whitney's complex), formalized as

$$S^0(\Omega) \xrightarrow{grad} S^1(\Omega) \xrightarrow{curl} S^2(\Omega) \xrightarrow{div} S^3(\Omega) \tag{3.38}$$

By noting $\mathcal{P}_i$ the projection map from $F^i(\Omega)$ to $S^i(\Omega)$, d_i the differential operator (*i.e.* grad, curl or div in the continuous domain) between $F^i(\Omega)$ and $F^{i+1}(\Omega)$ and D_i the differential operator (*i.e.* grad, curl or div in the discrete domain) between $S^i(\Omega)$ and $S^{i+1}(\Omega)$, one has (see Figure 3.7)

$$\mathcal{P}_{k+1} d_k = D_k \mathcal{P}_k \tag{3.39}$$

and the complexes of De Rham and of Whitney are isomorphic. This isomorphic relation demonstrates the mathematical relevance of using Whitney's elements to interpolate the electromagnetic fields and potentials.

$$\begin{tikzcd}
F^0(\Omega) \arrow[r, "d_0"'] \arrow[d, "\mathcal{P}_0"'] & F^1(\Omega) \arrow[r, "d_1"'] \arrow[d, "\mathcal{P}_1"'] & F^2(\Omega) \arrow[r, "d_2"'] \arrow[d, "\mathcal{P}_2"'] & F^3(\Omega) \arrow[d, "\mathcal{P}_3"'] \\
S^0(\Omega) \arrow[r, "D_0"'] & S^1(\Omega) \arrow[r, "D_1"'] & S^2(\Omega) \arrow[r, "D_2"'] & S^3(\Omega)
\end{tikzcd}$$

Figure 3.7: Relations between the spaces of De Rham and of Whitney

On the other hand, Whitney's elements ensure the conformity of the fields and potentials in the finite-element spaces $S^0(\Omega)$, $S^1(\Omega)$, $S^2(\Omega)$ and $S^3(\Omega)$. As a matter of fact, the Whitney's basis functions definitions imply

- the continuity of the s_{n_i} through the elements facets ;
- the continuity of the tangential traces of the $\boldsymbol{s}_{e_{ij}}$ through the elements facets ;
- the continuity of the normal traces of the $\boldsymbol{s}_{f_{ijk(l)}}$ through the elements facets ;
- the discontinuity of the s_v through the elements facets.

The conformity of spaces yielded by Whitney elements is fundamental for an adequate projection of the fields on the discrete geometry. Hence, the potential v (continuous at interfaces), the potential $\mathbf{a}$ or the electric field $\mathbf{e}$ (conserving their tangential component) and the magnetic flux density $\mathbf{b}$ and current density $\mathbf{j}$ (conserving their normal component) are naturally and respectively projected on nodal, edge and facet elements.

3.4.3 Establishing the system of equations

Up to this point, we have demonstrated how the finite-element method combines adequately a spatial and a mathematical discretizations for expressing the field with a finite number of degrees of freedom. Solving the problem requires to ease the partition of its formulation on the elements. Indeed, the conventional formulation of a problem described by partial differential equations on a bounded domain is difficult to transpose on a discrete domain. Therefore, the differential formulation is transformed in an equivalent integral formulation, directly decomposable on the discretized domain. To that end, various methods are available, among which the variational method or the weighted residual method. The latter is more general and more systematic than the former and is preferred in this thesis (even if the former provides a direct physical intuition in some cases).

Let consider a partial differential equations problem involving a vector field $\mathbf{u}$ belonging to the space of square-integrable vector fields ($\mathbf{u} \in \boldsymbol{L}^2(\Omega)$) as unknown. The latter problem can be described by the general following general form

$$\mathcal{L}\ \mathbf{u} = \mathbf{f} \text{ on the domain } \Omega \tag{3.40}$$

$$\mathcal{B}\ \mathbf{u} = \mathbf{g} \text{ on the boundary } \Gamma \tag{3.41}$$

where $\mathcal{L}$ and $\mathcal{B}$ are some operators defined on Ω and relative to Γ. When the exact solution $\mathbf{u}$ is replaced by an approximation $\hat{\mathbf{u}}$, an error $\mathcal{R}$ (also called a residual) is committed with

$$\mathcal{R}\ \hat{\mathbf{u}} = (\mathcal{L}\ \hat{\mathbf{u}} - \mathbf{f}) + (\mathcal{B}\ \hat{\mathbf{u}} - \mathbf{g}) \tag{3.42}$$

The weighted residual method stipulates that the residue $\mathcal{R}$ is null (*i.e.* that $\hat{\mathbf{u}} = \mathbf{u}$) if the solution $\hat{\mathbf{u}}$ verifies [102]

$$\int_\Omega (\mathcal{L}\ \hat{\mathbf{u}} - \mathbf{f}) \cdot \mathbf{w}\ d\Omega\ - \oint_\Gamma (\mathcal{B}\ \hat{\mathbf{u}} - \mathbf{g}) \cdot \mathbf{w}\ d\Gamma = 0 \qquad \forall \mathbf{w} \in \boldsymbol{L}^2(\Omega) \tag{3.43}$$

where the weights $\mathbf{w}$ are any square-integrable vector fields. As each $\mathbf{w}$ aims to "test" the cancellation of the weighted residue, the functions $\mathbf{w}$ are often called the test-functions. One can notice that the portion of Γ subject to a Dirichlet boundary condition does not have to be tested as the unknown $\mathbf{u}$ is directly fixed by such a condition. The test-functions are therefore null on the related boundary portion. The expression (3.43) is an integral description of the problem which is completely equivalent to the initial differential description. Despite the absence of any loss in strength, the latter expression is usually called the *weak form* of the problem by abuse of terms. This has to do with the fact that the form (3.43) is supposed to be weakly verified (*i.e.* verified as best as possible) on the domain by a numerical resolution method involving a finite number of degrees of freedom.

In the context of the finite-element method, the system of equations is obtained by describing the unknown field(s) via the finite elements with a finite number N_{dof} of degree of freedoms, and by testing the formulation residue using N_{dof} different test-functions $\mathbf{w}_i$ (with $1 \leq i \leq N_{dof}$). A number of N_{dof} equations for N_{dof} numerical unknowns are hence defined. Implementing a particular weighted residual method reverts to define a method for choosing the test-functions. In this thesis, the Galerkin's method is employed since it is most popular method in the framework of the finite-element method. It consists in choosing the test-functions among the basis functions of the space $S^i(\Omega)$ (with $0 \leq i \leq 3$) related with the type of Whitney's element employed for the approximation of the unknown.

For readability purposes, the mathematical expression of weak formulations is lightened by agreeing on the following notation

$$\int_\Omega \mathbf{f} \cdot \mathbf{g} \; d\Omega = (\mathbf{f}, \mathbf{g})_\Omega \qquad \int_\Gamma \mathbf{f} \cdot \mathbf{g} \; d\Gamma = \langle \mathbf{f}, \mathbf{g} \rangle_\Gamma \qquad \text{with } \mathbf{f}, \mathbf{g} \in \boldsymbol{L}^2(\Omega)$$

3.5 Finite-element method for a - v magnetodynamics

In this section, the principles of the finite-element method are implemented on the **a** - v magnetodynamics formulation. The developments presented here describe the classical **a** - v magnetodynamic implementation of the method, employed here as a state-of-the-art brute-force approach. After discussing the limitations of this approach, adequate modifications in the method will be proposed and implemented.

3.5.1 Weak form

An equivalent description of the magnetodynamic problem is obtained by applying the weighted residual method to the **a** - v magnetodynamic differential formulation (3.18) on Ω and to the Neumann or mixed boundary conditions implying $\mathbf{n} \wedge \mathbf{h} = \mathbf{n} \wedge \mathbf{h}_s$ on Γ_h. The terms of (3.18) being homogeneous to the electric field **e**, the test-functions - denoted **e'** - are chosen in the space $F^1_e(\Omega)$ which corresponds to the space $F^1(\Omega)$ including the Dirichlet conditions on Γ_e. Hence, the weak form for **a** - v magnetodynamics must ensure that

$$\begin{aligned}(\text{curl }\, (\nu \text{ curl } \mathbf{a}) \,, \mathbf{e'})_\Omega + (\sigma \partial_t \mathbf{a} + \sigma \text{grad } v, \mathbf{e'})_\Omega \\ - (\mathbf{j}_s, \mathbf{e'})_\Omega - \langle \mathbf{n} \wedge \mathbf{h} - \mathbf{n} \wedge \mathbf{h}_s, \mathbf{e'} \rangle_{\Gamma_h} = 0 \qquad \forall \mathbf{e'} \in F^1_e(\Omega)\end{aligned} \tag{3.44}$$

The differentiation order (and thus the continuity requirements) on **a** in the first left-hand-side term can be decreased by applying the Green's theorem

$$(\text{curl }\, (\nu \text{ curl } \mathbf{a}) \,, \mathbf{e'})_\Omega = (\nu \text{ curl } \mathbf{a} \;,\; \text{curl } \mathbf{e'})_\Omega + \langle \mathbf{n} \wedge \underbrace{\nu \text{ curl } \mathbf{a}}_{\mathbf{h}} \,, \mathbf{e'} \rangle_\Gamma \tag{3.45}$$

Introducing (3.45) in (3.44) and recalling that $\mathbf{e'}|_{\Gamma_e} = 0$, that σ is non-zero on Ω_c only and that $\mathbf{j}_s$ is non-zero on Ω_s only, one has

$$\begin{aligned}(\nu \text{ curl } \mathbf{a}, \text{ curl } \mathbf{e'})_\Omega + (\sigma \partial_t \mathbf{a} + \sigma \text{grad } v \;, \mathbf{e'})_{\Omega_c} \\ - (\mathbf{j}_s \;, \mathbf{e'})_{\Omega_s} + \langle \mathbf{n} \wedge \mathbf{h}_s \;, \mathbf{e'} \rangle_{\Gamma_h} = 0 \qquad \forall \mathbf{e'} \in F^1_e(\Omega)\end{aligned} \tag{3.46}$$

According to the properties of the De Rham's complex, the field of weight **e'** can be decomposed in the sum of two vector fields $\mathbf{a'} \in F^1_e(\Omega)$ and grad $v' \in F^1_e(\Omega)$ with $v' \in F^0_e(\Omega)$ (corresponding to the space $F^0(\Omega)$ including the Dirichlet conditions on Γ_e). Using those test-functions **a'** and v', solving an electromagnetic problem consists in finding $\mathbf{a} \in F^1_e(\Omega)$ and $v \in F^0_e(\Omega)$ so that

$$\begin{aligned}(\nu \text{ curl } \mathbf{a}, \text{ curl } \mathbf{a'})_\Omega + (\sigma \partial_t \mathbf{a} + \sigma \text{grad } v \;, \mathbf{a'})_{\Omega_c} \\ - (\mathbf{j}_s \;, \mathbf{a'})_{\Omega_s} + \langle \mathbf{n} \wedge \mathbf{h}_s \;, \mathbf{a'} \rangle_{\Gamma_h} = 0 \qquad \forall \mathbf{a'} \in F^1_e(\Omega)\end{aligned} \tag{3.47}$$

$$\begin{aligned}\big(\sigma \partial_t \mathbf{a} + \sigma \text{grad } v, \text{grad } v'\big)_{\Omega_c} \\ - \big(\mathbf{j}_s \;, \text{grad } v'\big)_{\Omega_s} + \langle \mathbf{n} \wedge \mathbf{h}_s \;, \text{grad } v' \rangle_{\Gamma_h} = 0 \qquad \forall v' \in F^0_e(\Omega)\end{aligned} \tag{3.48}$$

3.5.2 Spatial and fields discretizations

For taking profit from the structural and the conformity properties of the Whitney's elements, the vector field $\mathbf{a}$ is projected on edge elements (*i.e.* $\mathbf{a} \in S_e^1(\Omega)$, with $S_e^1(\Omega)$ corresponding to the space $S^1(\Omega)$ including the Dirichlet conditions on Γ_e) and the scalar field v is projected on nodal elements (*i.e.* $v \in S_e^0(\Omega)$, with $S_e^0(\Omega)$ corresponding to the space $S^0(\Omega)$ including the Dirichlet conditions on Γ_e). The fields $\mathbf{a}$ and v are respectively expressed on the domain Ω as

$$\mathbf{a} = \sum_{e_{ij} \in \mathcal{E}} \mathbf{s}_{e_{ij}} a_{e_{ij}} \tag{3.49}$$

$$v = \sum_{n_i \in \mathcal{N}} s_{n_i} v_{n_i} \tag{3.50}$$

with a total of $N_{dof} = N_{\mathcal{E}} + N_{\mathcal{N}}$ degrees of freedom. Moreover, the formulation (3.47)-(3.48) is transposed in the discrete domain by applying the Galerkin's method, consisting in choosing the functions **a'** among the $\mathbf{s}_{e_{ij}} \in S_e^1$ and the functions v' among the $s_{n_i} \in S_e^0(\Omega)$. The numerical resolution of an electromagnetic problem consists therefore in finding $\mathbf{a} \in S_e^1(\Omega)$ and $v \in S^1_{e(\Omega)}$ verifying

$$\begin{aligned}\left(\nu \text{ curl } \mathbf{a},\ \text{curl } \mathbf{s}_{e_{ij}}\right)_\Omega &+ \left(\sigma \partial_t \mathbf{a} + \sigma \text{grad } v\ , \mathbf{s}_{e_{ij}}\right)_{\Omega_c} \\ &- \left(\mathbf{j}_s\ , \mathbf{s}_{e_{ij}}\right)_{\Omega_s} + \langle \mathbf{n} \wedge \mathbf{h}_s\ , \mathbf{s}_{e_{ij}} \rangle_{\Gamma_h} = 0 \qquad \forall \mathbf{s}_{e_{ij}} \in S_e^1(\Omega)\end{aligned} \tag{3.51}$$

$$\begin{aligned}(\sigma \partial_t \mathbf{a} + \sigma \text{grad } v, \text{grad } s_{n_i})_{\Omega_c}& \\ - (\mathbf{j}_s\ , \text{grad } s_{n_i})_{\Omega_s} &+ \langle \mathbf{n} \wedge \mathbf{h}_s\ , \text{grad } s_{n_i} \rangle_{\Gamma_h} = 0 \qquad \forall s_{n_i} \in S_e^0(\Omega)\end{aligned} \tag{3.52}$$

This discrete formulation allows to define $N_{\mathcal{E}}$ independent equations of type (3.51) and $N_{\mathcal{N}}$ independent equations of type (3.52) for solving the $N_{dof} = N_{\mathcal{E}} + N_{\mathcal{N}}$ degrees of freedom. A system of N_{dof} equations for N_{dof} unknowns is obtained. For a test-function $\mathbf{s}_{e_{mn}} \in S_e^1(\Omega)$, an equation of type (3.51) can be written as follows

$$\begin{aligned}\sum_{e_{ij} \in \mathcal{E}} a_{e_{ij}} (\nu \text{ curl } \mathbf{s}_{e_{ij}},\ \text{curl } \mathbf{s}_{e_{mn}})_\Omega &+ \sum_{e_{ij} \in \mathcal{E}} \partial_t a_{e_{ij}} (\sigma \mathbf{s}_{e_{ij}}, \mathbf{s}_{e_{mn}})_{\Omega_c} \\ + \sum_{n_i \in \mathcal{N}} v_{n_i} (\sigma \text{grad } s_{n_i}\ , \mathbf{s}_{e_{mn}})_{\Omega_c} &= (\mathbf{j}_s\ , \mathbf{s}_{e_{mn}})_{\Omega_s} - \langle \mathbf{n} \wedge \mathbf{h}_s\ , \mathbf{s}_{e_{mn}} \rangle_{\Gamma_h}\end{aligned} \tag{3.53}$$

By definition of the Whitney's basis function, the majority of the terms in the latter equation is zero. As a matter of fact, $\mathbf{s}_{e_{ij}}$ and $\mathbf{s}_{e_{mn}}$ are simultaneously different from zero if the edges e_{ij} and e_{mn} are belonging to a common element, whereas s_{n_i} and $\mathbf{s}_{e_{mn}}$ are simultaneously different from zero if the node n_i and the edge e_{mn} are belonging to a common element. The same remark can be reiterated for an equation of type (3.52) tested by $s_{n_p} \in S_e^0(\Omega)$, with

$$\begin{aligned}\sum_{e_{ij} \in \mathcal{E}} \partial_t a_{e_{ij}} \left(\sigma \mathbf{s}_{e_{ij}}, \text{grad } s_{n_p}\right)_{\Omega_c} &+ \sum_{n_i \in \mathcal{N}} v_{n_i} \left(\sigma \text{grad } s_{n_i}, \text{grad } s_{n_p}\right)_{\Omega_c} \\ &= \left(\mathbf{j}_s\ , \text{grad } s_{n_p}\right)_{\Omega_s} - \langle \mathbf{n} \wedge \mathbf{h}_s\ , \text{grad } s_{n_p} \rangle_{\Gamma_h}\end{aligned} \tag{3.54}$$

where $\mathbf{s}_{e_{ij}}$ and s_{n_p} are simultaneously different from zero if the edge e_{ij} and the node n_i are belonging to a common element, whereas s_{n_i} and s_{n_p} are simultaneously different from zero if the nodes n_i and n_p are belonging to a common element.

The resulting system of equation can be written as

$$[\mathbf{K}] \cdot [e] = [\mathbf{f}_s] \tag{3.55}$$

where the matrix $\mathbf{K}$ is called the *stiffness* matrix. Due to the aforementioned cancellation of the majority of terms in (3.53) and (3.54), the latter matrix is sparse. A further analysis demonstrates that the stiffness matrix is also symmetric and positive-definite. Those properties are particularly interesting for the numerical resolution of the system of equations, which is expected to be less cumbersome.

3.5.3 Strong coupling with an external circuit

Beyond identifying the parameters of WPT windings at the circuit level, the virtual laboratory developed here must render the windings impact at the fields level during the operation of the WPT system. The modeling of a resonant WPT system requires thus to associate the $\mathbf{a}$ - v magnetodynamic formulation with circuit relations, directly embedded in the finite-element system of equations (*i.e.* implementing a *strong* coupling with an external circuit). Dular *et al.* have proposed a general and natural method for achieving such a strong coupling [69]. The latter method is described here and will be extended in Chapter 4 to formulations using surface impedance boundary conditions, as an original contribution of this thesis.

Defining constraints on global quantities

The subtlety behind the incorporation of circuit relations in an electromagnetic problem consists in expressing at the local level constraints on global quantities, such as the circuit voltage or current. An approach for doing so proposes to insert an electromotive force between two infinitely close cross-sections representing the electrodes of a conductor $\Omega_c^i \in \Omega_c$ (with $1 \leq i \leq N_c$ and N_c the number of conductors), as shown in Figure 3.8. The volume Ω_g^i between those electrodes is extracted from the domain Ω and connected to an external source or circuit, as shown in Figure 3.8. Let V_i and I_i be the voltage between the electrodes and the current across one or the other electrode, respectively. By denoting Γ_g^i the latter electrode, one has

$$\int_{\gamma_i} \mathbf{e}\ d\mathbf{l} = V_i \text{ and } \int_{\Gamma_g^i} \mathbf{n} \cdot \mathbf{j}\ ds = I_i \tag{3.56}$$

where γ_i is any path in Ω_g^i connecting the electrodes, $d\mathbf{l}$ is an element of contour tangential to γ_i and ds is an element of surface.

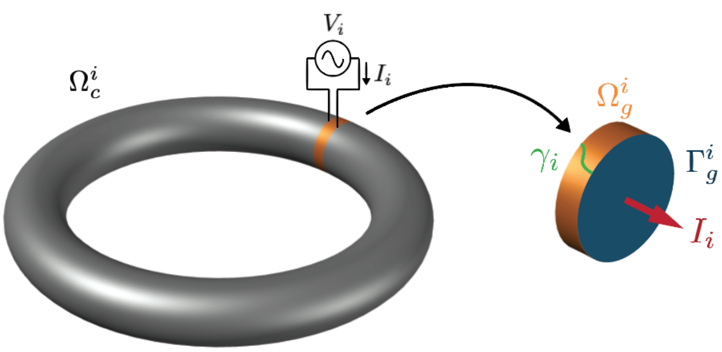

Figure 3.8: Electromotive force definition in a conductor Ω_c^i

Thanks to the properties of the De Rham's complex, the global quantities V_i and I_i can be easily and naturally introduced in the **a** - v magnedodynamic formulation which, as a reminder, is

$$
\begin{aligned}
&(\nu \text{ curl } \mathbf{a},\ \text{curl } \mathbf{a'})_\Omega + (\sigma\partial_t \mathbf{a} + \sigma \text{grad } v\ , \mathbf{a'})_{\Omega_c} \\
&\qquad - (\mathbf{j}_s\ , \mathbf{a'})_{\Omega_s} + \langle \mathbf{n} \wedge \mathbf{h}_s\ , \mathbf{a'} \rangle_{\Gamma_h} = 0 \qquad \forall \mathbf{a'} \in F_e^1(\Omega)
\end{aligned} \tag{3.47}
$$

$$
\begin{aligned}
&\left(\sigma\partial_t \mathbf{a} + \sigma \text{grad } v, \text{grad } v'\right)_{\Omega_c} \\
&\qquad - \left(\mathbf{j}_s\ , \text{grad } v'\right)_{\Omega_s} + \langle \mathbf{n} \wedge \mathbf{h}_s\ , \text{grad } v' \rangle_{\Gamma_h} = 0 \qquad \forall v' \in F_e^0(\Omega)
\end{aligned} \tag{3.48}
$$

As a matter of fact, the inclusion of grad $F_e^0(\Omega)$ in $F_e^1(\Omega)$ ensures that the formulation (3.47) implies systematically the formulation (3.48). As a consequence, the magnetodynamic problem can be segmented in two successive sub-problems allowing to introduce successively and respectively the voltage as a strong global quantity and the current as a weak global quantity. One can note that the aforementioned implication is ensured by using Whitney's edge elements for the projection of **a** and Whitney's nodal elements for the projection of v.

Voltage as a strong global quantity

The first sub-problem consists in determining for each conductor Ω_c^i a source electric scalar potential v_0^i defined on Ω_c^i corresponding to the apparition of a unitary voltage across the electrodes of the conductor Ω_c^i so that the electric scalar potential v can be expressed as

$$
v = \sum_{i=1}^{N_c} V_i \cdot v_0^i \tag{3.57}
$$

The source electric scalar potential v_0^i can be obtained by the resolution of an electrokinetic pre-problem for each conductor Ω_c^i. However, for avoiding those electrokinetic problems, Dular *et al.* have proposed a generalized source electric scalar potential, which can be defined as the sum of the nodal basis functions on the electrode Γ_g^i, *i.e.*

$$
v_0^i = \sum_{n_i \in \Gamma_g^i} s_{n_i} \tag{3.58}
$$

According to the characteristics of the nodal basis functions s_{n_i}, the generalized source electric scalar potentials are supported only by the layer of elements adjacent to Γ_g^i in Ω_c^i and are decreasing from one on Γ_g^i to zero at the end of this layer. Using the latter generalized potentials does not impact the exactness of the global problem solution, but the evolution of the electric scalar potential v inside each conductor is not physical anymore. Nevertheless, this reinterpretation appears to be an optimal choice as it avoids pre-computations and yields an improved bandwidth in the related system of equations, as discussed in [69].

The second sub-problem requires to solve the weak form (3.47) where the voltages V_i have replaced the potential v as unknowns, thanks to the definition of the source electric scalar potential (3.57), *i.e.*[3]

$$
\begin{aligned}
&(\nu \text{ curl } \mathbf{a},\ \text{curl } \mathbf{a'})_\Omega + (\sigma\partial_t \mathbf{a}, \mathbf{a'})_{\Omega_c} + \\
&\qquad \sum_{i=1}^{N_c} V_i \left(\sigma \text{grad } v_0^i\ , \mathbf{a'}\right)_{\Omega_c} + \langle \mathbf{n} \wedge \mathbf{h}_s\ , \mathbf{s}_{e_{mn}} \rangle_{\Gamma_h} = 0 \qquad \forall \mathbf{a'} \in F_e^1(\Omega)
\end{aligned} \tag{3.59}
$$

[3]The source term $\mathbf{j}_s$ is assumed to be zero for the purpose of writing simplicity. Nevertheless, this source term is by no means incompatible with the present formulation.

Projecting $\mathbf{a}$ on edge elements and applying the Galerkin's method yields $N_{\mathcal{E}}$ equations, *i.e.*

$$\sum_{e_{ij}\in\mathcal{E}} a_{e_{ij}} \left(\nu \text{ curl } \mathbf{s}_{e_{ij}},\ \text{curl } \mathbf{s}_{e_{mn}}\right)_{\Omega} + \sum_{e_{ij}\in\mathcal{E}} \partial_t a_{e_{ij}} \left(\sigma \mathbf{s}_{e_{ij}}, \mathbf{s}_{e_{mn}}\right)_{\Omega_c}$$

$$+ \sum_{i=1}^{N_c} V_i \left(\sigma \text{grad } v_0^i \ , \mathbf{s}_{e_{mn}}\right)_{\Omega_c} + \langle \mathbf{n} \wedge \mathbf{h}_s \ , \mathbf{s}_{e_{mn}} \rangle_{\Gamma_h} = 0 \qquad \forall \mathbf{s}_{e_{mn}} \in F_e^1(\Omega) \quad (3.60)$$

The problem comprises $N_{\mathcal{E}}$ degrees of freedom $a_{e_{ij}}$ and N_c degrees of freedom V_i, whereas (3.60) provides $N_{\mathcal{E}}$ equations. The problem must be completed by defining as many circuit relations (involving the current I_i) as there are conductors in the domain.

Circuit relations (current as a weak global quantity)

The current I_k flowing in a conductor Ω_c^k appears naturally by developing the formulation (3.48) where the test-functions v' are the generalized source electric scalar potentials v_0^k. One has

$$\left(\sigma \partial_t \mathbf{a} + \sigma \text{grad } v, \text{grad } v_0^k\right)_{\Omega_c} + \langle \mathbf{n} \wedge \mathbf{h}_s \ , \text{grad } v_0^k \rangle_{\Gamma_h} = 0 \qquad \forall k \text{ with } 1 \leq k \leq N_c \quad (3.61)$$

with a boundary term which can be decomposed by using vector analysis rules

$$\langle \mathbf{n} \wedge \mathbf{h}_s \ , \text{grad } v_0^k \rangle_{\Gamma_h} = \int_{\Gamma_h} \mathbf{n} \cdot \text{curl } \left(\mathbf{h}_s \cdot v_0^k\right) d\Gamma - \int_{\Gamma_h} \mathbf{n} \cdot \text{curl } \left(\mathbf{h}_s\right) \cdot v_0^k \ d\Gamma \qquad (3.62)$$

The first right-hand-side term is zero since the application of the Stokes theorem transforms the latter term in an contour integral on the boundary of Γ_h, which is non-existent since Γ_h is a closed surface. The second right-hand-side term is equal to the current I_k. Indeed, by definition of the generalized source electric scalar potentials, v_0^k is different from zero only on Γ_g^k, where it is equal to one. Therefore, one has

$$\langle \mathbf{n} \wedge \mathbf{h}_s \ , \text{grad } v_0^k \rangle_{\Gamma_h} = - \int_{\Gamma_g^k} \mathbf{n} \cdot \text{curl } \left(\mathbf{h}_s\right) \ d\Gamma \qquad (3.63)$$

where $\mathbf{h}_s$ is associated, as a reminder, with the imposition of an external magnetic field on the boundary of the domain Ω. The curl of $\mathbf{h}_s$ can be interpreted as an external current density $\mathbf{j}_{ext}$ imposed by an external circuit on Γ_g^k so that

$$\langle \mathbf{n} \wedge \mathbf{h}_s \ , \text{grad } v_0^k \rangle_{\Gamma_h} = - \int_{\Gamma_g^k} \mathbf{n} \cdot \mathbf{j}_{ext} \ d\Gamma = I_k \qquad (3.64)$$

where I_k is a current entering the conductor (*i.e.* opposite to the exterior normal $\mathbf{n}$). The formulation expressed in terms of $\mathbf{a}$ and the voltages V_i (3.60) is therefore completed by the definition of N_c circuit relations, developed from the introduction of (3.64) in (3.61). One has, $\forall k$ with $1 \leq k \leq N_c$

$$I_k + \sum_{e_{ij}\in\mathcal{E}} \partial_t a_{e_{ij}} \left(\sigma \mathbf{s}_{e_{ij}}, \text{grad } v_0^k\right)_{\Omega_c} + \sum_{i=1}^{N_c} V_i \left(\sigma \text{grad } v_0^i \ , \text{grad } v_0^k\right)_{\Omega_c} = 0 \qquad (3.65)$$

Due to the fact that v_0^k is different from zero only on Ω_c^k, the latter expression can be simplified as follows, again $\forall k$ with $1 \leq k \leq N_c$

$$I_k + \sum_{e_{ij}\in\mathcal{E}} \partial_t a_{e_{ij}} \left(\sigma \mathbf{s}_{e_{ij}}, \text{grad } v_0^k\right)_{\Omega_c^k} + V_k \left(\sigma \text{grad } v_0^k \ , \text{grad } v_0^k\right)_{\Omega_c^k} = 0 \qquad (3.66)$$

Additional and external circuitry can be added to the problem by defining the V-I relations for each circuit component (*e.g.* resistances, inductances or capacitances), by defining V or I sources and by relating this assembly with network constraints (specifying how the external components and the finite-element conductors are interconnected).

3.6 Generalized Partial Element Equivalent Circuit method

For reducing the computational burden associated with the conventional 3-D finite-element modeling of the planar coils, the partial element equivalent circuit (PEEC) method is envisioned. As described hereunder, this method presents several features complying elegantly with the framework of WPT windings modeling. Since the PEEC method is subject to ongoing researches and developments in the Grenoble Electrical Engineering Laboratory (G2ELab) notably, we have taken profit from our collaboration with the latter laboratory for experimenting the recent advances in PEEC modeling (more precisely the generalized inductive PEEC method) on a WPT system. The theoretical development of the generalized PEEC method is proposed above.

3.6.1 General discussions about the PEEC method

Initially proposed by Hoer and Love [107] in 1965 and developed by Ruehli [108] during the 1970s, the principle of the PEEC method is to transpose an electromagnetic problem from the electromagnetic domain to the circuit domain. To this end, the conducting domains are spatially discretized in small parallelepipeds of which the electromagnetic behaviour and interactions are represented by partial lumped elements, determined (semi-)analytically via integral formulations (*e.g.* using the Biot-Savart law). The adequate interconnection of those partial elements results in an electrical circuit equivalent to the electromagnetic system.

Compliance with the WPT windings modeling problem

By definition, the PEEC method displays two main features complying with the modeling of WPT windings. On the one hand, its integral formulation is well-suited for free-space simulations as it accounts for the remote effects of the conducting parts without requiring the explicit discretization of the ambient non-conducting medium. This feature is especially elegant in the context of WPT. Firstly, the fields are expanding in the air surrounding the windings and must be taken into account, which can be cumbersome with non-integral method such as the finite-element method (especially in 3-D). Secondly, the appropriate modeling of the eddy-current effects requires to finely mesh the conductors boundaries, and therefore the air in direct vicinity when it has to be modeled. The application of the PEEC method to WPT windings is expected to avoid the inclusion of the major part of the system (*i.e.* the ambient air) in the model, with a drastic decrease in the number of elements and of degrees of freedom. Furthermore, the natural and physical circuit interpretation of the PEEC method is an important asset for the coupling of the windings electromagnetic model with an external circuit.

Generalization of the PEEC method

Originally proposed with partial inductances only, the PEEC formulations are nowadays accounting for the resistive and the capacitive natures of the investigated system. In this thesis, the magnetodynamic problem is tackled via the inductive PEEC method which computes the partial resistances, self-inductances and mutual inductances for each element of the mesh. Based on the conventional notation for the latter circuit components, this method is also called the RLM PEEC method.

Due to the analytical approach for the determination of the partial circuit elements, the conventional PEEC implementations are submitted to heavy constraints relative to their domain of applicability. Hence, its applicability is limited to thin conducting regions (with a skin depth larger than the conductors thickness) discretized in a quadrangular structured mesh.

Consequently, it has been largely and almost exclusively implemented for bus-bars, electronic tracks and interconnections in the context of digital electronics, and more recently of power electronics.

Over the last decades, the progresses of computational tools have paved the way to the resort to more complex numerical processes for diversifying and extending the scope of the PEEC method. More particularly, Nguyen *et al.* have recently proposed to generalize the implementation of the inductive PEEC method to unstructured meshes for extending its scope of application to volume domains with geometries presenting an industrial complexity [70]. Several methods combining the finite-element method for the projection of the fields with an integral formulation leading to a PEEC interpretation have been proposed. Notably, edge elements for the projection of the electric vector potential **t** and facet elements for the projection of the current density **j** have been investigated. In contrast with the former solution, the latter is applicable to multiply connected domains, like the conductors considered in this thesis. This approach is therefore applied to the WPT windings modeling, with a double scientific interest, *i.e.* the research of an innovative modeling method for those windings and the proposition of another applicative example for the generalized inductive PEEC method.

3.6.2 Generalized inductive PEEC method using Whitney's facet elements for the projection of the current density

The generalized inductive PEEC method is developed here for problems involving conducting and non-magnetic domains. It is based on an integral formulation ensuing from the expression of the electric field **e** as a function of the magnetic vector potential **a** and electric scalar potential v in the frequency domain, *i.e.*[4]

$$\mathbf{e} = -j\omega\mathbf{a} - \mathrm{grad}\ v \tag{3.67}$$

Since the domain of definition is limited to the conductors, the Ohm's law is verified everywhere, so that the electric field **e** can be expressed via the current density **j** with $\mathbf{e} = \mathbf{j}/\sigma$. The formulation becomes

$$\frac{\mathbf{j}}{\sigma} = -j\omega\mathbf{a} - \mathrm{grad}\ v \tag{3.68}$$

In absence of magnetic material (which would influence the shape of the field lines), the magnetic vector potential **a** can be analytically derived from the current density **j** thanks to the Biot-Savart law, with

$$\mathbf{a} = \frac{\mu_0}{4\pi} \int_{\Omega_c} \frac{\mathbf{j}}{\mathbf{r}}\ d\Omega \tag{3.69}$$

with **r** the distance between the point where **a** is observed and the source generating the magnetic field associated with **a**. By introducing (3.69) in (3.68), the integral formulation of the problem expressed in terms of **j** and v is obtained

$$\frac{\mathbf{j}}{\sigma} = -\frac{j\omega\mu_0}{4\pi} \int_{\Omega_c} \frac{\mathbf{j}}{\mathbf{r}}\ d\Omega - \mathrm{grad}\ v \tag{3.70}$$

[4]The underbar notation discriminating a frequency-domain field phasor from a time-domain field is dropped for a lighter writing. Nevertheless, each field is actually referring to the field phasor in this development.

3.6.3 Spatial and current density discretizations

The geometry of the system is discretized using tetrahedron and/or non-straight prisms and hexahedrons forming an unstructured mesh. The Whitney's facet elements (as defined in section 3.4.2) are employed for the projection of the current density $\mathbf{j}$, with

$$\mathbf{j} = \sum_{s_{f_{ijk(l)}} \in \mathcal{F}} \mathbf{s}_{f_{ijk(l)}} \cdot i_{f_{ijk(l)}} \tag{3.71}$$

The notation $i_{f_{ijk(l)}}$ is not trivial since the degrees of freedom of the current density $\mathbf{j}$ projected on the Whitney's facet elements are the current through each related facet. For lightening the following development, the facets are no more indexed with their vertices, but only by an index i with $s_{f_i} \in \mathcal{F}$ and $0 \leq i \leq N_{\mathcal{F}}$. Certain properties of the facet basis functions $\mathbf{s}_{f_{ijk(l)}}$ will be useful for the circuit interpretation of the weak formulation. More particularly, one can specify that

$$\mathbf{n} \cdot \mathbf{s}_{f_i} = \frac{1}{S_{f_i}} \qquad \text{and} \qquad \text{div } \mathbf{s}_{f_i} = \frac{1}{V_{\Omega_i}} \tag{3.72}$$

with S_{f_i} the surface of the facet f_i and V_{Ω_i} the volume of the element including the facet f_i, assumed to be oriented so that the normal $\mathbf{n}$ is exterior to the latter element.

Similarly to the finite-element method, the system of equations is assembled by resorting to the Galerkin's method applied on equation (3.70). The discrete problem consists in finding the degrees of freedom i_{f_i}, so that $\forall k$ with $0 \leq k \leq N_{\mathcal{F}}$, one verifies[5]

$$\sum_{i=1}^{N_{\mathcal{F}}} i_{f_i} \int_{\Omega_c} \frac{\mathbf{s}_{f_i} \mathbf{s}_{f_k}}{\sigma} \, d\Omega + \sum_{i=1}^{N_{\mathcal{F}}} i_{f_i} \frac{j\omega\mu_0}{4\pi} \int_{\Omega_c} \mathbf{s}_{f_k} \int_{\Omega_c} \frac{\mathbf{s}_{f_i}}{\mathbf{r}} \, d\Omega \, d\Omega = -\int_{\Omega_c} \text{grad } v \ \mathbf{s}_{f_k} \, d\Omega \tag{3.73}$$

3.6.4 Circuit interpretation

Focusing on the right-hand-side of expression (3.73), the divergence theorem yields

$$-\int_{\Omega_c} \text{grad } v \ \mathbf{s}_{f_k} \, d\Omega = -\int_{\Gamma_c} (\mathbf{n} \cdot \mathbf{s}_{f_k}) \ v \, d\Gamma + \int_{\Omega_c} \text{div } (\mathbf{s}_{f_k}) \ v \, d\Omega \tag{3.74}$$

Firstly, let consider that f_k is an internal facet of the system. Then, the first right-hand-side term of (3.74) is null, as $\mathbf{n} \cdot \mathbf{s}_{f_k}$ is null on any other facet than f_k (which is internal and therefore not included in Γ_c by assumption). The second right-hand-side term is different from zero for the elements sharing the facet f_k only. By denoting those two elements $\Omega_{k,1}$ and $\Omega_{k,2}$ and by resorting to the properties of facet elements (3.72), this term becomes

$$-\int_{\Omega_c} \text{grad } v \ \mathbf{s}_{f_k} \, d\Omega = \int_{\Omega_c} \text{div } (\mathbf{s}_{f_k}) \ v \, d\Omega \tag{3.75}$$

$$= \int_{\Omega_{k,1}} \text{div } (\mathbf{s}_{f_k}) \ v \, d\Omega + \int_{\Omega_{k,2}} \text{div } (\mathbf{s}_{f_k}) \ v \, d\Omega \tag{3.76}$$

$$= \frac{1}{V_{\Omega_{k,1}}} \int_{\Omega_{k,1}} v \, d\Omega - \frac{1}{V_{\Omega_{k,2}}} \int_{\Omega_{k,2}} v \, d\Omega = U_{f_k} \tag{3.77}$$

which is the difference between the average electrical potential on both sides of the facet f_k, *i.e.* the voltage U_{f_k} across the internal facet f_k.

[5]The reduced notation for the weak form introduced in section 3.4.3 is not employed here for an easier interpretation of the mathematical terms.

Secondly, let consider that f_k is an external facet belonging to Γ_c. Then, the first right-hand-side term is different from zero only on the facet f_k. The second right-hand-side term is different from zero on the only boundary element V_{Ω_k} including the facet f_k. By once again resorting to the properties of facet elements (3.72), the right-hand-side term of (3.73) is therefore simplified to

$$
\begin{aligned}
-\int_{\Omega_c} \text{grad } v \; \mathbf{s}_{f_k} \; d\Omega &= -\int_{f_k} (\mathbf{n} \cdot \mathbf{s}_{f_k}) \; v \; d\Gamma + \int_{\Omega_k} \text{div } (\mathbf{s}_{f_k}) \; v \; d\Omega & (3.78) \\
&= -\frac{1}{S_{f_k}} \int_{f_k} v \; d\Gamma + \frac{1}{V_{\Omega_k}} \int_{\Omega_k} v \; d\Omega = U_{f_k} & (3.79)
\end{aligned}
$$

which is the difference between the average electrical potential on the external facet f_k and the boundary element Ω_k, *i.e.* the voltage U_{f_k} across the external facet f_k.

Reminding that the degrees of freedom i_{f_i} are the currents through each facet f_i, each equation of type (3.73) can be interpreted as a circuit relation

$$\sum_{i=1}^{N_{\mathcal{F}}} R_{ik} \; i_{f_i} + \sum_{i=1}^{N_{\mathcal{F}}} j\omega L_{ik} \; i_{f_i} = U_{f_k} \tag{3.80}$$

where R_{ik} are the resistive terms, defined as

$$R_{ik} = \int_{\Omega_c} \frac{\mathbf{s}_{f_i}\mathbf{s}_{f_k}}{\sigma} \; d\Omega \tag{3.81}$$

and where L_{ik} are the inductive terms, defined as

$$L_{ik} = \frac{\mu_0}{4\pi} \int_{\Omega_c} \mathbf{s}_{f_k} \int_{\Omega_c} \frac{\mathbf{s}_{f_i}}{\mathbf{r}} \; d\Omega \; d\Omega \tag{3.82}$$

The electromagnetic problem is hence interpreted physically as a circuit problem. One can demonstrates that the circuit nodes are located on the barycenter of each element. Each node links up with the neighboring nodes via an impedance. External circuit elements can be coupled to the electromagnetic problem by defining a non-zero average electric potential on the external facets corresponding to the electrodes. An elementary example of the transition from the electromagnetic domain to the circuit domain is depicted in Figure 3.9. Once assembled, the system of equations of a magnetodynamic problem addressed via the generalized inductive PEEC method is a system of circuit relations like

$$[\mathbf{Z}] \cdot \mathbf{I}_f = ([\mathbf{R}] + j\omega[\mathbf{L}])\mathbf{I}_f = \mathbf{U}_f \tag{3.83}$$

where $[\mathbf{Z}]$ is an impedance matrix which can be decomposed in a resistive matrix $[\mathbf{R}]$ and an inductive matrix $[\mathbf{L}]$, $\mathbf{I}_f$ is the vector of the current through the facets and $\mathbf{U}_f$ in the vector of the voltage across the facets. In the resistive matrix $[\mathbf{R}]$, one can notice that each term results from the product of two facet basis functions. The latter product is different from zero only if the related facets are belonging to the same element. Similarly to the stiffness matrix from the finite-element method, the matrix $[\mathbf{R}]$ is therefore sparse. In contrast, the inductive matrix $[\mathbf{L}]$ is full and filled by terms resulting from an integral involving the Green's kernel, *i.e.* the expression $1/\mathbf{r}$.

Before presenting the implementation of both the finite-element and the PEEC methods, one finds interesting to comment its characteristics in the framework of a numerical resolution for a clearer comparison with the finite-element method. At the computational level, the fullness of the inductive matrix and thus of the impedance matrix complicates its resolution. Moreover, and most importantly, the mathematical treatment of the Green's kernel is particularly

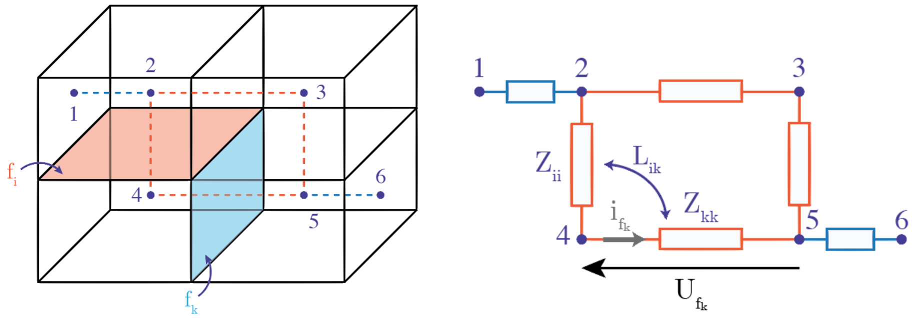

(a) Academic mesh (b) Associated equivalent circuit

Figure 3.9: Illustration of the circuit interpretation associated with the PEEC method

delicate. Especially, the determination of the self-inductances requires the integration of a facet element on itself and may lead to singularities. Computed with a Gaussian quadrature method in the tool provided by the G2ELab, the accurate numerical integration is secured by the shifting of the Gauss points during the assembly of the problem matrix.

Finally, the equivalent circuit made of partial elements is solved conventionally, using a circuit solver. Since the resultant circuit is highly meshed, the developers of the tool provided by the G2ELab have embedded an original pre-processing routine for accelerating the resolution of the problem via the identification of the independent circuit meshes. More details can be found in [70].

3.7 Conclusions

This chapter was dedicated to the presentation of the theoretical aspects associated with the numerical methods employed in this thesis, namely the finite-element method and the generalized PEEC method. Based on advanced concepts from the differential geometry theory also employed by the generalized PEEC method, the finite-element method has been broadly outlined in its practical essence for a sharper understanding of the modeling challenges addressed in this thesis and for the appraisal of the adequacy of the original contributions proposed in the following. The analogy between the De Rham's and Whitney's complexes has been addressed in order to demonstrate the clever appropriateness of the use of the finite elements for the discretization of electromagnetic problems. From a more practical point of view, the presentation of the different electromagnetic models and of the related assumptions has permitted to argue the choice of the $\mathbf{a}$ - v magnetodynamic formulation for addressing the modeling of WPT windings in the next chapter. For familiarizing the reader with the concept and the manipulation of weak forms, the detailed mathematical development of the conventional $\mathbf{a}$ - v magnetodynamic weak form, as well as the latter adaptation in order to implement a strong circuit coupling have been exposed. Finally, the mathematical development of the generalized PEEC formulation has allowed to highlight the direct circuit interpretation associated with the latter, as well as its intrinsic differences in comparison with the finite-element method.

CHAPTER
FOUR

NUMERICAL TESTS AND CONTRIBUTIONS

This chapter is dedicated to the exposition of the numerical tests and on the original developments contributing to the fulfilment of the first objective of this thesis, pertaining to the computational electromagnetic modeling of windings involved in resonant WPT. First, the software architecture employed for implementing the intended virtual laboratory approach is presented. Then, a progressive approach is adopted, by considering progressively more complex models (from 2-D to 3-D) using different methods (*i.e.* the finite-element and the PEEC methods) and guided by the discussions on the numerical results and performances associated with the simulations of experimental or academic test-cases, depending on the burden associated with the method under consideration.

4.1 Software architecture of the virtual laboratory

Beside scientific contributions, a central engineering contribution of this thesis consists in the development and the coding of a virtual laboratory for the digital prototyping and testing of WPT windings, with the finite-element method. Concretely, the virtual laboratory approach relies on a fully parametrized library of models, giving the user the freedom to simulate any configuration (within the framework of WPT windings). Such an approach requires to employ software tools and to develop computer codes enabling adaptability and automatization properties. The software tools used for the development of our virtual laboratory and their interactions are briefly presented here.

4.1.1 Core of the virtual laboratory

The core of the virtual laboratory is based on two software programs, which are GMSH [74] and GetDP (for *General Environment for the Treatment of Discrete Problem*) [75]. Both are open-source software developed in C++ by a team originating from both the University of Liège and the Catholic University of Louvain in Belgium.

GMSH handles the conception of geometries and the generation of meshes, thanks to its computer-aided design (CAD) engine and to different meshing algorithms (subject to numerous customizable options). GetDP is an environment for assembling and solving (using the PETSC module) weak formulations for partial differential problems in the discrete domain, and is mainly dedicated to the finite-element method. Interpreting computer codes written in dedicated languages, GMSH and GetDP offer powerful programming possibilities without reaching the complexity of a source code, thanks precisely to the dedication of their languages. The developer may operate at the lowest level of the computational modeling problem by programming the geometry, the spatial discretization (via the mesh control), the mathematical discretization (via the function spaces properties) and the resolution (by specifying the terms to embed in the formulation, the attributes of the weighted residual method and of the numerical resolution algorithm, but also custom post-processing). Seeming tedious at first sight, those possibilities enable nevertheless effective flexibility and modularity features fitting perfectly with the virtual laboratory concept.

Core libraries containing adaptative GMSH geometry files (presenting the *.geo* extension) and GetDP formulation files (presenting the *.pro* extension) have progressively been built during this thesis. Since both GMSH and GetDP are command-line programs without any interface, an additional software interface layer is needed. From the user's point of view, the effectiveness of a virtual laboratory depends strongly on the quality of the program interface. Therefore, a special effort has been made on the user interface, with two different approaches for driving the developed core software materials.

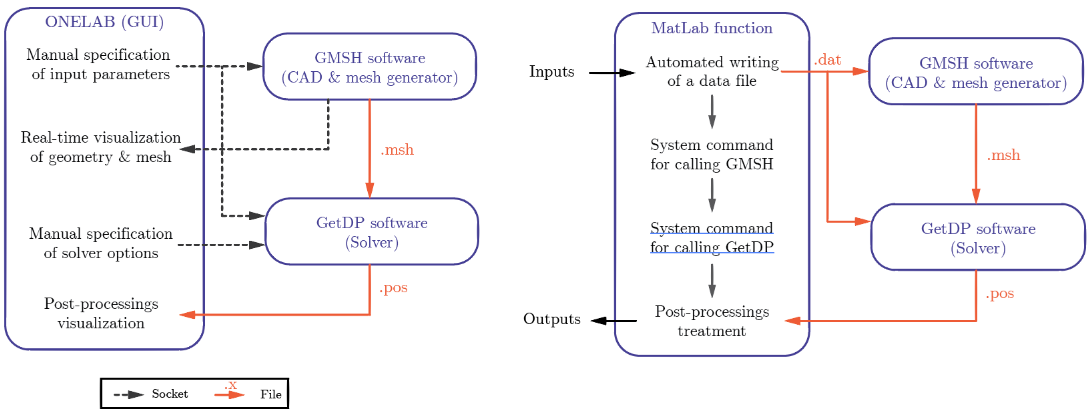

(a) Onelab version

(b) Matlab version

Figure 4.1: Software architecture of the virtual laboratory

4.1.2 User interfaces

Standalone program

The main version of the virtual laboratory is a standalone desktop program, with a graphic user interface (GUI) developed using ONELAB (*Open Numerical Engineering LABoratory*). ONELAB is an open-source GUI environment conceived by the same team as GMSH and GetDP, for precisely driving their executions using bidirectional socket communications. A diagram representing the interactions between the different software tools is shown in Figure 4.1a. The interface (see Figure 4.2) integrates different graphic tools (*e.g.* numerical entries, drop-down lists or checkboxes) for the specification of input parameters, which are directly sent to GMSH and GetDP. A window displays in real-time the geometry and the mesh relative to the current set of parameters. A console allows to debug the *.geo* and *.pro* computer codes and to monitor their executions. Once the mesh is built (and saved in a *.msh* file) using GMSH, the user may configure the solver options and run GetDP. The post-processing results are saved in a *.pos* file and are displayed visually in ONELAB. Different plug-ins are available for the further treatment of those results.

MatLab function

When the virtual laboratory must be embedded in an iterative process (*e.g.* an optimization algorithm), the GUI-version is not adapted anymore, since it requires the intervention of the user for specifying the input parameters and to trigger the computation. In such case, MatLab (as a privileged tool in computational engineering) is employed for driving the executions of GMSH and GetDP (see the diagram on Figure 4.1b). The input parameters are sent to each software via an automated formatting of a data file (in the *.dat* format) and the software are called successively via command lines. The post-processing results are saved, treated by MatLab and the desired outputs are sent back to the higher process.

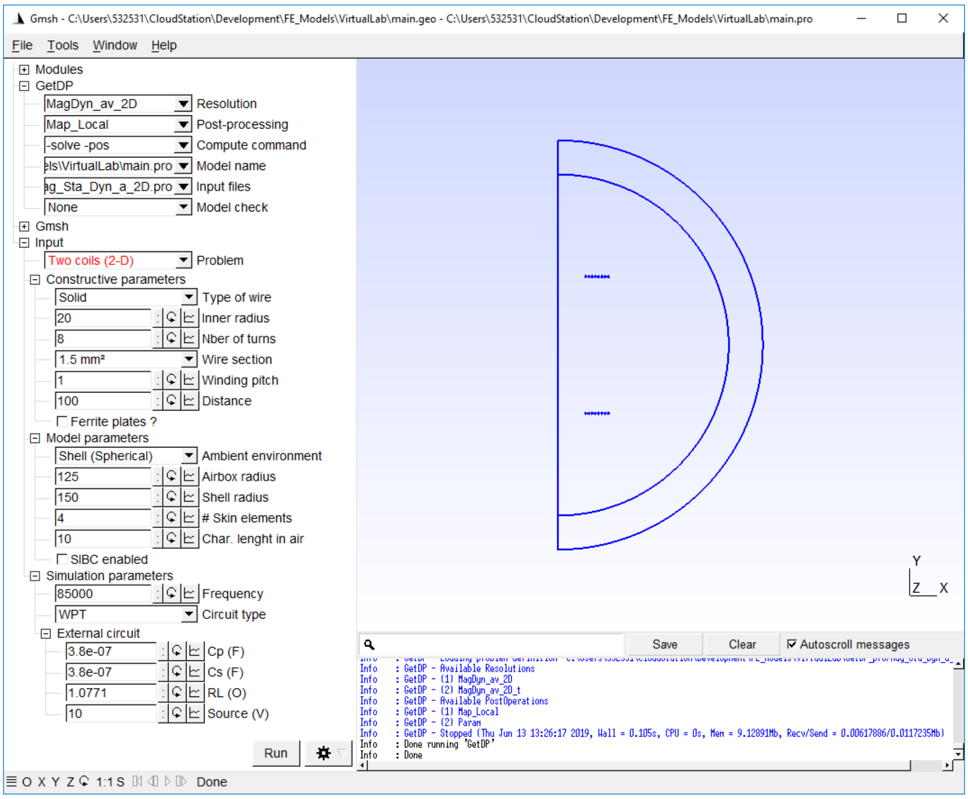

Figure 4.2: GUI of the Onelab version of the virtual laboratory

4.2 2-D finite-element model

As mentioned in Section 3.2.4 , the transformation of a 3-D problem into an equivalent 2-D problem offers numerous advantages, among which a drastical decrease in the computational burden. Basically, a system embedding spiral windings does not present any symmetry enabling this simplification. However, a simple approximation permits to reveal an axial symmetry for WPT windings in their nominal operating position, namely the concentric tori approximation.

In their nominal operating position (*i.e.* aligned), WPT coils display a virtual axial symmetry around their common axis, which is only broken by the pitch from the spiral windings shape. An aknowledged practice in electrical engineering consists in approaching an N-turn spiral winding by an equivalent set of N concentric toric conductors (see Figure 4.3). Applying this principle to aligned WPT windings provides a resulting system presenting a perfect axial symmetry. The latter symmetry enables the possibility to address the modeling problem using a 2-D formulation, as the electromagnetic fields are now expected to be constant during a revolution around the common WPT windings axis.

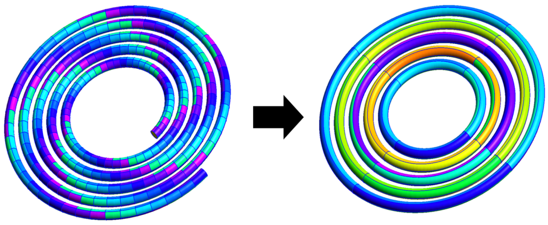

Figure 4.3: Approximation of a spiral coil via a set of concentric tori

4.2.1 Geometry

Thanks to the aforementioned symmetry, the model geometry is restricted to the half-plane containing and delimited on one side by the symmetry axis (which corresponds to the common windings axis). As shown in Figure 4.4[1], each coil is depicted by an assembly of discs, corresponding to the cross-sections of each of its turns. These discs are placed in a half-disc representing a sphere filled with ambient air and delimiting the domain of study. One can notice that this sphere presents a separate external shell, which consists in rejecting the external boundary to infinity. There, the space is distorted with the result that the external boundary is rejected to infinity. Practically, a particular Jacobian operator dedicated to the local topological treatment is employed to this end in the shell [74]. Such a feature is particularly useful in the context of this work. As a matter of fact, in absence of magnetic material (such couplers), the field lines spread in the surrounding air and the field is non-negligible in the air (even at long distances) for the accurate computation of the self- and mutual inductances of the windings.

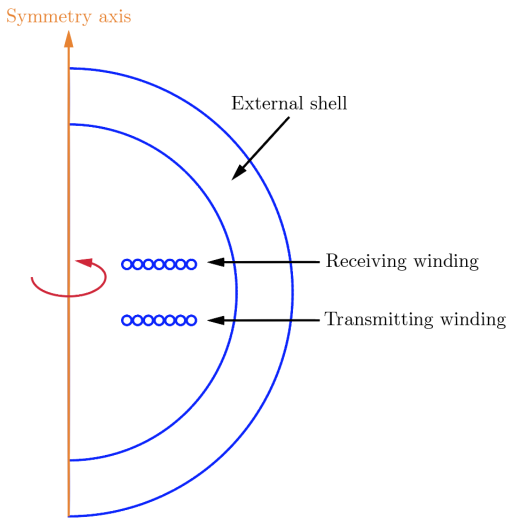

Figure 4.4: Typical 2-D geometry for WPT systems

4.2.2 Concerns relative to the mesh

The mesh density has an important effect on the method accuracy, but also on the computational burden associated with the resolution. Consequently, the mesh generation and control is a matter of compromises. For driving the meshing strategy and since the mesh determines the field interpolation shape, a particular attention has to be drawn on the areas subject to significant local field variations. With this in mind, the conductors cross-sectional mesh must

[1]In this figure, the conductors cross-sections are intentionally oversized for visibility purposes.

be considered in the light of the eddy-current effects appearance. A best-practice rule, widely adopted in the finite-element community, suggests to ensure the presence of two to three layers of elements in the skin depth, with a relaxed mesh in the conductor center (where the current density is expected to be low and uniform). In practice, this is achieved by imposing the elements characteristic length as a third of the skin depth on the conductors boundaries (see Figure 4.5). The mesh continuity guarantees a high density in the air directly surrounding the conductors, which is suited as quick variations in the magnetic field are expected to occur there. Elsewhere in the air, the mesh is usually relaxed. Despite its remoteness from the windings, the mesh in the external shell is not particularly relaxed since the local space distortion accelerates the fields variation in this region. The Delaunay algorithm (embedded in GMSH) is employed for generating the mesh under the specified constraints.

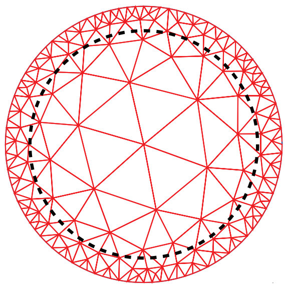

Figure 4.5: Skin-effect-based conductor mesh (dashed line corresponding to the skin depth)

4.2.3 Validation, illustrations and discussion

An experimental test-case is employed for validating and illustrating the implementation of the 2-D massive conductor magnetodynamic formulation. The latter test-case is typically designed for the mid-range power transmission. It is composed by two similar and aligned pancake windings, each presenting a 52 mm inner radius and made of 7 turns of a wire with a 4 mm^2 section. Adjacent turns being in contact, the turns are separated by 1.3 mm (corresponding to twice the 0.65 mm insulating sheath thickness). The 2-D model is validated by considering two configurations. The model ability for evaluating the windings equivalent circuit parameters is demonstrated via a no-load of the windings (one being connected to a source, the other being in open-circuit). Then, the effectiveness of the circuit-coupling capabilities of the formulation is shown via the testing of a complete WPT system (when the coils in the finite-element domain are connected to an external circuit including the resonant capacitors and a load). The geometry and mesh employed for this test-case are shown on Figure 4.6a and a picture of one winding with the latter is presented in Figure 4.6b.

Determination of the windings equivalent parameters

For serving as a validation reference, the self-parameters of a winding (*i.e.* the series resistance and the self-inductance) are determined experimentally with respect to the frequency, using a two-port impedance analyzer Wayne Kerr 6510B. The results are shown and compared to the 2-D model results, as well as the analytical model (presented in Section 2.2) results in Figures 4.7 and 4.8. The accuracy of the 2-D model appears clearly, with 2 % and less than 1 % error on the resistance and self-inductance determination, respectively, in the targeted operation range. The aforementioned limitations of the analytical resistance model are highlighted with an error increasing with the frequency and valued at more than 10 % at 200 kHz. Nevertheless, the relative accuracy of the analytical self-inductance model is noticeable, even if it is based on DC assumptions .

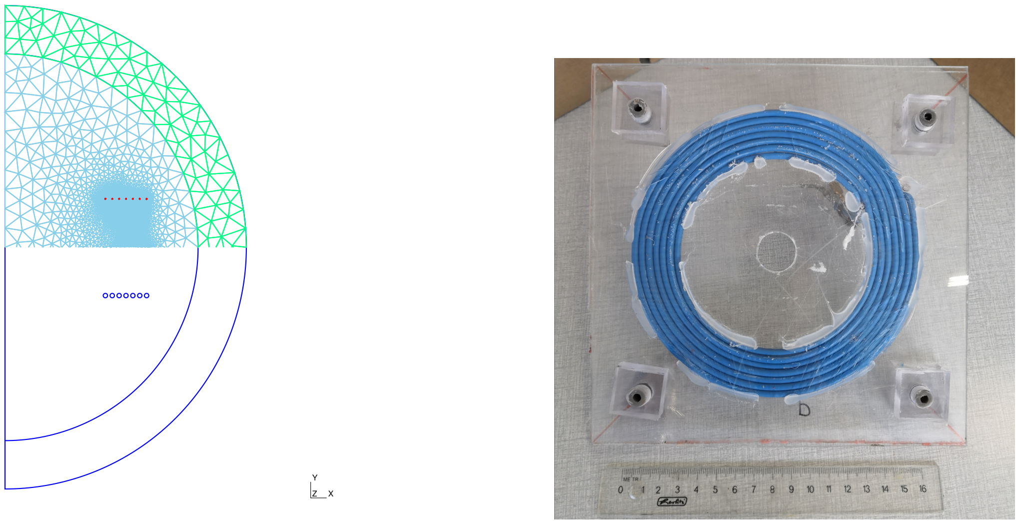

(a) (b)

Figure 4.6: (a) Geometry and mesh for the 2-D finite-element model and (b) picture of a winding from the experimental test-case

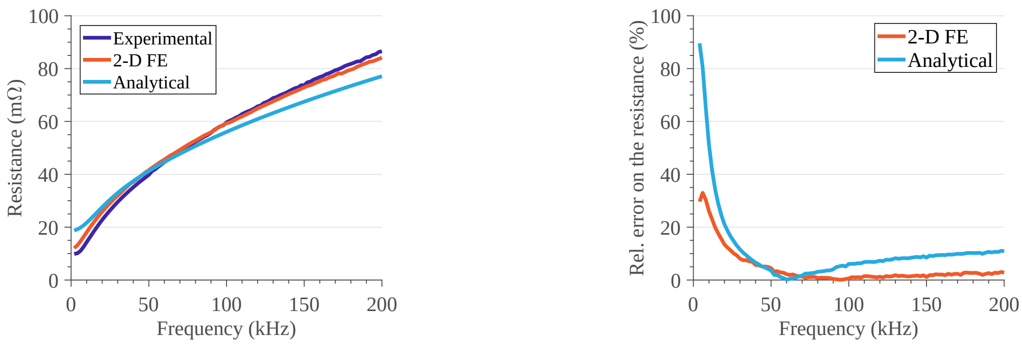

(a) Global value (b) Relative error (experimental as reference)

Figure 4.7: Validation of the 2-D model (parasitic resistance evaluation)

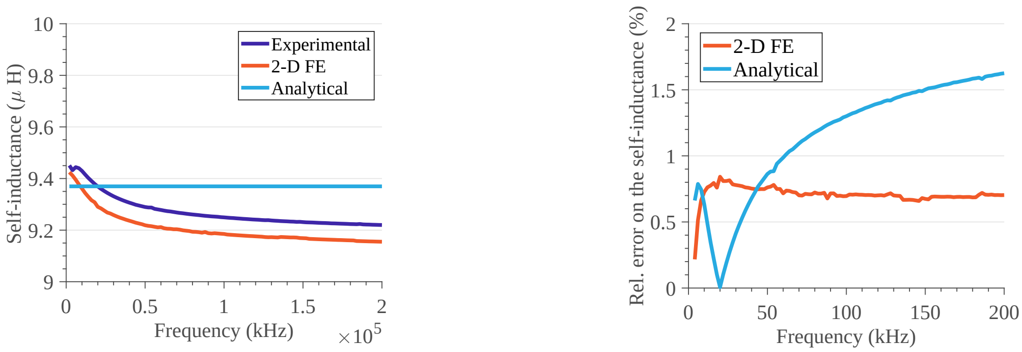

(a) Global value (b) Relative error (experimental as reference)

Figure 4.8: Validation of the 2-D model (self-inductance evaluation)

The measurement of the mutual inductance with a two-port impedance analyzer is not direct, requires multiple measures and accumulates severely the measurements errors. Therefore, the reference mutual inductance is computed via the proven and acknowledged analytical Babic's

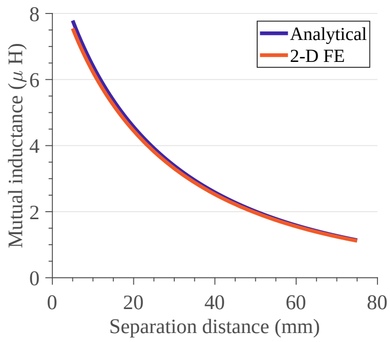

(a) Global value

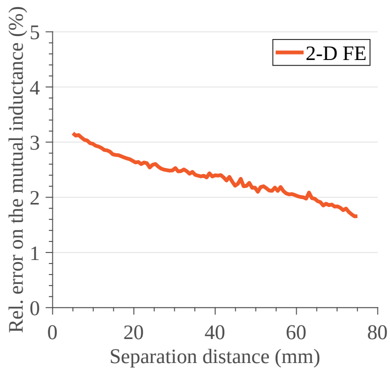

(b) Relative error (analytical as reference)

Figure 4.9: Validation of the 2-D model (mutual inductance evaluation)

approach for different separation distances. The results are shown and compared to the corresponding 2-D model results at 100 kHz for different separation distances between the coils (see Figure 4.9). Once again, the behaviour of the 2-D model is validated.

In terms of computational performances[2], a 100-kHz simulation requires the resolution of around 34 000 degrees of freedom (DoF), corresponding to a computation (CPU) time of 2.7 seconds (1.3 seconds for the meshing and 1.4 seconds for the solving). Due to the mesh adaptation with respect to the skin effect, a 200-kHz simulation requires the resolution of around 42 000 DoF, corresponding to a CPU time of 3.4 seconds (1.7 seconds for the meshing and 1.7 for the solving). The 2-D results accuracy is evident. Put in parallel with the computational performances, this accuracy obtained at an acceptable cost is demonstrating the 2-D finite-element method effectiveness for modeling WPT systems presenting an axial symmetry. Hence, the precise virtual prototyping of WPT windings in their nominal position (*i.e.* aligned) is proved to be effective with the proposed modelization.

Simulation of a complete WPT system

For demonstrating the effectiveness of the circuit-coupling capabilities of the 2-D formulation implemented by the virtual laboratory, the simulation of a complete WPT system including the coils, the resonant capacitor and a load is considered. The system is composed by the same couple of aligned windings as employed for the no-load test, but inserted here in a RIPT system presenting a self-resonant frequency of 85 kHz. Since the common self-inductance of the windings has been evaluated to 9.25 μH during the experimental no-load test, each winding is compensated with a series resonant capacitor presenting of 380 nF. The load is a pure resistance of 1 Ω. The circuit-coupled finite-element formulation described in the previous chapter is implement in 2-D for determining the input impedance $\underline{Z}$ of the complete WPT system. Two situations are considered, namely the situation where the coils are separated by 5 cm and the situation where the coils are separated by 10 cm.

Aligned windings separated by 5 cm The input impedance $\underline{Z}$ of the whole system when the coils are aligned and separated by 5 cm is determined numerically, and compared with the one measured experimentally (using the same impedance analyzer as for the previous validations). The corresponding results are shown in terms of module Z and phase ϕ_Z of $\underline{Z}$ with respect to the operating frequency (with a focus on the resonance zone) in Figure

[2]All the simulations presented in this thesis have been performed on a personal computer equipped with an 3.4 GHz Intel i5-4670 processor and 8 Go of RAM.

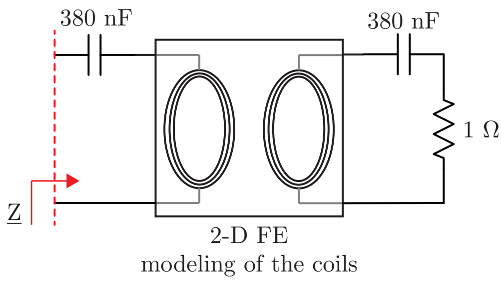

Figure 4.10: Schematic of the validation example circuit

4.11. The computational performances are identical to those displayed in the case of the no-load test since the finite-element model of the windings is identical in both situations. The comparison of the numerical and the experimental results demonstrates the effectiveness of the method for simulating the complex behavior of two coupled oscillators. Notably, one can observe the occurrence of the frequency splitting phenomenon with the typical duplication of the resonant frequency on both sides of the self-resonant frequency.

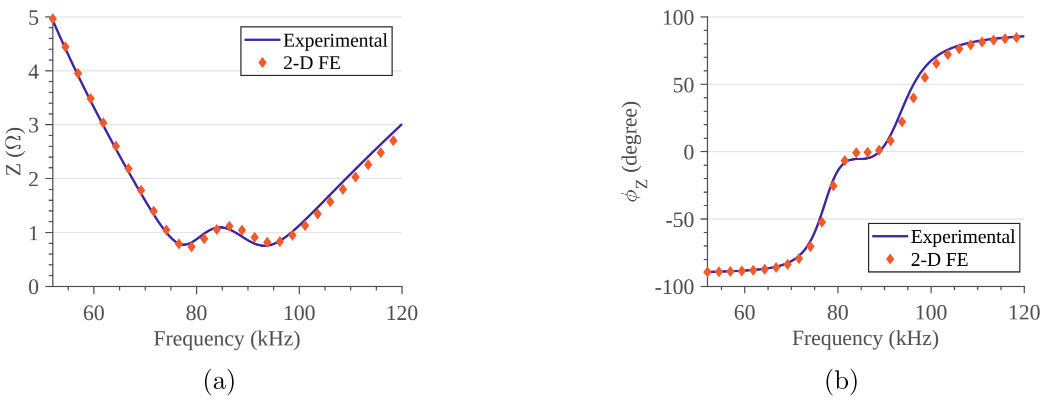

Figure 4.11: Validation of the 2-D finite-element model for the evaluation of (a) the module and (b) the phase of the input impedance of a complete WPT system at 5 cm range

Aligned windings separated by 10 cm The same comparison is made when the coils are further (*i.e.* aligned and separated by 10 cm) and the corresponding results are presented in Figure 4.12. Once again, the results demonstrates the effectiveness of the elaborated tool. In this position, the system is under-coupled and presents therefore a single resonant frequency corresponding to the common self-resonant frequency of both LC-oscillators. The computational performances associated with this execution of the tool corresponds to 46 096 DoF for a 100-kHz simulation with a CPU time of 3.3 seconds (1.4 seconds for the meshing and 1.9 seconds for the solving) and to 56 345 DoF for a 200-kHz simulation with a CPU time of 4.7 seconds (2.4 seconds for the meshing and 2.3 seconds for the solving). Once again, the paralleling of the attained accuracy with the low computational burden makes this 2-D model a promising option for an embedding in a design optimization procedure. Nonetheless, for further reducing the CPU time associated with this 2-D model, we propose an original approach for optimizing the conductors mesh.

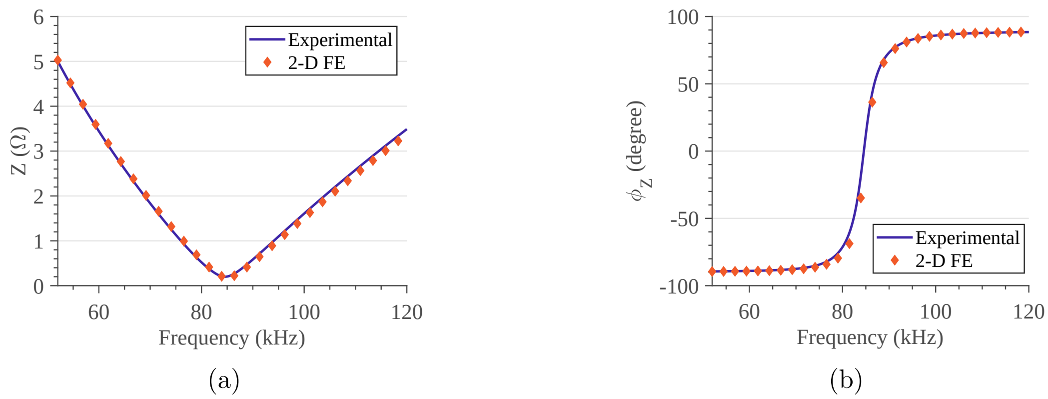

Figure 4.12: Validation of the 2-D finite-element model for the evaluation of (a) the module and (b) the phase of the input impedance of a complete WPT system at 10 cm range

4.2.4 Original approach for the conductors 2-D meshing

Although the 2-D model is fast and accurate, its performances can be further increased by having a fresh look on the 2-D meshing strategy. Until this point, this strategy has been based on a best-practice approach ensuring the presence of three elements layers in the skin depth. Such an approach is easy to implement via the simple specification of the elements characteristic length. However, the unstructured nature of the mesh involves a degree of randomness in the radial distribution of the elements in the skin depth during the mesh generation, as well as an azimuthal mesh density which is not necessarily required. Nonetheless, the mathematical current density evolution in a round wire submitted to skin effect is well-known and can be used as a more detailed information than the sole skin depth. Moreover, the mesh influence on the precision of the solution is also well-known, as the shape of the associated finite-element basis functions have been discussed previously. As a consequence, we intend to benefit from this combined information, and from the mesh structuring tools embedded in GMSH for proposing an optimal structured meshing strategy in the conductors.

The finite-element 2-D model employed in this work is based on the interpolation of the magnetic vector potential module via nodal first-order elements. On an element from the mesh, the module of the magnetic vector potential is thereupon constrained to evolve linearly and so does the module of the current density (as **j** belongs to the same function space as **a** in the Whitney's complex). The optimization of the mesh can be addressed by dealing as best as possible with this linearity constraint to represent the actual current density evolution. This problem can be approached by an one-dimension fitting problem, as demonstrated hereafter.

Reduction to a one-dimension problem

For a complete and deterministic control of the conductors meshing, each wire is decomposed in a structured mesh consisting in different azimuthal sectors, themselves containing different radial layers (see Figure 4.13). Since eddy-current effects produce current density variations mostly in the radial direction, the objective is to determine the optimal size and repartition of the radial layers. This problem can be simply formulated by noticing two important points.

On the one hand, the analytical description of the skin effect impacting a round wire demonstrates that the current density module evolves actually following a negative exponential with respect to the distance d from the surface of the conductor, *i.e.*

$$j(d) = j(0) \cdot e^{-d/\delta} \qquad \text{with } 0 \leq d \leq r \tag{4.1}$$

where δ is the skin depth and r is the radius of the wire. On the other hand, since the interpolated current density changes linearly on an element, its numerical evolution along a radius is expected to be piecewise linear (also described as polygonal). Moreover, the extent of each line segment is equal to the radial thickness of the related element. It pertains to the solver to determine the degrees of freedom for this polygonal line to fit as best as possible the actual current density allure. Under these conditions, using a best-practice rule for specifying a number of elements in the skin depth reverts to statically impose how many line segments are employed for approaching at best the evolution of the actual current density in the skin depth. Yet, although the current density varies quickly in the skin, its shape there could eventually be approached by a single line instead of three. Contrariwise, deeper than the skin depth, the actual allure of the current density could eventually evolve in such a way that several little segments would be required for approaching it at best. In such cases, the number of elements and their distribution are not optimal. Since the actual current density shape is known and expressed by (4.1), the mesh could be built in order to give the mean to the solver to approach as best as possible the negative exponential allure.

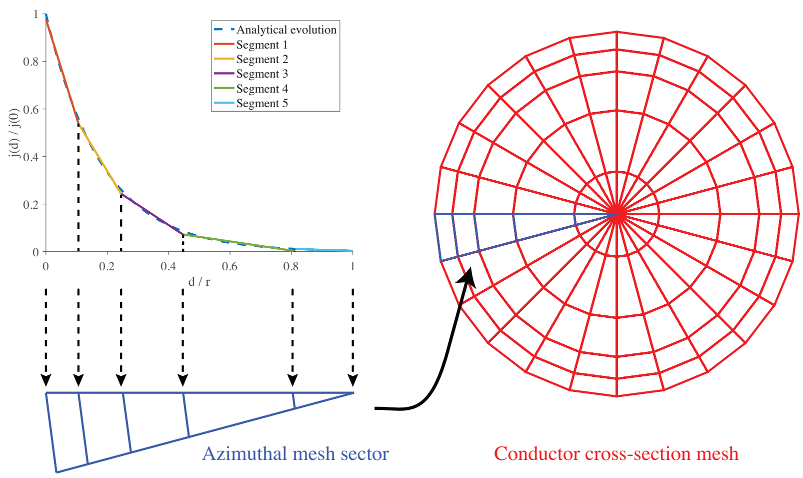

Figure 4.13: Illustration of the proposed meshing method

In consequence, we propose to address the mesh optimization via a clever approach which can be reduced to a one-dimension fitting problem, corresponding **to find how to distribute a minimal number of segments forming a polygonal line for approaching as best as possible a negative exponential**. Since the mesh influences only the shape of the current density on the system and not its value (which is determined by solving the numerical problem), this meshing problem is moreover dimensionless.

Fitting problem

By denoting N_s the number of segments and d_i the abscissa corresponding to the breaking points of the polygonal line (with $0 \leq i \leq N_s$, $d_0 = 0$ and $d_{N_s} = r$), the best segments distribution can be defined mathematically in the least square sense via a 1-D minimization along the abscissa x like

$$\min_{\substack{d_i \\ 0 \leq i \leq N_s}} \sum_{i=0}^{N_s - 1} \int_{d_i}^{d_{i+1}} \left(e^{-\frac{x}{\delta}} - (a_i x + b_i) \right)^2 dx \tag{4.2}$$

where $a_i x + b_i$ is the equation of the segment between the depth d_i and d_{i+1} and so that

$$a_i \; d_{i+1} + b_i = a_{i+1} \; d_{i+1} + b_{i+1} \tag{4.3}$$

When the breakpoints positions d_i are fixed and only the a_i and b_i must be determined, the problem is trivial. However in this case, the d_i are the unknowns of the problem and the interdependence between the problem degrees of freedom d_i, a_i and b_i hinders its analytical resolution. Based on the work of Bellman [109] and Stones [110], Gluss have proposed a numerical approach for such a problem [111]. Nevertheless, the associated computational burden for targeting a sufficient precision would be too important, especially as this optimization problem must be solved before each mesh generation and thus, before each finite-element simulation. As a consequence, we opted for a less rigorous but more pragmatic approach for determining the radial distribution of the elements.

The proposed heuristic approach is based on several successive linear regressions, as described hereunder with the help of the diagram in Figure 4.14. First, the negative exponential to fit (with the adequate δ) is discretized in a sufficiently high number N_p of equally-spaced points. Then, starting from the two first points, an increasing number of those points is employed for computing a linear regression. The sum of the squared error e_k associated with the current linear regression for each point considered in the latter is employed as a residue. After the inclusion of each additional point in the linear regression, the residue is evaluated and is expected to rise, given the concavity of the negative exponential curve. When the residue exceeds a given threshold value fixed to res_{max}, the current linear regression is supposed to be inefficient anymore for approaching the points from the exponential curve (and so would be the interpolated current density with respect to the actual current density). The last point added to the regression set before exceeding this threshold is considered as an optimal breaking point in the desired polygonal line. Then, a new linear regression is initiated from this point and the process is reiterated until reaching the last discretization point. The breaking points hence determined are used for setting the radial repartition of the elements along a wire radius (as shown on Figure 4.13). The number of azimuthal sectors is fixed to a number ensuring a sufficient mesh density.

Implementation and results

The proposed method has been implemented in a Matlab script driving the virtual laboratory. Here, the aim is the comparison of the optimality and the relevance of different meshing techniques, with the search of a compromise between the number of mesh elements (and thus, the number of DoF) and the associated results accuracy. As a consequence, three different techniques are compared, namely

- a brute-force approach considering an extremely fine unstructured mesh, corresponding to the negligence of the computational burden to the profit of the results accuracy. The elements characteristic length is uniformly set to a fourth of the skin depth for the highest tested frequency (200 kHz in the following). This approach is considered as the reference in the following ;

- a best-practice approach considering a fine unstructured mesh, currently applied in the virtual laboratory and corresponding to the presence of three elements in the skin depth and relaxing progressively the mesh near the conductor center. The elements characteristic length is set to a third of the skin depth for the test frequency and to four skin depths in the center ;

- the proposed approach, considering a structured mesh based on a pre-computed fitting problem, solved via the practical approach detailed above.

For illustration purposes, different cases are addressed here and differ by the tolerance on the maximal per-segment fitting residue, fixed successively to 1 %, 0.1 % and 0.01 %. Hence,

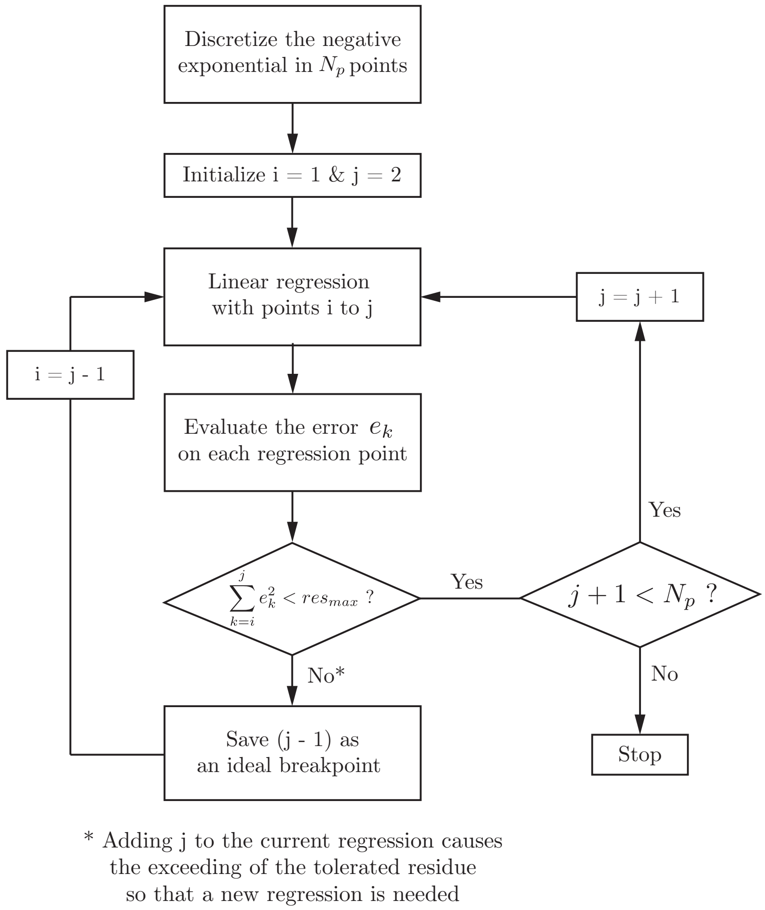

Figure 4.14: Block diagram relative to the proposed heuristic approach

the sensibility to the tolerated residue can be shown. The negative exponential depicting the expected current density evolution in the conductor is discretized in 1000 points. The experimental test-case for a mid-range power transmission is reconsidered for illustrating the computational and accuracy gain provided by the proposed method. For the wire employed in the test-case, one can note that the skin depth is higher than the radius for operating frequencies higher than 33 357 Hz. Since the objective is the comparison of meshing techniques, the unavoidable measurement errors should not interfere so that the numerical results from the brute-force approach are chosen as a reference. During the study detailed hereafter, the number of azimuthal sectors is fixed to 24 in order to render correctly the round shape of the wire.

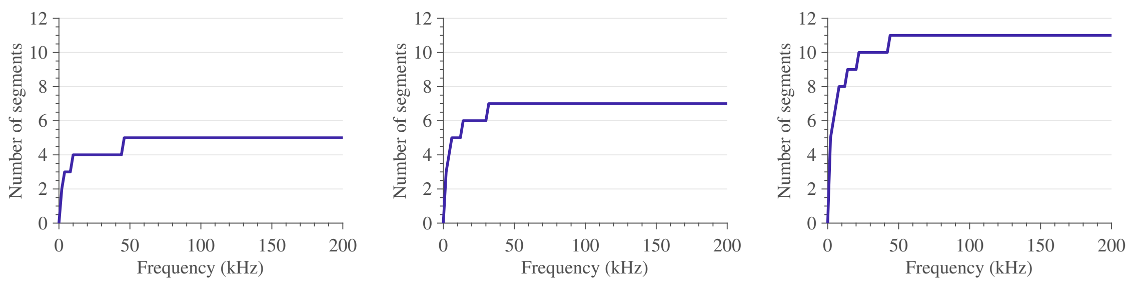

(a) 1 % residue (b) 0.1 % residue (c) 0.01 % residue

Figure 4.15: Number of segments for a given tolerated residue

The total number of segments required for keeping each per-segment fitting residue under a given tolerance varies logically with the latter and with respect to the frequency (see Figure 4.15). The increasing in the number of segments occurs logically around 33 kHz, where the skin depth becomes smaller than the wire radius. With the increase of the frequency, the allure of the negative exponential is expected to bend more, explaining the need for a higher number of segments for fitting it under a constant per-segment residue tolerance.

Considering an operating frequency of 100 kHz, the compared meshes are shown in Figure 4.16 and the related computational performances are gathered in Table 4.1 (the CPU time for the proposed method includes the fitting algorithm execution). The accuracy is judged based on the relative error impacting the winding resistance. One can note that the relative errors on the self- and mutual inductances is below 1 % for all the approaches. One can observe the computational gain provided by the proposed method, without any detrimental effect on the result accuracy. The number of DoF is divided by three and the CPU time (including the processing of the fitting problem) is divided by more than two, reaching around 1 second. Moreover, the control of the azimuthal mesh refinement permits to relax the mesh density in the air, with an increased gain in DoF number.

An interesting feature displayed by the proposed method is the maintaining of the computational performances despite doubling the operating frequency (up to 200 kHz), as demonstrated by Figure 4.17 and in Table 4.2. While the best-practice approach increases the number of DoF and the CPU time, the proposed approach reorganizes the elements, without adding any new element. The computational gain of the proposed method is logically further increased with a number of DoF almost divided by four and a CPU time divided by more than three. By the consideration of this two cases, the effectiveness of this original approach is clearly demonstrated. The computational performances are optimized with moreover an increased precision on the results, thanks to the proposed meshing strategy. One can note that the method can be extended to second-order or elements by performing parabolic regressions instead of linear regressions.

	Brute-force	Best-practice	Proposed		
			1 %	0.1 %	0.01 %
R ($m\Omega$) (Rel. error)	58.51 (Reference)	59.34 (+ 1.42 %)	60.16 (+ 2.82%)	59.38 (+1.48 %)	59.07 (+0.95 %)
DoF	170 700	33 492	9 438	10 110	11 454
CPU Time (s)	14.9	2.7	1	1.1	1.1

Table 4.1: Computational performances at 100 kHz

	Brute-force	Best-practice	Proposed		
			1 %	0.1 %	0.01 %
R ($m\Omega$) (Rel. error)	83.41 (reference)	84.12 (+ 0.9%)	85.80 (+2.87 %)	84.54 (+ 1.35 %)	84.05 (+0.8 %)
DoF	170 700	42 374	9 438	10 110	11 454
CPU Time (s)	14.9	3.4	1	1.1	1.1

Table 4.2: Computational performances at 200 kHz

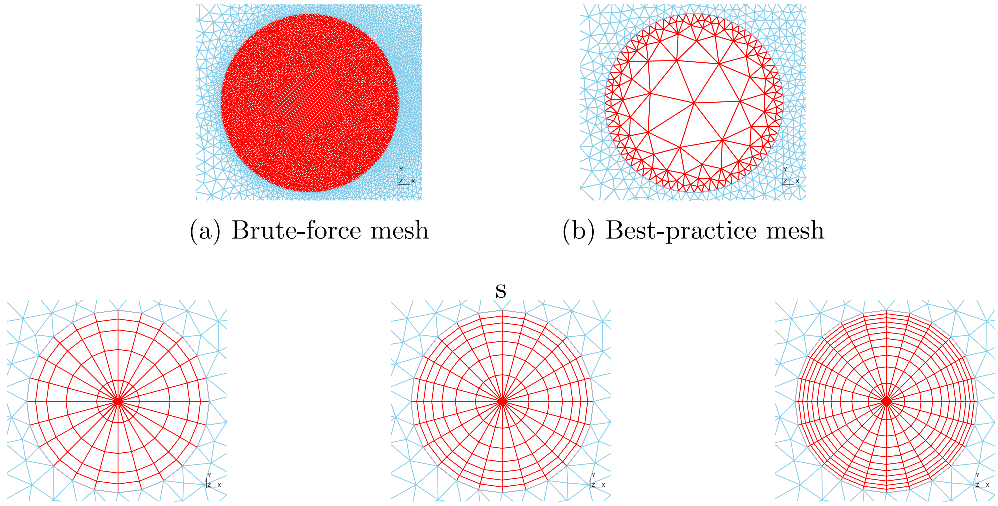

(a) Brute-force mesh (b) Best-practice mesh

(c) Proposed mesh (1 %) (d) Proposed mesh (0.1 %) (e) Proposed mesh (0.01 %)

Figure 4.16: Compared meshes at 100 kHz

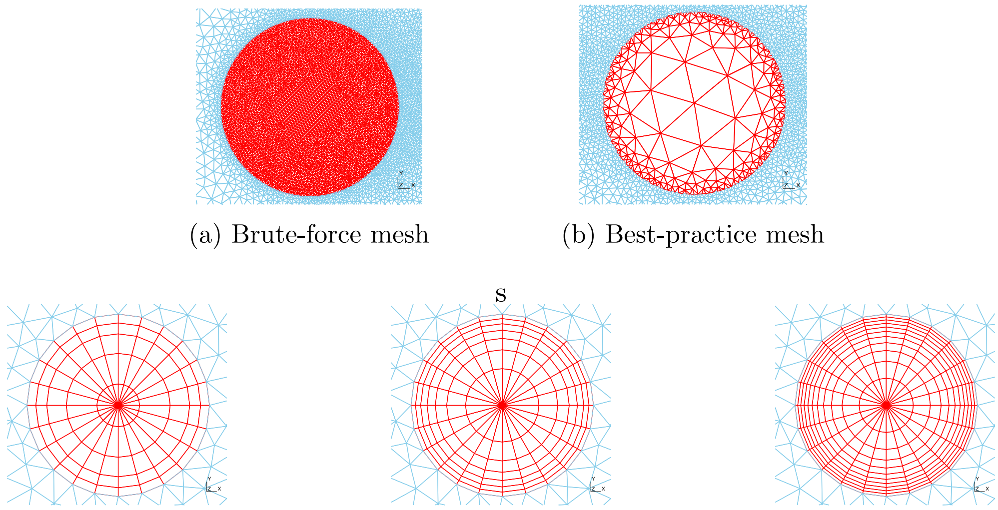

(a) Brute-force mesh (b) Best-practice mesh

(c) Proposed mesh (1 %) (d) Proposed mesh (0.1 %) (e) Proposed mesh (0.01 %)

Figure 4.17: Compared meshes at 200 kHz

4.2.5 Intermediate conclusions

In this section, the WPT windings finite-element modeling is undertaken primarily via an equivalent 2-D finite-element model. Valid when the coils are aligned, this model permits hence to simulate the behavior of the windings in their nominal configuration. With a meshing strategy based on a best-practice approach and despite a weak computational burden, the 2-D model has demonstrated its accuracy by matching the experimental measurements with only a few percent errors on the equivalent parameters of the windings. The simulation of a complete WPT system has also demonstrated the effectiveness of the virtual prototyping capabilities of the proposed tool. By proposing an original approach for the optimal meshing of round solid-wire submitted to eddy-current effects, the 2-D model performances have been further improved by providing even more accurate results, with a CPU time decreasing approximately to 1 second per frequency. Such performances allows to embed the finite-element 2-D model in an iterative optimization process, for example.

4.3 3-D numerical state-of-the-art models

After the elaboration, the validation and the improvement of the 2-D model, the transition to a 3-D model is envisioned. Such a transition is primordial for extending the modeling tool scope of application to situations which does not present an axial symmetry. Among the latter, one can find a simple situation corresponding to laterally of angularly shift coils, the consideration of non-symmetric couplers or the presence of surrounding objects (*e.g.* a car chassis). The transition from 2-D to 3-D turned out to be the main challenging task for the modeling part of this thesis. For surmounting this challenge, the development of an original formulation (*i.e.* a circuit-coupled surface impedance boundary conditions finite-element method) will be addressed. But first, the difficulties pertaining to the implementation of the classical finite-element and to the generalized PEEC methods are explained and discussed.

4.3.1 3-D finite-element brute-force model

Geometry and mesh

Keeping the virtual laboratory approach despite the transition to 3-D is a challenge *per se* for the programming of the parametrical geometry. The control and the cohesion of the volume mesh is particularly difficult.

Despite the possibility to render the windings spiral shape in 3-D, the considerations relative to the mesh prevent an actual spiral modeling of the coils. As a matter of fact, the implementation of the circuit coupling described in Section 3.5.3 requires to insert an electromotive region in a conductor which must be multiply connected, for constantly verifying the cancellation of div $\mathbf{j}$ in the conducting domain. In other words, it causes the impossibility for the conductor electrodes to be floating apart, so that modeling the coils spiral shape would require to model an interconnection. Such a local geometrical complexity would have a detrimental effect on the computational burden. Therefore, similarly to the 2-D case, the N-turns coils are replaced by a set of N concentric tori in which the electrodes are close.

Inside and along a conductor, the longitudinal variation of the current density is expected to be minor. However, the current density transversal variation (*i.e.* in a cross-section) is significant and dictated by the occurence of eddy-current effects. With this in mind, the conductor volume mesh is built by the extrusion of the typical cross-sectional 2-D mesh proposed for the 2-D model, leading to a set of non-straight prisms with a triangular base. For reducing the number of elements, the number of extrusions can reasonably be limited in order to simply ensuring the conductor curvature correct modeling. Nevertheless, this limitation is mitigated by the air mesh considerations.

Indeed, high local fields variations are occurring in the air directly surrounding the conductors. Limiting the longitudinal extrusions number inside the conductors will produce long elements on the conductors boundaries. Due to the mesh continuity at the conductor-air interface, the air directly surrounding the conductors would be roughly discretized, leading to an important error on the computation of the local fields. As a consequence, the number of longitudinal extrusions inside the conductors must be increased. In this case, the number of elements is surging due to the combined cross-sectional and longitudinal high mesh density.

A typical 3-D geometry is presented on Figure 4.18. Each winding is a set of concentric tori placed in a sphere filled with air and delimiting the domain of study. As in 2-D, an external shell is employed for rejecting the boundary to infinity. Based on the above discussions, a typical mesh is presented in Figure 4.19a for the global system and in Figure 4.19b for a focus on the conductors.

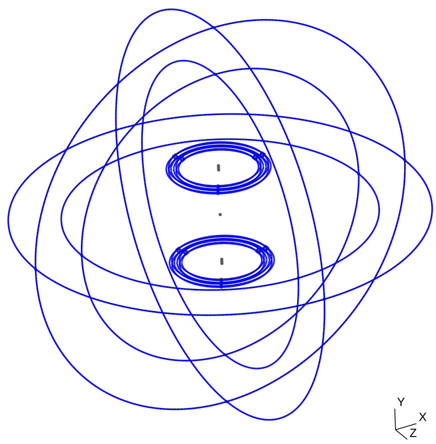

Figure 4.18: Typical geometry related to the 3-D finite-element model

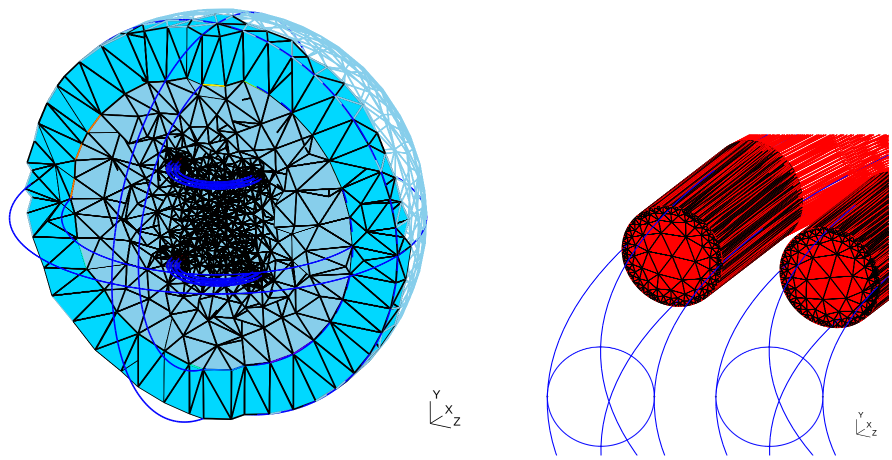

(a) Global system (b) Conductors (at 100 kHz)

Figure 4.19: Typical mesh related to the 3-D model

Validations, illustrations and discussions

The surging increase of the computational burden produced by the transition from 2-D to 3-D prevents from using the experimental test-case employed for the 2-D model validation for validating the 3-D model. Therefore, less cumbersome academic test-cases are considered for discussing the behavior of the 3-D model. However, experimental measurements on such test-cases are not relevant due to the smallness of the related windings parameters (with notably a resistance with a value of a few $m\Omega$ and mainly influenced by the slightest contact resistance). As a consequence, the parameters of the validation reference are evaluated using the 2-D model, validated and discussed previously.

Consisting first in a small single loop, the academic test-case evolves towards a practical one by considering two progression axes, namely the increase of the windings inner radius and the increase of the windings number of turns. A particular attention is paid to the conductors longitudinal mesh for two main reasons. On the one hand, the conductors cross-sectional mesh relevance has been demonstrated in 2-D. On the other hand, the longitudinal deployment of the conductors is the main specificity of the transition from 2-D to 3-D.

First test-case Let us consider two aligned simple loops presenting a 20 mm radius and made of a wire with a 4 mm^2 section separated by 20 mm and solicited at 100 kHz. Preliminary manipulations of the tool have permitted to identify the optimal elements characteristic length in the air and the optimal size for the air sphere delimiting the system. The conductors longitudinal mesh is progressively refined by increasing the number of extrusions (from 24 to 120, by step of 6) for completing a revolution around its axis. The 3-D model is employed for identifying the equivalent parameters for each refinement step, and the relative error made on each parameter is represented with respect with the associated number of DoF (see Figure 4.20).

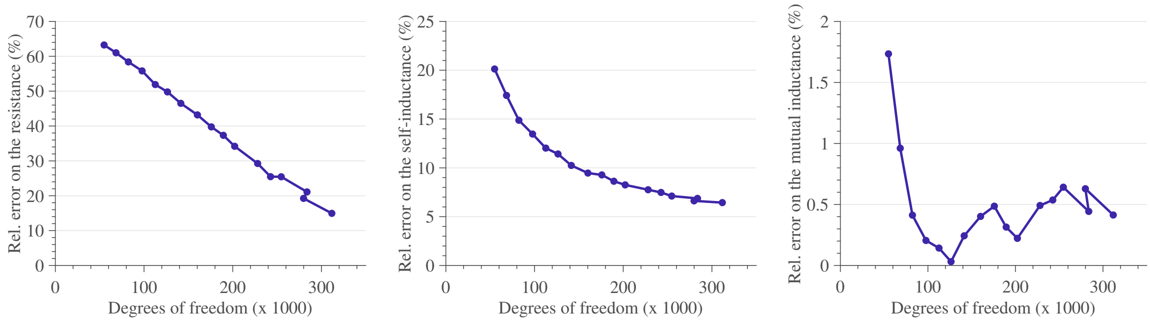

(a) Resistance (b) Self-inductance (c) Mutual inductance

Figure 4.20: Relative errors on the equivalent parameters with respect to the number of DoF for the first test-case (R = 20 mm, N = 1, f = 100 kHz) using the 3-D model

The increase in the extrusions number permits logically to improve the model precision, at the price of a drastic rise of the DoF number. Notably, 120 extrusions are required for reaching a 15 % error on the resistance and 7 % error on the self-inductance, leading to a DoF number of 311 734 corresponding to a total CPU time of 150 seconds (25 seconds for the meshing and 125 seconds for the solving). Nevertheless, one can ascertain the quality of the mutual inductance evaluation with a error under 2 % with the lowest number of extrusions. Contrary to what one might imagine, the extrusions number influence on the resistance accuracy is not particularly associated with the correct modeling of the shape of the conductor (which is quite well represented with the initial 24 extrusions per turn). However, this influence is associated with the mesh density in the direct surrounding air, and which plays a role in the rendering of the eddy-current effect. Hence, as explained in the previous section, the conductors meshing via successive extrusions is not crucial for the modeling of the conductor itself, but for ensuring a sufficiently dense mesh in the air close to the loops. For confirming this statement, a simulation of the same test-case has been performed in DC conditions, and the latter is not (or at least extremely slightly) influenced by the extrusions number and gives accurate results. The combination of such a high computational burden for such a simple system with such a low accuracy is clearly eliminatory for the classic massive conductor 3-D finite-element model. However, we propose to observe the evolutions of the burden and of the accuracy when more extended systems are considered.

Second test-case (increased number of turns) The same system is considered with an additional turn to each winding (bringing the number of turns to two) with a 1 mm space between the adjacent turns. Starting from 24 and progressing by step of 6, the extrusions number is limited to 90 due to the exploding computational burden, undermining the operation of the employed computer. The windings equivalent parameters are evaluated thanks to the 3-D model and the relative errors on these parameters are represented in Figure 4.21. For a given extrusion number, the first ans the second test-cases produce the same accuracy. However, doubling the number of conductors in the problem provokes an important rise in the DoF number which reaches around 600 000 for 90 extrusions (instead of 230 000 for the same extrusions number with the first test-case). A CPU time corresponding to 520 seconds (120 seconds for the meshing and 400 seconds for the solving) is required for such a configuration. Once again and as expected, the 3-D finite-element model limitations are exacerbated by the consideration of this second test-case.

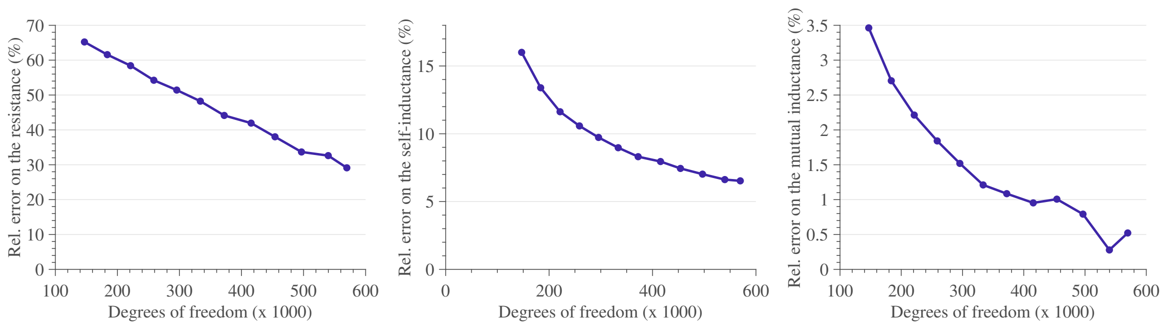

(a) Resistance (b) Self-inductance (c) Mutual inductance

Figure 4.21: Relative errors on the equivalent parameters with respect to the number of DoF for the second test-case ($R = 20$ mm, $N = 2$, $f = 100$ kHz) using the 3-D model

Third test-case (increased inner radius) Let now consider a couple of loops similar to the first test-case, but presenting an increased size with a 30 mm inner radius. Once again, the number of extrusions has been risen from 24 to 120 and the relative error made on the loops equivalent parameters are shown in Figure 4.22. Globally, the errors on all the parameters have increased. For explaining this, one can notice that a constant extrusions number for a longer loop yields longer elements leading logically to higher errors. In comparison with the first test-case, a slight decrease in the DoF number is observable and explained by the mesh relaxation in the system center since the conductors are more extended.

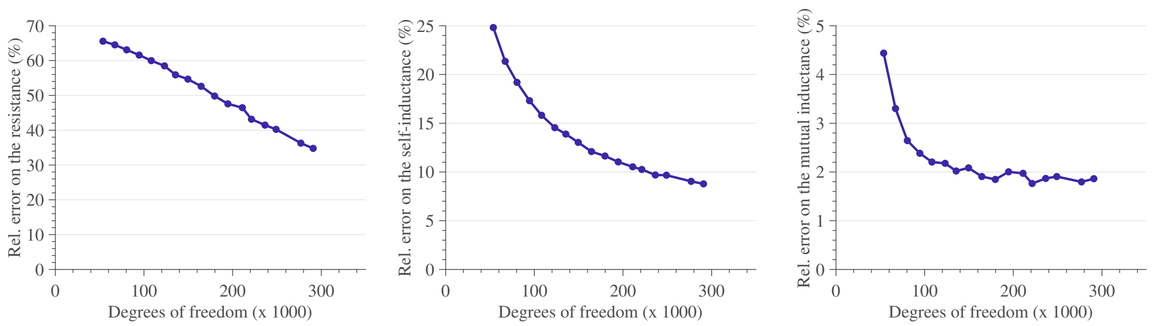

(a) Resistance (b) Self-inductance (c) Mutual inductance

Figure 4.22: Relative errors on the equivalent parameters with respect to the number of DoF for the third test-case ($R = 30$ mm, $N = 1$, $f = 100$ kHz) using the 3-D model

Fourth test-case (increased number of turns and inner radius) The last test-case consists in two windings presenting a 30 mm inner radius with two turns separated by 1 mm, as a combination of the second and the third test-cases. The detrimental effects on the computational performances observed for theses two cases are cumulated. Despite a critical DoF number around 600 000, the model accuracy is poor with more than 40 % error on each winding resistance, nearly 10 % error on each winding self-inductance. The mutual inductance is however tarnished by a relatively small 3 % error.

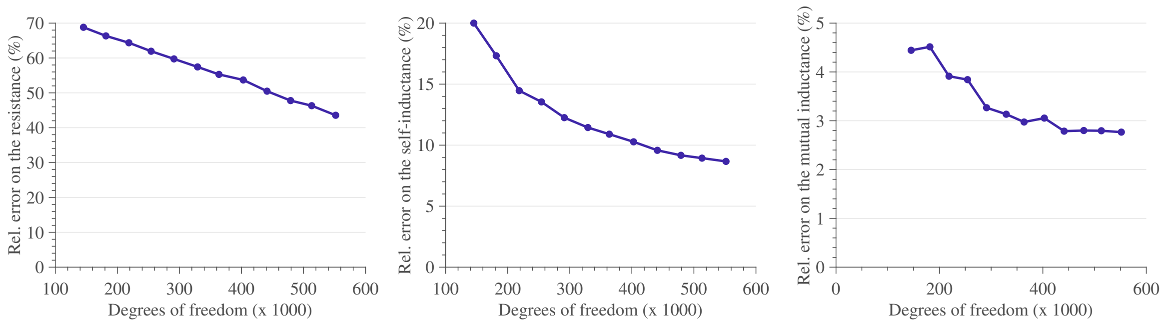

(a) Resistance (b) Self-inductance (c) Mutual inductance

Figure 4.23: Relative errors on the equivalent parameters with respect to the number of DoF for the fourth test-case (R = 30 mm, N = 2, f = 100 kHz) using the 3-D model

Intermediate conclusions

From our experience and by observing the results presented above, the 3-D mesh management for the solid-wire WPT windings modeling is highly complicated. Despite the obvious axisymmetry in the simulated test-cases, the longitudinal refinement of the conductors mesh seems to influence drastically the solution, according to the presented results. We found that this phenomenon has two origins. The first and main origin is the mesh quality in the conducting regions. As a matter of fact, a small extrusions number combined with the fine cross-sectional mesh lead to the generation of stretched prisms in the conductors. Such an element shape has a detrimental effect on the edge elements numerical integration and are qualified as low-quality elements. Hence, the positive impact of a longitudinal mesh refinement on the windings resistance is attributed to the improvement of the elements quality. The second origin is the impact of the conductors mesh on the refinement, by continuity, of the air mesh in the direct vicinity. The combination of refined cross-sectional and longitudinal meshes leads to an impracticable computational burden. Even for such simple test-cases, a personal computer limits have been reached for a 100 kHz operating frequency. Since the modeling of practical systems would require to raise far greater the size and the number of turns in comparison with the test-cases addressed here and since the frequency range must exceed 100 kHz (stressing the model even more), the classic massive conductor 3-D finite-element method is not practicable for the simulation of solid-wire pancake windings.

In the next section, the generalized PEEC is envisioned as a potential alternative to the 3-D finite-element method. First, the resort to facet elements instead of edge elements may provide an richer interpolation space allowing to decrease the constraint on the mesh and on the elements quality. Second, the generalized PEEC avoids the need to mesh the ambient air and permits to remove hence the major part of the system volume.

4.3.2 3-D generalized PEEC model

In this section, the application of the generalized PEEC method for the modeling of solid-wire windings is addressed. For better understanding and analysis of the following results, one has to notice that this method has been employed as a black-box. As a matter of fact, benefitting from our Unit collaboration with the G2ELab members, we were granted an access to their development forge by the end of 2016. The generalized PEEC was presented in the form of a Java code of which the complexity exceeds the scope of this thesis. Moreover, this method was (and still is) under continuous developments subject to several research projects. At the time, we were warned by the developers of the lack of optimality in certain auxiliary numerical tools necessary for the assembling and the resolution of the method, with however work in progress for improving the related performances. Moreover, some features were not available as, notably, the support of triangular-based prisms.

Geometry and mesh

Thanks to the integral nature of the PEEC method, the geometry and the mesh of the system are limited to the conducting regions. Although it is restricted to a small spatial region, the test we performed demonstrated the high complexity associated with the generation of an adequate mesh. More particularly, the close relation between the abstract integration numerical processes (due to our black-box approach) and the characteristics of the mesh has complicated the optimization of the meshing procedure. Indeed, the assembling of the inductance matrix of the PEEC method is based on spatial integrations on elements from the mesh. The shape and the disposition of the elements are logically interfering intricately with the precision and the good conditioning of the numerical processes for assembling and further solving the PEEC matrix. As a consequence, it has been particularly difficult to find a pertinent and objective way to improve the results obtained with the PEEC method via the optimization of the mesh, notably regarding the precision on the parasitic resistance. Some erratic variations (beneficial as detrimental) of the precision on the results furnished by the PEEC method have impeached an objective and methodical highlights of its limitations, in contrast with the procedure proposed for the 3-D finite-element method.

Globally, the conditioning of the numerical integration processes associated with the computation of the partial self-inductances is harshly affected by the occurrence of long elements. Although this issue could be addressed by increasing the number of Gauss integration points in the longitudinal direction, the consecutive surge in the CPU time required for the assembling of the inductance matrix hinders this solution. Consequently, the conductors mesh is submitted to the same constraints as with the 3-D finite-element method for avoiding the occurrence of long elements, namely the required conjunction of a cross-sectional refinement (for an accurate determination of the windings parasitic resistance) and a longitudinal refinement (for an accurate determination of the windings inductances) of the mesh. Although the absence of ambient air in the discretized system, these constraints associated with the increased numerical cumbersomeness of the PEEC method (due to the assembling of the inductance matrix, as well as to the fullness of the problem matrix) require to realize strong compromises between the precision of the results (notably regarding the resistance) and the computational performances.

Illustrations and intermediate conclusions

For illustrating these statements, the modeling of the no-load test at 100 kHz of an academic test-case consisting couple of two aligned loops of 20 mm made of a 4 mm^2 wire and separated by 20 mm (similar to the first test-case considered for the 3-D finite-element modeling) is performed using the generalized PEEC method. Different meshes are compared and are respectively built by N_L successive extrusions of three different cross-sectional meshes (see Figure 4.24). The mesh A corresponds to a uniform cross-sectional mesh, the mesh B corresponds to the presence of one element in the skin depth and the mesh C corresponds to the presence of two elements in the skin depth. For avoiding the formation of triangular-based prisms, these cross-sectional meshes are made of hexahedra. Different numbers of extrusions are considered (from 24 to 72 by step of 12) and the correspondent relative errors of the windings parasitic resistance, self-inductance and mutual inductance (by using the validated 2-D finite-element model as a reference) are presented in the different tables in Figure 4.25. The related computational performances are gathered in Table 4.3. The cells filled with a dash are corresponding to simulations which have not been performed due to an expected simulation time over 1000 seconds.

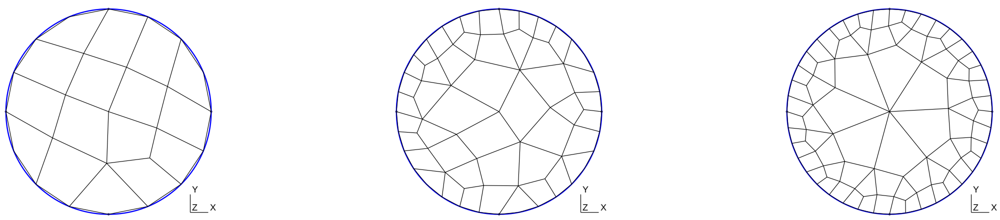

(a) Mesh A (b) Mesh B (c) Mesh C

Figure 4.24: Cross-sectional meshes employed for the testing of the generalized PEEC method

N_L	Mesh A	Mesh B	Mesh C
24	20.7 %	8.0 %	1.5 %
36	8.9 %	4.2 %	10.7 %
48	15.7 %	2.0 %	/
60	18.3 %	1.1 %	/
72	20.1 %	/	/

(a) Resistance

N_L	Mesh A	Mesh B	Mesh C
24	7.4 %	16.5 %	18.5 %
36	4.6 %	8.3 %	9.5 %
48	3.7 %	5.3 %	/
60	3.3 %	3.1 %	/
72	3.1 %	/	/

(b) Self-inductance

N_L	Mesh A	Mesh B	Mesh C
24	1.7 %	1.7 %	1.5 %
36	2.3 %	2.4 %	2.6 %
48	2.5 %	2.6 %	/
60	2.6 %	2.5 %	/
72	2.6 %	/	/

(c) Mutual inductance

Figure 4.25: Evolution of the relative error on the parameter of a couple of loops of 20-mm radius at 100 kHz using the generalized PEEC method

N_L	Mesh A	Mesh B	Mesh C
24	1808 DoF 11.5 s	6094 DoF 132 s	9558 DoF 388
36	2694 DoF 25 s	9105 DoF 349 s	14546 DoF 1079 s
48	3582 DoF 42 s	12086 DoF 691 s	/
60	4470 DoF 68 s	14332 DoF 1068 s	/
72	5338 DoF 106 s	/	/

Table 4.3: Computational performances (DoF and CPU time) associated with the execution of the generalized PEEC method for a couple of loops of 20-mm radius at 100 kHz

The difficulty to orientate the meshing strategy regarding the precision on the resistance is demonstrated by the non-monotonic decrease of its relative error following certain longitudinal or cross-sectional mesh refinements. Nonetheless, the approximation via facet elements demonstrates its richness by paralleling the (insufficient, but interesting) relative precision on the resistance with such loose densities of elements in the cross-section. Also, these results demonstrate clearly the beneficial effect of the elements shortening (corresponding to an increase of N_L) on the self-inductance value, with however a detrimental effect on the mutual inductance value. The excellent ratio between the accuracy on the inductances and the computational performances associated with the column dedicated to the mesh A confirms the well-known adequacy of the PEEC method for approaching the inductive modeling of electrical systems.

However, as expected, the results producing the highest accuracy for all the parameters correspond to a concomitant refinement of the longitudinal and cross-sections meshes (with 48 or 60 extrusions with the mesh B). The CPU times associated with these simulations are not practicable in the framework of a time-efficient modeling required by the virtual laboratory approach. This even more true in that the considered test-case is purely academic and the considerations of a practical winding would require to increase the number of turns, with a linear increase of the number of DoF, but an exponential increase in CPU time. This hinders the interest for the 3-D generalized PEEC method (as in its version by the end of 2016) as a practical method for the electromagnetic modeling of solid-wire WPT windings.

4.4 3-D finite-element model with surface impedance boundary condition and circuit coupling

As highlighted previously, the 3-D finite-element modeling of the coils employed for WPT as massive conductors is submitted to an important computational burden. As a consequence, alternatives need to be considered for ensuring the 3-D modeling of the solid-wire WPT windings. Requiring the modeling of the active parts of the system only, the generalized inductive PEEC method has been envisioned for removing the air from the domain. Although the air constitutes the most important part of the system volume, it is not the region where the mesh is the most constrained. Conversely, the PEEC method has demonstrated that the conductor is precisely the region from which the computational burden originates. Therefore, an antagonist approach is adopted here by proposing and developing a method allowing to remove the conductor volume mesh from the problem domain of definition by using surface impedance boundary conditions (SIBCs) [72, 73]. Reflecting the important influence of the external circuit on the power transfer (through the resonant effect), a circuit coupling needs to be applied in order to model the resonant conditions at the circuit and fields levels. The combination of SIBCs with a circuit-coupled $\mathbf{t}$ - ϕ formulation has already been addressed [112]. Here and as argued in the previous chapter, the $\mathbf{a}$ - v magnetodynamic formulation is considered. In this chapter, the method described in Section 3.5.3 for coupling an external circuit with an $\mathbf{a}$ - v formulation involving massive conductor is adapted and extended to the use of SIBCs. Permitting to couple a finite-element system without any conducting volume to an external circuit, this original method leads to a new way and original to implement SIBCs. The development, the implementation in 3-D and the experimental validation of this method are major scientific contributions from this thesis.

Concept of surface impedance boundary condition

In the general domain of definition of a magnetodynamic problem, the conducting parts Ω_c can be removed from Ω while continuing to account for the conductors influence into the problem. Indeed, following from Snell's law for refraction, the law relating the tangential traces of the magnetic and electric fields on the dielectric-conductor interface (due to the presence of the conductor) can be established. This relation is assumed to be constant over the entire conductor surface (independently of the position) and may thus act as a particular local boundary condition applied on the conductor skin Γ_c, which becomes a part of the boundary Γ_h after the removal of Ω_c from Ω. Since the difference in conductivity between the conductor and the ambient dielectric (*i.e.* the air) is significant, the electromagnetic fields are assumed to penetrate the conductor normally to its surface. Under these conditions, the fields tangential traces on Γ_c are related as

$$\mathbf{n} \wedge \mathbf{h} = Z_c^{-1} \, \mathbf{n} \wedge (\mathbf{n} \wedge \mathbf{e}) \tag{4.4}$$

One can intuitively understand that the coefficient linking an electric and a magnetic fields component is pertaining to an impedance on each point of the conductor skin. The coefficient Z_c^{-1} is therefore the local surface impedance of the conductor and the relation (4.4) employed as a mixed boundary condition is called a *surface impedance boundary condition* (SIBC). However, implementing SIBCs requires primarily to characterize and express Z_c^{-1}.

Development of the surface impedance

In the frequency domain, the surface impedance is approached by an asymptotic expansion with respect to the skin depth [73]. The first-order contribution (known as the Leontovitch approximation) is rigorously exact for an infinite conducting plane, presenting a finite conductivity. The second-order contribution (known as the Mitzner approximation) introduces a possible curvature of the conductor surface. The third-order contribution (known as the Rytov approximation) accounts further for the tangential diffusion of the fields. Yuferev *et al.* have proposed a selection criteria for choosing the correct approximation [71]. In this thesis framework, the frequency-level is supposed to be high enough for the skin depth to be negligible in front of the conductors dimensions. Under theses conditions, the Leontovitch approximation is relevant, as confirmed by the aforementioned selection criteria.

In this case and assuming that the conductor conductivity is significantly greater than the product of the angular frequency and the dielectric permittivity, the surface impedance Z_c is a scalar complex

$$Z_c = \frac{\omega\mu}{2}(1+j)\delta = \frac{(1+j)}{\sigma\delta} \tag{4.5}$$

Introduction in the magnetodynamic a - v weak formulation

Now that the surface impedance expression has been established, the magnetodynamic problem can be expressed without the terms related to Ω_c in the weak form (3.47)-(3.48) by using the relation (4.4) as a non-homogeneous mixed boundary condition on $\Gamma_c \subset \Gamma_h$, with

$$\begin{aligned}\langle \mathbf{n} \wedge \mathbf{h}_s, \mathbf{e}' \rangle_{\Gamma_c} &= \langle Z_c^{-1}\ \mathbf{n} \wedge (\mathbf{n} \wedge (\partial_t \mathbf{a} + \text{grad } v)) , \mathbf{e}' \rangle_{\Gamma_c} \\ &= \langle Z_c^{-1}\ \mathbf{n} \wedge (\partial_t \mathbf{a} + \text{grad } v) , \mathbf{n} \wedge \mathbf{e}' \rangle_{\Gamma_c} \end{aligned} \tag{4.6}$$

where $\mathbf{e}'$ is whether $\mathbf{a}' \in F_e^1(\Omega)$ or grad $v' \in F_e^1(\Omega)$. The conductors are now represented by their tubular skin only and the electric scalar potential v is only defined on and supported by the boundary Γ_c. In absence of stranded inductor, the weak formulation (3.47)-(3.48) becomes

$$\begin{aligned}&(\nu \text{ curl } \mathbf{a},\ \text{curl } \mathbf{a'})_\Omega \\ &\quad + \langle Z_c^{-1}\ \mathbf{n} \wedge (\partial_t \mathbf{a} + \text{grad } v) , \mathbf{n} \wedge \mathbf{a}' \rangle_{\Gamma_c} + \langle \mathbf{n} \wedge \mathbf{h}_s\ , \mathbf{a'} \rangle_{\Gamma_h \backslash \Gamma_c} = 0 \qquad \forall \mathbf{a'} \in F_e^1(\Omega) \end{aligned} \tag{4.7}$$

$$\begin{aligned}&\langle Z_c^{-1}\ \mathbf{n} \wedge (\partial_t \mathbf{a} + \text{grad } v) , \mathbf{n} \wedge \text{grad } v' \rangle_{\Gamma_c} \\ &\qquad\qquad + \langle \mathbf{n} \wedge \mathbf{h}_s\ , \text{grad } v' \rangle_{\Gamma_h \backslash \Gamma_c} = 0 \qquad \forall v' \in F_e^0(\Omega) \end{aligned} \tag{4.8}$$

Employing the SIBC formulation (4.7)-(4.8) as an alternative to the massive conductor formulation (3.47)-(3.48) in the proposed virtual laboratory requires to extend the circuit-coupling technique exposed in Section 3.5.3 to a problem without any massive conductor. This extension is an original contribution of this thesis.

Strong coupling with an external circuit

As exposed in Section 3.5.3, the coupling of the electromagnetic problem with an external circuit requires to define local constraints on Γ_c involving global quantities, *i.e.* the voltage across and the total current in each modeled conductor. As for the massive conductor formulation, the constraint definition can be achieved by locating an electromotive force between the remaining traces of two infinitely close cross-sections representing the electrodes of a conductor $\Omega_c^i \in \Omega_c$ (with $1 \leq i \leq N_c$ and N_c the number of conductors), as shown in Figure 4.26. Since Ω_c has been removed from the domain using SIBCs, the remaining parts from the electrodes are their respective contour exclusively and the conductor initially included in Ω_c^i is represented by its skin Γ_c^i. For clarity purposes, from this point, a conductor initially represented by Ω_c^i will be referred by its index i. The thin tube separating the electrodes contours of conductor i is denoted Γ_g^i and extracted from Ω. Let V_i and I_i be the voltage between the electrodes and the current across one or the other electrode, respectively. By denoting γ_g^i the latter electrode contour, one has

$$\int_{\gamma_i} \mathbf{e}\ d\mathbf{l} = V_i \text{ and } \oint_{\gamma_g^i} \mathbf{h}\ d\mathbf{l} = I_i \tag{4.9}$$

where γ_i is any path on Γ_g^i connecting the electrodes contours and $d\mathbf{l}$ is an element of contour. In contrast with the method presented in Section 3.5.3 and due to the absence of conducting parts, the total current I_i is no more expressed via the current density $\mathbf{j}$ (which is zero on the whole domain Ω), but via the circulation of the magnetic field $\mathbf{h}$ along an electrode contour. A particular effort is expected to be furnished for the definition of circuit relations, involving precisely I_i in a local formulation.

Here again, the inclusion of grad $F_e^0(\Omega)$ in $F_e^1(\Omega)$ ensures that the formulation (4.7) implies systematically the formulation (4.8). Like for the massive conductor formulation, using Whitney's edge elements for the projection of $\mathbf{a}$ and Whitney's nodal elements for the projection of v permits the segmentation of the problem in two successive sub-problems for introducing the voltage V_i as a strong global quantity.

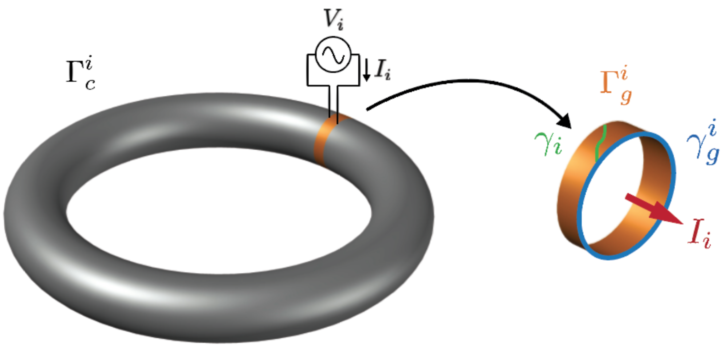

Figure 4.26: Electromotive force definition in a conductor i

Voltage as a strong global quantity

The first sub-problem consists in determining for each conductor i a source surface electric scalar potentials $v_{0,s}^i$ defined on Γ_c^i and corresponding to the apparition of a unitary voltage across the electrodes of the conductor i. Hence, the surface electric scalar potential can be expressed as

$$v = \sum_{i=1}^{N_c} V_i \cdot v_{0,s}^i \tag{4.10}$$

The source surface electric scalar potentials $v_{0,s}^i$ can be obtained by the resolution of an electrokinetic problem for each conductor i. Similarly to the approach proposed for massive conductor, we propose to define a general source surface electric scalar potential for avoiding the resolution of preliminary electrokinectic problems. Inspired by the generalized source electric scalar potential proposed by Dular *et al.* for massive conductors [69], the surface source potential can be defined as the sum of the nodal basis functions on the contour γ_g^i

$$v_{0,s}^i = \sum_{n_i \in \gamma_g^i} s_{n_i} \tag{4.11}$$

The latter potential support is limited only to the layer of facets adjacent to γ_g^i in Γ_c^i and is decreasing from one on γ_c^i to zero at the end of this layer. As for massive conductor, the generalized potential does not tarnish the validity of the global problem solution, but the evolution of the surface electric scalar potential v is not physical anymore. The improvements in the system of equations bandwidth associated with this reinterpretation of v and evoked in Section 3.5.3 are maintained in this SIBC-based formulation.

The second sub-problem is the resolution of the weak form (4.7) where the voltages V_i have been introduced vie the reinterpretation of the surface electric scalar potential. One has

$$\begin{aligned}&(\nu \text{ curl } \mathbf{a},\ \text{curl } \mathbf{a'})_\Omega + \langle Z_c^{-1}\ \mathbf{n} \wedge \partial_t \mathbf{a}, \mathbf{n} \wedge \mathbf{a'} \rangle_{\Gamma_c} \\ &\quad + \sum_{i=1}^{N_c} V_i \langle Z_c^{-1}\ \mathbf{n} \wedge \text{grad } v_{0,s}^i, \mathbf{n} \wedge \mathbf{a'} \rangle_{\Gamma_c} + \langle \mathbf{n} \wedge \mathbf{h}_s\ , \mathbf{a'} \rangle_{\Gamma_h \backslash \Gamma_c} = 0 \qquad \forall \mathbf{a'} \in F_e^1(\Omega)\end{aligned} \tag{4.12}$$

Projecting $\mathbf{a}$ on edge elements and applying the Galerkin's method yields $N_{\mathcal{E}}$ equations, *i.e.*

$$\begin{aligned}&\sum_{e_{ij} \in \mathcal{E}} a_{e_{ij}} \left(\nu \text{ curl } \mathbf{s}_{e_{ij}},\ \text{curl } \mathbf{s}_{e_{mn}}\right)_\Omega + \sum_{e_{ij} \in \mathcal{E}} \partial_t a_{e_{ij}} \langle Z_c^{-1}\ \mathbf{n} \wedge \mathbf{s}_{e_{ij}}, \mathbf{n} \wedge \mathbf{s}_{e_{mn}} \rangle_{\Gamma_c} \\ &+ \sum_{i=1}^{N_c} V_i \langle Z_c^{-1}\ \mathbf{n} \wedge \text{grad } v_{0,s}^i, \mathbf{n} \wedge \mathbf{s}_{e_{mn}} \rangle_{\Gamma_c} + \langle \mathbf{n} \wedge \mathbf{h}_s\ , \mathbf{s}_{e_{mn}} \rangle_{\Gamma_h \backslash \Gamma_c} = 0 \quad \forall \mathbf{s}_{e_{mn}} \in F_e^1(\Omega)\end{aligned} \tag{4.13}$$

whereas the problem disposes of $N_{\mathcal{E}}$ degrees of freedom $a_{e_{ij}}$ and N_c degrees of freedom V_i. The problem is completed by the definition of N_c circuit relations involving the current I_i flowing in each conductor.

Circuit relations (current as a weak global quantity)

The current I_k flowing in the conductor k is introduced in the problem by using the generalized source surface electric scalar potentials $v_{0,s}^k$ as test-functions in the formulation (4.8). One has

$$\begin{aligned}\langle Z_c^{-1}\ \mathbf{n}\wedge(\partial_t\mathbf{a}+\text{grad}\ v)\,,\mathbf{n}\wedge\text{grad}\ v_{0,s}^k\rangle_{\Gamma_c}&\\ +\langle\mathbf{n}\wedge\mathbf{h}_s\ ,\text{grad}\ v_{0,s}^k\rangle_{\Gamma_h\setminus\Gamma_c}&=0 \qquad \forall k \text{ with } 1\leq k\leq N_c\end{aligned} \tag{4.14}$$

The term relative to the boundary $\Gamma_h\setminus\Gamma_c$ can be processed for highlighting the current I_k. Indeed, using vector analysis rules and similarly to the case considering massive conductors, the latter term can be decomposed as

$$\langle\mathbf{n}\wedge\mathbf{h}_s\ ,\text{grad}\ v_{0,s}^k\rangle_{\Gamma_h\setminus\Gamma_c}=\int_{\Gamma_h\setminus\Gamma_c}\mathbf{n}\cdot\text{curl}\ \left(\mathbf{h}_s\cdot v_{0,s}^k\right)d\Gamma-\int_{\Gamma_h\setminus\Gamma_c}\mathbf{n}\cdot\text{curl}\ (\mathbf{h}_s)\cdot v_{0,s}^k\ d\Gamma \tag{4.15}$$

In contrast with the method presented in Section 3.5.3, the first right-hand-side is different from zero and treated hereafter, while the second right-hand-side term is zero in this case, since a generalized potential $v_{0,s}^k$ is defined on Γ_c only. Applying the Stokes theorem on the first right-hand-side, the surface integral on $\Gamma_h\setminus\Gamma_c$ turns into a path integral on its boundary, denoted $\partial(\Gamma_h\setminus\Gamma_c)$. As the electromotive tubes Γ_g^i (with $1\leq i\leq N_c$) have been extracted from Ω, the electrode contours γ_g^i (with $1\leq i\leq N_c$) are all included in the boundary $\partial(\Gamma_h\setminus\Gamma_c)$. However, $v_{0,s}^k$ is, by definition, different from zero only on γ_g^k, so that

$$\int_{\Gamma_h\setminus\Gamma_c}\mathbf{n}\cdot\text{curl}\ \left(\mathbf{h}_s\cdot v_{0,s}^k\right)d\Gamma=\int_{\partial(\Gamma_h\setminus\Gamma_c)}\mathbf{h}_s\cdot v_{0,s}^k\ d\mathbf{l} \tag{4.16}$$

$$=\oint_{\gamma_g^k}\mathbf{h}_s\ d\mathbf{l}=I_k \tag{4.17}$$

Via Ampère's law, the circulation of an external magnetic field $\mathbf{h}_s$ can be interpreted as the current I_k entering the conductor k. The discrete SIBC-based magnetodynamic formulation expressed in terms of $\mathbf{a}$ and the voltages V_i is hence completed by N_c circuit relations, ensuring $\forall k$ with $1\leq k\leq N_c$ that

$$\begin{aligned}I_k+\sum_{e_{ij}\in\mathcal{E}}\partial_t a_{e_{ij}}\langle Z_c^{-1}\ \mathbf{n}\wedge\mathbf{s}_{e_{ij}},\mathbf{n}\wedge\text{grad}\ v_{0,s}^k\rangle_{\Gamma_c}&\\ +\sum_{i=1}^{N_c}V_i\langle Z_c^{-1}\ \mathbf{n}\wedge\text{grad}\ v_{0,s}^i,\mathbf{n}\wedge\text{grad}\ v_{0,s}^k\rangle_{\Gamma_c}&=0\end{aligned} \tag{4.18}$$

Since $v_{0,s}^k$ is different from zero on Γ_c^k only, the latter circuit relations can be simplified to the following, again $\forall k$ with $1\leq k\leq N_c$

$$\begin{aligned}I_k+\sum_{e_{ij}\in\mathcal{E}}\partial_t a_{e_{ij}}\langle Z_c^{-1}\ \mathbf{n}\wedge\mathbf{s}_{e_{ij}},\mathbf{n}\wedge\text{grad}\ v_{0,s}^k\rangle_{\Gamma_c^k}&\\ +V_k\langle Z_c^{-1}\ \mathbf{n}\wedge\text{grad}\ v_{0,s}^k,\mathbf{n}\wedge\text{grad}\ v_{0,s}^k\rangle_{\Gamma_c^k}&=0\end{aligned} \tag{4.19}$$

As for the massive conductors, conductors represented via an SIBC can be coupled with additional and external circuitry. The circuit relation associated to each external component is added to the problem, with a network constraint specifying the way the finite-element and the external components are interconnected.

4.4.1 Experimental validation

The formulation (4.13)-(4.19) is validated experimentally by anew considering the experimental test-case introduced in Section 4.2.3. As a reminder, it is composed by two similar and aligned pancake windings, each presenting a 52 mm inner radius and made of 7 turns of a wire with a 4 mm^2 section. Adjacent turns being in contact, the turns are separated by 1.3 mm (corresponding to twice the 0.65 mm insulating sheath thickness). The ability of the proposed formulation to determine the equivalent parameters of a windings couple is demonstrated by considering a no-load test configuration. Then, the formulation circuit-coupling capabilities are highlighted by considering the inclusion of the windings in a WPT system.

Determination of the windings equivalent parameters

The SIBC-based magnetodynamic formulation is employed in 3-D for simulating a no-load test, aiming at the determination of the windings self-parameters with respect to the operating frequency. The results are compared with the measurements performed using a two-port impedance analyzer Wayne Kerr 6510B. The resistance values are compared in Figure 4.27b, while the self-inductance values are compared in Figure 4.28b. In absence of volume mesh in the conductor, the same mesh (generated within a CPU time of 27 seconds) is employed for all the simulated frequencies, since a frequency-dependent volume mesh is no longer required. Each resolution uses 369 537 DoF and lasts 120 seconds. Keeping in mind that a complex practical system is modeled here, the computational performances (in terms of burden, CPU time and accuracy) are significantly improved in comparison with the ones displayed by the classic 3-D finite-element model for academic test-cases.

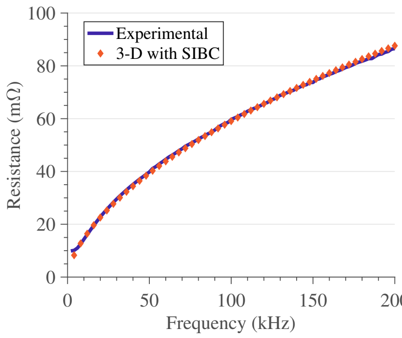

(a) Global value

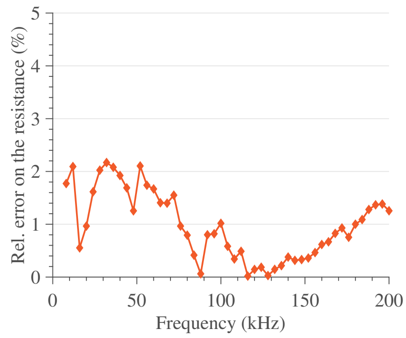

(b) Relative error (experimental as reference)

Figure 4.27: Validation of the 3-D SIBC-based model (parasitic resistance evaluation)

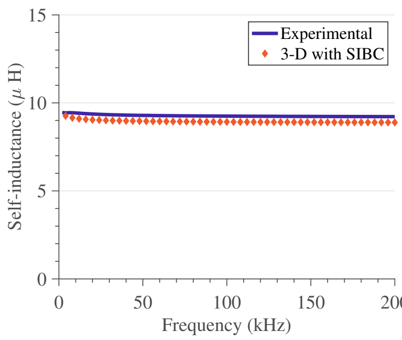

(a) Global value

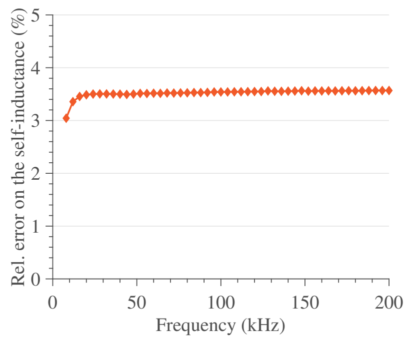

(b) Relative error (experimental as reference)

Figure 4.28: Validation of the 3-D SIBC-based model (self-inductance evaluation)

Simulation of a complete WPT system

The 3-D finite-element SIBC-based formulation is validated experimentally on a complete WPT system depicted by the schematic in Figure 4.29. The experimental setup is identical to the one employed for the validation of the 2-D finite-element model. As a reminder, the system is composed by the same couple of aligned windings as employed for the no-load test presented above. However, the windings are integrated in a complete RIPT system presenting a self-resonant frequency of 85 kHz thanks to the series connection of a resonant 380 nF capacitor to each winding. The load is a pure resistance of 1 Ω. The SIBC-based formulation is used for determining the input impedance $\underline{Z}$ of the complete WPT system, using a 3-D finite-element modeling of the coils strongly coupled with the external lumped elements. Two situations are considered, namely the situation where the coils are separated by 5 cm and the situation where the coils are separated by 10 cm.

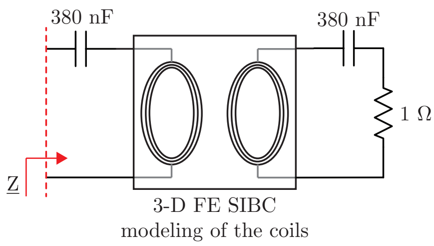

Figure 4.29: Schematic of the validation example circuit

Aligned windings separated by 5 cm The input impedance $\underline{Z}$ of the whole system when the coils are aligned and separated by 5 cm is determined numerically, and compared with the one measured experimentally (using the same impedance analyzer as for the previous validations). The corresponding results are shown in terms of module Z and phase ϕ_Z of $\underline{Z}$ with respect to the operating frequency (with a focus on the resonance zone) in Figure 4.30. Since the discretized model of the windings is strictly identical to the one employed for the no-load test validation, each simulated frequency includes 369 575 DoF (with 8 more DoF than the no-load test, corresponding to the additional circuit relations) and lasts 120 seconds. In absence of volume mesh inside the conductor, the same mesh (generated, as a reminder, within 23 seconds) is used for all the simulated frequencies. The comparison of the numerical and the experimental results demonstrates the clear effectiveness of the method which reproduces accurately the frequency-domain behavior of the WPT system and notably, the occurrence of the frequency splitting phenomenon.

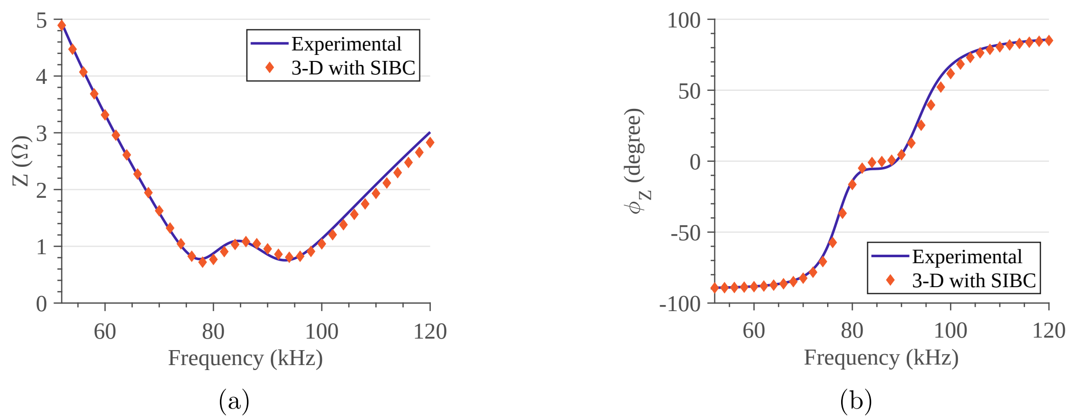

Figure 4.30: Validation of the 3-D SIBC-based model for the evaluation of (a) the module and (b) the phase of the input impedance of a complete WPT system at 5 cm range

Aligned windings separated by 10 cm The same comparison is made when the coils are placed further from each other (*i.e.* aligned and separated by 10 cm) and the corresponding results are presented in Figure 4.31. Once again, one can notice the matching between the results provided by the proposed method and the experimental measurements. Each simulation includes 391 086 DoF and lasts 162 seconds. The mesh employed for all the simulated frequencies has been generated in 39 seconds.

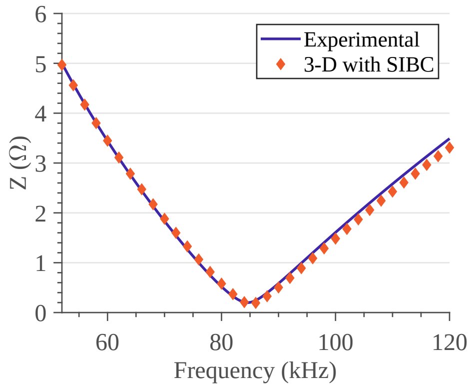

(a)

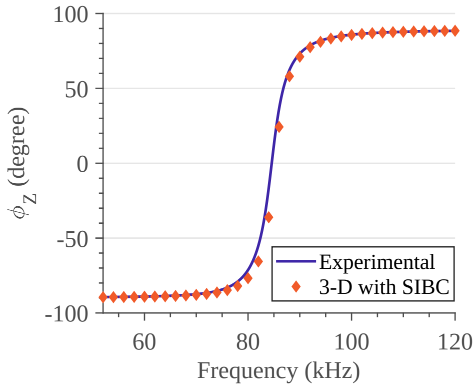

(b)

Figure 4.31: Validation of the 3-D SIBC-based model for the evaluation of (a) the module and (b) the phase of the input impedance of a complete WPT system at 10 cm range

4.5 Conclusions

This chapter gathered the presentation of the different computational models employed in the framework of this thesis, associated with discussions based on topical numerical results, destined to mark out our investigations concerning the electromagnetic modeling of solid-wire planar windings.

Following a progressive approach from less to more complex models, a first 2-D finite-element model has been used and validated experimentally. The latter provided interesting results, by producing a relative error of less than 2 % on the determination of the windings self-parameters in the targeted operating frequency range, while requiring around 3 seconds for solving between 30 000 to 40 00 DoF. Fostered by these promising results, an original optimal approach for the 2-D meshing of round solid wire submitted to eddy-current effects has been proposed. The latter is based on a procedure (limited to a 1-D fitting problem) aiming at determining the optimal radial distribution of the mesh layers inside the conductors for the interpolated approximation of the current density to fit as best as possible its actual evolution, determined analytically. Whereas providing slightly more accurate results, the implementation of the proposed meshing strategy has resulted in the division by four of the number of DoF and by more than three of the CPU time in comparison with the conventional best-practice meshing technique. With a simulation time reaching 1 second, the resort to this optimized 2-D model combined with the virtual laboratory approach promoted in this thesis is particularly adapted for its integration in an iterative optimization process of the design of the coils.

The transition from 2-D to 3-D has been initiated with the consideration of a classic massive conductor 3-D finite-element, employed as a brute-force approach. A procedure destined to monitor the evolution of the related computational burden by considering progressively more complex academic test-cases has been applied. The associated results have demonstrated the non-practicability of the such a method due to the surge in the computational burden. Due to the necessity to produce high cross-sectional and longitudinal mesh densities, the simulation of a simple academic test-case required, for example, more than 600 000 DoF and more than 500 seconds of CPU time for achieving a relative error of 40 % on the windings parasitic resistance.

Benefiting from an access to an under-development version (dating from the end of 2016) of the generalized PEEC method as a part of the G2ELab's MIPSE project, the latter method has been considered for alleviating the computational burden in 3-D thanks to the intrinsic advantages pertaining to its integral nature. Nevertheless and despite a drastic decrease in the number of unknowns, the numerical treatment of its integral formulation associated with the complex relation between the latter and the elements shape balance the apparent advantages of the method, especially regarding the precision on the windings resistance. For reaching a relative error under 3 % on an academical single loop test-case, the method requires more than 1000 seconds of CPU times. However, the generalized PEEC method demonstrates an ability to seize more efficiently (*i.e.* with a looser mesh more quickly) the order of magnitude of the windings parameters than the 3-D finite-element method, but with an insufficient accuracy on the windings parasitic resistance.

For proposing a practicable and accurate 3-D model of the windings, the resort to SIBCs has been envisioned for removing the conducting domains from the modeling problem, while still rendering the eddy-current effects. Regarding the importance of the circuit external to the windings in the resonant phenomenon, an original weak formulation for implementing a strong circuit coupling with an $\mathbf{a}$ - v magnetodynamic finite-element model using SIBC has been developed and validated experimentally. In comparison with the performances displayed by the brute-force finite-element method on academic test-case, the computational improvements are highly significant. Hence, the proposed method requires less than 400 000 DoF and up to 160 seconds for the modeling of our experimental test-case, with relative errors below 4 % on the self-parameters in comparison with experimental results. Moreover, the effectiveness of the circuit coupling is demonstrated by the experimental validation of the numerical modeling of a complete WPT system and notably the reproduction of the typical and complex frequency splitting phenomenon.

At this point, the virtual laboratory developed here disposes therefore of a fast and accurate 2-D optimized model, which can be integrated in optimal design procedures (as it is valid for the nominal position of the coil), and of a practicable and accurate 3-D model, which can be selectively employed for evaluating more general configurations.

The publications associated with this chapter are (in chronological order)

- A. Desmoort, Z. De Grève and O. Deblecker, "A virtual laboratory for the modeling of Wireless Power Transfer systems," *2015 International Conference on Electromagnetics in Advanced Applications (ICEAA)*, Turin, Italy, 2015, pp. 1353-1356.

- A. Desmoort, Z. De Grève and O. Deblecker, "Analytical, Numerical and Experimental Modeling of Resonant Wireless Power Transfer Devices (Research & Development Award)," in *SRBE/KBVE Revue E Tijdschrift*, 132nd year, no. 1-4, 2016.

- A. Desmoort, J. Siau, G. Meunier, J.-M. Guichon, O. Chadebec, O. Deblecker, "Comparing partial element equivalent circuit and finite element methods for the resonant wireless power transfer 3D modeling," *2016 IEEE Conference on Electromagnetic Field Computation (CEFC)*, Miami, United States, 2016, pp. 1-1.

- A. Desmoort, Z. De Grève, P. Dular, C. Geuzaine and O. Deblecker, "Surface impedance boundary condition with circuit coupling for the 3D finite element modeling of wireless power transfer," *2016 IEEE Conference on Electromagnetic Field Computation (CEFC)*, Miami, United States, 2016, pp. 1-1.

- A. Desmoort, Z. De Grève, P. Dular, C. Geuzaine and O. Deblecker, "Surface Impedance Boundary Condition With Circuit Coupling for the 3-D Finite-Element Modeling of Wireless Power Transfer," in *IEEE Transactions on Magnetics*, vol. 53, no. 6, pp. 1-4, June 2017, Art no. 7402104.

- A. Desmoort, Z. De Grève and O. Deblecker, "Modeling and Optimal Control of Resonant Wireless Power Transfer," *2018 IEEE Young Researcher Symposium Benelux (YRS2018)*, Brussels, Belgium, 2018.

Part II

Optimal command strategy for resonant inductive power transfer systems

CHAPTER

FIVE

INTRODUCTION TO RESONANT POWER CONVERTERS

The second part of this thesis is dedicated to the proposition and the development of a power conversion topology as well as a command methodology for achieving an optimal transfer with respect to the transmission power efficiency. The most elementary, but typical form for the power conversion chain is represented in Figure 5.1. The latter comprises a switched-mode inverter for exciting the system with an AC current or voltage. In practice, a voltage-source inverter is preferred due to the simplicity associated with its command and due to the lack of the switching devices employed in a current-source inverter. On the other side of the transmission system, the secondary (*i.e.* the receiving) circuit is interfaced with the DC load via a rectifier, usually consisting in a diode bridge. As the switched-mode inverter is the key converter in the operation of an RIPT system, this introductory chapter is focusing on the presentation of the inverter topology and of the inverter command which will be considered further in this thesis.

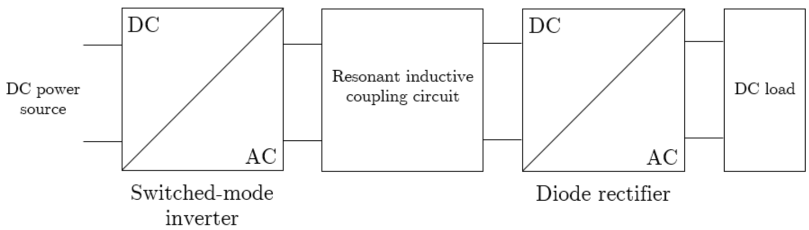

Figure 5.1: Typical power conversion chain for resonant inductive power transfer

However, the combination of such a switched-mode converter with a resonant circuit leads to the creation of a resonant converter, typically employed for enabling soft switching of the semiconductor devices, thereby reducing the switching losses [113–117]. Depending on the dynamic behavior of the real semiconductor components and on the converters command, switching losses are however more difficult to address and to evaluate than static conduction losses. As discussed later in this chapter, a solution for mitigating (or even avoid) switching losses consists in including an adequate resonant network in conventional power conversion chains. In the framework of resonant WPT, the intrinsic resonant nature of the useful circuit is an obvious asset. Employed properly, the resonant WPT circuit can solve the switching losses issue, which is precisely problematic for this application, leading to a global synergistic solution. The study of the soft-switching operation of a resonant converter requires to address precisely the switches network topology and the command scheme. As a consequence, we propose to describe the topology and command of the inverter through the prism of the resonant converter concept, in order to concomitantly analyze briefly the soft-switching operation of RIPT inverters.

One can note that, depending on the actual implementation of the system and on its operational features, additional DC-DC converter(s) can be included between the DC source and the inverter, and/or between the rectifier and the DC load. Also, the rectifier can be equipped with switches instead of diodes for achieving active rectification. Such modifications are addressed in the next chapter, for serving the proposed methodology.

5.1 Hard-switching and switching losses

In switched-mode converters, the switches are often caused to turn on by short-circuiting the load voltage and to turn off by cutting the load current, thereby achieving what is known as *hard-switching*. Whereas current and voltage transitions are usually considered as instantaneous for simplifying the holistic study of a converter operation, real switches (passive, like diodes, as well as active, like transistors) are made of charge-controlled semiconductor components requiring some time delays for commutating from the on-state to the off-state, and vice versa. During these time intervals, hard-switched devices are concomitantly submitted to non-negligible current and voltage, leading to an energy dissipation occurring for each switching transition and therefore called *switching losses*. One can notice that over-voltages and/or over-currents also occur during hard switchings due to the parasitic elements in the switching circuit.

A simple example of hard-switched circuit for investigating the switching losses - inspired from [113] - is shown in Figure 5.2a. The related current i_s and voltage v_s schematic linearized waveforms are represented in Figure 5.2b. In the following, the diode D is supposed to be ideal, since we focus our study on the switch S only. The source I_o emulates a constant load current, while the circuit is supplied by a DC voltage V_o.

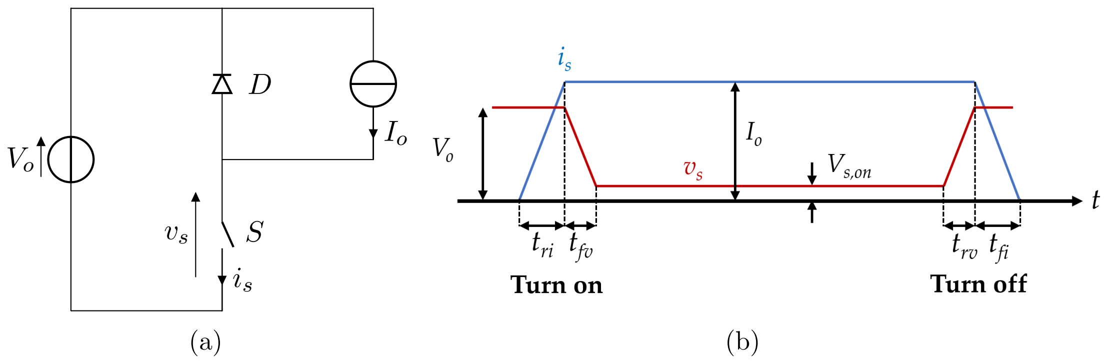

Figure 5.2: Example of a (a) hard-switched circuit and associated (b) linearized waveforms

Initially, the switch is supposed to be off so that it supports the DC source voltage V_o. When the turn-on signal is transmitted to S, the current starts building progressively up to I_o during a time interval t_{ri}. Once the current is established to I_o, the voltage falls to the on-state voltage $V_{s,on}$ during a time interval t_{fv}. Hence, during the switch entire turn-on time interval $(t_{ri} + t_{fv})$, a current $i_s \neq 0$ and a voltage $v_s \neq 0$ coexist and an energy $W_{sw,on}$ is dissipated with

$$W_{sw,on} \approx \frac{1}{2} V_o I_o \left(t_{ri} + t_{fv}\right) \tag{5.1}$$

Afterward, when the turn-off signal is transmitted to S, the voltage starts building progressively up to V_o during a time interval t_{rv}. Once the voltage is established to V_o, the current falls to zero during a time interval t_{fi}. Hence, during the switch entire turn-off time interval $(t_{rv} + t_{fi})$, a voltage $v_s \neq 0$ and a current $i_s \neq 0$ coexist and an energy $W_{sw,off}$ is dissipated with

$$W_{sw,off} \approx \frac{1}{2} V_o I_o \left(t_{rv} + t_{fi}\right) \tag{5.2}$$

Consequently, a total amount of energy $W_{sw,on} + W_{sw,off}$ is dissipated for each switching period so that a power

$$P_{sw} = \left(W_{sw,on} + W_{sw,off}\right) f_{sw} \approx \frac{1}{2} V_o I_o \left(t_{ri} + t_{fv} + t_{rv} + t_{fi}\right) f_{sw} \tag{5.3}$$

is dissipated in average by the switch S due to hard-switching, with f_{sw} the switching frequency. As demonstrated by expression (5.3), switching losses are logically proportional to the switching frequency and increasing with the product of the load current and voltage, which poses a problem for the WPT applied to high-power applications regarding the usual operating frequencies around 100 kHz. The frequency, the voltage and the current being fixed by the targeted application, the switching losses can be decreased by reducing the rise and fall time intervals using faster semiconductor components. However, it is a dangerous option as it would increase the di/dt and the dv/dt during commutations, leading to higher stresses on the components, and to electromagnetic interferences (EMI) issues. Decreasing the system efficiency and stressing the components, hard-switching should obviously be avoided, and hence *soft-switching* must be considered.

5.2 Soft-switching and resonance

Soft-switching consists in mitigating the switching losses by commanding a switch turn-on and/or turn-off when its voltage is zero - achieving zero-voltage switching (ZVS) - or when its current is zero - achieving zero-current switching (ZCS). Depending on constraints associated with the circuit and on its command, both turn-on and turn-off or only one of them can be performed without loss. Soft-switching is usually implemented by resorting to resonant circuits. As a matter of fact, a resonant circuit presents filtering properties which permits to shape the switch voltage or the switch current for canceling it at the switching instants. Depending on the converter type and on the localization of the resonant elements, two categories of soft-switched converters are defined, namely the quasi-resonant converters (QRCs) and the resonant power converters (RPCs).

5.2.1 Quasi-resonant converters (QRCs)

QRCs are based on the insertion of two auxiliary reactive components (an inductor and a capacitor) around each switch in any usual hard-switched converter. The local resonant circuits hence created are shaping the switch voltage as a pulse for achieving ZVS at turn-on and at turn-off (yielding a ZVS-QRC), or the switch current as a pulse for achieving ZCS at turn-on and at turn-off (yielding a ZCS-QRC). For illustration purposes, the examples of quasi-resonant ZVS and ZCS buck converters are presented in Figure 5.3. The typical voltage and current waveforms in the switch are shown in Figure 5.4.

5.2.2 Resonant power converters (RPCs)

In contrast with QRCs, RPCs (see Figure 5.5) are based on the insertion of two or more reactive components (with at least an inductor and a capacitor) forming a resonant tank network (RTN) placed before the useful circuit, in cascade of any conventional AC-output hard-switched converter, called in this context a controlled switch network (CSN). The RTN

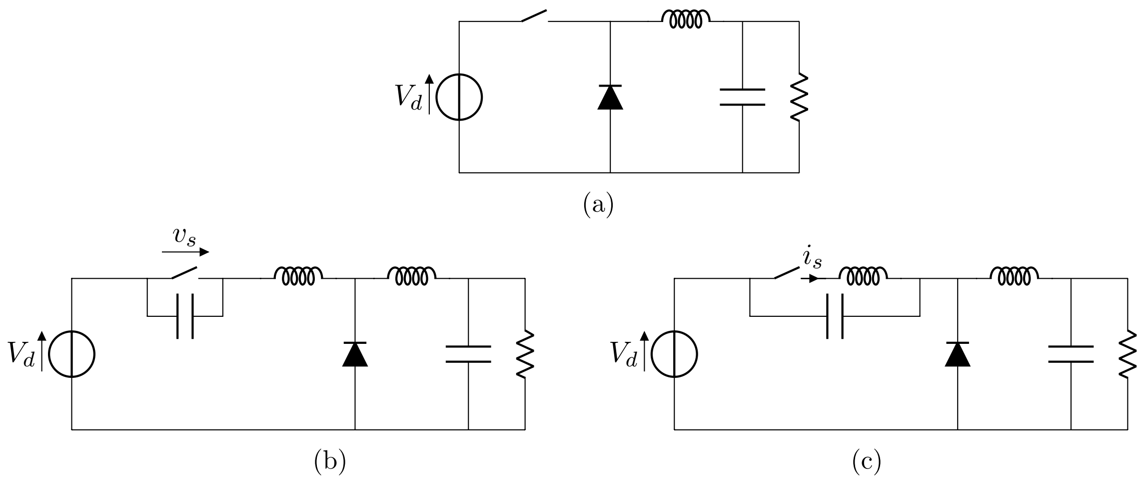

Figure 5.3: Example of QRC with an (a) usual buck converter, its (b) ZVS-QRC equivalent and its (c) ZCS-QRC equivalent

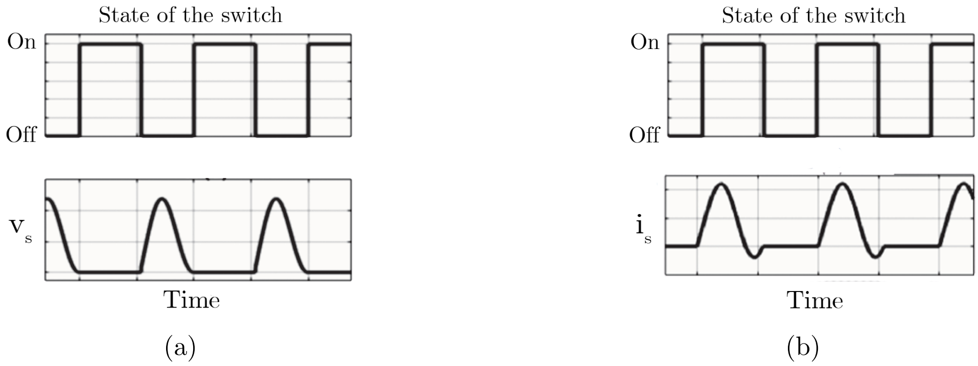

Figure 5.4: Typical (a) switch voltage waveform in a ZVS-QRC buck converter [116]

aims to produce an oscillation in the voltage across a current-source CSN or in the current through a voltage-source CSN, allowing its switches to turn-on and/or to turn-off softly. As a matter of fact, the oscillation produced by the RTN causes the natural cancelation of the voltage across or the current through the switches in the CSN, enabling therefore soft-switching when the commutations are tuned correctly with respect to the latter oscillation.

In the framework of resonant WPT, it seems clear that the useful circuit (consisting in the inductively coupled resonators) can act as an RTN, without any need for additional reactive components. Hereafter, the use of a resonant WPT circuit as an RTN is detailed in the light of its inverter soft-switching operation. The attention is drawn on voltage-source converters only, as current-source converters are not addressed in this thesis due to their marginality, fostered by the lack of the associated switching devices. In this context, investigating the soft-switching operation requires to determine clearly

- the CSN switching sequence for achieving a given output voltage, depending on its topology and on the type of switches command ;
- the resulting evolution of the current waveform, depending on the RTN (*i.e.* the resonant WPT circuit, in this case).

Both the CSN and the WPT circuit (as an RTN) are investigated in the following sections, for determining specific rules allowing to ascertain the soft-switching operation of the system voltage-source inverter.

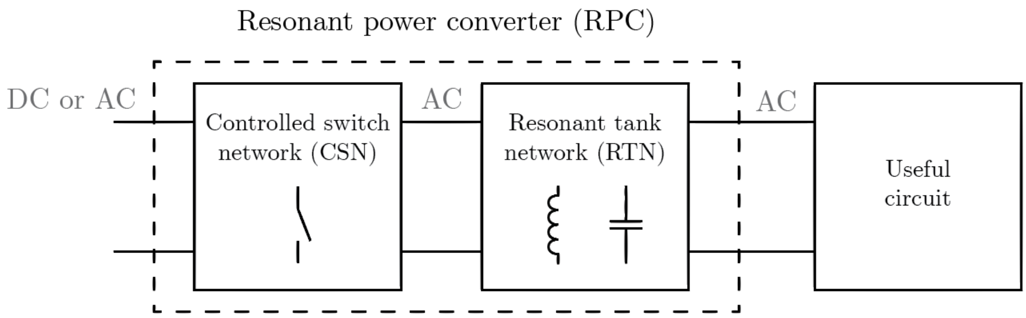

Figure 5.5: Typical resonant power converter (RPC) structure

5.3 Characterization of the CSN

5.3.1 Topology of the CSN

Conventional two-level converters are usually employed for supplying a resonant WPT system. Apart from the push-pull topology (which is rarely employed for WPT and therefore not addressed here), there are mainly two conventional two-level converter topologies, namely the half-bridge and the full-bridge converters (see Figure 5.6).

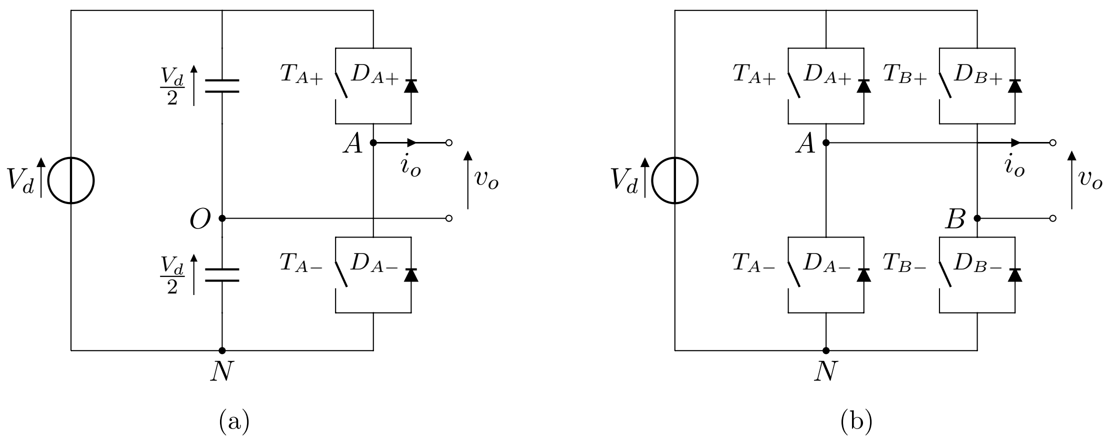

Figure 5.6: Topologies of (a) half-bridge and (b) full-bridge inverters

Half-bridge converter

The half-bridge converter consists in a leg composed by two switching cells respectively denoted $A+$ and $A-$, including each an active switch and an anti-parallel diode. The output AC voltage v_o is taken between the middle-point A in the leg and the middle-point O in a leg composed of two identical capacitors supporting each half the DC source voltage V_d. Therefore, the AC voltage is worth either $V_d/2$ or $-V_d/2$, enabling an output voltage control using bipolar pulse-width modulation (PWM) techniques (with adjustable frequency and duty ratio). Finally, the input average current of the half-bridge converter is reversible so that the useful power flow can be bidirectional.

Full-bridge converter

The full-bridge converter consists in two legs composed each by two switching cells respectively denoted $A+$ and $A-$ and $B+$ and $B-$, including each an active switch and an anti-parallel diode. The output AC voltage v_o is taken between the middle-point A of the first leg and the middle-point B of the second leg. Therefore, the AC voltage is worth either V_d, 0 or $-V_d$. With more switching combinations, the full-bridge converter offers a wider scope of output voltage control strategies, enabling bipolar and unipolar PWM techniques (adjustable in frequency and duty ratio). With an instantaneous output voltage amplitude equal to V_d, the full-bridge converter consumes less current for converting the same amount of power in comparison with a half-bridge converter. Like the half-bridge converter, the input average current of the full-bridge converter is reversible so that the useful power flow can be bidirectional.

For limiting the converter current consumption and for benefiting from a wider scope of control strategies (notably unipolar PWM strategies), the full-bridge is chosen as the converter topology prevailing in the following of this thesis.

Remark. *Besides the classic switch-mode converter topologies derived in QRCs or RPCs, it is worth considering the class E inverter. The latter, based on the use of a single switching cell, is a combination of a QRC (as it relies on a local reactive element to shape the switch-related waveforms as smooth pulses) and an RPC (as its operation depends on a downstream resonant circuit). The class E inverters are hence very particular. The specific resonant circuit involved in a class E ZVS inverter (see Figure 5.7) is notably compatible with an RIPT circuit. Its use for RIPT has therefore been investigated in [118–120].*

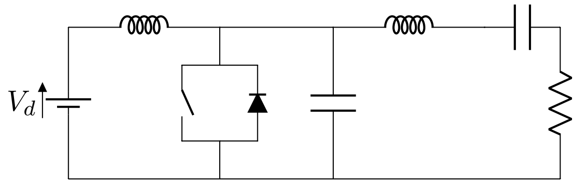

Figure 5.7: Class E ZVS inverter

Properly designed, this resonant network provides ZVS for both the turn-on and the turn-off of the switch, cancelling theoretically the switching losses. Another advantage of the Class E ZVS inverter is the limited number of semiconductor components (only a switch and a diode) and the simplicity of its control (as the soft-switching is basically ensured by its resonant circuit). However, the class E ZVS inverter suffers from a poor diversity in the practicable control strategies and operates correctly for a limited load range. Moreover, its input average current is non-reversible, so that it is not practicable for bidirectional power transfer.

5.3.2 Command of the CSN

In this section, different PWM command strategies practicable with the full-bridge inverter [113, 115] are discussed in the framework of RIPT and its constraints (notably in terms of switching frequency).

Sinusoidal pulse width modulation

The sinusoidal PWM command of the full-bridge inverter is widely implemented in power electronics. The latter consists in commanding switchings according to the comparison of a sinusoidal signal presenting the frequency of the desired output voltage with a carrier signal. Consequently, the switching frequency is a multiple of the circuit operating frequency. Nevertheless, the current delivered by the converter is oscillating at the operating frequency, so that it does not necessarily (actually, rarely) change sign during a switching period. Implementing the soft-switching operation of the full-bridge in these conditions is therefore not practicable. Moreover, the relatively high ratio between the switching and the operating frequencies required for a proper use of the sinusoidal PWM is not compatible with the framework of RIPT. The required operating frequency (around 100 kHz) and power levels (several kW) hinders the realistic consideration of such a command scheme. In the light of the foregoing, the attention is drawn on square-wave command and its derivatives.

Square-wave control

The square-wave command is the most elementary command strategy for controlling an inverter. As illustrated in Figure 5.8a, it consists in generating a square-wave voltage with a positive value (*i.e.*, V_d) during a first operating half-period (with T_{A+} and T_{B-} turned on) and a negative value (*i.e.*, $-V_d$) during the second operating half-period (with T_{A-} and T_{B+} turned on). The switching frequency is equal to the operating frequency, enabling a potential soft-switching operation. The square-wave command is obviously simple, but the corresponding output voltage suffers from an unfavorable harmonic content, although the waveform symmetry with respect to the half period suppresses the harmonics from even orders. Moreover, the filtering effect of the resonant circuit supplied by the converter soften this issue. The operational drawback of the square-wave control lies in the fact that the output voltage is only controllable in phase and frequency, but not in amplitude. The amplitude of the fundamental output voltage is constant and equal to

$$\hat{V}_o^{(1)} = \frac{4}{\pi} V_d \tag{5.4}$$

The adjustment of the output voltage amplitude requires accordingly to insert an extra power conversion stage upstream to the inverter such as, *e.g.*, a switch-mode DC-DC controller.

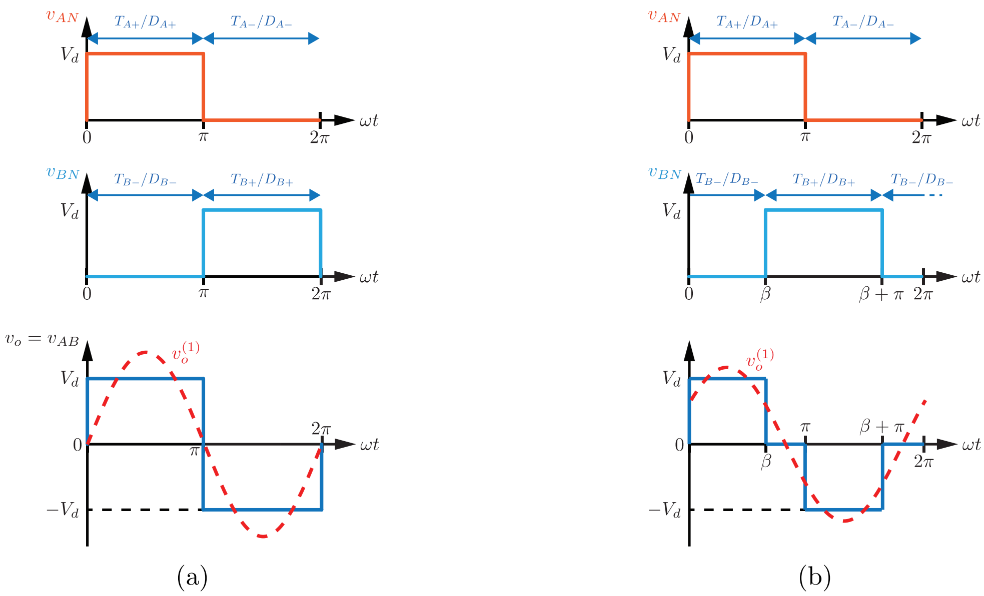

Figure 5.8: Voltage waveforms associated with a (a) square-wave and (b) an SVC-command

Symmetric voltage cancellation command

The symmetric voltage cancellation (SVC) command (also called phase-shift command) consists in commanding each full-bridge leg using a square-wave command (for producing respective square-wave voltage between the node N and each node A and B), while shifting the command of the legs by an angle β, called the conduction angle. It results in an output voltage with positive and negative alternance separated by zero-voltage levels. The waveforms related with the SVC-command are presented in Figure 5.8b.

Without being overcomplicated, the SVC-command permits to adjust the frequency, but also the amplitude of the output voltage using the angle β. During the zero-voltage levels, the load current circulates within the upper side or within the lower side of the full-bridge and the load circuit is disconnected from the source. Such states are called freewheeling states, as the system evolves as dictated by itself. During the non-zero-voltage states (called the active states), the load is reconnected to the DC source. The amplitude of the fundamental output voltage is depending on β and given by

$$\hat{V}_o^{(1)} = \frac{4}{\pi} V_d \ \sin(\beta/2) \tag{5.5}$$

One may notice that the square-wave command is a particular application of the SVC-command for $\beta = \pi$. For completeness purpose, we could mention another variant of the command, consisting in the variation of the duty cycle for the command of one out of the two legs, leading to an asymmetrical voltage waveform and called asymmetric voltage cancellation (AVC). Nevertheless, to our appreciation, the implementation of an SVC-command appears as a perfect compromise between controllability possibilities (as the output voltage is adjustable in frequency, in phase and in amplitude) and simplicity. The soft-switching operation of the full-bridge as a CSN commanded with an SVC-command is investigated in the following. The following conclusions are extended to square-wave commands, with $\beta = \pi$.

5.3.3 Soft-switching in a full-bridge converter

In a full-bridge converter where the switches belonging to the same leg are commanded complementarily, soft-switching depends on the direction of the current. In this section, the soft-switching mechanism is discussed for the switch T_{A+} and extended to the other switches by proceeding to appropriate analogies.

Soft-switching of T_{A+}

The notation employed here refers to Figure 5.6b. When the voltage V_{AN} is required to transit from 0 to V_d, the switch T_{A-} is supposed to turn off and to support a non-zero voltage, while the switch T_{A+} is supposed to turn on for connecting the node A to the DC source positive terminal and ensuring the conduction continuity. Let consider the current i_o taken as positive as it exits the bridge. If the current i_o is positive at T_{A-} turn-off, the diode D_{A+} is reverse-polarized so that T_{A+} must be turned on to ensure the current conduction while clamping V_{AN} to V_d, performing hard-switching. However, if the current i_o is negative at T_{A-} turn-off, the current establishes naturally in the diode D_{A+} and the voltage V_{AN} is naturally clamped to V_d. Therefore, the switch T_{A+} can be turned on with a marginal delay (actually, before the next change in the current i_o direction) and achieve a soft ZVS turn-on.

When the voltage V_{AN} is required to transit from V_d to 0, the switch T_{A+} is supposed to turn off and to support a non-zero voltage, while the switch T_{A-} is supposed to turn on for connecting the node A to the node N (*i.e.* the DC source negative terminal). If the current i_o is positive at T_{A+} turn-off, the diode D_{A+} is reverse-polarized so that the current flows in T_{A+} and the latter must be turned off while cutting the current i_o, performing hard-switching. If the current i_o is negative at T_{A+} turn-off, the current flows in the diode D_{A+} and the switch T_{A+} can be turned off with a marginal advance (actually, after the previous change in the current i_o direction) and achieve a soft ZCS turn-off.

Consequently, a simple rule can be obtained for determining soft-switching operation of the switch T_{A+} in a full-bridge: the current i_o must be negative in order to flow in the anti-parallel diode D_{A+} at the T_{A+} switching instant, so that T_{A+} achieves ZVS at turn-on and ZCS at turn-off.

Extension to the other switches

The generalization of the simple soft-switching rule established in details for T_{A+} stipulates logically that for any switch in the bridge to perform soft-switching, the current must flow in its anti-parallel diode at its switching instant. By relating this general rule with the respective switches position in the bridge, one can gather their switching behavior with respect to the current i_o direction in Table 5.1.

	$i_o > 0$	$i_o < 0$
T_{A+}	Hard	**Soft**
T_{A-}	**Soft**	Hard
T_{B+}	**Soft**	Hard
T_{B-}	Hard	**Soft**

Table 5.1: Switching type with respect to i_o direction at the switching instant in a full-bridge converter

By reading Table 5.1 and bearing in mind that two switches belonging to the same leg are switched simultaneously, one can ascertain that both switches in a leg can not achieve soft switchings at the same time. As a consequence, two out of four commutations occurring in a leg are necessarily hard switchings. Since the switches in a leg are commanded complementarily and since the current direction changes between their switching instants, two situations can occur. On the one hand, both switches can achieve ZVS at their respective turn-on and a hard switching at their respective turn-off. On the other hand, both switches can achieve ZCS at their respective turn-off and a hard switching at their respective turn-on. For each situation, the switching losses during the unavoidable and remaining hard switchings can be decreased using snubbers.

Snubber circuits

Snubber circuits consists in an auxiliary reactive circuitry localized around a switching devices and aiming at assisting the latter device during a hard switching, for decreasing the switching losses in the semiconductor components.

A capacitive snubber (see Figure 5.9a) consists elementarily in an auxiliary capacitor connected in parallel with a controlled switch and aims at slowing the voltage rise during a hard turn-off, with a consecutive reduction of the switching losses. The combination of a capacitive snubber with a switch performing naturally a ZVS turn-on is particularly suitable, as the energy stored in the auxiliary capacitor during a "snubbed" turn-off will be restored to the useful circuit during the next soft turn-on. If, conversely, the switch performs a hard turn-on, the energy stored in the auxiliary capacitor is dissipated in the switch with a consecutive increase of the switching losses. In such a case, this energy can be dissipated in an auxiliary resistor in order to deviate these additional losses from the semiconductor device. In the light of the foregoing, the combination of a soft ZVS turn-on with a capacitively "snubbed" turn-off is particularly suitable as it permits to avoid the turn-on losses (as this commutation is natural) and to decrease the turn-off losses (as this commutation is assisted by the capacitive snubber), with the restoration of the energy stored in the snubber to the useful circuit.

An inductive snubber (see Figure 5.9b) consists elementarily in an auxiliary inductor connected in series with a controlled switch and aims at slowing the current rise during a hard turn-on, with a consecutive reduction of the switching losses. Analogously to the capacitive snubber case, the combination of an inductive snubber with a switch performing naturally a ZCS turn-off is particularly suitable, as the energy stored in the auxiliary inductor during a "snubbed" turn-on will be restored to the useful circuit during the next soft turn-off. If, conversely, the switch performs a hard turn-off, the energy stored in the auxiliary inductor is dissipated in the switch with a consecutive increase of the switching losses and causes the occurrence of a detrimental over-voltage due to the related high di/dt. Once again, this energy can be dissipated in an auxiliary resistor in order to deviate these additional losses from the semiconductor device. Regarding the reasoning above, the combination of a ZCS turn-off with an inductively "snubbed" turn-on is particularly suitable as it permits to avoid the turn-off losses (as this commutation is natural) and to decrease the turn-off losses (as this commutation is assisted by the inductive snubber), with the restoration of the energy stored in the snubber to the useful circuit.

(a) (b)

Figure 5.9: (a) Capacitive snubber and (b) inductive snubber

Summary

In a full-bridge RPC, a given transistor performs a soft switching (whether it is a turn-on or a turn-off) depending only on the direction of the current at the commutation instant. A current entering the bridge (*i.e.* $i_o < 0$) ensures soft-switching for the switches T_{A+} and T_{B-}, whereas a current exiting the bridge (*i.e.* $i_o > 0$) ensures soft-switching for the switches T_{A-} and T_{B+}.

In the steady-state, the SVC-commanded inverter output current is expected to be symmetric with respect to the half-period. Since the switches from a common leg are commanded complementarily, the switches from a common leg realize only one common type of soft switching, *i.e.* either both realize a ZVS at turn-on or both realize a ZCS turn-off. The other movement is necessarily a hard switching. The resort to snubbers can be envisioned for decreasing the losses during the latter remaining hard switching. One can notice that in the framework of resonant WPT, the most matured technology for realizing the switches in practice (regarding the power and frequency levels concerned by the resonant WPT) is the metal oxide semiconductor field effect transistor (MOSFET) which presents a parasitic parallel capacitance. The latter capacitance acts intrinsically as a capacitive snubber, with its benefits and its drawbacks. In the light of the contraindications raised relative to the use of capacitive snubbers, the functioning corresponding to a soft ZVS turn-on of the switches followed by a capacitively "snubbed" turn-off is more suitable.

5.4 Impact of the resonant inductive circuit

The impact of a typical resonant inductive circuit on the phase shift between the output current and the output voltage of the inverter is addressed in this last section.

Using a series-compensated primary, the resonant current (*i.e.*, the current circulating in the mesh comprising the resonant inductance and capacitance) is the current furnished by the inverter. Hence, the output current i_o of the converter is quasi-perfectly sinusoidal due to the filtering effect of the primary LC oscillator solicited around its self-resonant frequency. The first-harmonic analysis (FHA) of the system equivalent circuit in the frequency domain can be employed for determining the current with sufficient precision. Using a parallel-compensated primary, the full-bridge can not be connected directly in parallel with the resonant capacitance. As a matter of fact, as a voltage-source switched-mode converter, the inverter studied here produces relatively high dv_o/dt which could lead to significant and detrimental over-currents when applied directly to a capacitance. For avoiding such over-currents, a series inductance is introduced between the inverter output and the primary circuit. From the latter terminals, the voltage-source converter is seen as a current-source. In some contributions from the literature the additional inductance is not considered in the compensation scheme, so that the sinusoidal nature of the converter output current and therefore the relevance of an FHA approach are not always ensured. In this thesis (as explained in Chapter 8), a parallel-compensated primary is designed for integrating the additional converter output inductance in the compensation scheme. Therefore, the converter output current recovers its sinusoidal nature and the FHA approach is anew relevant for investigating the soft-switching operation of a resonant converter using an RIPT circuit as an RTN.

For this analysis, the inverter is replaced by an ideal AC voltage source V_o delivering the fundamental voltage of v_o and employed as a phase reference. Once the phase φ of the output current phasor $\underline{I}_o$ is computed via FHA, three different situations can occur when the full-bridge is commanded via SVC, which are

1. the current is sufficiently capacitive for the current zero-crossings to occur before each freewheeling state (*i.e.*, when $\varphi < -\frac{(\pi-\beta)}{2}$) ;
2. the current is sufficiently inductive for the current zero-crossings to occur after each freewheeling state (*i.e.*, when $-\frac{(\pi-\beta)}{2} < \varphi < +\frac{(\pi-\beta)}{2}$) ;
3. the current is nearly in phase with the voltage and its zero-crossings occurs during the freewheeling states (*i.e.*, when $\varphi > +\frac{(\pi-\beta)}{2}$).

The associated current and voltage waveforms are shown in Figure 5.10.

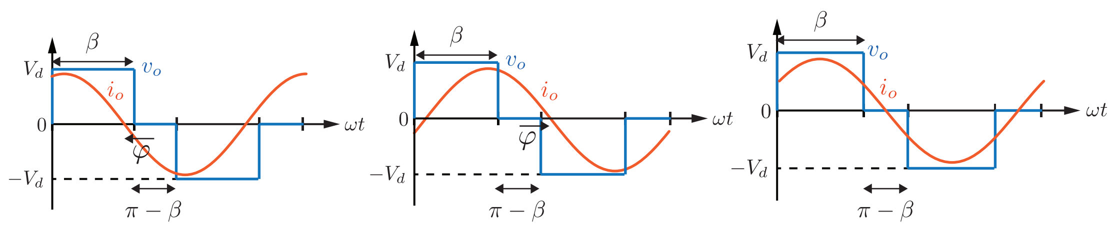

(a) Capacitive current (b) Inductive current (c) In-phase current

Figure 5.10: SVC-controlled resonant full-bridge output current and voltage

By observing the waveforms in Figure 5.10 in the light of the semiconductors devices switching sequence using an SVC-command, and of the rules established for analyzing the type of switching in a full-bridge employed as a CSN, one can ascertain that

- in the first situation (*i.e.*, a capacitive current), all the switches are performing a hard turn-on and a soft ZCS turn-off ;
- in the second situation (*i.e.*, an inductive current), all the switches are performing a soft ZVS turn-on and a hard turn-off ;
- in the third situation (*i.e.*, a weakly inductive or capacitive current), the switches from one leg of the full-bridge (*i.e.* T_{A+} and T_{A-}) observe a capacitive current and the latter are performing a hard turn-on and a soft ZCS turn-off, while the switches from the other leg (*i.e.* T_{B+} and T_{B-}) observe an inductive current and the latter are performing a soft ZVS turn-on and a hard turn-off.

Ideally, as argued in the previous section, the second situation is fostered. Nevertheless, an RIPT system is designed and operated for precisely ensure a zero phase angle between the inverter voltage and current. When the freewheeling state durations are sufficiently short, a small phase shift can be applied (via a tenuous variation of the frequency) for ensuring to operate similarly to the second situation. However, when the freewheeling state durations are more important, such a phase shift would be problematic for the volt-ampere rating of the inverter. As a consequence, the situation is similar to the third among those mentioned above, where the leg A performs a ZCS turn-on and a hard turn-off and the leg B performs a ZVS turn-off and a hard turn-on. For reducing the losses associated with the remaining hard commutations, the resort to adequate snubbers, specifically adapted to the switching type in each leg, can be envisioned. However, as specified in Chapter 6, the objective of this thesis is to consider bidirectional systems, where the inverter may operate as an active rectifier. The inversion of the power flow direction in the converter is accompanied with a change in the converter current and the switching types in legs A and B interchange. As a consequence, for reducing at best the switching losses in the semiconductor components, we would suggest to draw a particular attention on the elaboration of more sophisticated snubber circuits, combining a capacitive and an inductive contributions.

5.5 Conclusions

In this chapter, we decided to present the converter topology and the command employed in the following developments through the prism of the resonant converter concept. Usually established purposely by adding a resonant network in conventional circuits, the resonant operation of the converter permits to reduce and further avoid its switching losses. Here, the resort to a switched-mode converter for the AC-DC or the DC-AC conversion in an RIPT results intrinsically in a resonant operation of the latter converter. Without being a key-concept in the developments presented further, we estimated interesting to address the soft-switching operation of converter involved in the power conversion for RIPT systems. By focusing our investigation on a full-bridge converter commanded via SVC, the rules for adjudicate on the nature of the switchings in the converter have been established. Thanks to the filtering effect associated with the resonant operation of the transmission circuit, this adjudication can be made on basis of an FHA, due to the systematic sinusoidal form of the converter output current. Based on the phase shift between the voltage and the current and on the waveform of the voltage, different situations distinctive by the nature of the switchings in the converter have been raised and commented.

CHAPTER

SIX

ACTIVE RECTIFICATION FOR THE OPTIMAL COMMAND OF RESONANT WIRELESS POWER TRANSFER

In the introductory aspects of this thesis, the development of the power efficiency of a resonant WPT system demonstrated that the latter efficiency depends on the design of the coupled windings (which can be addressed numerically via the virtual laboratory and the original approaches proposed in the first part of this thesis) and on the operating conditions of the transmission circuit. These operating conditions correspond to the resonant operation on the secondary side of the system (guaranteeing an optimal reactive power flow in the system) and to the value of the apparent load resistance (guaranteeing an optimal active power flow in the system). Basically, the optimality of the efficiency can be compromised by a poor design or by the alteration of the circuit components, as well as by the modification of the operating conditions. Nevertheless, adequately controlled, the power converters inherent to the practical implementation of resonant WPT can effect on the system operation, for ensuring a maximal efficiency despite any deviation on the operating conditions. Therefore, the establishment of an original optimal command of the power converters surrounding a resonant WPT system is proposed in this chapter.

Hereafter, a state of the art of the different existing control strategies is presented, with a particular focus on the most significant contributions addressing the operational maximization of the power efficiency of resonant WPT systems. Thanks to a progressive analysis of their respective advantages and drawbacks, the original positioning of this thesis is clarified, before the development, the illustration and the discussion of the proposed optimal command methodology and of the related results in the frequency and time domains.

6.1 State of the art

The definition of the optimality in the operation of a system is related to the operational objectives aimed by its designer. In the framework of resonant WPT, two types of operation prevail, namely the maximum power and the maximum efficiency operations. Both modes of operation correspond to different and non-compatible functioning conditions and can therefore not be achieved simultaneously. As briefly mentioned in the introductory aspects of this thesis, the maximum power operation is usually praised for low-power applications. As a matter of fact, the unavoidable compromise on the efficiency entailed by such operation mode is not problematic for low-power applications, as the consecutive losses represent a low amount of power in absolute terms. These losses are an acceptable price to pay for furnishing the maximum power regarding the operational constraints (*e.g.* a large range). Moreover, low-power transmissions are generally implemented in a high frequency range (*i.e.*, from a few to tens of MHz) guaranteeing a high figure-of-merit (as discussed in Section 1.3.3) and therefore intrinsically acceptable efficiencies. Conversely, the maximum efficiency operation is favored for mid- (hundreds of W) and high-power (from a few to tens of kW) applications, as each percent of the efficiency represents a non-negligible amount of power. In addition, the power is usually rated for such application type. Since this thesis focuses on the application of resonant WPT to high-power applications, our definition of the operational optimality corresponds to the maximization of the transfer power efficiency.

In this section are presented the contributions from the academia which address the maximum efficiency operation of resonant WPT systems and which are the most significant to our appreciation. This state of the art aims to present the outcome(s) from each of these contributions which led to the progressive establishment of the original optimal control methodology proposed in this thesis.

6.1.1 Variable-frequency control strategies

The operating frequency is obviously a key parameter in the functioning of a resonant WPT system and consequently in its performances setting. As exposed in Section 1.3.3, the operational maximization of the power efficiency of a resonant WPT system corresponds to the imposition of an optimal value for the apparent load resistance, seen from the secondary terminals. The value of the load resistance maximizing the transfer efficiency depends on the operating frequency and on the inductive coupling (via the mutual inductance value). Consequently, a frequency variation can be employed for ensuring optimal transfer performances despite deviations in the coils mutual inductance or in the actual load of the system. Different strategies consisting in varying the system operating frequency via an adequate command of the voltage-source inverter have been proposed [121, 122]. However, such command may require a frequency shift which can reach from 20 % to 30 % of the system nominal frequency. Such large frequency shifts result in a decrease in the system power transfer capability and in a reduction in stability and controllability due to the occurrence of the frequency splitting phenomenon [61]. Beyond these purely operational concerns, a variable operating frequency is likely to introduce issues related to EMI. Finally, ongoing standardization procedures tend to impose a fixed operating frequency for improving the universality and the normalization of the different resonant WPT systems. As already mentioned in the introduction of this thesis, the standard SAE J2954 prevails in the framework of EVs battery charging. The latter standard fixes the frequency to 85 kHz with a permitted deviation within -4.7 % (corresponding to 81.9 kHz) and +5.8 % (corresponding to 90 kHz). In [123], the authors propose a variable-frequency control based on an impedance matching network for countering variations in the inductive coupling, while complying with the SAE J2954 standard frequency-deviation tolerance. Though, the paper does not inform about the quantitative variations in the coils coupling which are tolerated without infringing the standard, since only the geometrical misalignments of the coils are specified without any reference to the latter impact on the mutual inductance.

As a consequence of the different drawbacks raised above, the use of the operating frequency as a control parameter is not considered in the following of this thesis. The attention is therefore drawn on fixed-frequency control strategies.

6.1.2 Fixed-frequency control strategies

Fixed-frequency control strategies are commonly based on the source and load voltages modulation for the apparent AC-side load resistance to match the optimal load resistance value. The most elementary technique corresponds to adding a DC-DC converter between the secondary AC-DC converter and the actual load resistance, so that the apparent AC-side load resistance can be modulated for meeting its optimal value by the adequate setting of the DC-DC converter duty cycle. Concomitantly, the primary DC-AC converter adapts the AC-side primary voltage for regulating the transmitted power. Nonetheless, the value of the optimal load resistance depends on the coils equivalent lumped parameters, namely their mutual inductance and their respective parasitic resistance. The measurement of these parameters is delicate (justifying in passing the usefulness of a virtual prototyping laboratory as developed in the first part of this thesis). For avoiding such measurements, a first control strategies category is based on a perturbation and observation (P&O) algorithm for seeking step-by-step via trial-and-error the operating point providing the maximum efficiency, without requiring the measurement or the determination of the circuit parameters. These techniques are called the **maximum efficiency point tracking (MEPT) techniques** as a reference to the maximum power point tracking from which it is inspired and which is well-known for the exploitation of photovoltaic panels or wind turbines.

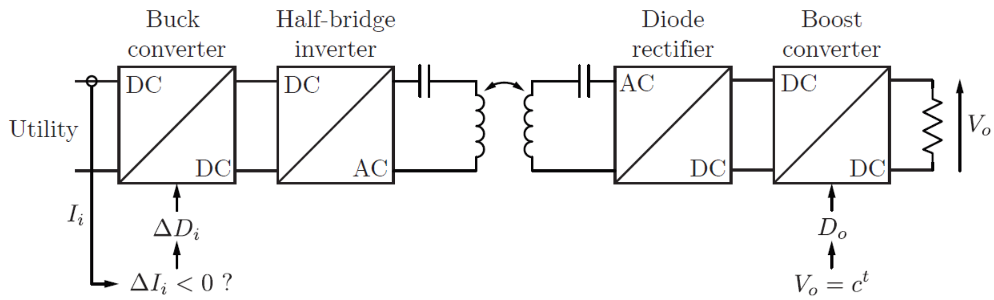

Figure 6.1: Schematized topology of the MEPT technique proposed by Li *et al.*

Li *et al.* have proposed and extensively investigated an MEPT technique implemented thanks to the topology schematized on Figure 6.1 [124]. A first DC-DC converter interfacing the secondary diode rectifier with the load aims to maintain a constant output voltage V_o across the load by effecting on its duty ratio D_o. A second (front-end) DC-DC converter interfaces the DC voltage source of the system with the primary inverter, which produces a square-wave voltage. The latter DC-DC converter is employed for introducing (via the modification of its duty cycle D_i) a variation in the primary AC voltage. The P&O algorithm is implemented as follows. The controller induces a duty cycle change ΔD_i, while the input current I_i is monitored. Assuming that the regulation of V_o is sufficiently fast and that the load is constant, the output power is assumed to be constant. The monitored evolution of the input current I_i is therefore a reflection of the evolution of the efficiency, as a diminution of I_i corresponds to a higher efficiency and vice versa. As exposed by the authors, the evolution of the efficiency with respect to the input voltage is concave down. As a consequence, if the efficiency is growing (respectively, decreasing) subsequently to a duty cycle change ΔD_i, a similar (respectively, opposite) variation is applied for seeking the maximum efficiency. The authors have demonstrated that the steady-state optimal operating point corresponds to a situation where the secondary current is such that the AC-side apparent resistance is equal to its optimal value. Zhong *et al.* have proposed a similar MEPT scheme where the implementation of an SVC-commanded full-bridge inverter for the supplying the primary avoids the need for the input DC-DC converter, as the input perturbation is performed by applying a change in the SVC conduction angle [125]. **These contributions demonstrate that the converters surrounding the resonant transmission circuit are able to modulate the apparent load resistance by effecting on the amplitude of the primary and/or secondary AC voltages.**

Although effective, those strategies effect solely on the active power flow since only the apparent load *resistance* is modulated by the converters. The reactive power flow is, for its part and despite its preponderance for a proper resonant operation, free to vary with potential modifications or deviations in the reactive components parameters. Therefore, researches have investigated the replacement of the secondary diode rectifier by a switched-mode rectifier controlled for phase-shifting the secondary AC voltage, resulting thereby in the emulation of a modulated load reactance influencing the reactive power flow in the system. These techniques are called **active rectification techniques**.

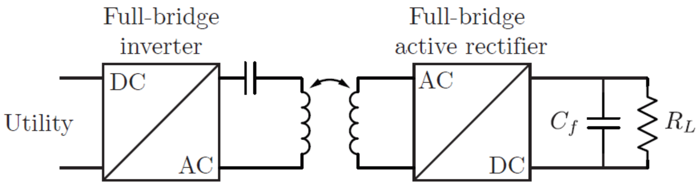

Figure 6.2: Schematized topology of the active resonance technique proposed by Zhao *et al.*

Zhao *et al.* have pioneered the resort to active rectification in the resonant WPT framework, by proposing the topology schematized in Figure 6.2 [126]. Without reasoning in terms of impedance emulation, the authors purpose is to employ the active rectifier for making the filtering capacitor C_f contribute to the reactive power compensation of a secondary side devoid of resonant capacitor. The transferred power and the efficiency are expressed with respect to the phase shift between the primary and the secondary voltages, which is the unique degree of freedom available for the control as both converters generate a square-wave voltage (with a fixed amplitude). The phase shift providing the highest efficiency is then applied to the secondary voltage via active rectification. One can note that the evolution of the efficiency with respect to the phase shift and the highest efficiency value are both depending on the actual load R_L. Since the primary voltage is kept constant, the transferred power is not adjustable and is fixed by the applied phase shift and by the actual load R_L.

Although innovative and validated experimentally, this approach does not operate the system in its optimal conditions. Despite the reactive power flow is effectively influenced and optimized via the phase shift control, the constancy of both AC voltages amplitude inhibits the regulation (and therefore, the optimization) of the active power flow. In other words, the resistive and the reactive parts of the apparent load impedance seen from the secondary terminal are not controlled independently. The emulated apparent reactance may reproduce the resonant conditions despite the avoidance of secondary resonant capacitor, but the corresponding apparent resistance is not equal to the optimal load resistance value. As a consequence, **the performances achieved by implementing the method proposed by Zhao *et al.* are non-optimal in absolute terms**, as demonstrated by their strong dependence with respect to the actual load resistance. **However, this contribution demonstrates that the converters surrounding the resonant transmission circuit are able to modulate the apparent load reactance by effecting on the phase shift between the primary and secondary AC voltages.**

Aware of the aforementioned issues but interested by the reactance emulation idea, Berger *et al.* have presented a contribution explicitly based on [126] in [127, 128] where the controls of the real and of the imaginary parts of the load impedance are independent. Despite being equipped with an active rectifier and in contrast with the previous contribution, the proposed system comprises here a secondary resonant capacitor for reducing the effort sustained by the active rectifier. As shown in Figure 6.3, the method employs the active rectifier for imposing

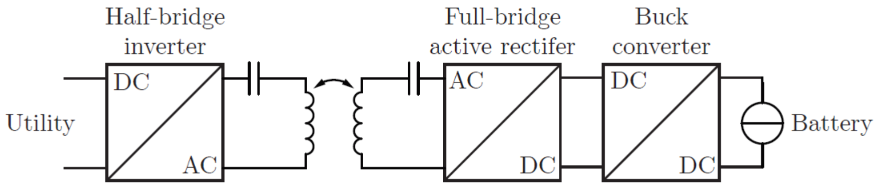

Figure 6.3: Schematized topology of the active rectification technique proposed by Berger *et al.*

the phase shift between the primary and secondary AC voltages (with an effect on the apparent reactance of the load) and an additional buck converter interfacing the rectifier with the actual load, which modifies the amplitude of the secondary AC voltage (with an effect on the apparent resistance of the load). As a result, the resistive and the reactive parts of the apparent load can be controlled independently. An experimental validation proves the methodology implementability. **Nevertheless, the approach for computing the optimal loading conditions is not ideal to our appreciation, as the targeted operating point is only optimal under a specific constraints but not in absolute terms**. Indeed, since the primary voltage amplitude is kept constant, the efficiency and the transferred power are related by the apparent load impedance. The optimal loading conditions are calculated for maximizing the efficiency, *provided that* a specific power amount is transferred under the fixed primary voltage. Consequently and on a holistic point of view, the optimal loading conditions and the optimal efficiency (as defined in these papers) are dependent on the output power and the system does not always operate at the maximum efficiency physically achievable by the resonant transmission circuit (*i.e.*, the equivalent load resistance is different from its optimal value). Moreover and on a more practical point of view, the computation of these loading conditions are achieved either via a constrained numerical optimization process of the efficiency or via a complex constrained analytical minimization of the input current using Lagragian multipliers. **Nonetheless, this contribution demonstrates that the converters surrounding the resonant transmission circuit are able to modulate independently and simultaneously the apparent load resistance and reactance by effecting on the amplitude of the secondary AC voltage and on the phase shift between the primary and the secondary AC voltages.**

6.1.3 Positioning of this work

The progressive approach in the state of the art presented above demonstrates that the idea consisting in employing active rectification for interfering with the active as well as reactive powers management in a resonant WPT system is applicable. Inspired by those contributions, we decided to propose an original optimal control technique based on an active rectification and innovative in two main aspects.

On the one hand, we propose to **simplify the power conversion chain topology** (see Figure 6.4). For this purpose, the non-synchronous rectification is performed by controlling the active rectifier using a symmetric voltage cancellation (SVC) command, enabling the combined control of the amplitude and of the phase of the secondary voltage without any additional DC-DC converter. The remaining topology comprises two reversible full-bridge converters separated by a transformer, which is usually known as a dual active bridge (DAB) structure. Here, the resonant capacitors are added to the conventional DAB structure in such way that we decided to nuance the topology designation by referring to the latter as resonant dual active bridge (RDAB). Such structure results in a topological symmetry which provides intrinsic **power-reversibility capabilities for the proposed resonant WPT system**, which is a farsighted asset since enabling bidirectional power-flows permits to use EVs as storage units for vehicle-to-home (V2H) and vehicle-to-grid (V2G) applications [33]. In contrast, the aforementioned state-of-the-art contributions use asymmetric topologies and are only practicable for a unidirectional power transfer. One can note that bidirectional resonant WPT systems are proposed in the literature [129–132]. Such systems are usually equipped with a secondary converter comprising switches, but the latter purpose consists in the system topological reversibility only (by using only the anti-parallel diode on the receiver side, without performing any active rectification).

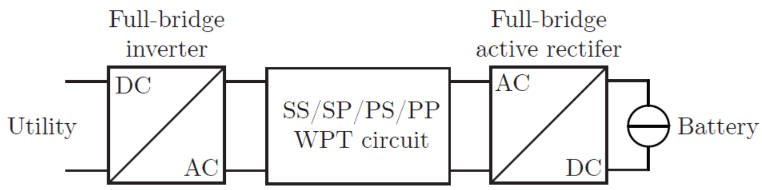

Figure 6.4: Schematized topology of the proposed system

On the other hand and most importantly, we propose an **original approach for the determination of the system optimal operating conditions**. More precisely and in contrast with the most advanced state-of-the-art contribution proposed by Berger *et al.*, we propose to **operate the system at the maximum efficiency achievable by the transmission circuit, regardless of the required output power**. For enabling such functioning, the modulation of the primary voltage amplitude is considered. The primary voltage amplitude variability confers an extra degree of freedom to our approach (in addition to the secondary voltage amplitude and to the phase shift between the primary and the secondary voltages), allowing therefore to adjust independently the output power, the apparent load resistance and the optimal load reactance. Addressing separately the power efficiency and the output power permits to derive the optimal loading conditions **analytically**, via a simple unconstrained optimization of the efficiency expression. Finally and as demonstrated hereafter, the simplicity and the methodical aspect of the proposed approach enhances its **generalization to any compensation topology** (*i.e.*, the series-series, the parallel-parallel, the parallel-series and the series-parallel compensations), whereas state-of-the-art methodologies are only developed for the series-series compensation scheme.

The proposed method is precisely detailed for a series-series resonant WPT system, before being extended to the other compensation types in Chapter 8.

6.2 Series-series resonant dual active bridge (SS-RDAB)

The proposed resonant WPT system topology is presented in Figure 6.5. This system interfaces the utility (represented by the rectifier utility voltage V_u) and a battery (represented by the battery voltage V_b). Each oscillatory circuit is connected to a full-bridge converter interfacing the resonant WPT system with the rectified utility voltage V_u on one side and with the battery voltage V_b on the other side. One can notice the power-reversibility capabilities offered by the proposed topology, which is moreover perfectly symmetric with respect to the coupled windings. For clarity and non-redundancy purposes, only the case of a power transfer from the utility to the battery is addressed in the following developments. Given the system topological symmetry, the case of a transfer from the battery to the utility can be treated similarly by interchanging the primary and the secondary roles in the expressions.

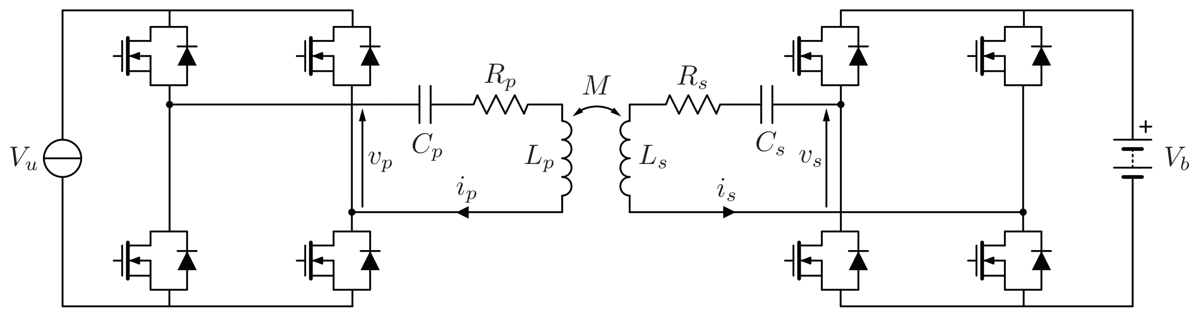

Figure 6.5: Proposed series-series resonant WPT topology

As a reminder, the system is designed so that the primary and the secondary circuits share a common self-resonant frequency ω_0, *i.e.*

$$\omega_0 = \frac{1}{\sqrt{L_p C_p}} = \frac{1}{\sqrt{L_s C_s}}. \tag{6.1}$$

Operated with an angular frequency ω equal to ω_0, one reminds that the system of coupled resonators displays a theoretical infinite power transfer capability whereas presenting a unitary power efficiency. In practice, these transfer performances are limited by the components parasitic resistances R_p and R_s.

6.2.1 Equivalent first-harmonic circuit

Considering the filtering action of each LC circuit on the converters AC currents, a first harmonic analysis performed on the equivalent circuit shown in Figure 6.6 is sufficient *a priori* for analyzing the system operation. The currents and voltages are represented by their respective phasors phasors. The power converters and their respective DC voltage sources can be replaced by ideal AC voltage sources $\underline{V}_p$ and $\underline{V}_s$, as their respective AC voltages v_p and v_s are controllable in module and phase via an SVC-based command.

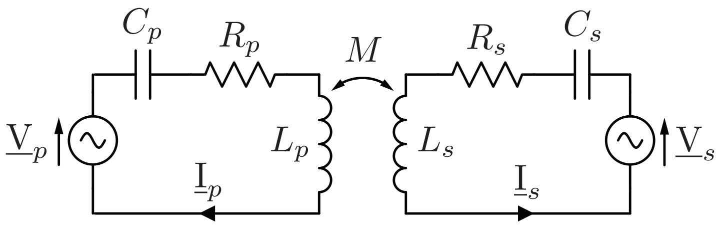

Figure 6.6: Equivalent circuit for the first-harmonic analysis

Before developing the proposed methodology, the circuit is solved for obtaining the primary and the secondary currents $\underline{I}_p$ and $\underline{I}_s$ with respect to the source voltages $\underline{V}_p$ and $\underline{V}_s$. By applying Kirchhoff's voltage law to the equivalent circuit presented in Figure 6.6, one has

$$\underline{V}_p = \underline{Z}_p \underline{I}_p + j\omega M \underline{I}_s \tag{6.2}$$

$$\underline{V}_s = \underline{Z}_s \underline{I}_s + j\omega M \underline{I}_p \tag{6.3}$$

with the primary circuit impedance $\underline{Z}_p$ and the secondary circuit impedance $\underline{Z}_s$ defined as

$$\underline{Z}_p = R_p + j\omega L_p + 1/j\omega C_p \tag{6.4}$$

$$\underline{Z}_s = R_s + j\omega L_s + 1/j\omega C_s \tag{6.5}$$

Solving (6.2) and (6.3), the expression for each current is obtained with

$$\underline{I}_p = \frac{\underline{Z}_s \underline{V}_p - j\omega M \underline{V}_s}{\underline{Z}_p \underline{Z}_s + \omega^2 M^2} \qquad (6.6) \qquad\qquad \underline{I}_s = \frac{\underline{Z}_p \underline{V}_s - j\omega M \underline{V}_p}{\underline{Z}_p \underline{Z}_s + \omega^2 M^2} \qquad (6.7)$$

6.2.2 Power efficiency and optimal load impedance

The proposed topology enables the ability to modulate the apparent load impedance and the proposed approach consists in imposing the load impedance which maximizes the transmission power efficiency. For analyzing the efficiency and given the assumed direction of the useful power (*i.e.*, from the primary to the secondary), the secondary voltage source $\underline{V}_s$ is replaced by an equivalent load impedance $\underline{Z}_L = R_L + jX_L$. The power efficiency can be expressed as

$$\eta = \frac{R_L I_s^2}{R_p I_p^2 + R_s I_s^2 + R_L I_s^2} \tag{6.8}$$

where I_p and I_s are the root-mean-square (RMS) values of the primary and of the secondary currents, respectively. The values I_p and I_s can be related by applying the Kirchhoff's voltage law to the secondary circuit mesh. One has

$$j\omega M \underline{I}_p = -(R_s + \underbrace{j\omega L_s + \frac{1}{j\omega C_s}}_{jX_s} + R_L + jX_L)\ \underline{I}_s = -(R_s + R_L + jX_s + jX_L)\ \underline{I}_s$$

so that the RMS value of the primary current I_p can be expressed as

$$I_p = \frac{\sqrt{(R_s + R_L)^2 + (X_s + X_L)^2}}{\omega M}\ I_s \tag{6.9}$$

By introducing the relation (6.9) in the expression (6.8), the efficiency becomes

$$\eta(R_L, X_L) = \frac{R_L}{R_p \frac{(R_s+R_L)^2+(X_s+X_L)^2}{\omega^2 M^2} + R_s + R_L} \tag{6.10}$$

One can anew observe that the efficiency depends on two types of parameters, namely

- the transmission circuit intrinsic parameters (*i.e.* the parasitic resistances R_p and R_s, the secondary self-inductance L_s, the secondary resonant capacitance C_s and the mutual inductance M), which are imposed by the LC oscillators design ;
- the resistive part R_L and the reactive part X_L of the apparent load impedance, which can be modulated by controlling adequately the secondary power converter.

For taking full advantage of a given transmission circuit, the transfer efficiency can therefore be maximized by imposing the optimal load resistance R_L^{opt} and reactance X_L^{opt} so that

$$\frac{\partial \eta}{\partial R_L}(R_L^{opt}, X_L^{opt}) = 0 \text{ and } \frac{\partial \eta}{\partial X_L}(R_L^{opt}, X_L^{opt}) = 0 \tag{6.11}$$

The problem (6.11) is solved analytically as a system of two equations involving two unknowns (see Appendix B for the detailed developments) and the solutions are

$$R_L^{opt} = R_s \sqrt{1 + \frac{\omega^2 M^2}{R_p R_s}} \qquad (6.12) \qquad\qquad X_L^{opt} = -X_s = \frac{1}{\omega C_s} - \omega L_s \qquad (6.13)$$

One can notice that the optimal load reactance X_L^{opt} is null when the secondary LC oscillator is correctly tuned (*i.e.*, when $\omega = 1/\sqrt{L_s C_s}$), whereas it ensures the cancellation of the residual reactance in the secondary circuit in the case of a mistuned secondary oscillator.

Ensuring $R_L = R_L^{opt}$ and $X_L = X_L^{opt}$ guarantees to operate the system at its maximum intrinsically (or physically) achievable efficiency η_{max}, which is imposed by the design of the LC circuits only and given by

$$\eta_{max} = \frac{\omega^2 M^2}{R_p R_s \left(1 + \sqrt{1 + \frac{\omega^2 M^2}{R_p R_s}}\right)^2} \tag{6.14}$$

6.2.3 Methodology for the system optimal command

The methodology consists in determining the source voltages $\underline{V}_p$ and $\underline{V}_s$ ensuring simultaneously the maximization of the power efficiency and the setting of the output power.

Maximization of the power efficiency

According to the developments above, the system achieves its maximum intrinsic efficiency when the equivalent resistance and reactance seen from the secondary oscillator terminal are respectively equal to R_L^{opt} and to X_L^{opt}. Therefore, the mathematical condition for the system to achieve the maximum efficiency is written as

$$\underline{V}_s = -(R_L^{opt} + jX_L^{opt})\underline{I}_s \tag{6.15}$$

By eliminating the secondary current using (6.7) in (6.15), the condition becomes

$$-j\omega M(R_L^{opt} + jX_L^{opt})\underline{V}_p + (\underline{Z}_p\underline{Z}_s + \omega^2 M^2 + R_L^{opt}\underline{Z}_p + jX_L^{opt}\underline{Z}_p)\underline{V}_s = 0 \tag{6.16}$$

which is a first equation linking the complex unknowns $\underline{V}_p$ and $\underline{V}_s$. The definition of another equation is mandatory for creating a solvable system of complex equations. This additional equation is associated with the setting of the required active output power.

Setting of the required output power

Achieving a reference power P_{ref} to the load is accomplished by setting adequately the module of the secondary current. Indeed, assuming that condition (6.16) is achieved, the real part of the load impedance is equal to R_L^{opt} so that a power P_{ref} is transmitted to the load when

$$I_s = \sqrt{\frac{P_{ref}}{R_L^{opt}}} \tag{6.17}$$

Conventionally, the primary voltage $\underline{V}_p$ is chosen as a phase reference due to its source role. However, no assumption can be made regarding the phase shift between the secondary current $\underline{I}_s$ and the primary voltage $\underline{V}_p$ without interfering with the circuit natural operation. As a consequence and for convenience, the secondary current $\underline{I}_s$ is chosen here as a phase reference and the complex condition for achieving an output power P_{ref} becomes

$$\underline{I}_s = \sqrt{\frac{P_{ref}}{R_L^{opt}}} \tag{6.18}$$

Using (6.7) and (6.18), this condition is expressed in terms of voltages $\underline{V}_p$ and $\underline{V}_s$ as

$$-j\omega M\underline{V}_p + \underline{Z}_p\underline{V}_s = (\underline{Z}_p\underline{Z}_s + \omega^2 M^2)\sqrt{\frac{P_{ref}}{R_L^{opt}}} \tag{6.19}$$

which is a second equation linking the voltages. Finally, the desired operating point is reached by imposing the voltages $\underline{V}_p$ and $\underline{V}_s$ solving simultaneously equations (6.16) and (6.19).

6.2.4 Illustration and interpretation of the method beneficial effects

Via an first-harmonic analysis performed on the equivalent circuit from Figure 6.6 in the Matlab environment, the main principle of the proposed methodology is illustrated on a EV test-case designed using the virtual laboratory elaborated in the previous part of this thesis. This test-case comprises two identical windings presenting a 50-cm outer diameter and consisting in 16 turns of 10-mm^2 solid wire, each separated by 5 mm. In their nominal position, the coils are aligned and separated by a distance of 25 cm (corresponding to a typical car underbody height). The nominal circuit parameters of this test-case are gathered in Table 6.1, with capacitances compensating perfectly each winding self-inductance at the nominal operating frequency of 85 kHz.

f	$R_p = R_s$	$L_p = L_s$	$C_p = C_s$	M
85 kHz	176 mΩ	109 μH	32.2 nF	13.3 μH

Table 6.1: Nominal parameters of the test-case circuit

The system is expected to supply a reference output power $P_{ref} = 3.7$ kW to the load. For comparison purposes, the performances afforded by the proposed system are contrasted with the performances of an equivalent *passive* system, equipped with a diode rectifier. For a fairer and a more readable comparison, the passive system output power is kept constant by adapting its primary voltage for each investigated situation. In the latter system, the diode rectifier and the battery are represented by an accordant equivalent load resistance given by

$$R_L^{pas} = \frac{8}{\pi^2} \frac{V_b^2}{P_{ref}} = 28.40\ \Omega \tag{6.20}$$

where V_b is taken equal to 360 V, corresponding to a standard voltage for EV battery packs. The optimal load impedance $\underline{Z}_L^{opt}$ corresponding to the test-case nominal parameters is purely resistive, as X_L^{opt} is null since the primary and secondary sides are perfectly tuned. One has

$$\underline{Z}_L = R_L^{opt} = 7.11\ \Omega$$

and the system produces a power efficiency of 95.2 %, which is the maximum achievable efficiency. Due to the difference between the optimal load resistance R_L^{opt} and the equivalent passive load resistance R_L^{pas}, the passive system delivers a power efficiency of 90.4 %.

Hereafter, we propose a detailed comparison between the proposed SS-RDAB and the passive systems when the circuit parameters deviate from their nominal values. Deviations in the windings self-parameters (*i.e.*, the windings parasitic resistances and self-inductances) are not considered because unlikely to vary (as planar coils are simple and reliable components, essentially characterized by their geometry[1]).

Variation of the mutual inductance M

As a first illustration, the decrease of the mutual inductance M is addressed as the most important case because very likely and frequently occurring during a practical WPT system operation (due to the windings misalignment). Impacting R_L^{opt} as evinced by expression

[1] One can note that the parasitic resistances of the windings may change with respect to the operating frequency. However and as argued above, our investigation domain is limited to a fixed-frequency functioning.

(6.12), a modification of M challenges the active power modulation abilities of the system.

By starting from the reference point indicated in Table 6.1, a relative variation of the mutual inductance M down to -90 % is considered. The corresponding evolutions of the power efficiency are shown in Figure 6.7a and compared to the maximum achievable efficiency. One can observe that the proposed method adapts the apparent load resistance (see Figure 6.7b) for reaching constantly the maximum achievable efficiency, which decreases slowly as M declines. The passive system efficiency is on the other hand clearly more impacted by the decreasing of M, with a surge of the difference between its efficiency and the maximum achievable efficiency.

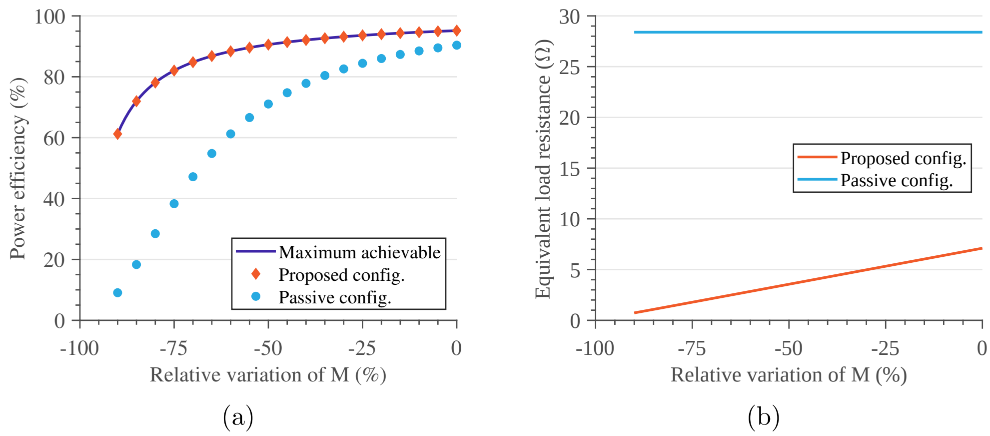

Figure 6.7: Evolutions of the (a) power efficiency and of the (b) equivalent load resistance with respect to a decrease of M for the proposed and the passive systems

Up to this point, the proposed methodology features have been established on a pure mathematical basis and illustrated with a global quantity as the power efficiency. Although necessary, such an approach is nevertheless abstract as regards the proposed method actual action on the electric quantities in the operated resonant WPT system. Therefore, we propose to observe in Figures 6.8 and 6.9 the phasors of the voltages and currents in the complex space for permitting an intuitive understanding of the overall action of the proposed method.

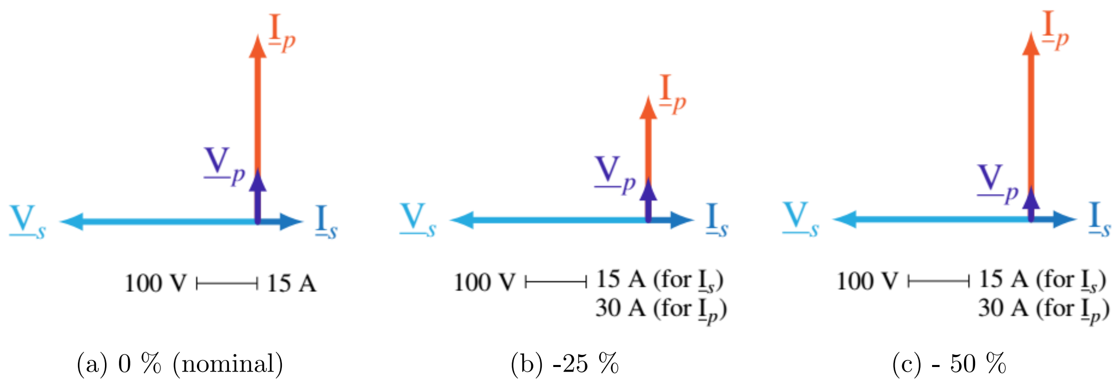

Figure 6.8: Representation of the voltages and currents phasors for different relative variations of M impacting the passive system

For the passive configuration, a decline in M increases significantly the primary current $\underline{I}_p$ since the system has to achieve a constant output power despite harsher coupling conditions. The secondary current $\underline{I}_s$ is constant since the output power and the apparent load resistance

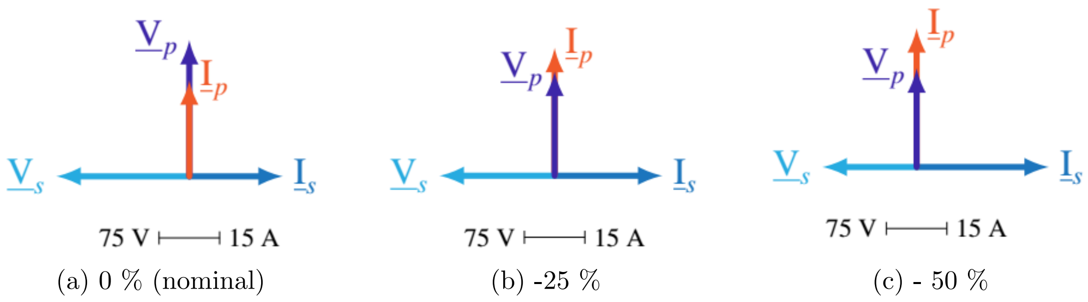

Figure 6.9: Representation of the voltages and currents phasors for different relative variations of M impacting the proposed system

are both constant. The power efficiency is therefore deteriorated due to increased Joule losses in the primary side. Facing up those conditions, the proposed method takes an action on the voltages $\underline{V}_p$ and $\underline{V}_s$ for an optimal repartition of the losses in the system, by decreasing the primary current $\underline{I}_p$ while increasing the secondary current $\underline{I}_s$. The balance between both currents modules provided by the proposed system is clearly shown in Figure 6.10a, displaying a quasi unitary ratio between the latter modules in contrast with the currents imbalance in the passive system. As demonstrated on Figure 6.10b, the implementation of the proposed method results in a lower total current $I_p + I_s$ in the system and accordingly in lower losses.

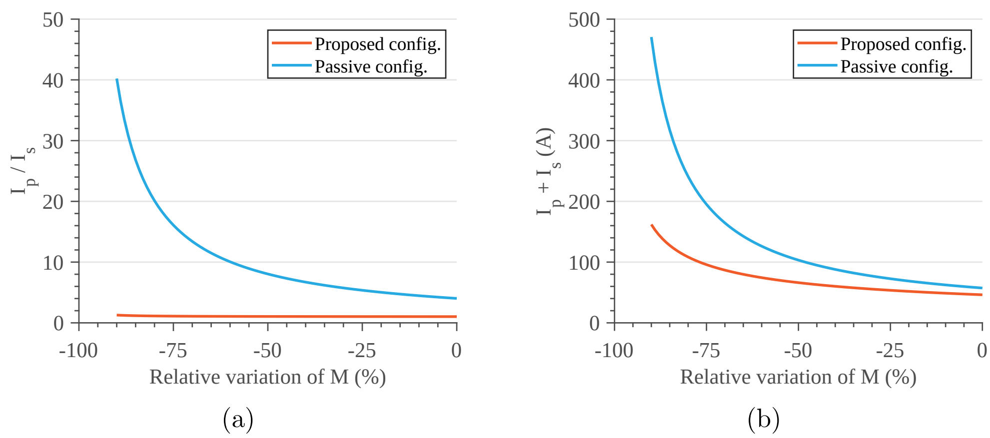

Figure 6.10: Evolutions of the currents modules (a) ratio and (b) sum with respect to a decrease of M for the proposed and the passive systems

Variation of the secondary capacitor C_s

As a second illustration, the variation of the secondary capacitance C_s is addressed. Both the increase and the decrease of the capacitance are relevant for investigating the proposed and passive systems behavior in the case of a healthy but mistuned capacitance (either and respectively undersized or oversized). Also, a progressive decrease of C_s may occur in practice due to the deterioration of the related capacitor. Impacting X_L^{opt} as evinced by expression (6.13), a modification of C_s challenges the reactive power modulation abilities of the system. By starting from the reference point indicated in Table 6.1, a relative variation down to -90 % and up to +90 % is considered. The corresponding evolutions of the power efficiency are shown in Figure 6.11a and compared to the maximum achievable efficiency. One can notice that the proposed method emulates an adequate load reactance for reaching constantly the maximum achievable efficiency. In contrast, the passive system endures an efficiency loss for any C_s variation. Also, the latter system is more sensitive to a capacitance decrease

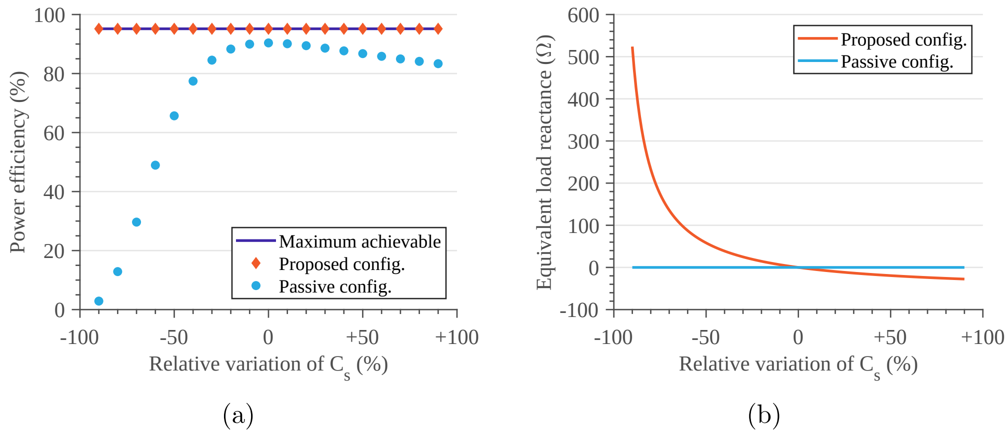

Figure 6.11: Evolutions of the (a) power efficiency and of the (b) equivalent load reactance with respect to a variation of C_s for the proposed and the passive systems

rather than a capacitance increase. This asymmetrical sensitivity is due to the fact that a secondary capacitance declining down to zero results in an asymptotic rise of the related capacitor impedance and to a progressive decoupling of the load from the circuit.

Once again and with even more relevance in this case, the voltages and currents phasors are observed in the complex space for an easier interpretation of the proposed method action (see Figures 6.12 and 6.13). For a passive configuration, a lowering of C_s raises the primary current $\underline{I}_p$ since the system has to achieve a constant output power despite an increasing phase shift between the primary current $\underline{I}_p$ and voltage $\underline{V}_p$. As a consequence, the system efficiency drops due to increased Joule losses in the primary side. As mentioned above, the load is progressively decoupled from the system and the system struggles to furnish the reference output power. A rising C_s produces the same effect with however a moderate impact on the primary current and voltage phase shift, as the load remains coupled to the system. By performing an active rectification, the proposed method shifts adequately the voltage $\underline{V}_s$ which sweeps the current $\underline{I}_p$ away until the latter alignment with the voltage $\underline{V}_p$. Since the proposed system must ensures a constant apparent load resistance equal to its optimal value, the tip of the phasor $\underline{V}_s$ moves perpendicularly to the direction of the secondary current $\underline{I}_s$. The mistuning penalty is therefore displaced from the primary current $\underline{I}_p$ to the secondary voltage $\underline{V}_s$, with a consequential rise of the secondary volt-ampere rating. However, both currents $\underline{I}_p$ and $\underline{I}_s$ are back in their nominal position so that the deleterious impact of a C_s variation on the system efficiency is fully compensated.

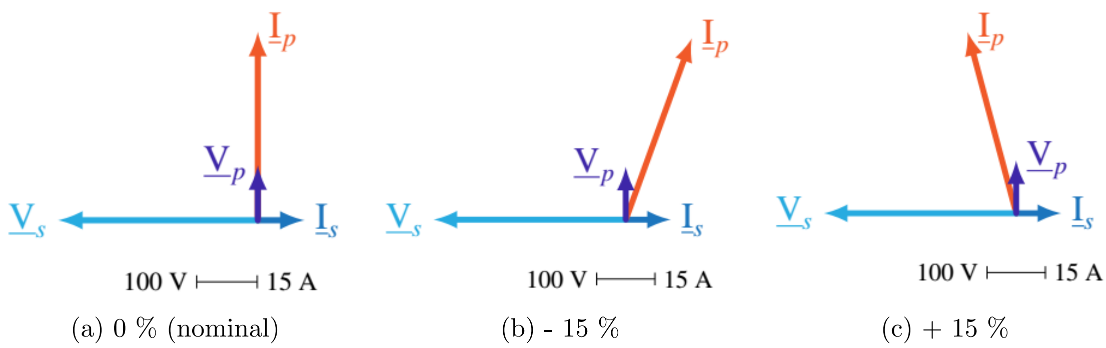

Figure 6.12: Representation of the voltages and currents phasors for different relative variations of C_s impacting the passive system

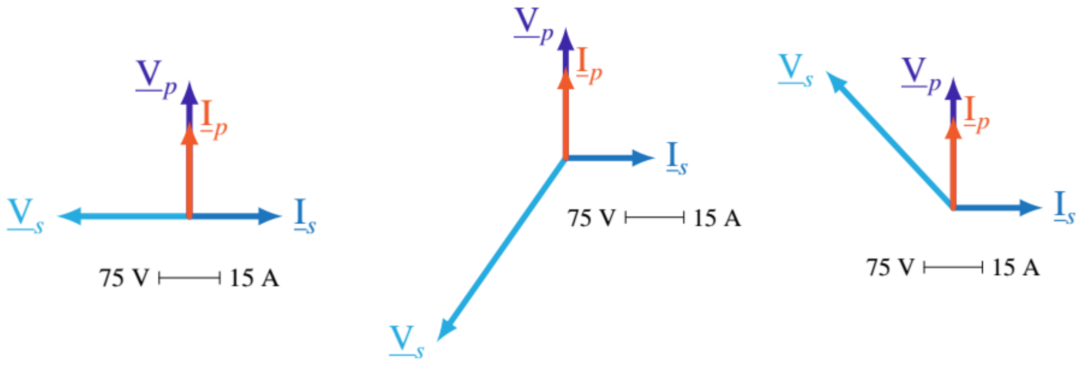

(a) 0 % (nominal)

(b) - 15 %

(c) + 15 %

Figure 6.13: Representation of the voltages and currents phasors for different relative variations of C_s impacting the proposed system

In the illustration above, the secondary capacitance positive deviation has been limited to nearly the doubling of its nominal value for realism purposes, as such deviation from the nominal capacitance value is already representative of a potential severe misconception in the resonant circuit. However, the secondary capacitor reactance declines with the rise of C_s. Therefore, considering an extremely high value of C_s is virtually indicative for the operation of the circuit when it is devoid of secondary capacitor. Such case is investigated by multiplying C_s by 10^9 (leading to a negligible secondary reactance of 60 nΩ), the correspondent phasors are represented on Figure 8.10. One can observe that the proposed system emulates a capacitive function compensating entirely the secondary winding self-inductance. Since the system has to sustain the rated output power, the secondary voltage increases drastically. Nevertheless, the proposed system maintains its efficiency to the optimal value of 95.2 % despite the absence of secondary capacitor, while the passive system efficiency incurs a drastic decrease down to 65.7 % in similar conditions.

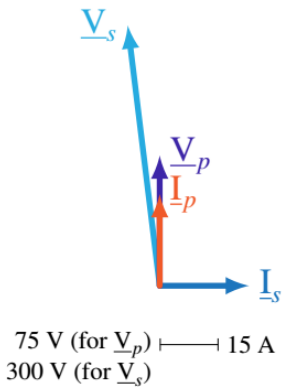

Figure 6.14: Representation of the voltages and currents phasors for the proposed system with a capacitor-free secondary

Remark. *Disregarding temporarily the contextual restriction to a fixed operating frequency, one can note that an efficient capacitor-free secondary equipped with an active rectifier controlled as proposed here can be considered and employed as a universal receiver in frequency. Although being topologically able to transfer power in both directions, such system would lose in practice its power-reversibility capabilities since a transfer from the capacitor-free secondary to the primary would imply a high volt-ampere rating in the secondary converter.*

Variation of the primary capacitance C_p

As demonstrated by the development realized in Section 6.2.2, neither the efficiency nor the optimal load impedance depend on the primary side capacitance. As a matter of fact, the primary compensation purpose is the minimization of the primary side volt-ampere rating. Facing a C_p variation, both the proposed and the passive systems simply increase and shift the primary voltage $\underline{V}_p$ for ensuring the constancy of the primary current $\underline{I}_p$ as they must furnish a constant output power to a constant load resistance. Such behavior is not addressed in the following as it pertains to any circuit to adapt its input voltage for furnishing a constant active power while facing an increasing reactive load.

Remark. *Disregarding once again the contextual restriction to a fixed operating frequency, the proven ability of the SS-RDAB system to compensate the secondary mistuning can be employed for minimizing the primary side volt-ampere rating while producing an optimal efficiency. Indeed, in case of a C_p variation, the operating frequency can be modified for matching the new primary side self-resonant frequency, minimizing hence the primary volt-ampere rating. Logically, the modification of the operating frequency results in the mistuning of the secondary side, which can however be compensated by the proposed system as demonstrated above. The system performances will however vary, since a change in the operating frequency has an impact on the maximum achievable efficiency as shown by expression (6.14).*

6.2.5 Time-domain implementation of the voltage-source converters

At this stage, the methodology has been developed and illustrated considering ideal and sinusoidal voltage sources. In this section, the actual voltage-source converters shown in Figure 6.5 and the related pulse-width modulation (PWM) commands are practically implemented in a realistic time-domain model running under the *PSIM* software [133]. Consistently, the WPT test-case described in Table 6.1 is anew considered. The time-step is fixed to 10^{-8} second. Ideal MOSFETs have been selected as switches. The DC voltage V_u is equal to the rectified European utility line voltage, which corresponds to

$$V_u = \frac{2\sqrt{2}}{\pi} \cdot 230 \cdot \sqrt{3} = 358,2 \text{ V} \approx 360 \text{ V} \tag{6.21}$$

As mentioned previously, the DC battery voltage V_b is also fixed to 360 V, which is coincidentally a standard voltage for EV battery packs. For each operating point, the primary (respectively, the secondary) full-bridge is controlled following an SVC-based command in such a way that the fundamental of the produced AC voltage is equal to the optimal value of $\underline{V}_p$ (respectively, $\underline{V}_s$), ensuing from the resolution of equations (6.16)-(6.19).

Variations of the mutual inductance M (from -90 % to 0 % by steps of 5 %) and of the secondary capacitance C_s (from -90 % to +90 % by steps of 5 %) are applied to the system. The input and the output powers are obtained in *PSIM* via *wattmeter* tools (presenting a cut-off frequency equal to a tenth of the operating frequency) placed downstream of the primary inverter and upstream of the secondary rectifier. In addition to being a further step in the proposed system modeling, this time-domain implementation aims also to verify the relevance of the FHA-based methodology despite the enriched harmonic content of the actual voltage waveforms. The corresponding time-domain results are compared to target operating points computed in the frequency domain (see Figures 6.15 and 6.17). One can ascertain that the proposed methodology leads to an optimal operation of the system, despite parameters deviations. The legitimacy of the FHA-based methodology is hence demonstrated.

The system performs with a clear effectiveness when facing any coupling variation. However, the applicability of the proposed approach seems restricted since the simulated system is

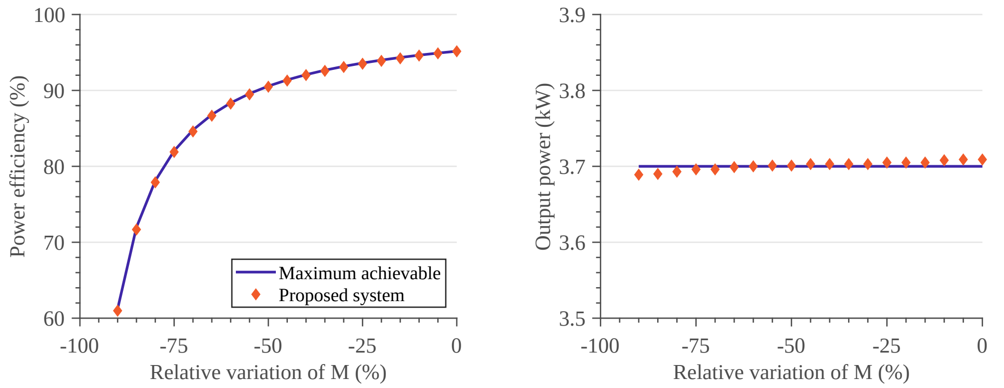

(a) (b)

Figure 6.15: Simulated measurement of the (a) power efficiency and of the (b) output power for deviations of M impacting the proposed system

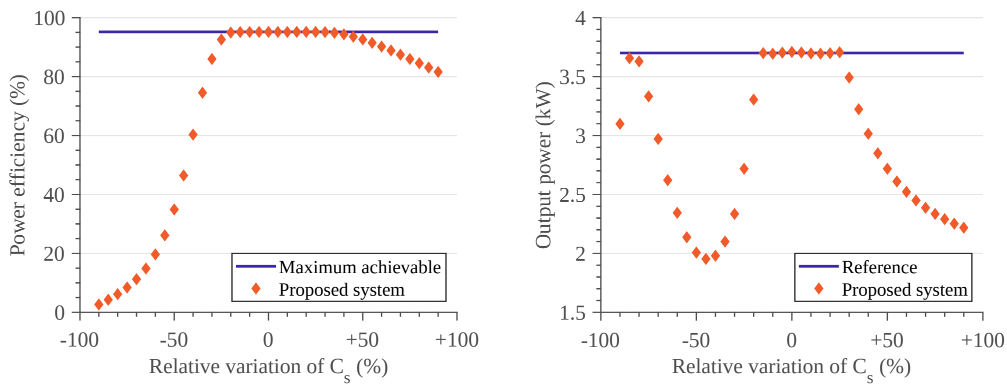

(a) (b)

Figure 6.16: Simulated measurement of the (a) power efficiency and of the (b) output power for deviations of C_s impacting the proposed system

not able to compensate C_s variations further than -15 % and than +25 %. This restriction correlates with the limited voltage range of the converters, as discussed in the next section. Before addressing the latter, the voltage and currents waveforms for the -15 % C_s deviation and the +25 % C_s deviation are respectively presented in Figures 6.17a and 6.17b. First of all, the LC-circuits filtering effect is qualitatively appreciable regarding the near-perfect sinusoidal allure of the each current waveform, despite non-sinusoidal voltages and despite the secondary capacitor disadvantageous detuning (because reducing the secondary filtering effect at the operating frequency). One can observe that the primary current and voltage are in phase for both cases, as expected from the frequency domain illustration. For a decline in C_s, the residual secondary reactance X_s is capacitive so that the active rectifier must emulate an inductive optimal load $X_L^{opt} > 0$. The secondary current i_s (exiting the rectifier by convention, as specified in Figure 6.5) leads on the secondary voltage v_s. Conversely, for a rise in C_s, the residual reactance X_s is inductive so that the active rectifier must emulate a capacitive optimal load $X_L^{opt} < 0$ and the conventional current i_s is logically lagging the secondary voltage v_s.

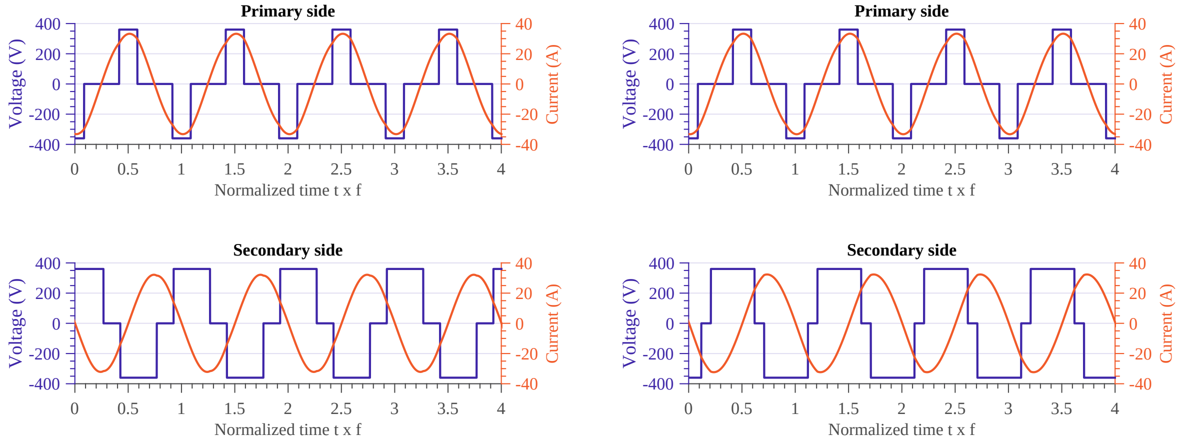

(a) (b)

Figure 6.17: Simulated primary (up) and secondary (down) waveforms in the proposed system for (a) -15 % and (b) +25 % C_s deviation impacting the proposed system

6.2.6 Highlight on controllability restrictions

Among the different non-idealities of conventional voltage-source converters, the limitation in the producible voltage is the cause of the controllability restrictions pointed out in the previous section. As a matter of fact, the amplitude of the voltage on the converter AC-side is limited by the DC-side voltage source. Implementing an SVC command, the module $V_{AC}^{(1)}$ of the fundamental of the AC voltage produced by the converter is

$$V_{AC}^{(1)} = \frac{2\sqrt{2}}{\pi}\, V_d \, \sin\,(\beta/2)$$

where, as a reminder from Section 5.3.2, V_d is the voltage on the DC-side of the converter (which is *a priori* fixed by the related source) and β is the SVC conduction angle. As a consequence, the maximal practicable AC voltage module is $\frac{2\sqrt{2}}{\pi}\, V_d$ for $\beta = \pi$, corresponding to a square-wave command of the converter. Therefore, the solutions of equations (6.16) and (6.19) requiring a primary and/or a secondary voltage(s) higher than $\frac{2\sqrt{2}}{\pi}\, V_u$ and $\frac{2\sqrt{2}}{\pi}\, V_b$, respectively, are not achievable in practice.

When C_s varies, we shown in the previous frequency-domain illustration that the proposed method requires to increase substantially the module of the secondary voltage for shifting it while maintaining a constant output power. The method ability to compensate C_s variations can therefore be hindered by the secondary converter limitation in producible voltage. For the considered test-case, the secondary voltage required for the implementation of the proposed methodology is represented in Figure 6.18, where it its compared to the maximum voltage producible by the secondary converter. One can see that the proposed methodology is not implementable for C_s deviations more severe than -17.5 % in one side and than +27 % in the other side. The interval comprised between these values corresponds to the interval where the optimal command is effective in Figure 6.17, proving the point developed here.

When M declines, we shown in the previous frequency-domain illustration that the system primary and the secondary currents inevitably increase. The system output power being maintained constant, the primary and secondary voltages required for implementing the proposed method are accordingly decreasing with M and the converters are not subject to a voltage-limitation issue. For overcoming the restrictions discussed here, two solutions for boosting the converters DC-side voltages are investigated in the following chapter.

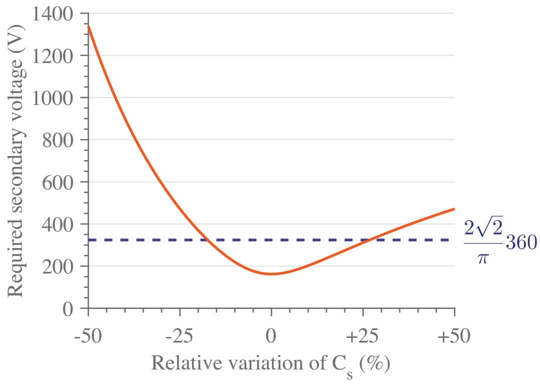

Figure 6.18: Comparison between the required secondary voltage (orange/solid) for applying the proposed method and the maximum producible secondary voltage (blue/dashed)

6.3 Conclusions

In this chapter, an original methodology for the optimal command of bidirectional resonant WPT systems has been proposed. Based on an series-series RDAB topology, this method considers to perform non-synchronous active rectification for modulating simultaneously and independently the apparent resistance and the apparent reactance of the load, as seen from the secondary terminals. Consequently, the former can meet the value of the load resistance maximizing the efficiency (for all actual loading or coupling conditions) and the latter can emulate an eventual reactive function for reinstating a resonant state of operation in case of detuning. The additional variation of the primary voltage furnishes moreover an additional degree of freedom employed for maintaining the output power to a reference value, without compromising the maximum efficiency operation.

Considering the filtering action of the LC-circuits on the primary and secondary currents, the optimal loading conditions are derived analytically using an FHA. The method beneficial action has been illustrated in the frequency domain on an EV test-case. Facing deviations of the mutual inductance, the proposed method has demonstrated its ability to adapt the voltage on both sides of the transmission system for an optimal repartition of the losses between the primary and the secondary sides. Facing deviations of the secondary capacitor, the proposed method has evinced its ability to emulate either an inductive or a capacitive function in order to reinstate a resonant mode of operation. Using the same test-case, the method has been validated in the time-domain, despite the enriched harmonic content of the voltages produced by the switched-mode converters. Nevertheless, controllability restrictions associated with the limited voltage range of the active rectifier has been highlighted for large deviations in the secondary capacitance.

The publications associated with this chapter are (in chronological order)

- A. Desmoort, O. Deblecker and Z. De Grève, "Active Rectification for the Optimal Control of Bidirectional Resonant Wireless Power Transfer," *2018 International Symposium on Power Electronics, Electrical Drives, Automation and Motion (SPEEDAM)*, Amalfi, 2018, pp. 756-761.
- A. Desmoort, O. Deblecker and Z. De Grève, "Active Rectification for the Optimal Command of Bidirectional Resonant Wireless Power Transfer Robust to Severe Circuit Parameters Deviations," in reviewing process in *IEEE Transactions in Industry Applications*

CHAPTER

SEVEN

VOLTAGE STEP-UP SOLUTIONS FOR THE EXTENSION OF THE PROPOSED OPTIMAL COMMAND METHODOLOGY

So far, we proposed an original approach using the active rectification for the optimal command of resonant WPT systems. However, the proposed technique has shown limitations in its ability to emulate adequate reactive functions as it proved to require the active rectifier to feature a wide voltage range on its AC-side, whereas the DC-side voltage is constant and fixed by the load. Using a traditional voltage-source converter, the DC-side voltage must nevertheless be greater than the AC-side voltage, yielding the aforementioned limitations.

For overcoming this issue, **two different solutions are addressed and compared** in this chapter. The insertion of a **current-reversible DC-DC two-quadrant chopper** between the rectifier and the DC load is investigated as a first and conventional solution complying with the proposed topologies power bidirectionality requirements. Nonetheless, this choice leads to the inclusion of two additional converters (one on either side, for preserving the topological symmetry in the power conversion chain), which is a practice that we decided to preferably avoid in our positioning with regard to the current state of the art. Consequently, an alternative solution consisting in the transition from the traditional voltage-source converters to **impedance-source (or Z-source) converters** is considered as an second and unconventional solution. As a matter of fact, the impedance-source topology is a relatively recent and elegant concept elaborated for precisely extending a converter AC-side voltage range with a constant DC-side voltage [134]. Consisting topologically in the association of a traditional converter with a specific arrangement of reactive components, this solution is a consistent way to extend the optimal command applicability without requiring extra power converters. In the context of resonant WPT, the Z-source converter has already been envisioned as a front-end converter [135, 136], notably for performing power factor correction [137, 138]. Here, Z-source converters are employed both as an inverter on the source side and as an active rectifier on the load side. To our knowledge, using a Z-source as an active rectifier has not been proposed yet in the framework of WPT.

In this chapter, the attention is drawn on the voltage conversion for interfacing a DC voltage with an AC voltage so that the latter amplitude is higher than the former. The topologies and the developments presented here are deliberately independent from the current direction (and hence, from the power flow direction) for them to be valid for a DC-to-AC conversion as well as for an AC-to-DC conversion. In this context and for preventing any ambiguity, the term *source* designates a *voltage source* which can either be a power source (such as the rectified voltage in the example previously addressed) or an active load (such as the battery in the same example), depending on the current direction. Similarly, a *voltage production* must not be confused with a power production.

7.1 Conventional solution

A conventional solution for producing a wide AC voltage range from a fixed DC voltage source is the cascading of a two-quadrant chopper with a full-bridge converter (see Figure 7.1). As explained hereafter, such chopper produces a voltage across the full-bridge legs which is consistently equal to or higher than the DC source voltage.

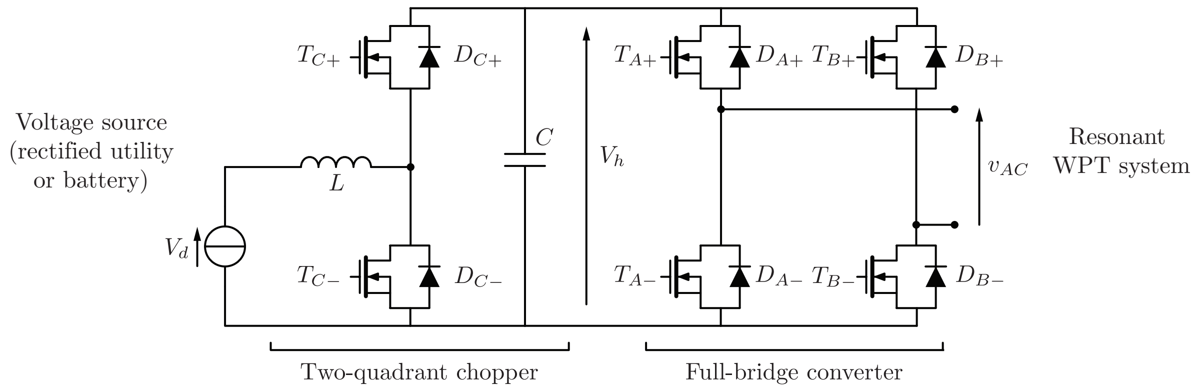

Figure 7.1: Topology of the conventional solution comprising a current-reversible two-quadrant chopper cascading a full-bridge converter

7.1.1 Circuit and operation analysis

Since the converters operations are totally independent, each one can be addressed separately. The full-bridge converter is operated as presented previously, *i.e.*, as an inverter or an active rectifier controlled via an SVC-based command. Its operation is therefore no longer addressed. The two-quadrant chopper operation is for its part investigated hereafter.

The two-quadrant chopper is a current-reversible DC-DC converter including two bidirectional switches arranged in a leg, with an inductor (presenting an inductance L) connecting the leg mid-point to the DC voltage source V_d. The two switches are controlled complementarily. A filtering capacitor C is added to the circuit for maintaining the voltage V_h as constant as possible. Such converter produces a voltage V_h consistently equal to or higher than the source voltage V_d, regardless of the current direction. For this purpose, this converter operates as a step-up converter when the current (and hence, the power) is flowing from the voltage source to the full-bridge and as a step-down converter otherwise. For the following developments, the converter is idealized by considering ideal switches and by neglecting the inductance and the capacitor parasitic resistances. Also, we assume that the inductance L and the capacitance C are sufficiently high for the current i_L and for the voltage V_h to be constant, respectively. The required values of L and C for these assumptions to be valid are determined further in this section.

Step-up operation

When the power is transmitted from the voltage source to the resonant WPT system, the current is transiting from the former to the latter so that only the switch T_{C-} and the diode D_{C+} can conduct. The chopper presents the same structure (and therefore operates) as a conventional step-up (or boost) converter (see Figure 7.2a). When T_{C-} is on, the current circulates in the mesh restricted to the voltage source, the inductance L and the switch T_{C-}. The voltage is equal to the DC-source voltage, *i.e.*

$$v_L = V_d \tag{7.1}$$

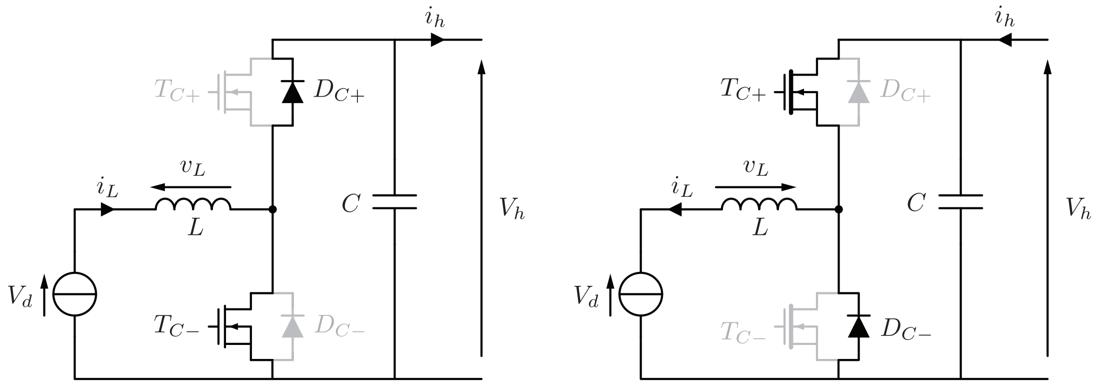

(a) (b)

Figure 7.2: Current-reversible two-quadrant chopper in (a) step-up and (b) step-down operations

When T_{C-} is off, the current circulates from the voltage source to the WPT system through the inductance L and the diode D_{C+}. The voltage across the inductance is given by

$$v_L = V_d - V_h \tag{7.2}$$

In steady state, the average voltage V_L across the inductance over a switching period is null. By denoting D the duty cycle of the switch T_{C-} (*i.e.*, the portion of the switching period T_s during which T_{C-} is on), one has

$$V_L = \frac{1}{T_s}\int_0^{T_s} v_L dt = DV_d + (1-D)(V_d - V_h) = V_d - (1-D)V_h = 0 \tag{7.3}$$

and the voltages V_d and V_h can be related as

$$V_d = (1-D)V_h \qquad \text{with } 0 \leq D \leq 1 \tag{7.4}$$

Step-down operation

When the power is transmitted from the resonant WPT system to the voltage source, the current is transiting from the former to the latter so that only the switch T_{C+} and the diode D_{C-} can conduct. The chopper presents the same structure (and therefore operates) as a conventional step-down (or buck) converter (see Figure 7.2a). When T_{C+} is on, the current circulates from the WPT system to the voltage source through the switch T_{C+} and the inductance L. The voltage across the latter inductance is given by

$$v_L = V_h - V_d \tag{7.5}$$

When T_{C+} is off, the current circulates in the mesh comprising the diode D_{C-}, the inductance L and the voltage source. The voltage across the inductance is therefore equal but opposite to the DC-source voltage V_b, *i.e.*

$$v_L = -V_d \tag{7.6}$$

In steady state, the average voltage V_L across the inductance over a switching period is null. Since T_{C+} and T_{C-} are controlled complementarily, the duty cycle of the switch T_{C+} corresponds to $(1-D)$ and one has

$$V_L = \frac{1}{T_s}\int_0^{T_s} v_L dt = (1-D)(V_h - V_d) + D(-V_d) = D^* V_h - V_d = 0 \tag{7.7}$$

and the voltages V_d and V_h can be related as

$$V_d = (1 - D)V_h \qquad \text{with } 0 \leq D \leq 1 \tag{7.8}$$

One can note that the relation between the voltages V_d to V_h is independent from the type of operation as well as from the power direction.

7.1.2 Reactive components dimensioning

The typical piecewise linear evolutions of the voltage across the capacitor and the current in the inductor are schematized in Figure 7.3. For the converter to operate properly, the capacitance C and the inductance L must be sufficiently high for considering the capacitor voltage v_h and the inductor current i_L as constant, respectively. One aims to confine the voltage ripple on v_h and the current ripple on i_L within a tolerated range. When either the switch T_{C-} or the diode D_{C-} conducts, the current in the capacitor is the average current transiting on the DC-link I_h and the voltage across the inductor is V_d so that the variations of the capacitors voltage ΔV_h and of the inductors current ΔI_L are given by

$$\Delta V_h = \frac{I_h}{C}\, D\, T_s \quad \text{and} \quad \Delta I_L = \frac{V_d}{L}\, D\, T_s \tag{7.9}$$

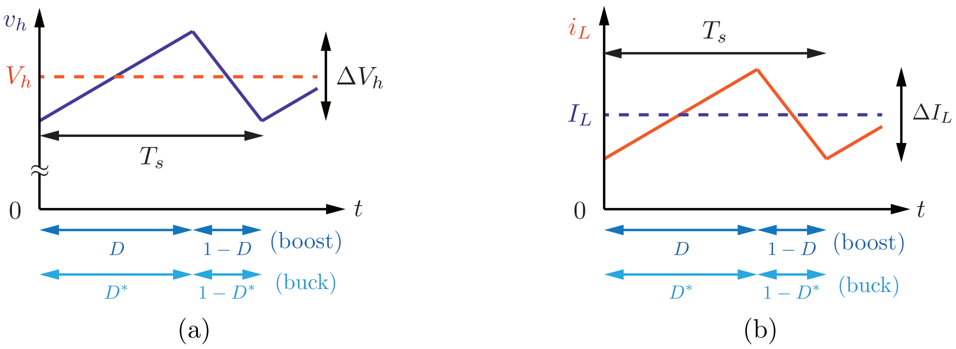

Figure 7.3: Schematic evolutions of the two-quadrant chopper (a) capacitor voltage and (b) inductor current

For maintaining these variations within relative peak-to-peak ripple rates K_v and K_i, the parameters L and C must be such that

$$K_v \geq \frac{\Delta V_h}{V_h} = \frac{I_h}{V_h\, C}\, D\, T_s \quad \Rightarrow \quad C \geq \frac{I_h}{K_v V_h}\, D\, T_s \tag{7.10}$$

$$K_i \geq \frac{\Delta I_L}{I_L} = \frac{V_d}{I_L\, L}\, D\, T_s \quad \Rightarrow \quad L \geq \frac{V_d}{K_i I_L}\, D\, T_s \tag{7.11}$$

Assuming that the converter is lossless, the average current I_h and the voltage V_h are related to the power P furnished or consumed by the voltage source V_d, with $I_h = P/V_h$. Also, the current I_L and the voltage V_d can be related to the power P, with $I_L = P/V_d$. The conditions on the parameters become

$$\begin{aligned} C &\geq \frac{P}{V_h^2 K_v}\, D\, T_s \\ &\geq \frac{P}{V_d^2 K_v}\, (1-D)^2\, D\, T_s \quad \text{using } V_d = (1-D)V_h \end{aligned} \tag{7.12}$$

and

$$L \geq \frac{V_d^2}{K_i P} D\, T_s \tag{7.13}$$

The inductance is strictly increasing with the duty cycle D and must be dimensioned with respect to the maximal voltage conversion ratio which must be produced by the two-quadrant chopper. Conversely to the inductance L, the required filtering capacitance C is not strictly increasing with the duty cycle D. The relation between the minimal value of the capacitance - expressed by (7.12) - and the duty cycle presents a negative concavity and therefore a maximum between 0 and 1, more precisely for $D = 1/3$. As a consequence, for the dimensioning to be effective for duty cycles ranging from 0 to higher than 1/3, the capacitance must verify

$$C \geq \left(\frac{2}{3}\right)^2 \left(\frac{1}{3}\right) \frac{P}{V_d^2 K_v} T_s = \frac{4}{27} \frac{P}{V_d^2 K_v} T_s \tag{7.14}$$

7.1.3 Control and producible AC voltage

As a reminder, the proposed methodology for the optimal command of resonant WPT systems is developed under a first-harmonic assumption and the targeted operation point is described by the fundamental voltages to impose on each side of the WPT circuit. By cascading the two-quadrant chopper (controlled via the duty cycle D) with a full-bridge converter (controlled via an SVC-command, with a conduction angle β), the RMS value of the fundamental AC voltage $V_{AC}^{(1)}$ produced by the full-bridge converter is related to the DC source voltage V_d as

$$V_{AC}^{(1)} = \frac{2\sqrt{2}}{\pi} \frac{V_d}{(1-D)} \sin(\beta/2) \tag{7.15}$$

Since the duty cycle D and the conduction angle β may respectively range from 0 to 1 and from 0 to π, the association of a two-quadrant chopper with a full-bridge converter enables the production of any AC voltage amplitude from zero to a theoretical infinity, regardless of the converted DC source voltage. One can note that in practice, when the power is transiting from the voltage source to the resonant WPT system (*i.e.* in step-up mode of operation), the voltage gain is limited by the parasitic elements from the circuit which causes the collapse of the latter gain for duty cycles D approaching 1.

When the required fundamental voltage is less than $\frac{2\sqrt{2}}{\pi} V_d$, the DC-DC converter duty cycle is chosen as null ($D = 0$) and the desired voltage is obtained by the imposition of the adequate SVC conduction angle β, as implemented in absence of voltage-boosting solution in the previous section. When the required fundamental voltage is greater than $\frac{2\sqrt{2}}{\pi} V_d$, the SVC conduction angle β is fixed to π (corresponding to a square-wave command) and the desired voltage is obtained by imposing of the adequate duty cycle D.

7.1.4 Implementation on the proposed SS-RDAB system

The SS-RDAB system applied to the EV test-case investigated in the previous section is anew considered. For extending the proposed optimal command methodology applicability and in the light of the foregoing, a current-reversible two-quadrant chopper is introduced on the receiving side of the circuit (between the active rectifier and the battery voltage) for extending the AC voltage range of the active rectifier. Another two-quadrant chopper is introduced on the transmitting side of the circuit (between the utility voltage and the inverter) in order to maintain the topological symmetry of the system and to ensure similar performances regardless of the power direction. The resulting circuit is shown in Figure 7.4.

The sizing of the additional reactive components denoted L and C depends on the targeted operating range of the two-quadrant choppers. Since the system is destined to operate regardless of the power direction and since the utility and the battery voltages are equal in the considered test-case, this dimensioning is valid both for the utility-side and the battery-side

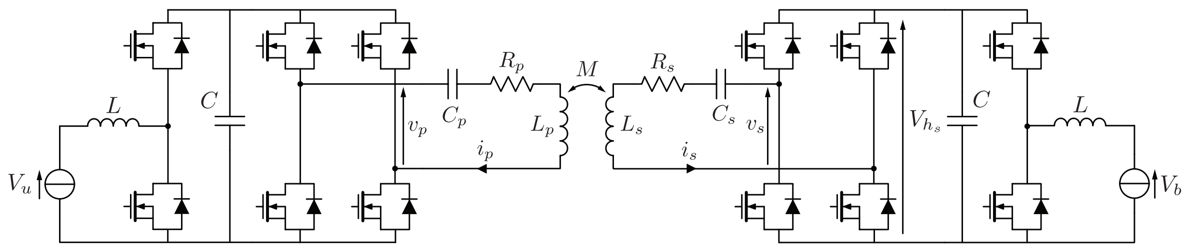

Figure 7.4: Proposed series-series resonant WPT topology including current-reversible two-quadrant choppers

choppers. Once again, for clarity and non-redundancy purposes, only the case of a power transfer from the utility to the battery is addressed in these developments. Hence, since the controllability restrictions are pertaining to the battery-side, no voltage step-up is required on the utility-side and the related chopper is not employed (its duty cycle is fixed to zero) and only the operation of the battery-side chopper is discussed in the following.

Delimitation of the operating range

As a reminder, the purpose of this investigation for voltage step-up solutions is the extension of the time-domain applicability of the proposed optimal command methodology. Especially, the aim is the increase of the voltage range producible by the secondary converter for ensuring the compensation to a wider range of deviations in the secondary resonant capacitance. The delimitation of the operating range of the two-quadrant choppers introduced in the system is therefore related to the targeted range extension for the secondary capacitance deviations compensable by the method. A decrease in C_s produces an unbounded increase of the absolute value of the optimal reactance X_L^{opt} which has to be emulated by the secondary-side active rectifier, since

$$X_L^{opt} = \frac{1}{\omega C_s} - \omega L_s \to \infty \text{ when } C_s \to 0 \tag{7.16}$$

Consequently, the amplitude of the secondary voltage required for the implementation of the proposed methodology increases drastically to a virtual infinity as the capacitance C_s decreases. Conversely, an increase in C_s produces a bounded increase of the absolute value of the optimal reactance X_L^{opt}, which tends progressively to the secondary winding self-reactance

$$X_L^{opt} = \frac{1}{\omega C_s} - \omega L_s \to -\omega L_s \text{ when } C_s \to \infty \tag{7.17}$$

As a result, the amplitude of the secondary voltage required for the implementation of the proposed methodology saturates progressively as the capacitance C_s increases. The maximum value corresponds to the situation where the system has to face an infinitely high secondary capacitance, *i.e.* where the capacitor is replaced by a short-circuit. For the EV test-case investigated earlier, the RMS value of this maximum voltage is obtained by computing the targeted operating point for $X_L^{opt} = -\omega L_s$ and is worth 1338 V. The voltage step-up solutions consisting in either the two-quadrant choppers or the Z-source converter are therefore designed in the following for ensuring an increase of the secondary voltage RMS value up to 1338 V. Under those conditions, the proposed system improved by the voltage step-up solutions would be able to counter any detuning corresponding to an increase of the secondary capacitance C_s and even to operate optimally with a secondary depraved of any resonant capacitor. Moreover, for a producible RMS voltage of 1338 V, the system would be able to compensate any decrease of the secondary capacitance down to -50 %[1].

[1] When the decrease of C_s corresponds to an usury of the related capacitor, one can notice that covering deviations down to -50 % is largely enough in practice.

The production of an RMS voltage of 1338 V on the AC-side of the active rectifier with a DC voltage of 360 V on its DC-side using a two-quadrant chopper duty cycle D for respecting

$$1338 = \frac{2\sqrt{2}}{\pi}\frac{360}{(1-D)} \tag{7.18}$$

The production of an RMS voltage of 1338 V on the AC-side of the active rectifier implies to impose a zero conduction angle (*i.e.*, $\beta = 0$) in the rectifier SVC-command and to command the chopper for imposing a DC-link voltage V_{h_s} corresponding to

$$V_{h_s} = \frac{\pi}{2\sqrt{2}} V_s = \frac{\pi}{2\sqrt{2}} 1338 = 1486 \text{ V}$$

The maximum voltage conversion ratio of the two-quadrant chopper is therefore given by

$$\frac{V_{h_s}}{V_b} = 4.13$$

and the maximum duty cycle D of the battery-side chopper is derived with

$$\frac{V_{h_s}}{V_b} = 4.13 = \frac{1}{(1-D)} \Rightarrow D = 0.758 \tag{7.19}$$

The maximum duty cycle D being determined, one can address the dimensioning of the reactive components before implementing the solution using the time-domain circuit simulator *PSIM*.

Dimensioning of the reactive components

Since the choppers are controlled independently from the full-bridge converters, a switching frequency of 20 kHz is chosen, as an example. Following the design procedure explained and presented above, the filtering capacitance C and inductance L can be dimensioned with respect to the maximum duty cycle defined above. For maintaining a $K_v = 1\%$ ripple on the voltage V_{h_s} and since the maximum duty cycle is higher than 1/3, the capacitance must be

$$C = \frac{4}{27}\frac{P_{ref}}{V_b^2 K_v} T_s = \frac{4}{27}\frac{3700}{360^2 \cdot 0.01}\frac{1}{20000} = 21 \ \mu\text{F} \tag{7.20}$$

As mentioned in the following section, the peak-to-peak current ripple in the inductors of the Z-source converter should be maintained between 10 % and 60 % [139, 140] and a value of 15 % is adopted for the sizing of the inductive components of the Z-source converter in the following. For a fair comparison of both solutions, the two-quadrant chopper inductance is determined on the basis of the same relative peak-to-peak ripple, with $K_i = 15$ %. Therefore, one has

$$L = \frac{V_b^2}{K_i P_{ref}} \ D \ T_s = \frac{360^2}{0.15 \cdot 3700} 0.758 \frac{1}{20000} = 8.9 \text{ mH} \tag{7.21}$$

Time-domain simulation results

The circuit presented in Figure 7.4 is implemented in the time-domain circuit simulator *PSIM*. The time-step is fixed to 10^{-8} second. Ideal MOSFETs are anew employed. The optimal command strategy developed in the previous chapter is employed for computing the fundamental voltages which have to be achieved on the AC-side of each full-bridge. Since the primary-side converter was not confronted to any limitation in the previous chapter, the primary two-quadrant chopper duty cycle is null. The secondary chopper and full-bridge converter are controlled as described in Section 7.1.3 for extending the applicability range of the proposed method with respect to C_s deviations. As a reminder, the initial system was able to compensate C_s variation ranging from - 17.5 % to + 27 % and the conventional voltage step-up solution presented here aims to extend the latter from - 50 % to any positive variation. By observing the time-domain results presented in Figure 7.6, one can ascertain the effectiveness of this solution, which provides the maximum achievable efficiency and the rated output power in the targeted and extended operating range. Notably, the situation corresponding to a capacitor-free secondary (corresponding to an infinite increase of C_s) achieves an efficiency 95.1 % (as a reminder, the maximum efficiency is theoretically 95.2 %) while furnishing an output power of 3701 W. These results are validating the relevance of the first-harmonic approach for computing the targeted operating point of the system and controlling accordingly the converters. The AC voltages, AC currents and secondary DC-link voltage waveforms for a capacitor-free secondary and for a C_s decrease of -50 % are presented in Figures 7.6a and 7.6b, respectively. One can observe the typical triangular shape of the secondary current, corresponding to a purely inductive in absence of resonant capacitor. Before addressing the voltage step-up solution based on a Z-source topology, the effectiveness of this improved system for countering a variation in the windings coupling is validated by considering the time-domain results corresponding to a decreasing in the mutual inductance M (see Figure 7.16). As evinced in the previous chapter, such a diminishing requires the AC-side voltages of the bridges to decrease so that both two-quadrant choppers are inactive and the system operates as exposed previously.

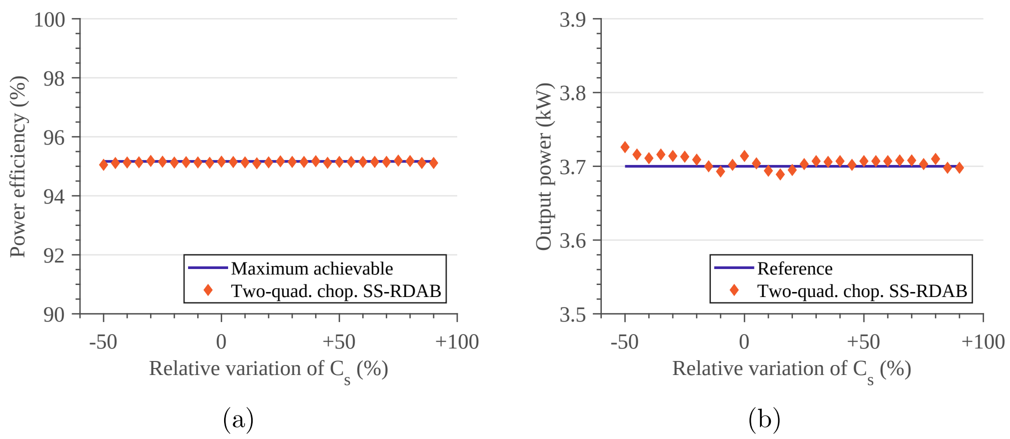

Figure 7.5: Simulated measurement of the (a) power efficiency and of the (b) output power for deviations of C_s impacting the SS-RDAB system with additional two-quadrant choppers

7.2 Solution based on Z-source converters

Broadly speaking, Z-source converters designate alternatives to conventional voltage-source and current-source converters, proposed by Peng in 2002 [134]. Adapted to a wide conversions variety [141, 142], these converters can be characterized without any loss of generality by the insertion of a specific impedance network between a traditional switched-mode converter and its current or voltage source. This impedance network has been conceived for enabling an additional state in the converter operation, thus providing unique features which are unachievable with traditional topologies. Notably, the Z-source inverter (see Figure 7.8) has been developed for extending the voltage range usually achievable with classic voltage-source inverters [134]. Hence, it is able to produce AC voltages ranging from zero to a theoretical infinity, regardless of the DC source voltage V_d and without requiring any additional DC-DC converter. Besides, its operation can be made independent from the current direction

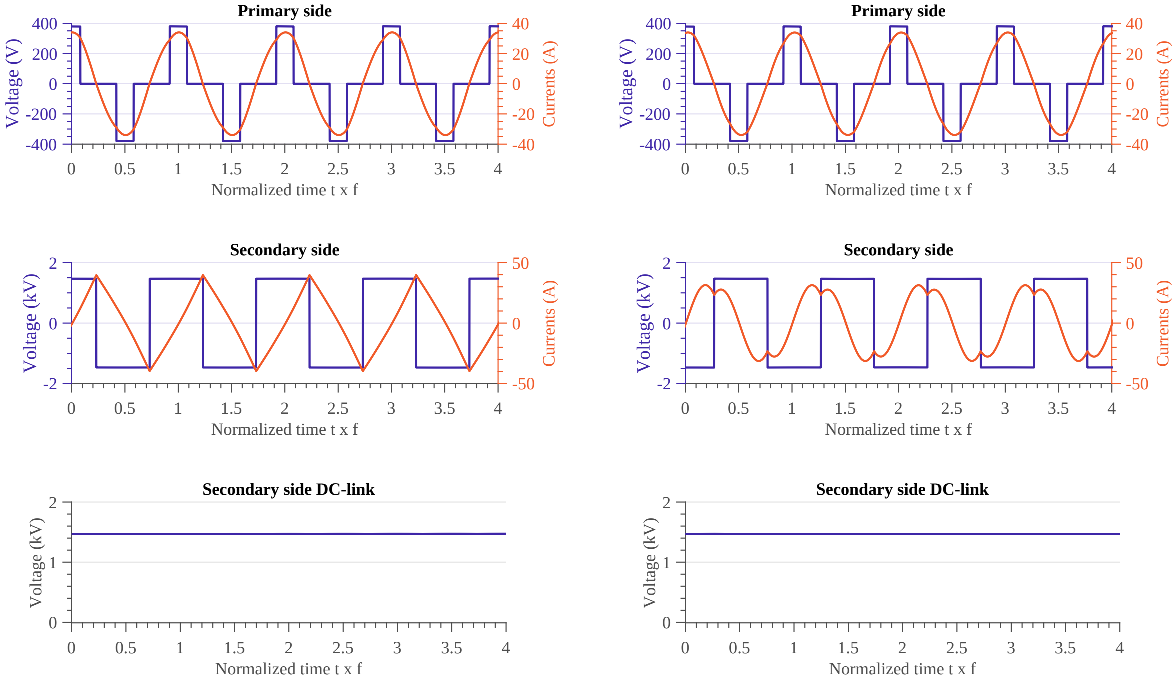

(a) (b)

Figure 7.6: Simulated primary (up), secondary (middle) and secondary DC-link (down) waveforms in the SS-RDAB system with additional choppers for (a) a capacitor-free secondary and (b) -50 % C_s deviation

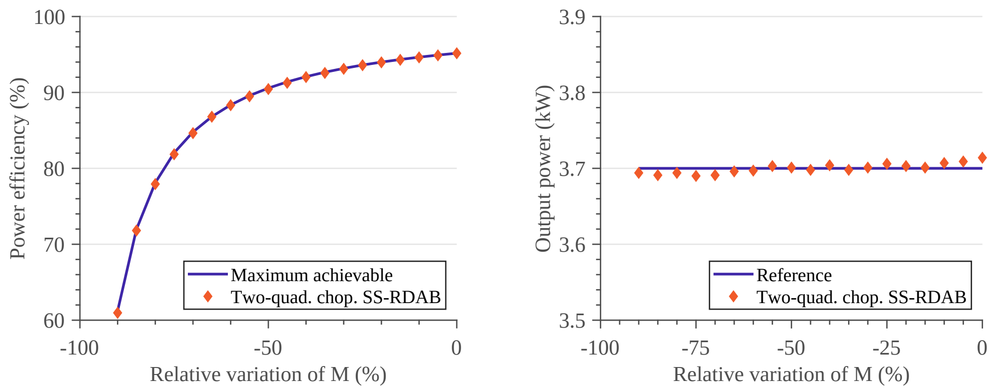

(a) (b)

Figure 7.7: Simulated measurement of the (a) power efficiency and of the (b) output power for deviations of M impacting the SS-RDAB system with additional choppers

with a simple topological adjustment consisting in replacing the diode D_d by a bidirectional switch [143], enabling the converter to function as an inverter as well as an active rectifier. In the light of the foregoing, a transition from traditional voltage-source converters to Z-source converters appears to be an innovative and elegant solution for ensuring both the DC-to-AC and the AC-to-DC conversions in the RDAB-based WPT systems while deprecating the controllability restrictions highlighted in the previous chapter. Before implementing such transition in the time-domain simulation model on *PSIM*, the Z-source inverter/active rectifier (referred simply as Z-source converter in the following) circuit and operation are analyzed hereafter.

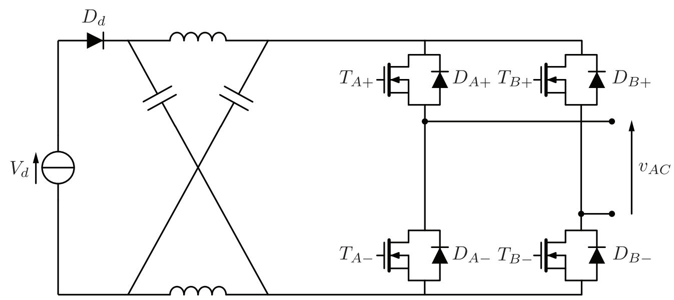

Figure 7.8: Single-phase Z-source inverter

7.2.1 Circuit and operation analysis

As illustrated in Figure 7.9, the Z-source impedance network consists in a two-port network including two line inductors interconnected with two capacitors forming a cross shape. Presenting current limitation properties, this specific topology tolerates the shorting of the converter legs (*i.e.*, the closing of both switching devices equipping a same leg) which is usually forbidden with a traditional converter for ensuring its integrity against over-currents. Therefore, in comparison with the conventional converter, the Z-source disposes of an extra state corresponding to the shorting of one of its legs, called the *shoot-through* state. The additional switch T_d serves to decouple the DC voltage source V_d from the rest of the circuit during the shoot-through states. Combined with the reactive nature of the Z-source impedance network, the shoot-through state grants an additional degree of freedom in the converter command, enabling the production of a virtual infinite AC voltage range. The development leading to this feature is presented hereafter.

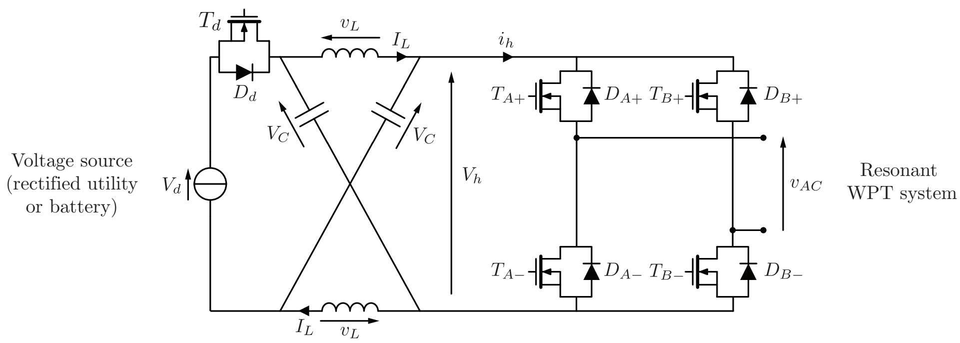

Figure 7.9: Current-reversible Z-source converter

For simplicity purposes, both inductors and both capacitors in the Z-source impedance network are usually assumed to respectively present the same inductance L and the same capacitance C, for making the network symmetric. Moreover, the latter inductance and capacitance are supposed to be sufficiently high for assuming the constancy of the inductors current I_L and of the capacitors voltage V_C. The adequate dimensioning of the reactive component is investigated further in this section. As for the two-quadrant chopper, in the following development, the parasitic resistances are neglected and ideal switches are considered.

Depending on the switches states combination, the converter presents three different operating states, namely the traditional active and freewheeling states and the additional shoot-through state.

During **active and freewheeling** states, the converter is equivalent to the circuit depicted in Figure 7.10a. Seen from the impedance network terminals, the bridge and the WPT circuit can be replaced by an equivalent current source. The related current can either circulates towards the bridge (when the converter operates as an inverter) or from the bridge (when the converter operates as an active rectifier) during active states or can be zero (corresponding to an open-circuit) during freewheeling states. On the other side of the impedance network, the additional switch T_d is turned on so that either the switch T_d or the diode D_d conducts, depending on the direction of the current. As a result, the voltage source V_d is connected to the converter. During these states, the voltage in the converter are related as

$$v_L = V_d - V_C \qquad v_h = V_C - v_L = 2V_C - V_d \tag{7.22}$$

During **shoot-through** states, the converter is equivalent to the circuit on Figure 7.10b. Since one leg from the bridge is shorted, the latter is represented by a short-circuit. The additional switch T_d is turned off and the voltage source V_d is disconnected from the converter because D_d is reverse-biased. During this state, the voltage in the converter are related as

$$v_L = V_C \qquad v_h = 0 \tag{7.23}$$

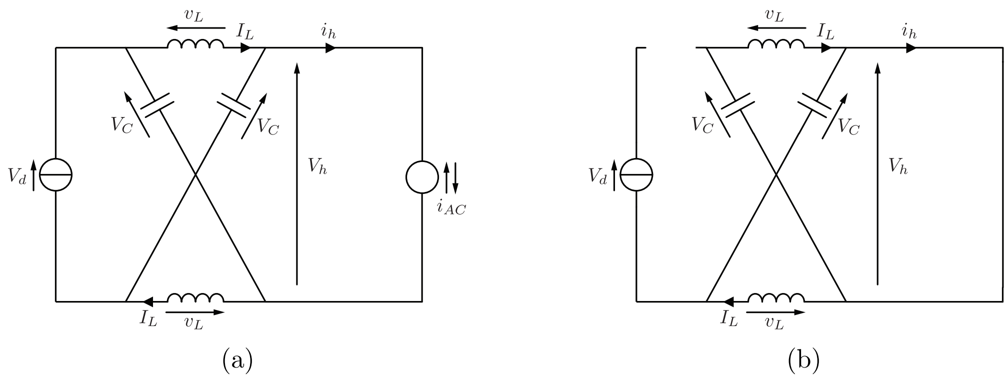

Figure 7.10: Equivalent circuit of the Z-source converter in (a) active, freewheeling and (b) shoot-through states

In steady state, the converter operation is characterized by the absence of net energy storage in the reactive component over a switching period. As a result, the average voltage across the inductors V_L during a complete switching period must be zero. One has

$$V_L = \frac{1}{T_s}\int_0^{T_s} v_L dt = (D_A + D_{FW})(V_d - V_C) + D_{ST}V_C = 0 \tag{7.24}$$

where D_A, D_{FW} and D_{ST} are the portions of the switching period T_s during which the active, the freewheeling and the shoot-through states prevail, respectively. From expression (7.24), the constant steady-state value of the capacitors voltage V_C is deduced with

$$\begin{aligned} V_C &= \frac{(D_A + D_{FW})}{(D_A + D_{FW} - D_{ST})} V_d \\ &= \frac{1 - D_{ST}}{1 - 2D_{ST}} V_d \end{aligned} \tag{7.25}$$

Consequently, when the converter is in an active state and produces therefore a voltage on its AC-side, the DC-link voltage V_h is equal to

$$V_h^A = 2V_C - V_d = \frac{1}{1 - 2D_{ST}} V_d \tag{7.26}$$

Benefiting from its unique topology, the Z-source converter can hence produce a DC-link voltage ranging from V_b to a virtual infinity by introducing shoot-through states with $0 \leq D_{ST} < 0.5$. To a certain extent, the Z-source impedance network can be seen as a passive DC-DC stage performing a voltage step-up when the converter is employed as an inverter and a voltage step-down when the converter is employed as an active rectifier. From this, one can ascertain the holistic equivalence between the sole Z-source converter and the cascading of a full-bridge converter with a two-quadrant chopper.

7.2.2 Reactive components dimensioning

The typical piecewise linear evolutions of the voltage across the capacitors and the current in the inductors are schematized in Figure 7.11. For the converter to operate properly, the capacitance C and the inductance L must be sufficiently high for considering the capacitor voltage v_c and the inductor current i_L as constant, respectively. In practice and as already exposed for the two-quadrant reactive components dimensioning, one aims to confine the voltage ripple on v_c and the current ripple on i_L within a tolerated range. During the shoot-through states, the current in the capacitors is I_L and the voltage across the inductors is V_C so that the variations of the capacitors voltage ΔV_C and of the inductors current ΔI_L are given by

$$\Delta V_C = \frac{I_L}{C}\, D_{ST}\, T_s \quad \text{and} \quad \Delta I_L = \frac{V_C}{L}\, D_{ST}\, T_s \tag{7.27}$$

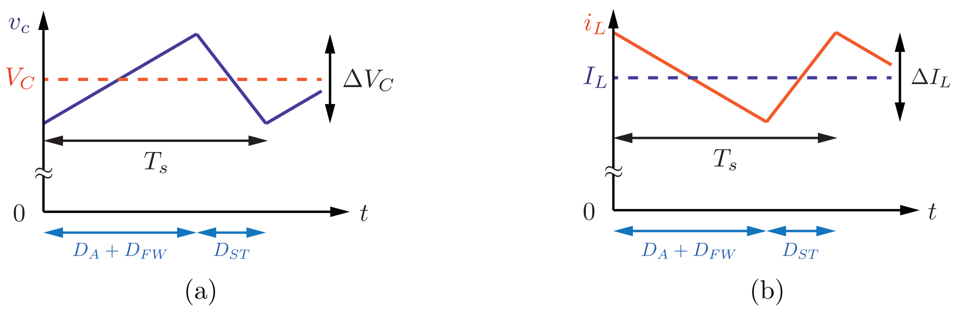

Figure 7.11: Schematic evolutions of the Z-source (a) capacitors voltage and (b) inductors current

For maintaining these variations within relative peak-to-peak ripple rates K_v and K_i, the parameters L and C must be such that

$$K_v \geq \frac{\Delta V_C}{V_C} = \frac{I_L}{V_C\ C}\, D_{ST}\, T_s \quad \Rightarrow \quad C \geq \frac{I_L}{K_v V_C}\, D_{ST}\, T_s \tag{7.28}$$

$$K_i \geq \frac{\Delta I_L}{I_L} = \frac{V_C}{I_L\ L}\, D_{ST}\, T_s \quad \Rightarrow \quad L \geq \frac{V_C}{K_i I_L}\, D_{ST}\, T_s \tag{7.29}$$

Assuming that the converter is lossless, the current I_L can be related to the power P furnished or consumed by the voltage source V_d, with $I_L = P/V_d$. As a matter of fact, the average current through the voltage source is equal to I_L since the average current in the capacitor is zero in steady state. Also, the voltage V_C can be expressed with respect to the voltage V_d using expression (7.25). The conditions on the parameters become

$$C \geq \frac{P}{K_v V_d^2}\frac{1-2D_{ST}}{1-D_{ST}}\, D_{ST}\, T_s \quad \text{and} \quad L \geq \frac{V_d^2}{K_i P}\frac{1-D_{ST}}{1-2D_{ST}}\, D_{ST}\, T_s \tag{7.30}$$

As in the case of the two-quadrant chopper, the inductance is strictly increasing with the shoot-through duty cycle and must be dimensioned with respect to the maximal voltage conversion ratio which must be produced by the Z-source converter. Conversely, the expression of the minimal required capacitance with respect to the shoot-through duty cycle presents a negative concavity and therefore a maximum between 0 and 0.5, more precisely for $D_{ST} = 1 - 1/\sqrt{2} = 0.293$. As a consequence, for the dimensioning to be effective for shoot-through duty cycles ranging from 0 to higher than 0.293, the capacitance must verify

$$C \geq 0.172 \frac{P}{K_v V_d^2} T_s \quad \text{(obtained for } D_{ST} = 0.293\text{)} \tag{7.31}$$

7.2.3 Control and producible AC voltage

For controlling the Z-source converter, a variant of the conventional SVC-command integrating shoot-through states is proposed. This variant has been established in order to ensure a uniform reparation of the constraints on the switches, by balancing their conduction time and the number of sustained shoot-throughs on a switching period. As for the classic SVC-command, the switching period T_s is equal to the operating period T. Referring on the switches notations in Figure 7.9, the corresponding gate signal for each switch and the resulting AC voltage are represented in Figure 7.12a. By proceeding in this manner, the RMS value of the fundamental voltage $V_{AC}^{(1)}$ produced by the Z-source converter is related to the DC source voltage V_d as

$$V_{AC}^{(1)} = \frac{2\sqrt{2}}{\pi} \frac{V_d}{1 - 2D_{ST}} \sin\left[\frac{(1 - D_{ST} - D_{FW})\pi}{2}\right] \tag{7.32}$$

When the required fundamental RMS voltage is less than $\frac{2\sqrt{2}}{\pi}V_d$, the shoot-though is chosen as null ($D_{ST} = 0$) and the required voltage is obtained by the imposition of the adequate SVC conduction angle $\beta = (1 - D_{FW})\frac{\pi}{2}$, as implemented in absence of voltage step-up solution in the previous section. When the required fundamental RMS voltage is greater than $\frac{2\sqrt{2}}{\pi}V_d$, the freewheeling states duty cycle D_{ST} is fixed to zero and the desired voltage is obtained by imposing of the adequate shoot-through duty cycle D_{ST}. One can notive that in contrast with the solution using a two-quadrant chopper, the operation of the full-bridge converter is not independent from the DC-DC conversion effected by the Z-source impedance network. As a matter of fact, the cancellation of the voltage produced on the bridge AC-side during the shoot-through state has an impact on the shape of the fundamental voltage, observable by the intervention of D_{ST} in the sinusoidal shape factor ensuing from the harmonic analysis. Although this sinusoidal contribution tends to decrease the voltage module $V_{AC}^{(1)}$, the hyperbolic factor $1/(1 - 2D_{ST})$ predominates when D_{ST} increases so that $V_{AC}^{(1)}$ is always greater than $\frac{2\sqrt{2}}{\pi}V_d$ when $D_{FW} = 0$ and $D_{ST} > 0$, as evinced by Figure 7.12b.

7.2.4 Implementation on the proposed SS-RDAB system

As for the conventional voltage step-up solution, the SS-RDAB system applied to the EV test-case investigated in the previous section is anew considered. For extending the proposed optimal command methodology applicability and in the light of the foregoing, a Z-source converter is employed as an active rectifier on the receiving side of the circuit for extending the secondary AC voltage range. On the transmitting side, another Z-source converter is resorted to in order, once again, to maintain the topological symmetry of the system and to ensure identical performances regardless of the power direction. The SS-RDAB system equipped with Z-source converters is shown in Figure 7.9. The dimensioning of the Z-source impedance network depends on the targeted operating range of the Z-source converters and since the considered system is perfectly symmetric, identical impedance networks are employed on both sides of the system. Similarly to the conventional solution, no voltage step-up is required on

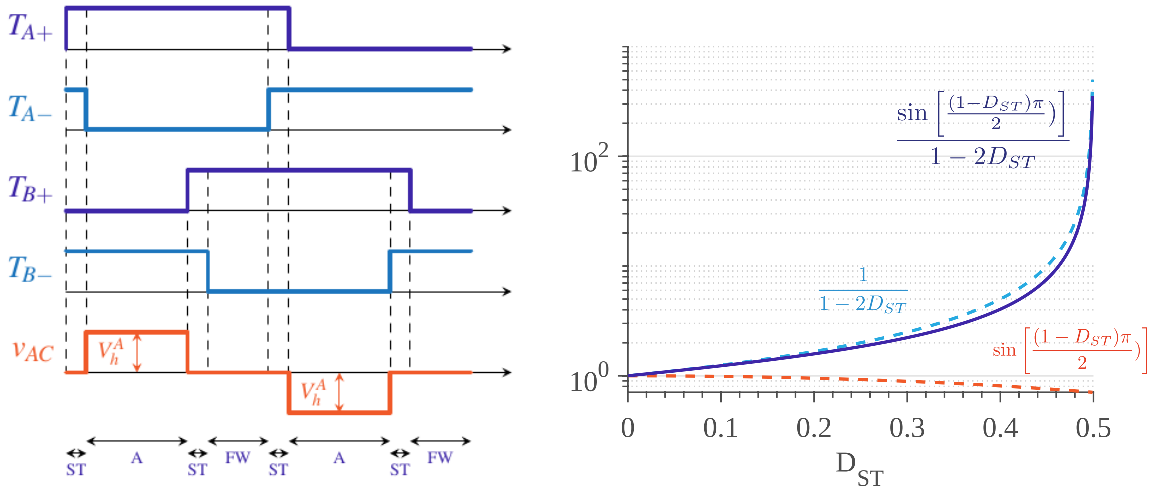

(a) (b)

Figure 7.12: (a) SVC-command integrating shoot-through states and (b) evolution of the $V_{AC}^{(1)}/V_d$ conversion ratio with respect to D_{ST} (for $D_{FW} = 0$)

the utility-side so that the shoot-through states are removed from the command of the related Z-source inverter (its shoot-through duty cycle is fixed to 0) and only the operation of the battery-side Z-source active rectifier is discussed in the following.

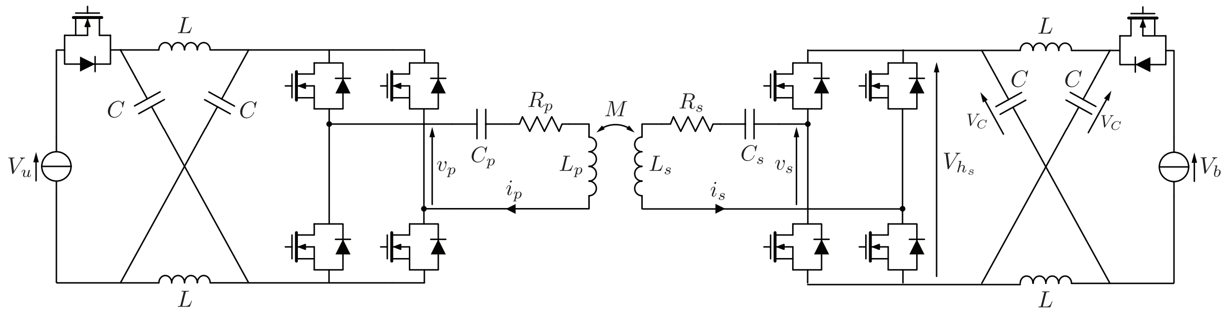

Figure 7.13: Proposed series-series resonant WPT topology based on Z-source converters

Delimitation of the operating range

The Z-source solution must provide a similar operating range as the conventional solution, *i.e.*, being able to produce a secondary AC voltage presenting a RMS value up to 1338 V with a battery voltage of 360 V. The production of an RMS voltage of 1338 V on the AC-side of the Z-source rectifier with a DC voltage of 360 V on its DC-side implies to eliminate the freewheeling states (*i.e.*, $D_{FW} = 0$) from its command and to impose a shoot-through duty cycle D_{ST} verifying

$$1338 = \frac{2\sqrt{2}}{\pi}\frac{360}{1-2D_{ST}}\ \sin\left[\frac{(1-D_{ST})\pi}{2}\right] \Rightarrow D_{ST} = 0.402 \qquad (7.33)$$

For such a value of D_{ST}, the voltage produced on the rectifier DC-link during the active state $V_{h_s}^A$ and the capacitor voltage V_C are given by

$$V_{h_s}^A = \frac{V_b}{1-2D_{ST}} = 1842 \text{ V and } V_C = \frac{1-D_{ST}}{1-2D_{ST}}V_b = 1101 \text{ V} \qquad (7.34)$$

One can observe that the DC-link voltage seen by the rectifier during its active states is higher than the DC-link voltage with the conventional solution (which was worth 1487 V, as a reminder). As a matter of fact and as mentioned previously, the voltage on the AC-side of the Z-source rectifier is null during the shoot-through states so that for producing a given AC voltage, its DC-link voltage during the active states must be higher than the DC-link voltage of the conventional solution, where the bridge is always active. Conversely, the Z-source capacitor voltage V_C is smaller than the voltage of the filtering capacitor employed in the two-quadrant chopper (which is equal to the DC-link voltage, *i.e.* 1487 V).

Dimensioning of the reactive components

Following the design procedure presented above, the Z-source network capacitances C and inductances L can be dimensioned with respect to the maximum shoot-through duty cycle defined above. For maintaining a $K_v = 1\%$ peak-to-peak ripple on the voltage V_C and since the maximum shoot-through duty cycle ($D_{ST}^{max} = 0.402$) is higher than 0.293, the capacitance must be

$$C = 0.172 \frac{P_{ref}}{K_v V_b^2} T = 0.172 \frac{3700}{0.01 \cdot 360^2} \frac{1}{85000} = 5.78 \ \mu\text{F} \quad (7.35)$$

and the inductance for ensuring an inductor current peak-to-peak ripple $K_i = 15\%$ is equal to

$$L = \frac{V_b^2}{K_i P_{ref}} \frac{1 - D_{ST}}{1 - 2D_{ST}} D_{ST} \ T_s = \frac{360^2}{0.15 \cdot 3700} \frac{1 - 0.402}{1 - 2 \cdot 0.402} 0.402 \ \frac{1}{85000} = 3.38 \text{ mH} \quad (7.36)$$

The higher switching frequency and the lower capacitor voltage have a beneficial effect on the value of the capacitance, which is lower than the required filtering capacitor in the conventional solution. However, the inductance value is relatively high in comparison with the filtering inductance value required for the equivalent two-quadrant chopper, taking the difference in switching frequencies into account (since both inductance value are inversely proportional to the latter).

Time-domain simulation results

The circuit presented in Figure 7.9 is implemented in the time-domain circuit simulator $PSIM$. The time-step is fixed to 10^{-8} second. Ideal MOSFETs are anew employed. The optimal command strategy developed in the previous chapter is employed for computing the fundamental voltages which have to be achieved on the AC-side of each full-bridge. Since the primary-side converter was not confronted to any limitation in the previous chapter, the primary shoot-through duty cycle is null and the voltage step-up feature of the primary Z-source converter is not used. The secondary Z-source active rectifier is controlled as described in Section 7.1.3 for extending the applicability range of the proposed method with respect to C_s deviations with a single conversion stage (in contrast with two, using a conventional two-quadrant chopper). Once again, one reminds that the initial system was able to compensate C_s variation ranging from - 17.5 % to + 27 % and the conventional voltage step-up solution presented here aims to extend the latter from -50 % to any positive variation. By observing the time-domain results presented in Figure 7.15, one can ascertain the effectiveness of the Z-source active rectifier for lifting partially the controllability restrictions highlighted in the previous chapter. As a matter of fact, the system (with only a transition from a conventional to a Z-source topology) provides the maximum achievable efficiency and the rated output power in the targeted and extended operating range. Notably, the situation corresponding to a capacitor-free secondary (corresponding to an infinite increase of C_s) achieves an efficiency of 95 % (as a reminder, the maximum efficiency is theoretically 95.2 %) while furnishing an output power of 3658 W (corresponding to a relative error of 1.1 % on the rated power). These results are globally validating the relevance of the first-harmonic approach for computing the targeted operating point of the system and for controlling accordingly the converters. The AC voltages, AC currents and secondary DC-link voltage waveforms for a capacitor-free secondary and for a C_s decrease of -50 % are presented in Figures 7.15a and 7.15b, respectively. One can observe the typical piecewise linear shape of the secondary current, corresponding to a purely inductive secondary and therefore to the absence of resonant capacitor. As mentioned previously, for producing the same RMS voltage on the AC-side, the DC-link voltage during the non-shoot-through states (1842 V) is higher than the DC-link voltage for the conventional solution (1486 V) due to the cancellation of the AC voltage during shoot-through states. The effectiveness of this third version of the proposed system for countering a variation in the windings coupling is also validated by considering the time-domain results corresponding to a decreasing in the mutual inductance M (see Figure 7.16). As for the conventional solution, the reduction of the mutual inductance requires the AC-side voltages to decrease so that the shoot-through states and the specific voltage step-up feature of the Z-source converters are not resorted to.

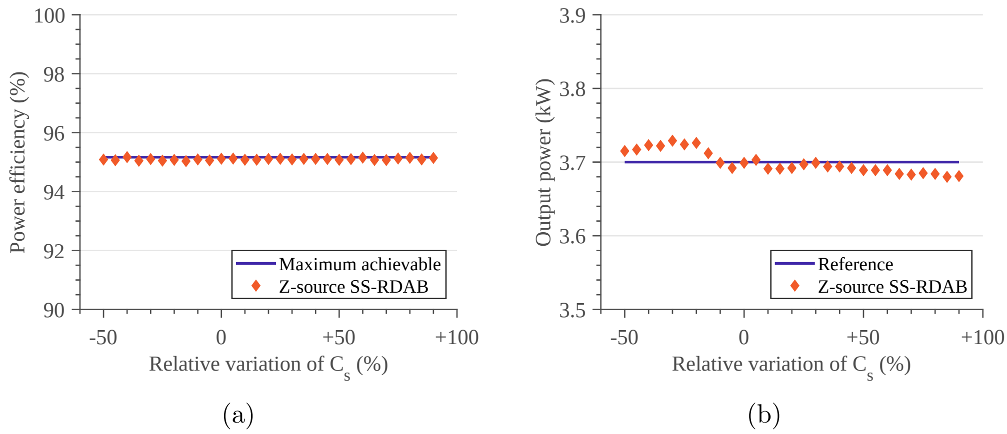

Figure 7.14: Simulated measurement of the (a) power efficiency and of the (b) output power for deviations of C_s impacting the SS-RDAB system with Z-source converters

7.3 Comparison

Since the effectiveness of the solutions based on two-quadrant choppers and on Z-source converters has been demonstrated in the framework of the proposed optimal command topology, a comparison between the two solutions is proposed before concluding. The aim of this thesis is the development of high-level strategies for the optimal command of resonant WPT systems. The solutions which are presented here are investigated with a holistic point of view, whereas more practical considerations would be raised by considering the optimal design of a concrete WPT system and of the related converters. Accordingly, the comparison proposed here is essentially qualitative. For comparing both solutions regarding the generated losses without using the specification of particular switching devices, a *per unit* study based on normalized indexes and presented in [137] is employed as a best-effort approach, regarding the aforementioned context.

7.3.1 Qualitative comparison

The conventional solution consists in two different conversion stages including (in addition to the full-bridge converter) two additional switching devices, one additional inductance and one

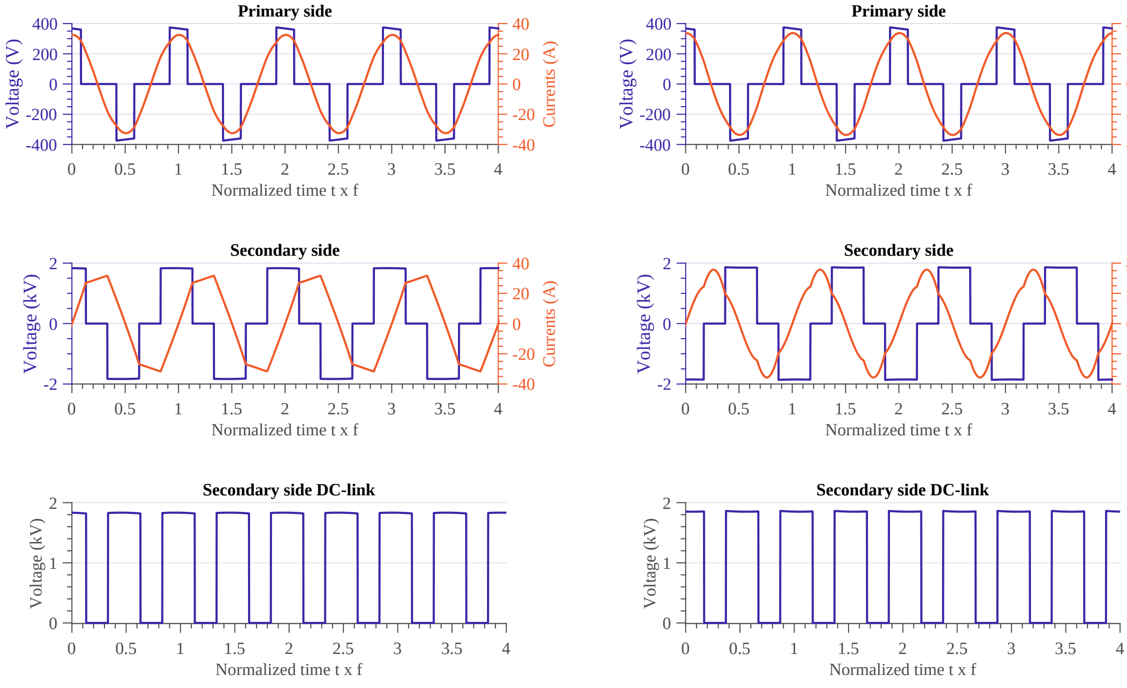

Figure 7.15: Simulated primary (up), secondary (middle) and secondary DC-link (down) waveforms in the SS-RDAB system with Z-source converters for (a) a capacitor-free secondary and (b) -50 % C_s deviation

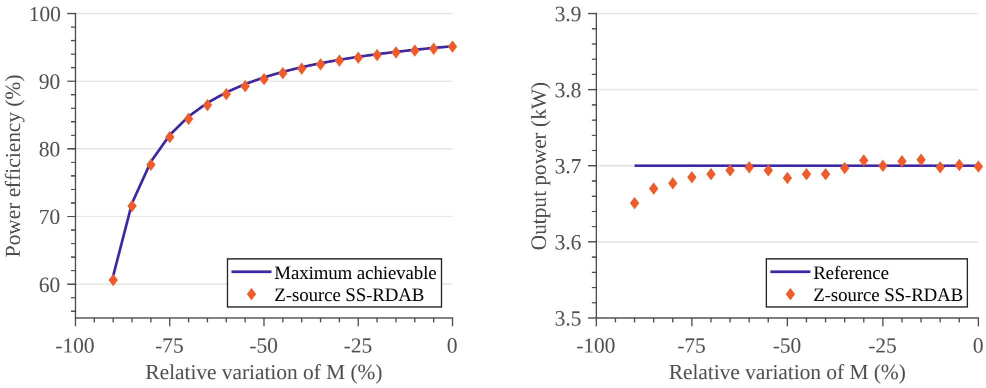

Figure 7.16: Simulated measurement of the (a) power efficiency and of the (b) output power for deviations of M impacting the SS-RDAB system with Z-source converters

additional capacitor, corresponding to the components employed for building the additional two-quadrant chopper interfacing the DC source voltage with the full-bridge. The Z-source-based solution consists in a single conversion stage with an additional switching device as well as two additional inductances and two additional capacitors, corresponding to the components involved in the Z-source impedance network. The Z-source topology saves therefore one active device and employs two more passive components (*i.e.* an inductor and a capacitor). The active components being the more likely to fail, the saving of a switching device is an advantage with respect to the reliability of the system. Due to their high reliability, the inductors are not influencing the global reliability of the system whereas the additional capacitor, more likely to fail, is a slight drawback for the Z-source-based solution. Addressing the reliability question, one have to notice that the Z-source is *per se* immune to an eventual leg short-circuit thanks to the Z-source impedance, while the conventional solution must be protected from a possible leg shorting in both the chopper and full-bridge converters.

In the conventional solution, each conversion stage can be controlled independently, with the advantage of operating the chopper with a switching frequency lower than the operating frequency, leading to lower switching losses and to lower stresses on the semiconductor components. Nevertheless, an independent controller is therefore required. For its part, the Z-source converter requires only to introduce new state (*i.e.* the shoot-through state) in the traditional command technique initially employed for a conventional full-bridge converter, without the need for any extra controller in the system. However, as mentioned earlier in this chapter, the introduction of shoot-through states in the command of the full-bridge has an impact on the waveform of the produced AC voltage so that the DC-link voltage which must be produced across the legs of the full-bridge (and therefore which has to be supported by the switches) is higher for the same RMS voltage on the converter AC-side.

7.3.2 Conduction and switching losses comparison

The comparison of the conventional solution with the Z-source-based solution with respect to the conduction and switching losses is addressed following the adaptation of the procedure exposed in [137].

Conduction losses

For estimating the conduction losses in a general framework, a normalized conduction index ξ expressed in *per unit* is proposed and defined as

$$\xi = \frac{\sum_{k=1}^{N_c} N_k I_k}{I_{base}} \tag{7.37}$$

where N_c is the number of conversion stages, N_k is the number of semiconductor devices which are concomitantly conducting an average current I_k in the stage k and I_{base} is a base current employed for normalizing this index. The conduction indexes relative to each solution is computed and compared with respect to the ratio $V_{AC}^{(1)}/V_d$ (with V_d, the DC source voltage).

Two-quadrant chopper cascading a full-bridge inverter In the chopper, a current I_L (corresponding to the average current in the inductor included in the chopper) is flowing either through the lower switching device during a portion D of the switching frequency or through the upper switching device during a portion $(1-D)$ of the switching frequency. An average current corresponding to the RMS value of the AC-side current I_{ac} is always circulating simultaneously through two switching devices in the full-bridge converter. By taking I_{ac} as the base current, the conduction index of the conventional solution ξ_C is given by

$$\xi_C = \frac{I_L D + I_L(1-D) + 2I_{ac}}{I_{ac}} \tag{7.38}$$

The currents I_L and I_{ac} can be approximatively related as

$$I_L \approx \frac{I_{ac}}{1-D} \tag{7.39}$$

so that the conduction index for the conventional solution ξ_C can be expressed as a function of the duty cycle D of the two-quadrant chopper, with

$$\xi_C = \frac{1}{1-D} + 2 = \frac{3-2D}{1-D} \tag{7.40}$$

Z-source converter In the Z-source-based solution and during the non-shoot-through states (*i.e.* the active and the freewheeling state), an average current I_L (corresponding to the average current in each inductor from the Z-source impedance network) is flowing through the switching device connecting the DC voltage source V_d to the Z-source impedance network and a average current corresponding to the RMS value of the AC-side current I_{ac} is always circulating simultaneously through two switching devices in the full-bridge converter. During the shoot-through states, all the switches in the full-bridge converter are conducting so that one of the upper switches is conducting a current $I_L - I_{ac}/2$ and the other upper switch is conducting a current $I_L + I_{ac}/2$ and a similar configuration prevails for the pair of lower switches. By taking I_{ac} as the base current, the conduction index of the Z-source-based solution ξ_Z is given by

$$\xi_Z = \frac{(I_L + 2I_{ac})(1 - D_{ST}) + 2(I_L + I_{ac}/2 + I_L - I_{ac}/2)D_{ST}}{I_{ac}} \tag{7.41}$$

where D_{ST} is, as a reminder, the shoot-through duty cycle. The currents I_L and I_{ac} can be approximatively related as

$$I_L \approx \frac{I_{ac}}{1 - 2D_{ST}} \tag{7.42}$$

As a result, the Z-source converter conduction index ξ_Z can be expressed as a function of the shoot-through duty cycle D_{ST}, with

$$\xi_Z = 2\frac{D_{ST}^2 + 2}{1 - 2D_{ST}} \tag{7.43}$$

The respective duty cycles D and D_{ST} are related to the respective DC-AC voltage conversion ratios $V_{AC}^{(1)}/V_d$, with

$$\frac{V_{AC}^{(1)}}{V_d} = \frac{2\sqrt{2}}{\pi}\frac{1}{1-D} \text{ for the conventional solution} \tag{7.44}$$

$$\frac{V_{AC}^{(1)}}{V_d} = \frac{2\sqrt{2}}{\pi}\frac{\sin\left[(1-D_{ST})\frac{\pi}{2}\right]}{1-2D_{ST}} \text{ for the Z-source-based solution} \tag{7.45}$$

and the respective conduction index for each solution is represented as a function of the DC-AC voltage conversion ratio in Figure 7.17.

One can observe that according to the latter high-level approach, the conduction losses are expected to be more important using the Z-source-based solution for DC-AC voltage conversion ratio higher than 1.5. Although the extreme situations considered above (*i.e.* a -50 % variaton of C_s or the absence of secondary resonant capacitor) requires a high voltage conversion ratio (*i.e.* 3.71 for the investigated test-case), the Z-source solution is more interesting for the nominal operation of the system (when the voltage step-up effect is not required), for situations where only the mutual inductance M is varying or for lower (and more realistic) deviations in the secondary capacitance. Such an observation is significant as both of the latter cases are the most likely to occur during the functioning of a practical resonant WPT system.

Switching losses

The question of the switching losses is much more difficult to address without any loss of generality. As a matter of fact, the switching losses are tightly related to the dynamic behavior of a switching device and therefore to a particular converter design. Nevertheless, one may,

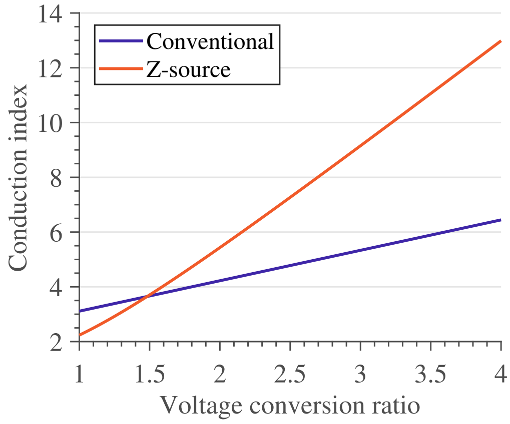

Figure 7.17: Conduction index as a function of the DC-AC voltage conversion ratio $V_{AC}^{(1)}/V_d$ for each voltage step-up solution

as a best effort, compare the switching behavior of both solutions by realizing once again a *per unit* analysis with respect to the DC-AC voltage conversion ratio [137]. The approached expression of the switching losses developed in Section 5.1 is used here and the different rise and fall times (*i.e.* t_{ri}, t_{fi}, t_{rv} and t_{fv}) are summed up in a single time interval denoted t_d. Before presenting this analysis, one can note that, as introduced in Chapter 5, the filtering effects yielded by the resonant circuit connected to the converter entails different types of soft-switching operation, related to the oscillatory current in the full-bridge converter. Although the simple and high-level rules established in Chapter 5 are still applicable to the full-bridge switches in the conventional solution, such rules are not relevant any more for the Z-source converter, due to the introduction of the shoot-through states and to associated internal current circulations. For a fairer comparison, all the switching are therefore considered as hard and the switching losses are grossed-up for this analysis. Also, only the active switch component are addressed in this study.

Two-quadrant chopper cascading a full-bridge inverter The conventional solution comprises two independent converters, *i.e.* the chopper and the full-bridge converter. In the chopper, both switches commutates a current I_L and a voltage V_h with a switching frequency f_s different from the operating frequency f. In the full-bridge converter, the four switches commutates a current I_{ac} and a voltage V_h with a switching frequency equal to the operating frequency f. In this context, the switching losses can be approached by

$$P_{sw,C} = 2 \cdot \frac{1}{2} t_d I_L V_h f_s + 4 \cdot \frac{1}{2} I_{ac} V_h t_d f \tag{7.46}$$

$$= t_d \frac{I_{ac}}{1-D} \frac{V_d}{1-D} f_s + 2 I_{ac} \frac{V_d}{1-D} t_d f \tag{7.47}$$

By choosing the set $[t_d, I_{ac}, V_d, f]$ as base values and relating f_s and f as $f_s/f = 20000/85000 = 0.235$ as an example accordant with the test-case previously considered, the per unit switching losses index $P_{sw,C}^{p.u.}$ associated with the conventional solution is

$$P_{sw,C}^{p.u.} = \frac{0.235}{(1-D)^2} + \frac{2}{1-D} \tag{7.48}$$

Z-source converter In the Z-source converter, the switch connecting the DC source voltage to the Z-source impedance network commutates a current I_L and a voltage V_h with a switching frequency equal to the double of the operating frequency (as the converter incur two shoot-through states per operating period). In the full-bridge, all the switches commutate at the operating frequency a voltage V_h, two out of four switches commutate a current $I_L + I_{ac}/2$ and the two other commutate a current $I_L - I_{ac}/2$. Therefore, the switching losses can be approached by

$$\begin{aligned}
P_{sw,Z} &= \frac{1}{2}t_d I_L V_h 2f + \frac{1}{2}t_d 2(I_L + I_{ac}/2 + I_L - I_{ac}/2)V_h f && (7.49)\\
&= 2t_d \frac{I_{ac}}{1-2D_{ST}} \frac{V_d}{1-2D_{ST}} f + 2I_L \frac{V_d}{1-2D_{ST}} f && (7.50)\\
&= 2t_d \frac{I_{ac}V_d}{(1-2D_{ST})^2} f + 2t_d \frac{I_{ac}}{1-2D_{ST}} \frac{V_d}{1-2D_{ST}} f && (7.51)\\
&= 4t_d \frac{I_{ac}V_d}{(1-2D_{ST})^2} f && (7.52)
\end{aligned}$$

By choosing the same set $[t_d, I_{ac}, V_d, f]$ of base values as for the conventional solution, the per unit switching losses index $P_{sw,Z}^{p.u.}$ associated with the Z-source-based solution is

$$P_{sw,Z}^{p.u.} = \frac{4}{(1-2D_{ST})^2} \tag{7.53}$$

The switching losses index associated with each solution is represented as a function of the DC-AC voltage conversion ratio in Figure 7.18. One can observe that according to this study, the switching losses are more important with the Z-source-based solution. This result seems relevant and can be explained due to the higher switching frequency of the switch interfacing the DC source with the converter, to the higher voltage on the DC-link and to the higher current circulating in the full-bridge during shoot-through states. Moreover, a significant surge in these losses occur with the increasing of the voltage conversion ratio, notably for the conversion ratio considered in the test-case above. Although appearing as eliminatory for the Z-source-based solution, these conclusions can be moderated. On the one hand, the test-case investigated earlier in this chapter is extreme case corresponding to eminently severe deviations in the secondary capacitance. In practice, lower conversion ratio suffices. On the other hand, one reminds that the approach proposed here for the comparison of the losses impacting both solutions is a best-effort approach, grossing-up the losses and with important simplifying assumptions. A more precise comparison of both solutions would require to consider specific switching devices.

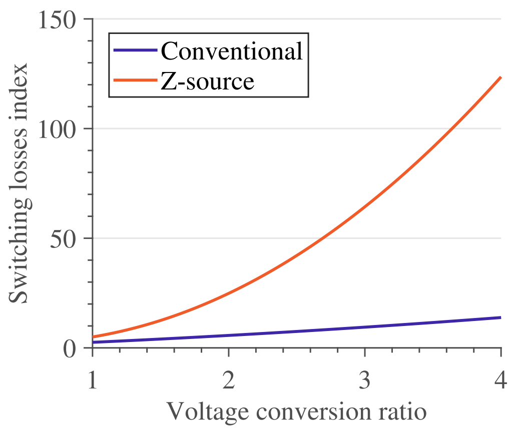

Figure 7.18: Switching losses index as a function of the DC-AC voltage conversion ratio $V_{AC}^{(1)}/V_d$ for each voltage step-up solution

7.4 Conclusions

In the previous chapter, the time-domain implementation of the series-series RDAB topology controlled via the proposed optimal command has highlighted the occurrence of controllability restrictions when the system has to face severe deviations in the secondary capacitance. It has been established that these restrictions are related to the limitation in the voltage producible on the AC-side of the active rectifier.

For extending the AC voltage range of the latter and therefore extending the scope of applicability of the proposed optimal command, a transition to Z-source converters has been envisioned and compared with a more conventional solution, consisting in adding two additional (one front- and one back-end) current-reversible choppers. The circuit, the operation and the dimensioning of the reactive components related to both solutions have been presented. According to their time-domain simulation on the EV test-case investigated previously, both methods have successfully demonstrated their equivalent effectiveness for extending the range of compensable secondary capacitance deviations (up to the extreme case of a secondary side devoid of any resonant capacitor). Via the simple introduction of shoot-through states, the Z-source employed as an active rectifier has hence demonstrated its ability to combine in a single conversion stage the rectification and the DC-DC conversion functions.

Besides reducing the number of conversion stages, the Z-source converter presents a higher reliability and a simpler control. However, it requires the switches to withstand a higher voltage in comparison with the conventional solution, for the same range extension. A dimensionless study of the losses, employed as a best effort in this holistic approach, has indicated that the Z-source converter is mainly interesting for slight extensions of the voltage range, for which its lower conduction losses could balance its higher switching losses. For high extensions of the voltage range, the conventional solution is however more recommended due to higher conduction and switching losses impacting the Z-source-based solution.

The publication associated with this chapter is

- A. Desmoort, O. Deblecker and Z. De Grève, "Active Rectification for the Optimal Command of Bidirectional Resonant Wireless Power Transfer Robust to Severe Circuit Parameters Deviations," in reviewing process in *IEEE Transactions in Industry Applications*

CHAPTER

EIGHT

EXTENSION OF THE OPTIMAL COMMAND METHODOLOGY TO OTHER TOPOLOGIES

An original methodology for the optimal command of series-series compensated resonant WPT systems has been proposed in Chapter 6. Further, two effective solutions for overcoming the controllability restrictions when the systems are confronted to severe parameters deviations have been proposed in Chapter 7.

In this chapter,we propose to widen the scope of applicability of the proposed methodology by extending its implementation to other compensation topologies. The case of a parallel-parallel compensation scheme is exposed in details in this chapter. The extensions to series-parallel and parallel-series compensation schemes, being based on a highly similar procedure, are not addressed here, but presented in Appendix C for non-redundancy purposes.

8.1 Parallel-parallel resonant dual active bridge (PP-RDAB)

Developed and discussed for systems based on a series-series compensation scheme, the proposed methodology is extended to systems presenting a parallel-parallel compensation scheme. The topology of the corresponding conversion chain is presented in Figure 8.1.

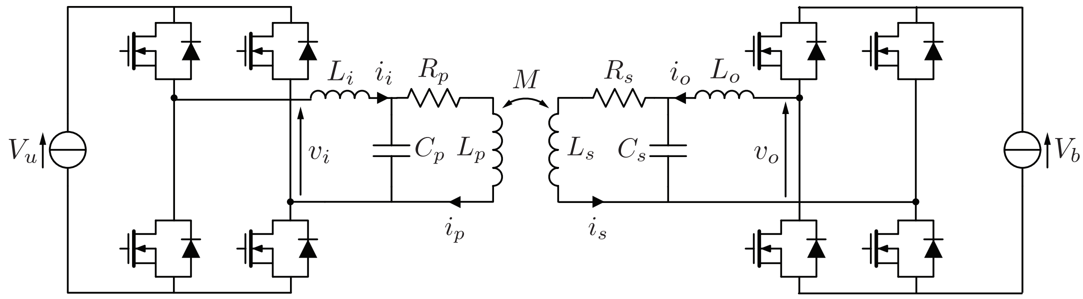

Figure 8.1: Proposed parallel-parallel resonant WPT topology

One can notice the presence of an additional inductor on each side of the transmission circuit, employed for filtering the voltage produced by the converters. As a matter of fact, the voltage-source converters produce relatively high dv/dt during switching transitions and can therefore not be connected directly to a parallel capacitor, at the risk of generating detrimental over-currents in the system. Current-source converters could be employed instead of voltage-source converters, but the marginality of the former (essentially resulting of the scarcity of the associated switching devices) lowers strongly the interest for such transition. Therefore, voltage-source converters in series with a filtering inductor (which are seen as an equivalent current source from the WPT terminals) are implemented. The parasitic resistances of these inductors are neglected in the following development, which focuses on the resonant WPT system.

8.1.1 Equivalent first-harmonic circuit

Usually, the control strategies which are developed for series-series compensated resonant WPT systems are hardly extended to any other compensation scheme. As a matter of fact, the mathematical description of a series-series compensated system presents a simple formalism, thanks to the presence of voltage sources and to use of the conventional mutual inductance model for the representation of the coupled windings. Actually, the latter is an impedance-based model which fits perfectly for the description of a series compensation (as witnessed by the lightness of the expression manipulated in Section 6.2). However, the conservation of the mutual inductance model for the analysis of parallel-compensated circuits burdens significantly the related mathematical developments, lessens the expressions readability and complicates consequently the establishment of control strategies.

For bypassing this formalism issue, we propose a novel approach consisting in addressing the parallel-parallel compensated resonant WPT systems by building a first-harmonic equivalent admittance-based model, comprising exclusively elements connected in parallel and equivalent current sources. This approach is exposed hereafter.

8.1.1.1 Equivalent model of the converters

As mentioned in the section dedicated to the SS-RDAB topology, the voltage-source converter controlled via an SVC-command are producing AC voltages v_i and v_o which are controllable in both module and phase. These converters are therefore assimilable to AC voltage sources $\underline{V}_i$ and $\underline{V}_o$, respectively. As depicted in Figure 8.2 for the primary side, each voltage source in series with its filtering inductance can be replaced by an equivalent current source in parallel with the same inductance, thanks to the Thevenin-Norton equivalence. One has

$$\underline{I}_i^N = \frac{\underline{V}_i}{j\omega L_i} \quad \text{and} \quad \underline{I}_o^N = \frac{\underline{V}_o}{j\omega L_o} \tag{8.1}$$

(a) Thevenin equivalent

(b) Norton equivalent

Figure 8.2: Application of the Thevenin-Norton equivalence on the primary side

8.1.1.2 Equivalent model for the coupled windings

Coupled windings are ordinarily represented using an equivalent mutual inductance model, which is an impedance-based model as it comprises on each side a resistance in series with an inductance and an electromotive force. Although being more adapted to the physical interpretation of the mutual induction phenomenon, this impedance-based model is converted into an admittance-based model, comprising on each side a resistance in parallel with an inductance and a magnetomotive force (see Figure 8.3).

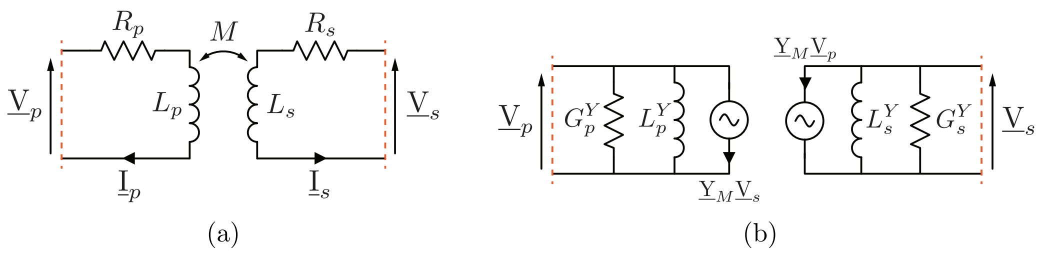

Figure 8.3: (a) Impedance- and (b) admittance-based model for the coupled windings

For doing so in a simple way, the mutual inductance model can be seen as a two-port network described by its impedance matrix $\mathbf{Z}$, expressing the mathematical relation between each side voltage with respect to each side current. One has

$$\begin{bmatrix}\underline{V}_p\\ \underline{V}_s\end{bmatrix} = \mathbf{Z}\begin{bmatrix}\underline{I}_p\\ \underline{I}_s\end{bmatrix} \qquad \text{with } \mathbf{Z} = \begin{bmatrix} R_p + j\omega L_p & j\omega M \\ j\omega M & R_s + j\omega L_s\end{bmatrix} \tag{8.2}$$

Thereafter, the same two-port network can be described by its admittance matrix $\mathbf{Y} = \mathbf{Z}^{-1}$, expressing this time the link between each side current with respect to each side voltage, *i.e.*

$$\begin{bmatrix}\underline{I}_p\\ \underline{I}_s\end{bmatrix} = \mathbf{Y}\begin{bmatrix}\underline{V}_p\\ \underline{V}_s\end{bmatrix} \text{ with } \mathbf{Y} = \begin{bmatrix} \frac{(R_s+j\omega L_s)}{(R_p+j\omega L_p)(R_s+j\omega L_s)+\omega^2M^2} & \frac{-j\omega M}{(R_p+j\omega L_p)(R_s+j\omega L_s)+\omega^2M^2} \\ \frac{-j\omega M}{(R_p+j\omega L_p)(R_s+j\omega L_s)+\omega^2M^2} & \frac{(R_p+j\omega L_p)}{(R_p+j\omega L_p)(R_s+j\omega L_s)+\omega^2M^2}\end{bmatrix} \tag{8.3}$$

The latter system of equations can be rewritten as

$$\underline{I}_p = (G_p^Y + jB_p^Y)\underline{V}_p + \underline{Y}_M\underline{V}_s \tag{8.4}$$
$$\underline{I}_s = (G_s^Y + jB_s^Y)\underline{V}_s + \underline{Y}_M\underline{V}_p \tag{8.5}$$

where G_p^Y and G_s^Y are respectively the primary and the secondary equivalent conductances, B_p^Y and B_s^Y are respectively the primary and the secondary equivalent susceptances and $\underline{Y}_M$ is the windings mutual admittance, with

$$G_p^Y = \mathbf{Re}\left(\frac{(R_s+j\omega L_s)}{(R_p+j\omega L_p)(R_s+j\omega L_s)+\omega^2M^2}\right) \quad B_p^Y = \mathbf{Im}\left(\frac{(R_s+j\omega L_s)}{(R_p+j\omega L_p)(R_s+j\omega L_s)+\omega^2M^2}\right)$$
$$G_s^Y = \mathbf{Re}\left(\frac{(R_p+j\omega L_p)}{(R_p+j\omega L_p)(R_s+j\omega L_s)+\omega^2M^2}\right) \quad B_s^Y = \mathbf{Im}\left(\frac{(R_p+j\omega L_p)}{(R_p+j\omega L_p)(R_s+j\omega L_s)+\omega^2M^2}\right)$$

$$\underline{Y}_M = \frac{-j\omega M}{(R_p+j\omega L_p)(R_s+j\omega L_s)+\omega^2M^2}$$

The annotation Y highlights the difference between these equivalent parameters and the parameters from the initial model (*e.g.* G_p^Y is different from $G_p = 1/R_p$). The analytical development of the expressions for B_p^Y and B_s^Y demonstrates that these susceptances are always negative, corresponding logically to an inductive behaviour. As a result, in the equivalent circuit, the susceptances B_p^Y and B_s^Y can be respectively replaced by the inductances L_p^Y and L_s^Y, given by

$$L_p^Y = -\frac{1}{\omega B_p^Y} \qquad\qquad L_s^Y = -\frac{1}{\omega B_s^Y}$$

According to the interpretation of this mathematical model, the resultant admittance-based equivalent circuit for the coupled windings is represented in Figure 8.3b.

Admittance-based equivalent circuit of the complete system

By combining the converters Norton equivalent circuit with the admittance-based circuit for the coupled windings, the equivalent circuit for the first-harmonic analysis of a PP-RDAB system is presented in Figure 8.4.

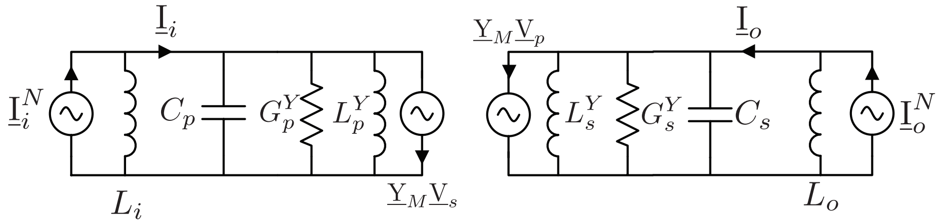

Figure 8.4: Equivalent admittance-based circuit for the first-harmonic analysis

Before addressing the optimal conditions for operating the latter, the primary and secondary voltages are solved. By applying the Kirchhoff's current law, one has

$$\underline{I}_i^N = \underline{Y}_p\underline{V}_p + \underline{Y}_M\underline{V}_s \tag{8.6}$$

$$\underline{I}_o^N = \underline{Y}_s\underline{V}_s + \underline{Y}_M\underline{V}_p \tag{8.7}$$

with the primary circuit admittance $\underline{Y}_p$ and the secondary circuit admittance $\underline{Y}_s$ defined as

$$\underline{Y}_p = G_p^Y + j\omega C_p + 1/j\omega L_p^Y + 1/j\omega L_i \tag{8.8}$$

$$\underline{Y}_s = G_s^Y + j\omega C_s + 1/j\omega L_s^Y + 1/j\omega L_o \tag{8.9}$$

For completeness purpose, the parasitic resistance of the filtering inductors (which are neglected here) can be included in the primary and the secondary conductance G_p^Y and G_s^Y. By observing equations (8.6) and (8.7), one can notice the intended analogy between the admittance-based formalism in this case (*i.e.*, a parallel-parallel compensated system) and the impedance-based formalism in the case of series-series compensated system. By solving equations (8.6) and (8.7), the expression for each voltage is obtained with

$$\underline{V}_p = \frac{\underline{Y}_s\underline{I}_i^N - \underline{Y}_M\underline{I}_o^N}{\underline{Y}_p\underline{Y}_s - \underline{Y}_M^2} \tag{8.10}$$

$$\underline{V}_s = \frac{\underline{Y}_p\underline{I}_o^N - \underline{Y}_M\underline{I}_i^N}{\underline{Y}_p\underline{Y}_s - \underline{Y}_M^2} \tag{8.11}$$

The aforementioned analogy paves the way to the adequate and analogous adaptation of the methodology presented for series-series topologies to parallel-parallel topologies.

8.1.2 Power efficiency and optimal load admittance

The duality between the impedance-based equivalent model for the SS-RDAB system and the admittance-based equivalent model for the PP-RDAB developed above enables a perfect analogy for establishing the optimal load admittance, maximizing the efficiency. Hence, the secondary current source $\underline{I}_o^N$ can be replaced by an equivalent load admittance $\underline{Y}_L = G_L + jB_L$. The power efficiency can be expressed as

$$\eta = \frac{G_L V_s^2}{G_p^Y V_p^2 + G_s^Y V_s^2 + G_L V_s^2} \tag{8.12}$$

where, as a reminder, V_p and V_s are the RMS values of the primary and the secondary voltages, respectively. In this expression of the power efficiency, the contribution to the losses of the mutual conductance between the primary and the secondary windings (quantified by the non-zero real part of the mutual admittance $\underline{Y}_M$) is neglected, for easing the mathematical development of the optimal operating conditions for a parallel-parallel compensated system. Indeed, the impact of this conductance on the system performances is negligible, as demonstrated further in this section. For developing the expression of the power efficiency, the values V_p and V_s can be related by applying the Kirchhoff's current low on the secondary circuit. One has

$$\begin{aligned}\underline{Y}_M \underline{V}_p &= -(G_s^Y + \underbrace{j\omega C_s + \frac{1}{j\omega L_s^Y} + \frac{1}{j\omega L_o}}_{jB_{tot_s}} + G_L + jB_L)\underline{V}_s \\ &= -(G_s^Y + G_L + jB_{tot_s} + jB_L)\underline{V}_s \end{aligned} \tag{8.13}$$

so that the RMS value of the primary voltage V_p can be expressed as

$$V_p = \frac{\sqrt{(G_s^Y + G_L)^2 + (B_{tot_s} + B_L)^2}}{Y_M} V_s \tag{8.14}$$

By introducting (8.14) in the expression (8.12), the efficiency becomes

$$\eta = \frac{G_L}{G_p^Y \frac{\sqrt{(G_s^Y + G_L)^2 + (B_{tot_s} + B_L)^2}}{Y_M^2} + G_s^Y + G_L} \tag{8.15}$$

For taking full advantage of a given transmission circuit, the transfer efficiency can therefore be maximized by imposing the optimal load conductance G_L^{opt} and susceptance B_L^{opt} so that

$$\frac{\partial \eta}{\partial G_L}(G_L^{opt}, B_L^{opt}) = 0 \text{ and } \frac{\partial \eta}{\partial B_L}(G_L^{opt}, B_L^{opt}) = 0 \tag{8.16}$$

Since this problem demonstrates a perfect analogy with the equivalent problem for the series-series compensated system (see (6.10)), their solutions are also analogous and one has

$$G_L^{opt} = G_s^Y \sqrt{1 + \frac{Y_M^2}{G_p^Y G_s^Y}} \tag{8.17}$$

$$B_L^{opt} = -B_{tot_s} = \frac{1}{\omega L_s^Y} + \frac{1}{\omega L_o} - \omega C_s \tag{8.18}$$

In contrast with the series-series compensated system, one can observe that the optimal load susceptance B_L^{opt} is different from zero when the secondary LC oscillator is tuned in accordance with the conventional practice (*i.e.*, when $\omega = 1/\sqrt{L_s C_s}$).

Ensuring $G_L = G_L^{opt}$ and $B_L = B_L^{opt}$ guarantees to operate the system at its maximum physically achievable efficiency η_{max}, which is imposed by the design of the LC circuits only and given by

$$\eta_{max} = \frac{Y_M^2}{G_p^Y G_s^Y \left(1 + \sqrt{1 + \frac{Y_M^2}{G_p^Y G_s^Y}}\right)^2} \tag{8.19}$$

8.1.3 Methodology for the system optimal command

The methodology consists in determining the source currents $\underline{I}_i^N$ and $\underline{I}_o^N$ ensuring simultaneously the maximization of the power efficiency and the setting of the output power.

Maximization of the power efficiency

According to the developments above, the system achieves its maximum achievable efficiency when the equivalent conductance and susceptance seen from the secondary oscillator terminals are respectively equal to G_L^{opt} and to B_L^{opt}. Therefore, the mathematical condition for the system to achieve the maximum efficiency is written as

$$\underline{\mathrm{I}}_o^N = -(G_L^{opt} + jB_L^{opt})\underline{\mathrm{V}}_s \tag{8.20}$$

By eliminating the secondary voltage using (8.10) in (8.20), the condition becomes

$$-\underline{\mathrm{Y}}_M(G_L^{opt} + jB_L^{opt})\underline{\mathrm{I}}_i^N + (\underline{\mathrm{Y}}_p\underline{\mathrm{Y}}_s - \underline{\mathrm{Y}}_M^2 + G_L^{opt}\underline{\mathrm{Y}}_p + jB_L^{opt}\underline{\mathrm{Y}}_p)\underline{\mathrm{I}}_o^N = 0 \tag{8.21}$$

which is the first equation linking the complex unknowns $\underline{\mathrm{I}}_i^N$ and $\underline{\mathrm{I}}_o^N$. However, the definition of another equation is mandatory for creating a solvable system of complex equations allowing to determine these unknowns. As for the series-series compensated system, this additional equation is associated with the setting of the required output power.

Setting of the output power

Achieving a reference output power P_{ref} to the load is accomplished by setting adequately the module of the secondary voltage. Assuming that condition (8.21) is achieved, the real part of the equivalent load admittance is equal to G_L^{opt} so that a power P_{ref} is transmitted to the load when

$$V_s = \sqrt{\frac{P_{ref}}{G_L^{opt}}} \tag{8.22}$$

The secondary voltage $\underline{\mathrm{V}}_s$ is chosen as a phase reference and the complex condition for producing a reference output power P_{ref} becomes

$$\underline{\mathrm{V}}_s = \sqrt{\frac{P_{ref}}{G_L^{opt}}} \tag{8.23}$$

Using (8.11) and (8.23), this condition is expressed in terms of currents $\underline{\mathrm{I}}_i^N$ and $\underline{\mathrm{I}}_o^N$ as

$$-\underline{\mathrm{Y}}_M\underline{\mathrm{I}}_i^N + \underline{\mathrm{Y}}_p\underline{\mathrm{I}}_o^N = (\underline{\mathrm{Y}}_p\underline{\mathrm{Y}}_s - \underline{\mathrm{Y}}_M^2)\sqrt{\frac{P_{ref}}{G_L^{opt}}} \tag{8.24}$$

which is a second equation linking the pursued currents. Finally, the desired operating point is reached by imposing the current $\underline{\mathrm{I}}_i^N$ and $\underline{\mathrm{I}}_o^N$ solving equations (8.21) and (8.24).

8.1.4 Illustration of the method beneficial effects

As for the series-series compensated system, the main principle of the proposed methodology is illustrated on the EV test-case employed previously via a first-harmonic analysis performed on the equivalent circuit from Figure 8.4 in the Matlab environment. The nominal circuit parameters of the test-case are reminded in Table 8.1.

f	$R_p = R_s$	$L_p = L_s$	M
85 kHz	176 mΩ	109 μH	13.3 μH

Table 8.1: Nominal parameters of the test-case circuit

For applying the proposed methodology, these parameters are converted for corresponding to the parameters intervening in the description of the admittance-based model. The related parallel-equivalent nominal parameters are reported in Table 1.2. In other existing works, the resonant capacitances C_p and C_s are usually designed for ringing with the series self-inductances L_p and L_s at the operating frequency, even in the case of parallel-parallel compensation. However, the series self-inductance and the parallel self-inductance values are different, and filtering inductances are present on each side of the circuit, influencing the reactive power flow. Therefore, the capacitances values must be adapted to this situation for ensuring the passive cancellation of both sides susceptance at its nominal operation point. These values have to be such that

$$\omega = \frac{1}{\sqrt{L_{tot_p} C_p}} \quad \text{with } L_{tot_p} = \frac{L_p^Y L_i}{L_p^Y + L_i} \tag{8.25}$$

$$\omega = \frac{1}{\sqrt{L_{tot_s} C_s}} \quad \text{with } L_{tot_s} = \frac{L_s^Y L_o}{L_s^Y + L_o} \tag{8.26}$$

The values of the filtering inductances are the result of a compromise between their impact on the WPT system operation (as a small value would deviate a large portion of the source currents $\underline{I}_i^N$ and $\underline{I}_o^N$ in the filtering inductance, referring to the equivalent circuit on Figure 8.4) and the voltages $\underline{V}_i$ and $\underline{V}_o$ which have to be produced by the converters (as a large inductance value would imply a high voltage for producing the required source currents $\underline{I}_i^N$ and $\underline{I}_o^N$). With this in mind, the filtering inductance L_i and L_o are chosen as equal to the series self-inductance L_p and L_s, respectively. For the considered test-case, this yields $L_i = L_o = 109\mu$H.

f	$G_p^Y = G_s^Y$	$L_p^Y = L_s^Y$	$C_p = C_s$	$\underline{Y}_M$
85 kHz	54.3 μS	107.4 μH	64.9 nF	2.1 $e^{-j90.35°}$ mS

Table 1.2: Parallel-equivalent nominal parameters of the test-case circuit

The system is expected to supply a reference output power $P_{ref} = 3.7$ kW to the load. One again, for comparison purposes, the performances afforded by the proposed system are contrasted with the performances of an equivalent passive system, comprising a diode rectifier for interfacing the secondary circuit with the actual load. The secondary filtering inductance L_o is not needed in such a circuit and is consequently removed. As a consequence, the secondary resonant capacitance of the passive system is compensating the inductance L_s^Y (*i.e.*, $C_s = 32.6$ nF for the passive system). Also, its output power is kept constant for each investigated situation by adapting its primary source current, for a fairer comparison. In the passive system, the cascading of the diode rectifier with the battery is represented by the equivalent resistance computed in section 6.2.4 and given by

$$R_L^{pas} = \frac{8}{\pi^2} \frac{V_b^2}{P_{ref}} = 28.40\ \Omega \tag{6.20}$$

Alternatively and for a better adequacy with the admittance-based model, the corresponding conductance G_L^{pas} is equal to

$$G_L^{pas} = \frac{1}{R_L^{pas}} = 35.2 \text{ mS} \tag{8.27}$$

The optimal load admittance $\underline{Y}_L^{opt}$ corresponding to the test-case nominal parameters is a pure conductance, as B_L^{opt} is null since the secondary capacitance compensate *per se* the inductive components in the circuit. One has

$$\underline{Y}_L^{opt} = G_L^{opt} = 2.1 \text{ mS} \tag{8.28}$$

and the proposed system produces a power efficiency of 95.05 %, which is the maximum achievable efficiency. Due to the difference between the optimal load conductance G_L^{opt} and the equivalent load conductance G_L^{pas}, the passive system delivers a power efficiency of 70.2 %. The weakness of the passive system power efficiency is due to the fact that such a small apparent load resistance (or such a high apparent load conductance) is not well adapted for a parallel compensation on the secondary side. Nevertheless, the relevance of this comparison is not depreciated since the proposed PP-RDAB system operates in the same conditions and still guarantees the maximum achievable efficiency. One can note the weakness of the difference between the optimal efficiency of 95.05 % obtained by neglecting the mutual conductance in the developments and the theoretical maximum achievable efficiency, which is 95.2 % (as demonstrated for series-series compensated systems). Moreover, the mutual conductance impact is decreasing with the mutual inductance M so that this error of 0.15 % efficiency is the highest for the system operating range (as only a decrease of the mutual inductance is possible).

Hereafter, we propose a detailed comparison between the proposed PP-RDAB and the passive systems when the circuit parameters deviate from their nominal values.

Variation of the mutual inductance M

Despite the transition from an impedance-based to an admittance-based model, the mutual inductance M remains the most appropriate parameter (from a physical point of view) for quantifying the quality of the windings coupling. The effect of a coupling deterioration is addressed here via the decreasing of the mutual inductance M. A modification of the mutual inductance M produces logically a variation of the mutual admittance $\underline{Y}_M$, but also a variation of the equivalent conductances G_p^Y and G_s^Y and of the equivalent inductances L_p^Y and L_s^Y. Therefore and in contrast with a series-series compensated system, the windings coupling influences both the active and the reactive power flows in the system and modifies the optimal value of both the apparent load conductance G_L^{opt} and susceptance B_L^{opt}.

By starting from the reference point indicated in Table 1.2, a relative variation of the mutual inductance down to -90 % is considered. The corresponding evolutions of the power efficiency are shown in Figure 8.5 and compared to the maximum achievable efficiency. From the results, one can note that the proposed method is effective and adapts both the conductance and the susceptance of the apparent load for reaching constantly the maximum achievable efficiency, which decreases slowly as M declines. Similarly to the case of a series-series compensated system, the equivalent passive system is clearly more impacted by the coupling, with a collapsing efficiency as M decreases.

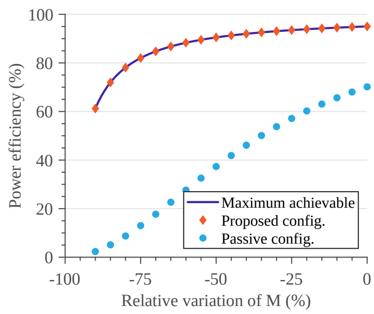

Figure 8.5: Evolutions of the power efficiency with respect to a decrease of M for the proposed and the passive systems

The multiplicity of the influences of an M variation on the active and reactive power flows makes the detailed illustration of the method action via the voltages and currents phasors delicate. Nevertheless, the aggregate effect of those different influences on a passive system and the consequent global action of the PP-RDAB system are shown hereafter.

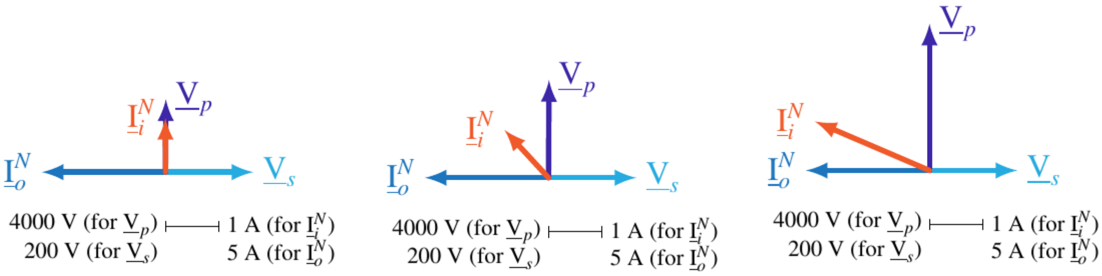

(a) 0 % (nominal) (b) -25 % (c) - 50 %

Figure 8.6: Representation of the voltages and currents phasors for different relative variations of M impacting the passive system

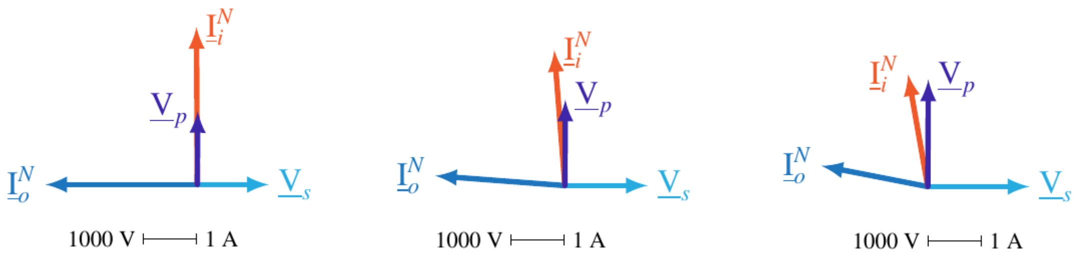

(a) 0 % (nominal) (b) -25 % (c) - 50 %

Figure 8.7: Representation of the voltages and currents phasors for different relative variations of M impacting the proposed system

For the passive configuration, a decline in M causes the surge of the primary voltage $\underline{V}_p$ since the system has to achieve a constant output power despite harsher coupling conditions. Also, the perturbation of both the primary and the secondary reactive power flows result in a large phase shift between the primary current $\underline{I}_i^N$ and voltage $\underline{V}_p$. As a consequence, the current $\underline{I}_o^N$ increases for maintaining a constant output power. The aforementioned inadequacy of the passive system with respect to the secondary parallel compensation is highlighted by the prominence of the related primary voltage amplitude. By performing active rectification, the proposed configuration takes action for optimally distributing the losses in the system by rebalancing the voltages $\underline{V}_p$ and $\underline{V}_s$. The residual secondary susceptance ensuing from the indirect variation of L_s^Y is compensated by shifting the secondary current $\underline{I}_o^N$ with respect to the secondary voltage $\underline{V}_s$. As a consequence, the phase shift between the primary current $\underline{I}_i^N$ and voltage $\underline{V}_p$ is therefore minimized, but not null. Indeed, the system faces an irremediable residual primary susceptance (ensuing from the indirect variation of L_p^Y) preventing the aligning of $\underline{I}_i^N$ and $\underline{V}_p$.

Variation of the secondary capacitance C_s

As for the series-series compensated system, the variation of the secondary capacitance C_s is addressed for observing the proposed system behavior when it suffers from a secondary detuning. In contrast with the mutual inductance M, a secondary capacitance deviation impacts only the optimal value of the apparent load susceptance B_L^{opt}.

By starting from the reference point indicated in Table 1.2, a relative variation of the mutual inductance down to -90 % is considered. The corresponding evolutions of the power efficiency are shown in Figure 8.8 and compared to the maximum achievable efficiency. One can notice that the proposed system emulates an adequate load susceptance for reaching constantly the maximum achievable efficiency. In contrast, the passive system suffers from an efficiency loss for any C_s variation, as for the series-series compensated configuration.

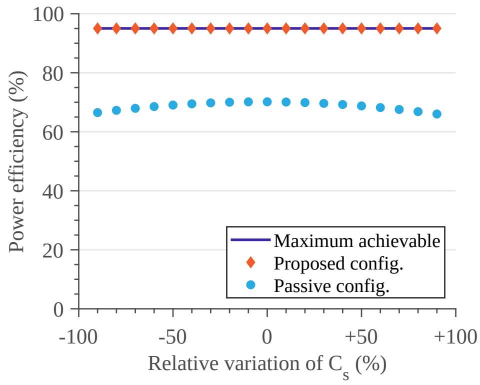

Figure 8.8: Evolutions of the power efficiency with respect to a variation of C_s for the proposed and the passive systems

Since the passive system is already far from an optimal operation in its nominal operation, the additional detrimental effect of a deviation in the capacitance C_s on the power efficiency is tenuous. As a result, the observation of the passive system voltage and current phasors for different deviations of the secondary capacitance C_s is not relevant here. Nonetheless, the impact of a C_s deviation on the passive system corresponds to an increasing phase shift of the primary voltage $\underline{V}_p$ with respect to the primary current $\underline{I}_i^N$. The phasors relative to the proposed configuration are represented in Figure 8.9 for showing the proposed method action for facing a C_s deviation. Facing a similar situation and by performing active rectification, the proposed method shifts adequately the secondary current $\underline{I}_o^N$ which sweeps the voltage $\underline{V}_p$ away until the latter alignment with the primary current $\underline{I}_i^N$. Since the proposed system must ensure a constant apparent load conductance equal to its optimal value, the tip of the phasor $\underline{I}_o^N$ moves perpendicularly to the real axis. The mistuning penalty is therefore displaced from the primary voltage $\underline{V}_p$ to the secondary current $\underline{I}_o^N$, with a consequential rise of the secondary volt-ampere rating. However, both voltages $\underline{V}_p$ and $\underline{V}_s$ are back in their nominal position so that the detrimental impact of a C_s variation on the system losses (via the conductances) and efficiency is fully compensated.

Before presenting the time-domain implementation of the PP-RDAB system, the operation of the latter in absence of secondary resonant capacitor is addressed. Indeed, the method has been developed for compensating any variation in the secondary capacitance C_s. Notably, the system is able to ensure the optimal performances when C_s is decreasing to zero. However, the reactance of the secondary resonant capacitor tends to infinity as C_s declines and the secondary capacitor behaves more and more as an open-circuit, so that the resultant situation is equivalent to a situation where the secondary circuit is freed from any resonant capacitor. Such a case is investigated and the corresponding phasors are represented in Figure 8.10. One can observe that the PP-RDAB system emulates a capacitive function compensating entirely the reactive power consumed by both the equivalent secondary self-inductance and the sec-

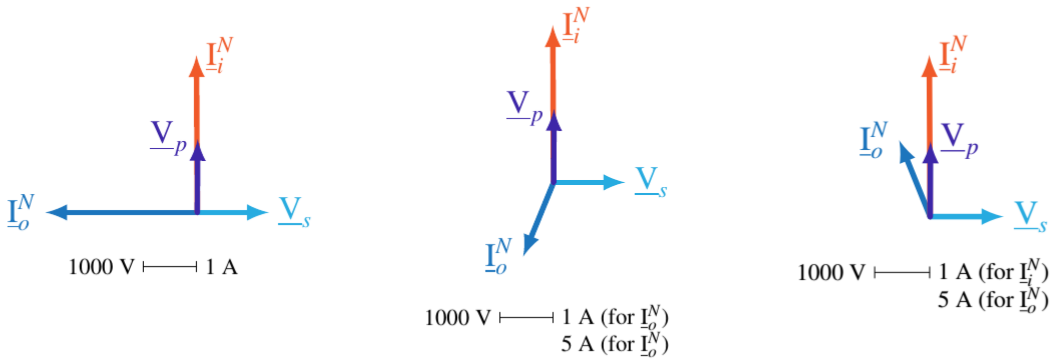

(a) 0 % (nominal) (b) - 15 % (c) + 15 %

Figure 8.9: Representation of the voltages and currents phasors for different relative variations of C_s impacting the proposed system

ondary filtering inductance L_o. Since the system must sustain the rated output power, the secondary current $\underline{I}_o^N$ increases significantly. Nonetheless, the system maintains its efficiency to the optimal value of 95.05 % despite the absence of any secondary capacitor, while the passive system efficiency falls down to 65.7 % (exactly as with a series-series compensation scheme).

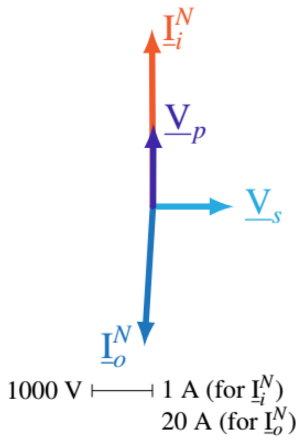

Figure 8.10: Representation of the voltages and currents phasors for the proposed system with a capacitor-free secondary

8.1.5 Time-domain implementation of the voltage-source converters

As for the SS-RDAB, the methodology related to the PP-RDAB has been developed and illustrated considering ideal and sinusoidal voltage sources. In this section, the actual voltage-source converters shown in Figure 8.1 and the related pulse-width modulation (PWM) commands are practically implemented in a realistic time-domain model running under the *PSIM* software. Consistently, the WPT test-case described in Table 8.1 is anew considered. The time-step is fixed to 10^{-8} second. Ideal MOSFETs have been selected as switches. The DC voltage V_u and V_b are fixed to 360 V. For each operating point, the primary (respectively, the secondary) full-bridge is controlled following an SVC-based command in such a way that the fundamental of the produced AC voltage is equal to the optimal value of $\underline{V}_i$ (respectively, $\underline{V}_o$), corresponding equivalent Thevenin voltage of the optimal current $\underline{I}_i^N$ (respectively, $\underline{I}_o^N$) which itself ensues from the resolution of the equations (8.21) and (8.24).

Variations of the mutual inductance M (from -90 % to 0 % by steps of 5 %) are applied to the system and the corresponding time-domain results are compared to target operating points computed in the frequency domain (see Figure 8.11). The effectiveness of the proposed methodology in the time-domain is demonstrated, with only however an relative error of 1.75 % on the output power for the most severe decrease of M.

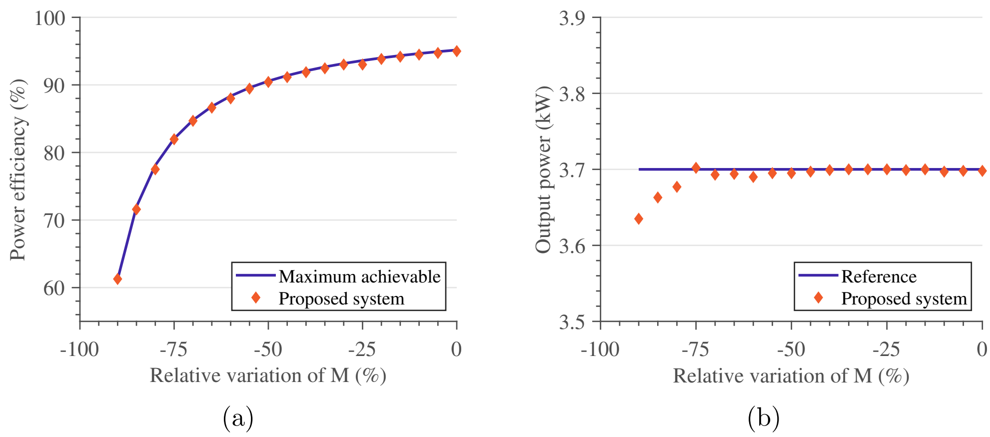

Figure 8.11: Simulated measurement of the (a) power efficiency and of the (b) output power for deviations of M impacting the proposed system

The variation of the secondary capacitance C_s is addressed differently. As a matter of fact, the analysis realized in the previous section demonstrates that a variation of the secondary capacitance requires that the system increases the Norton current $\underline{I}_o^N$ and therefore the fundamental voltage $\underline{V}_o$ which has to be produced by the secondary converter. As a result, the PP-RDAB system is confronted to controllability restrictions associated with the limited voltage producible by the secondary converter, analogously to those raised, addressed and solved via voltage step-up solutions in the case of the SS-RDAB system. The analysis of the voltage v_o required for compensating variations of C_s demonstrates that the PP-RDAB system is only able to compensate C_s deviations from -10 % to +10 % (without any voltage step-up solution). This range is smaller in comparison with the SS-RDAB case due to burden of the additional impedance associated with filtering inductor. The time-domain results corresponding to this deviation range are presented in Figure 8.12 and match clearly the targeted operating points.

The primary converter voltage v_i and current i_i and the secondary converter voltage v_o and current i_o are presented on Figure 8.13. For extending the application scope of the proposed method, the PP-RDAB can be improved by increasing the voltage range of the converters with two-quadrant choppers or by using Z-source topologies for the converters, as previously addressed for the analogous series-series compensated system. Since the implementation of such solutions is independent from the transmission circuit topology itself, these solutions are not anew discussed for non-redundancy purposes.

These results ascertain the effectiveness of the extension of the proposed optimal command methodology to a parallel-parallel compensation topology.

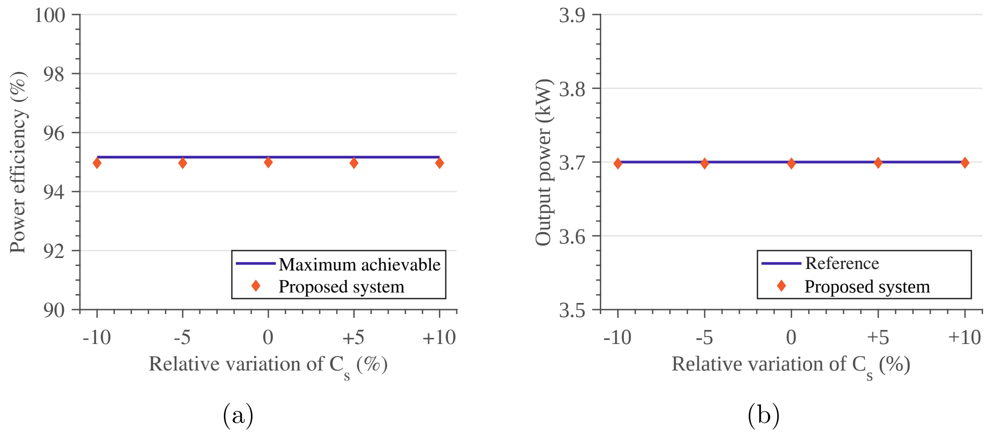

Figure 8.12: Simulated measurement of the (a) power efficiency and of the (b) output power for deviations of C_s impacting the proposed system

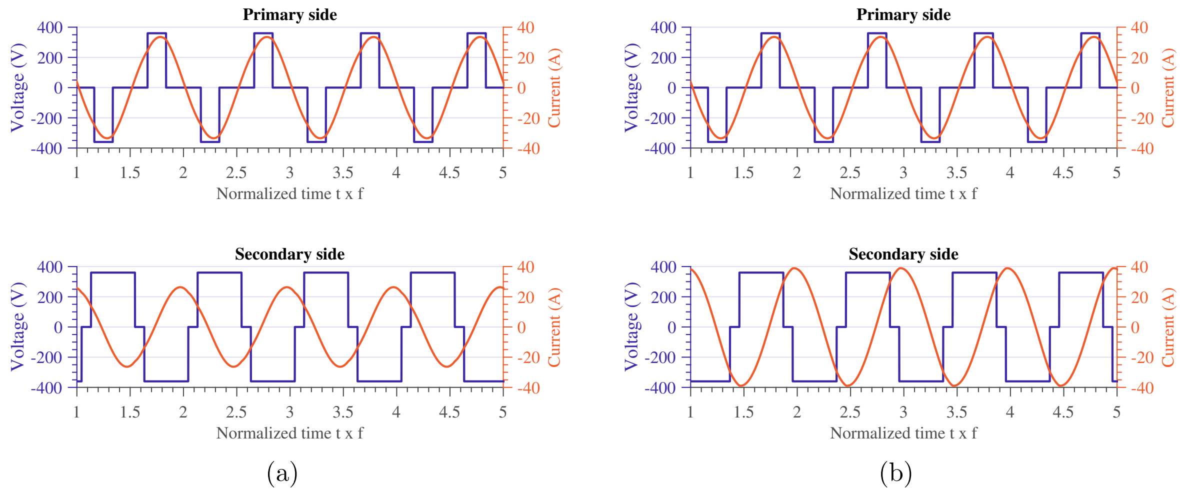

Figure 8.13: Simulated primary (up) and secondary (down) converters waveforms in the proposed system for (a) -10 % and (b) +10 % C_s deviation impacting the proposed system

8.2 Further extensions to other topologies

Following the procedure presented for the parallel-parallel compensated system, the proposed methodology can be extended to the series-parallel and to the parallel-series compensation schemes. As for the parallel-parallel configuration, the mutual inductance model of the coupled windings is transformed in an equivalent and hybrid impedance/admittance-based model (with series impedances and voltage source on the series-compensated side and with parallel admittances and current source on the parallel-compensated side). For avoiding any redundancy, the developments relative to those topologies are presented in Appendix C.

8.3 Conclusions

The extension of the proposed optimal command to parallel-parallel compensation schemes has been presented in this chapter. For conserving the elegant and intuitive formalism yielded by the the impedance-based equivalent circuit of an SS-RDAB system, a particular attention has been paid to the transformation of the equivalent circuit of a PP-RDAB system in an admittance-based model which is the perfect dual of the former.

Considering the EV test-case addressed previously, the extended method has been in turn illustrated and interpreted in the frequency domain. Larger and distinctive impacts of a mutual inductance variation have been observed, in comparison with a series-series compensated system. As for its series-series analogue, the FHA-based methodology has been validated via the time-domain simulation of the related power conversion chain. The parallel-parallel compensated system has demonstrated more critical controllability restrictions with respect to the active rectifier voltage range. However, these restrictions can be overcome by resorting to the solutions presented in the previous chapter.

Following a similar transformation procedure, the optimal command methodology has further been extended to series-parallel and parallel-series compensation schemes, following the developments available in Appendix C.

CHAPTER

NINE

EXPERIMENTAL PROOF-OF-CONCEPT

Before presenting the general conclusions and perspectives of this thesis, the proposed optimal command methodology is validated via an experimental low-power (*i.e.* 20 W) proof-of-concept, operating at 85 kHz and based on a SS-RDAB topology.

9.1 Technical challenge

As mentioned in the Chapter 1, this thesis pioneers the WPT research activity in the Electrical Power Engineering Unit of the University of Mons and further, the implementation of power electronics solutions in a new and higher frequency-range. Indeed, the customary domain of expertise of the Unit corresponds to the use and to the control of power electronic converters applied to the command and the drive of electrical machines. As a consequence, the available experimental equipment essentially consisted in

- didactic Semikron three-phase full-bridge converters based on insulated gate bipolar transistors (IGBTs), able to attain switching frequency up to typically 20 kHz in hard switching conditions ;

- *DSPACE* DS1103 and DS114 boards as control and measurement interfaces between the power converter and the control algorithm implemented in the *MatLab/Simulink* software environment, presenting sampling frequencies typically between 10 kHz and 15 kHz.

Given the frequency-level required for implementing an effective WPT system via resonant inductive coupling (typically around 100 kHz and precisely 85 kHz here), this experimental proof-of-concept necessarily requires to initiate the development and the elaboration of power converters including switching devices and controlling circuits adapted to this higher frequency range. Consequently, the experimental effort has essentially been focused on the progressive establishment from scratches (notably via different and improved versions) of a correspondent know-how, in parallel to the theoretical contributions presented earlier in this thesis. In this context, the detailed analysis and optimization of the elaborated converter exceed beyond the framework of this thesis. Here, the objective is set to the development of practical (but not always optimal) solutions, adapted to a frequency level of 85 kHz and allowing to prove experimentally the validity of the optimal command of an SS-RDAB system.

9.2 Description of the developed converters

An annotated picture of the current version of the developed high-frequency converter is shown in Figure 9.1. Each side of the resonant WPT system is equipped with such a converter, capable to operate as an inverter for supplying the primary side or an active rectifier for interfacing the secondary side with the DC load. This system is an all-in-one solution embedding a full-bridge converter, a micro-controller, the switches drivers and the power supply for the command circuits on a single printed board circuit. Each part of this system and its main features are briefly addressed below.

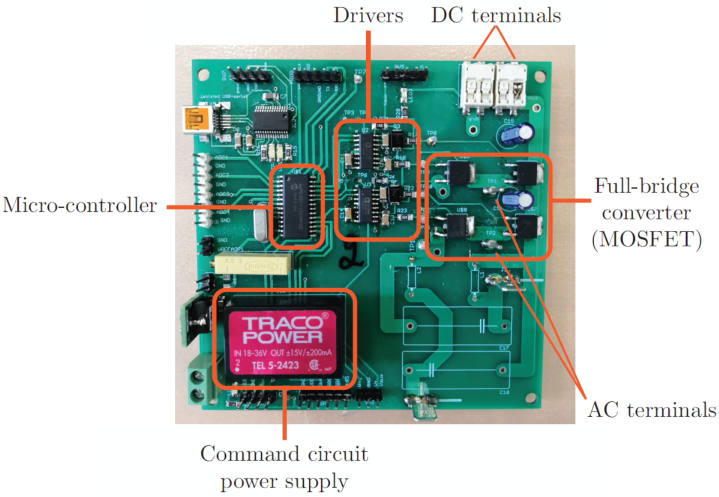

Figure 9.1: Annotated picture of the current version of the developed converter

Full-bridge converter The full-bridge comprises four packages TK55S10N1 integrating each a MOSFET and its anti-parallel diode. This switching device has been selected according to three particular points. Firstly, this transistor high switching speed ensures to mitigate significantly the switching losses, which can therefore be neglected in the following since the latter are not addressed. Secondly, this transistor is able to sustain high drain currents (up to 55 A in DC and 165 A pulsed), which is a practical concern for avoiding any permanent damage during the different test phases, notably when the converter is connected to a resonant circuit. As a matter of fact, the use of series-compensated windings causes the circulation of a resonant current through the converters and therefore through the semiconductor components. These currents can be particularly damaging for the primary-side inverter, as any accidental decoupling of the load causes the quasi-shorting of the inverter output, the latter supplying an LC-oscillator excited at its resonant frequency. Finally, this transistor presents a low drain-source resistance during its on-state (usually referred as the $R_{DS,on}$ resistance) corresponding to 5.5 mΩ, for reducing the conduction losses and the voltage drops despite the relatively high intensity of the resonant currents.

Micro-controller The converter is controlled by a *dsPIC* (for digital signal Peripheral Interface Controller) 70 MHz micro-controller (Microchip dsPIC33EV256GM102), which computes and generates the PWM command 5 V signals destined to control the state of the switches, via the drivers (see hereafter). This embedded controller is highly suitable for the control of power electronic converters, as it disposes of PWM modules programmable via a code in *C*. It enables the generation of three different pairs of complementary PWM signals (among which only two are employed here, one for each leg of the full-bridge converter). In the context of this proof-of-concept, the open-loop command of the SS-RDAB system is effected by programming separately the PWM module of each converter in order to implement the SVC-command producing the respective fundamental voltage derived from the first-harmonic methodology exposed in the Chapter 6. The introduction of dead times (which consist in small time intervals between a switch turn-off and the turn-on of the switch belonging to the same leg, for avoiding any shorting risk) is supported automatically by the PWM modules. Regarding the importance of the precise setting of the phase shift between the primary and the secondary voltages in the proposed optimal command, the PWM module of the secondary converter is synchronized with a clock signal emitted by the primary converter. Here, this signal is transmitted via a wired connection, as the elaboration of a wireless protocol for this data transmission lies out of the scope of this thesis. In anticipation of an eventual closed-loop control, the dsPIC micro-controller disposes of analog-to-digital converters valuable for the eventual feedback measurements.

Drivers The drivers are two identical circuits destined to convert the logic 5 V PWM signals generated by the dsPIC micro-controller into a PWM voltage with crenels surpassing the gate threshold voltage of the switches (comprised between 4 V and 20 V) in order to command their turn on and turn off. A driver is dedicated to each leg and supports the generation of the gate voltage for the two switches belonging to a same leg. In the proposed assembly, the drivers are the Analog Devices ADuM3223, which have been chosen for their speed (as they are able to generate PWM voltage with frequency up to 1 MHz) and for further extension purposes. Instead of presenting a single logic inputs for generating complementary gate voltages for the switches in a same leg, this driver disposes of two different inputs (one for each switch) and enables the independent command of each switch, with the possibility to command the shorting of the legs and further the introduction of shoot-through states in the extension (as a future perspective of this thesis) of the current design to a Z-source topology. One may notice in passing the presence of an alternate DC bus with slots destined to receive a Z-source impedance network on the bottom left of the converter in Figure 9.1.

9.3 Design of the windings

The planar windings employed in this experimental proof-of-concept are designed by using the virtual laboratory developed in the first part of this thesis, embedded in a simple procedure for maximizing the windings figure-of-merit (FOM) under practical constraints. The global requirements for this transmission system have been established for ensuring a high-efficiency transmission (*i.e.*, with a power efficiency equal or higher than 90 %) at a 5-cm range, while restricting each winding external diameter to a maximal value of 15 cm. In this context, the coils design depends on four parameters which are the windings common wire radius r, inner radius R, number of turns N and spacing p between two adjacent turns (*i.e.* the pitch of the windings).

The section of the wire has been fixed to 4 mm^2 (corresponding to a wire radius of 1.13 mm) since it has been observed that the optimization procedure will logically and systematically foster the maximum wire section when it is left free to vary as a decision variable, for the respective winding parasitic resistance. As single strand solid wires are considered, the section of 4 mm^2 is chosen as a compromise between a sufficiently large conducting section (for reducing each winding resistance) and a practicable rigidity for the wire, as a high rigidity can be disabling for the practical and precise winding process. Also, due to the complexity associated with the practical realization of an exact spacing between the turns, the latter are clamped and the effective spacing between two copper conductors corresponds to twice the insulation sleeve of the wire, *i.e.* 1.3 mm in this case. From these practical constraints, only two parameters (*i.e.*, the number of turns N and the inner radius R) are left free to vary as decision variables in the optimization process.

Finally, preliminary investigations have demonstrated that for a restricted external footprint, the FOM is maximal when the windings turns are expanded at most so that the latter are accumulated near the maximal external diameter of 15 cm. Therefore, by considering the aforementioned practical constraints as well as such a tendency, the windings inner radius R and the number of turns N are not independent parameters as they are linked by the maximal external radius R_e^{max}, the fixed wire radius $r = 1.13$ mm and the fixed spacing between the turn $p = 1.13$ mm, with

$$R_e^{max} = R + N \cdot (2r + p) \tag{9.1}$$

Therefore, the number of turns N is chosen as the unique decision variable in this design procedure, considering the discussion above. The design procedure consisted in the progressive increase of the number of turn(s) from 1 to the maximum number of turns fitting in the restricted radial footprint R_e^{max}. For each number of turns, the *Matlab*-driven version of the 2-D finite-element model developed in the first part of this thesis is employed for determining the FOM of the related windings. Since the operating frequency is constant and equal to 85 kHz, the FOM is only depending on the ratio between the mutual inductance of the winding and their parasitic resistance. Whereas the mutual inductance increases and progressively saturates with the rising number of turns, this effect is mitigated by the concomitant expansion of the windings parasitic resistance (see Figure 9.2). As a result, an optimal number of turns representing an optimal balance between these two contradictory contributions can be determined. In this case, the optimal number of turns is equal to 10 and the correspondent couple of windings presents a FOM of 20.19, yielding a maximum achievable efficiency of 90.6 %. In summary, these windings presents an inner radius R of 39 mm and are made of 10 turns separated by 1.3 mm and of a wire with a 4 mm^2 section. Their self-inductance is equal to 14 μH, their parasitic resistance is equal to 82 mΩ and their mutual inductance is worth 3.1 μH. A picture of the corresponding windings mounted on a their respective wooden stand is presented in Figure 9.3.

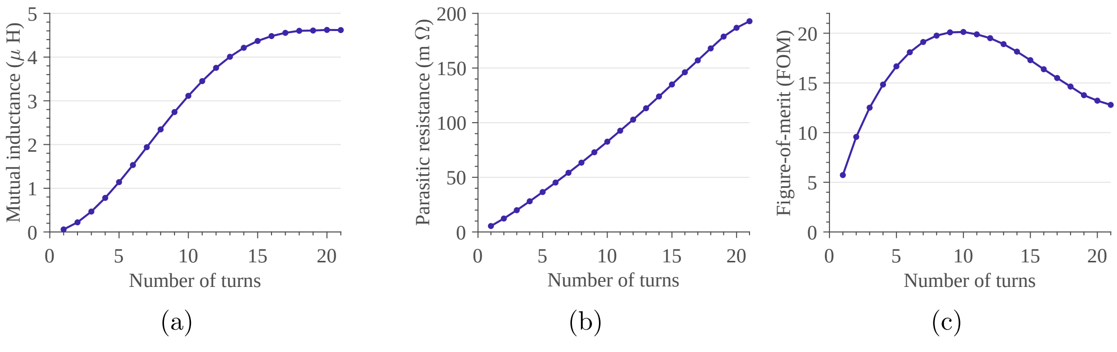

Figure 9.2: Evolutions of the windings (a) mutual inductance, (b) parasitic resistances and (c) FOM with respect to the number of turns

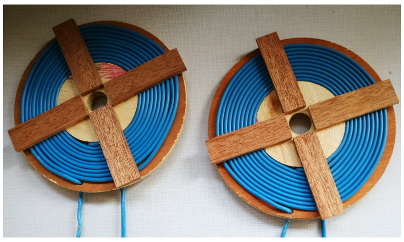

Figure 9.3: Picture of the couple of planar windings designed and employed for the experimental proof-of-concept

9.4 Experimental SS-RDAB system and results

Based on the converters and on the windings described in the previous sections, the experimental setup and its equivalent circuit schematic are shown in Figure 9.4 and 9.5, respectively. The system is intended to operate at a frequency of 85 kHz and to furnish a rated power of P_{ref} = 20 W to a DC load. The primary inverter is supplied by the utility with an adjustable DC voltage V_u (thanks to a system of autotransformer upstream to the input rectifier) fixed to 10 V here. This inverter drives the resonant inductive transmission system with an 85 kHz SVC-based AC voltage v_p. The transmission circuit itself is composed of two windings maintained aligned by a non-magnetic rod and separated by 5 cm. Each winding is connected in series with a resonant capacitor of 250 nF, for building two coupled LC-oscillators presenting a common self-resonant frequency matching the operating frequency of 85 kHz. The secondary side LC-oscillator is connected to an active rectifier, which modulates the apparent load impedance according to the method proposed in Chapter 6 by controlling the voltage v_s on its AC-side. On its DC-side, the power is ultimately transferred to a DC load consisting in a resistance R of 15 Ω connected in parallel with a filtering capacitor of 2.2 mF. The ouput voltage V_o is fixed by the power consumed by the load, with $V_o = \sqrt{P_{ref} \cdot R} = 17.32$ V.

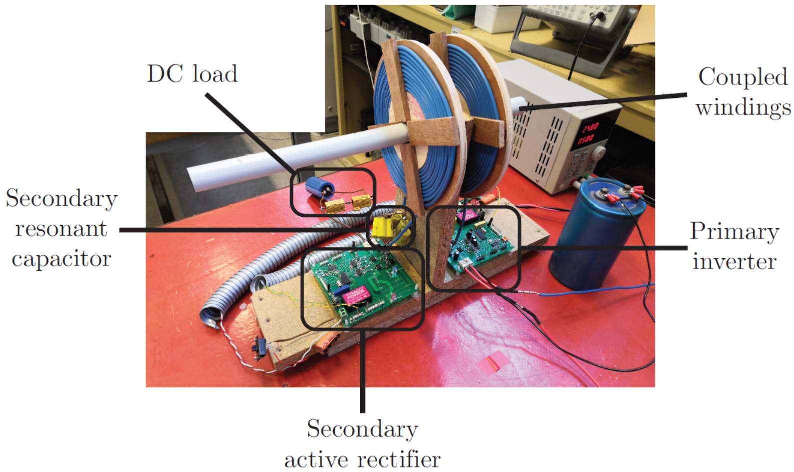

Figure 9.4: Picture of the experimental setup employed for the experimental proof-of-concept

For driving the system in open-loop, the optimal command developed in Chapter 6 is applied for obtaining the system optimal operating point, expressed in terms of the fundamental voltages which have to be produced by each converter. Both are controlled accordingly using an SVC-command programmed manually for each situation tackled in the following and implemented by the micro-controller and the switching drivers. The lumped parameters of

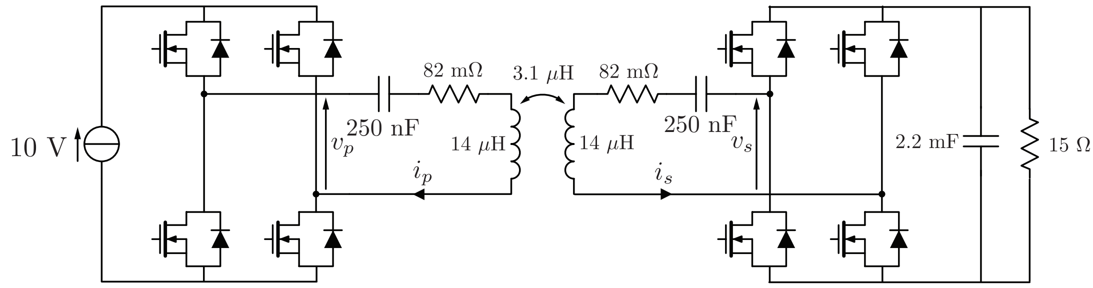

Figure 9.5: Equivalent circuit schematic of the experimental setup

the windings serving as input data for the computation of this optimal operating point are ensuing exclusively from the virtual laboratory developed in Chapter 4.

In the following, two different types of situations are considered. Firstly, the experimental system is tested for different values of the mutual inductance (starting from the nominal value to decreased value) in order to validate its capability to optimize the active power flow via the modulation of the apparent load resistance. Secondly, the experimental system is tested with a secondary devoid of resonant capacitor in order to validate its capability to optimize the reactive power flow by emulating an apparent load reactance compensating integrally the secondary winding self-inductance. For each situation, the experimental results are compared with the time-domain simulations of an equivalent passive system on the one hand (for easing the visualization of the proposed system benefits) and of the proposed system on the other hand (for validating the experimental implementation itself). As a reminder, the equivalent passive system is a system equipped with a passive diode rectifier and of which the primary voltage is adapted in order to achieve the rated output power in any situation, for a fairer comparison with the proposed system.

Finally, one can note that since the losses in the converters have not been addressed here and as the proposed optimal command methodology is based on the maximization of the transmission power efficiency, the performances of the system are evaluated by measuring and comparing the active power value on the respective AC terminals of the converters.

9.4.1 Nominal operation

The nominal operation corresponds to the situation where the windings are separated by the nominal distance of 5 cm and are compensated correctly by the resonant capacitor. Even in such situation, the proposed system is intended to present improved performances in comparison with a passive system. As a matter of fact, it is intended to adapt the apparent load resistance seen from the secondary LC-oscillator terminals (based on the values of the mutual inductance and of the parasitic resistances) for minimizing the losses by balancing the current between the primary and the secondary sides of the circuit. The corresponding experimental results (consisting in the measurements of the primary and secondary voltages and currents) are presented and compared to the time-domain simulations in Figure 9.6.

In this configuration, the passive system displays a power efficiency of 71.7 %, which is relatively low for a resonant inductive operation in such a close range due to the imbalance in the currents amplitude between the primary and the secondary sides of the system, with peak values of 13.16 A for the primary current and of 2.18 A for the secondary current. According to the time-domain simulation, the proposed system furnishes the rated power with a power efficiency of 90.6 % and produces peak currents amounting to 5.33 A on the primary side and 5.24 A on the secondary side. The currents in the experimental setup are respectively amounting to 5.76 A on the primary side and 5.44 A on the secondary side and demonstrate the adequate action of this proof-of-concept. On a more qualitative point of view, one can ascertain the comparability of the simulation and the experimental results. The experimental output power and efficiency are computed in post-processing via a numerical integration process which estimates the output power to 20.8 W and the power efficiency to 89.3 %. In the light of the foregoing, the concept proposed for the optimal command of an SS-RDAB system is proved experimentally. Before considering the following testing configurations, one can notice that the proximity between the simulated and experimental results are also validating anew the accuracy of the virtual laboratory, since the system is commanded in open-loop, based solely on the electrical parameters extracted from the finite-element simulation tool.

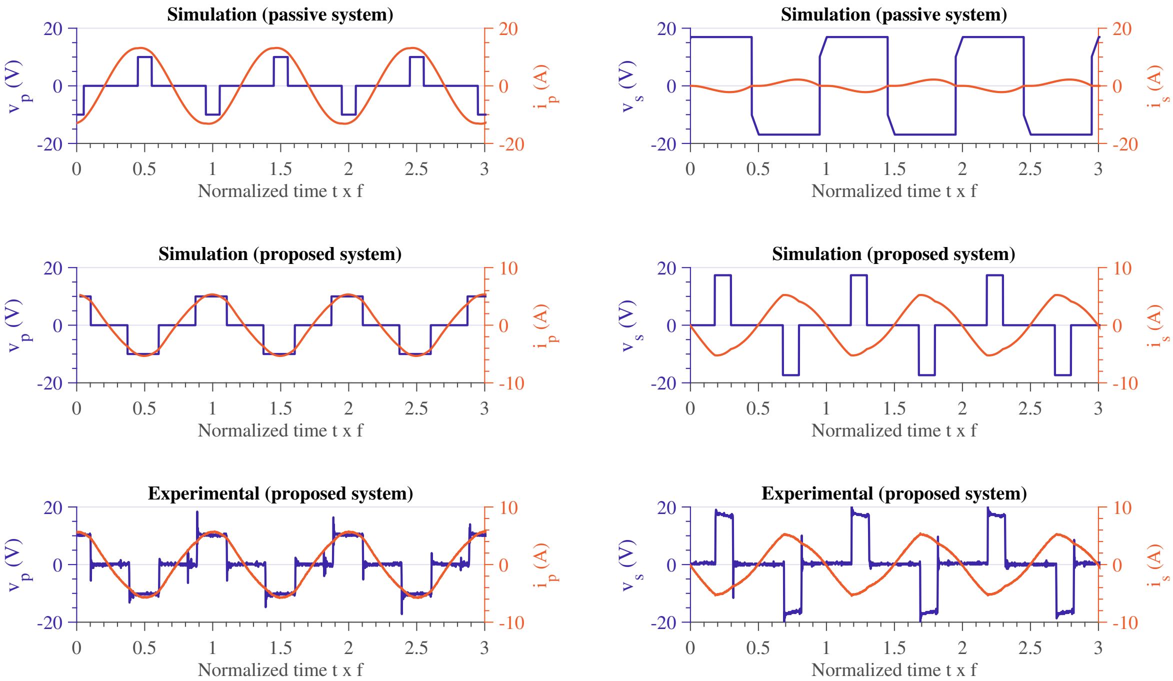

(a) Primary side

(b) Secondary side

Figure 9.6: Waveforms from the passive (up) and the proposed (middle) systems simulations and from the experimental measurements (down) for the nominal position of the coils

9.4.2 Decreasing of the mutual inductance

The case of a mutual inductance decrease is addressed by increasing the separation distance between the aligned windings from 5 cm to 7 cm, and further to 9 cm. Using the finite-element virtual laboratory, the mutual inductance for these two new relative positions of the windings are obtained, with a value of 1.85 μH for a 7-cm distance (corresponding to a relative variation of -38 % in comparison with to the nominal mutual inductance) and a value of 1.19 μH for a 9-cm distance (corresponding to a relative variation of -60 % in comparison with the mutual inductance). For each situation, the proposed system is intended to adapt adequately the primary and the secondary voltage for maintaining a unitary ratio between the primary and the secondary windings and minimizing hence the losses in the windings. The corresponding experimental results are presented and compared to simulation results in Figures 9.7 and 9.8.

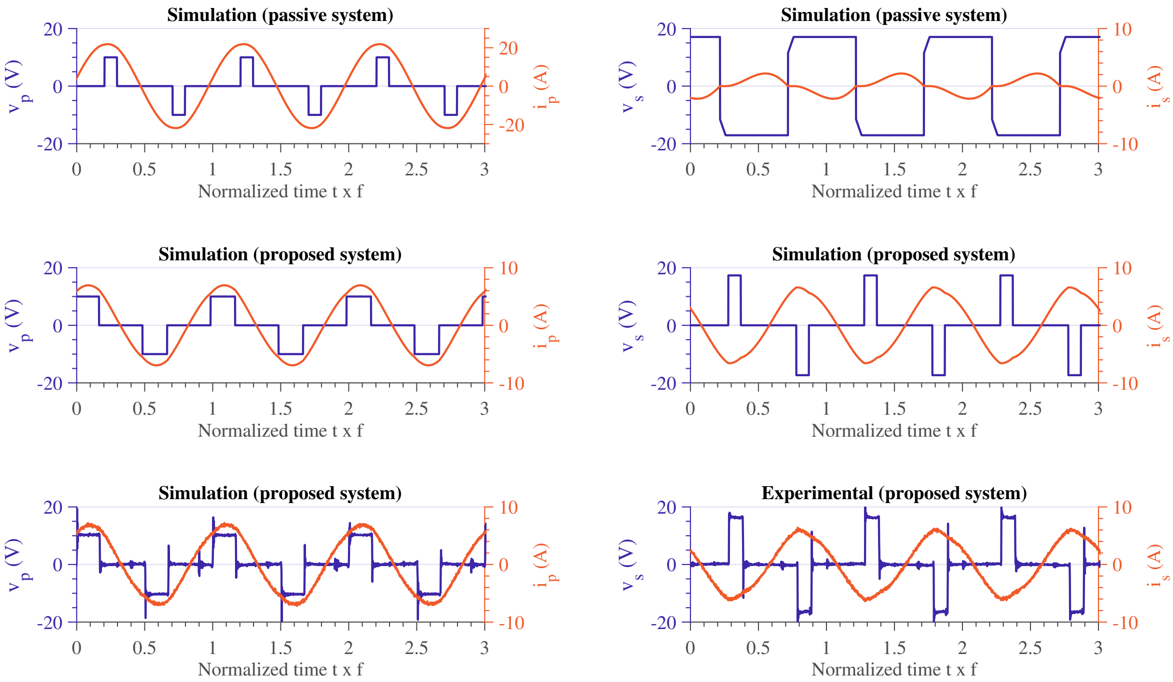

(a) Primary side (b) Secondary side

Figure 9.7: Waveforms from the passive (up) and the proposed (middle) systems simulations and from the experimental measurements (down) for a -38 % deviation of M

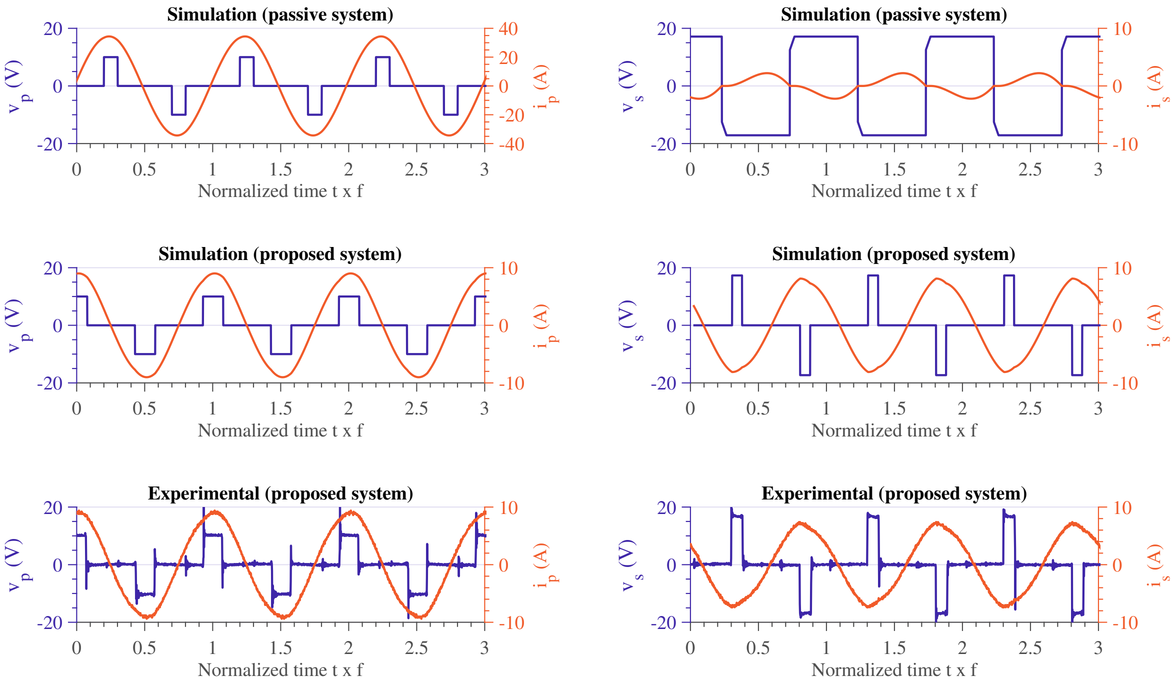

(a) Primary side (b) Secondary side

Figure 9.8: Waveforms from the passive (up) and the proposed (middle) systems simulations and from the experimental measurements (down) for a -60 % deviation of M

In theses configurations, the equivalent passive system suffers from a surge of the primary current with peak values up to 21.88 A (for a 7-cm separation distance) and 34.38 A (for a 9-cm separation distance) and a consecutive decrease in the power efficiency, equal to 46.3 % in the first case and to 28.8 % in the second case. For its part, the secondary current remains unchanged as the apparent load consumes the same rated power. According to the time-domain simulation, the proposed system furnishes the rated power with a power efficiency of 84.9 % in the first case and of 77.6 % in the second case. As it can be observed on the presented currents waveforms from the simulation results and the matching experimental results, the proposed methodology effects on the primary and secondary voltage for maintaining an optimal repartition between the primary and the secondary current. For a 7-cm separation distance, the proposed system is intended, according to the time-domain simulation, to present peak currents amounting to 6.95 A on the primary side and to 6.58 A on the secondary side. According to the corresponding experimental results, the practical setup presents a primary and a secondary currents amounting to 7.2 A and 6.4 A, respectively. The experimental output power and efficiency are anew computed via a numerical post-processing and are worth 18.95 W and 83.9 %, respectively. For a 9-cm separation distance, the proposed system is intended, according to the time-domain simulation, to present peak currents amounting to 9 A on the primary side and to 8.11 A on the secondary side. According to the corresponding experimental results, the practical setup presents a primary and a secondary currents amounting to 9.4 A and 7.6 A, respectively. The experimental output power and efficiency computed via a numerical post-processing are worth 19.6 W and 78.6 %[1], respectively. One can ascertain the comparability of the simulated and the experimental results. Notably, the experimental system demonstrates its faculty to maintain as best as possible, by adjusting the equivalent load resistance, a quasi unitary ratio between the amplitude of the primary and the secondary currents for minimizing the losses. Once again, the concept of the optimal command of an SS-RDAB system experiencing coupling variations is proven experimentally.

9.4.3 Emulation of the secondary capacitance

For validating experimentally the ability of the system to optimize the reactive power flow in the system via active rectification, the system is anew considered in its nominal configuration (with a 5-cm separation distance), but the secondary resonant capacitor is removed from the circuit and the secondary winding is directly connected to the AC-side terminals of the active rectifier. As highlighted in the analysis of the method action, the compensation of such extreme variation in the secondary capacitance C_s (*i.e.* which can be considered as infinitely high, here) requires a drastic increase of the secondary voltage. More precisely, here, the emulation of the entire capacitive function by the active rectifier requires an RMS value of 27 V for the secondary voltage, exceeding broadly the 17.32 V voltage supported by the DC load. In order to assess this particular and interesting situation, the resistive load is changed to a value of 60 Ω in order to attain a DC load voltage of 34.64 V, compatible with the voltage requirements of the proposed method on the AC-side of the active rectifier. The corresponding experimental results are presented and compared to equivalent simulation results in Figure 9.9.

In this configuration, the passive system produces a power efficiency of 38.5 %, due to the non-resonant operation of the secondary circuit. The primary peak current increases to 28.2 A for sustaining the rated output power and a more significant phase shift appears between the primary current and voltage, due to the reactive power reflection from the secondary.

[1]This result demonstrates the correct order of magnitude of the measured power efficiency, but evinces also the measurement and numerical error on the post-processing computations as this value can not be higher than the maximum achievable efficiency of 77.6 % in practice.

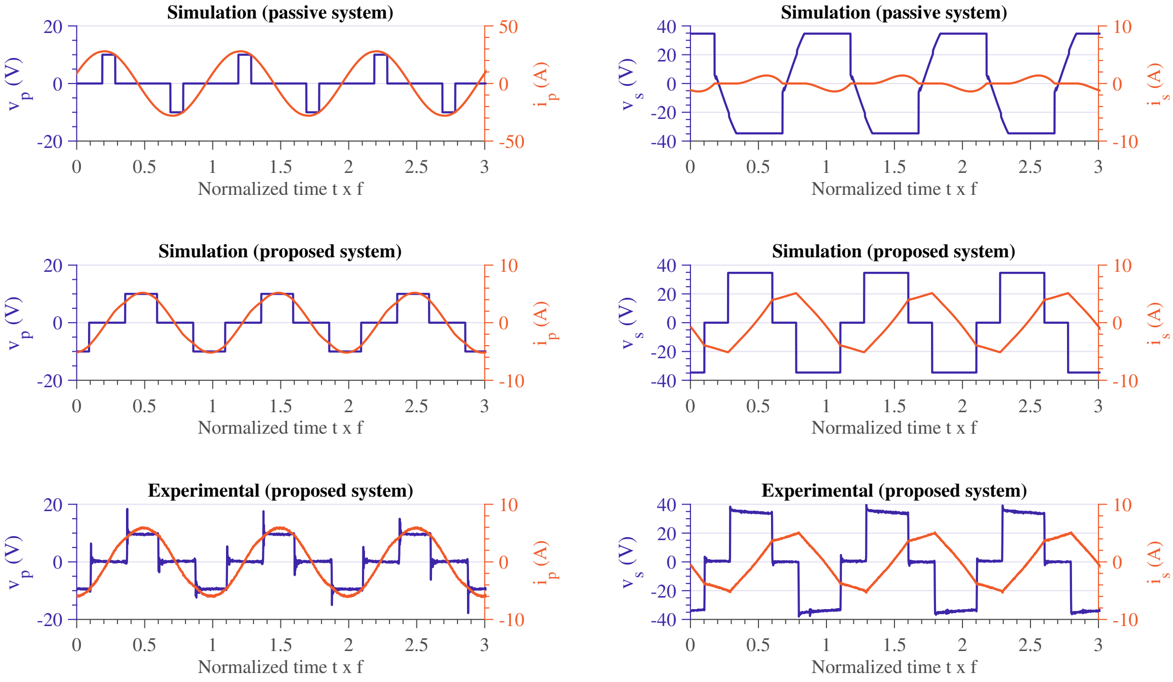

(a) Primary side (b) Secondary side

Figure 9.9: Waveforms from the passive (up) and the proposed (middle) systems simulations and from the experimental measurements (down) for a capacitor-free secondary

According to the time-domain simulation, the proposed method furnishes the rated power with a power efficiency of 90.6 % and produces peak currents amounting to 5.33 A on the primary side and 5.24 A on the secondary side. In other words, the reactive function emulated by the active rectifier permits an operation similar to the nominal situation regarding the currents levels, the windings losses and therefore the power efficiency. One can notice that the secondary current (exiting the active rectifier towards the WPT system, by convention in this thesis) is logically lagging the secondary voltage, evincing the generation of an equivalent capacitive load reactance. Moreover, the primary current and voltage are still in phase, due to the cancellation of the secondary reactive net power flow. Qualitatively, the correspondence between the simulation and the experimental results is clear. The observation of the secondary side waveforms demonstrates obviously the effective emulation of a reactive function by the active rectifier. On the primary side waveforms, one can observe that the primary current and voltage are in phase, accordingly to the expected results. The optimization of the reactive power flow is hence shown. Quantitatively, the experimental peak current in the windings are equal to 6 A in the primary and to 5.2 A in the secondary, so that the balance between the currents which is ensured by the optimization of the active power flow, already validated in the previous configurations, is still and simultaneously effective. According to the post-processing of the waveforms, the experimental system furnishes a power of 20.7 W with a power efficiency of 88 % which is clearly in the expected order of magnitude, regarding the measurements and numerical calculation errors. As a consequence, the concept of optimal command of an SS-RDAB experiencing a detuning (which is total, here) is proven experimentally.

9.5 Conclusions

In this last chapter, the optimal command proposed in this thesis has been successfully implemented experimentally on a 20-W SS-RDAB system operating at 85 kHz and conceived in our laboratory. As a first experimental work in the frequency range higher than 20 kHz within our Unit, this proof-of-concept has required to establish from scratch a know-how relative to high-frequency power converters. In this context and following a progressive approach, we confined ourselves to obtaining an operational design, although not optimized. Such an approach is moreover in accordance with the holistic approach adopted in this thesis and focusing on the optimization of the coil-to-coil efficiency, only. For designing the windings of this proof-of-concept, the virtual laboratory developed in the first part of this thesis has been employed in a simple optimal design procedure, with respect to practical and technical constraints.

The proposed optimal command methodology has been experimentally validated by the concordance between the measurements and the equivalent time-domain simulation results. Firstly, the system has demonstrated its ability to optimize the active power flow by approaching the maximum achievable efficiency despite the non-optimality of the actual load and for three different positions of the windings (corresponding to three different values of the mutual inductance), when the system was correctly tuned. Secondly, the system has demonstrated its ability to optimize both the active and the reactive power flows by approaching the maximum achievable efficiency despite non-optimality of the actual load and despite the absence of any resonant capacitor on the secondary side of the circuit. In this situation, the active rectifier has shown its capacity to emulate an apparent load reactance capable to compensate entirely the secondary winding for reinstating a resonant mode of operation without any secondary capacitor.

Finally, the comparability between the experimental and simulation results evinces once more the accuracy of the virtual laboratory, employed for the determination of the windings equivalent parameters useful to the setting of the open-loop reference operating point.

CHAPTER

TEN

GENERAL CONCLUSIONS AND PERSPECTIVES

Wireless power transfer (WPT) is a popular and trending topic in the scientific and industrial communities. The recent progresses in power electronics have paved the way for the implementation of resonant inductive power transfer (RIPT) to energy-greedy applications, such as electric vehicle (EV) battery charging. Bringing more convenience and more safety, the wireless charging for EVs reaches currently performances comparable to classical wired connections and is on the verge of fostering the upcoming change in paradigm for transportation, as an important infrastructural revolution. Nevertheless, considering the implementation of RIPT to high-power applications requires paying a specific attention to the optimization of the power transfer efficiency. As demonstrated by the mathematical analysis of an RIPT equivalent circuit, maximizing the power transfer efficiency requires two types of effort from the designer, namely

- the optimal design of the inductively coupled windings ;
- the elaboration of an optimal control strategy via the adequate command of the surrounding power electronic converters.

In this context, this thesis pursued a double objective.

First objective

The first objective of this thesis was associated with the development of a flexible, accurate and relatively fast electromagnetic model of the solid-wire planar windings involved in RIPT, following a virtual laboratory approach. Due to the poor adaptability and accuracy of analytical approaches, computational electromagnetics has been considered for fulfilling this objective. The modeling task was justifiably considered as complicated due to the combined and detrimental influences of the eddy currents in the conductors and of the large portion of air which must be integrated in the system on the computational burden. Regarding the importance of the resonance at the field and circuit levels, the coupling of the electromagnetic model of the windings with an external circuit was deemed essential.

Contribution 1

For **assessing the computational burden associated with conventional state-of-the-art numerical methods**, a circuit-coupled massive-conductors finite-element method in magnetodynamics has been employed as a brute-force approach. Using a 2-D model (valid when the windings are aligned, *i.e.* in their nominal position), the first model has provided promising results by requiring around 3 seconds and between 30 000 and 40 000 degrees of freedom (DoF) for the modeling of our experimental test-case (consisting in a couple of 7-turns and 15-cm diameter planar windings submitted to frequencies up to 200 kHz). The comparison of the numerical and experimental results has shown a high accuracy with less than 2 % relative error on the self-parameters in the targeted range of operating frequency. The transition from 2-D to 3-D, although necessary for extending the scope of application of our modeling tool, has been accompanied with a surge in the computational burden. Due to the concomitant need for a high cross-sectional and longitudinal mesh density in the conductors, and due to the large air mesh, even the simulation of a pure academic test-case (consisting in a couple of 2-turns and 7-cm diameter planar windings) has led to an unpracticable computational burden corresponding to more than 600 000 DoF and 500 seconds of CPU time, while presenting a relative error up to 40 % on the windings parameters.

Contribution 2

Regarding the promising results of the 2-D finite-element model based on a best-practice mesh, **an original approach for the optimization of the 2-D meshing of round conductors submitted to eddy-current effects has been proposed**. By comparing the assumed shape of the interpolated current density on the mesh with its assumed analytical evolution with respect to the skin effect occurrence, the optimal radial distribution of the elements layers in the conductors has been addressed via an equivalent 1-D fitting problem. For avoiding the large CPU time associated with the rigorous numerical resolution of the latter problem, a heuristic approach has been proposed. Implemented on our experimental test-case, the proposed meshing method has produced a significant computational gain with a number of DoF divided by four and a CPU time divided by more than three in comparison with the conventional best-practice mesh, without any loss in accuracy. In absolute terms, the CPU time associated with the simulation of a practical test-case falls around 1 second (including the mesh optimization, the meshing and the finite-element resolution), which enables the integration of such a model in an optimal design procedure.

Perspective An interesting perspective for further development of this optimal meshing strategy would be to approach the 1-D fitting problem via the Galerkin's method for a better matching with the finite-element numerical resolution scheme.

Contribution 3

As a possible alternative to the unpracticable 3-D finite-element method, **the potential of the 3-D generalized partial element equivalent circuit (PEEC) method has been evaluated for the modeling of RIPT windings**. The generalized PEEC method does not require the meshing of the air and presents natural circuit coupling possibilities, so that it appears as an elegant and interesting alternative to the finite-element method in the context of RIPT. Benefiting from our collaboration with the G2ELab from Grenoble (which develops the generalized PEEC method in the framework of the MIPSE project), we were granted an experimental version (dating from the end of 2016) of the method for magnetodynamics. Despite a drastic decrease in the number of numerical unknowns, the contemporary burden of the numerical treatment of its integral formulation (which is since then, and still is currently, under improvement investigations at the G2ELab) balances the apparent advantages of the PEEC method, especially regarding the precision on the windings resistance. Nevertheless, according to our different tests on academic examples, the PEEC method seems to seize the correct order of magnitude for the parameters of the coils more efficiently (on a computational point of view) than the 3-D finite-element method, with a better (but still insufficient) accuracy corresponding to a 20 % relative error on the windings resistance. The determination of the inductive parameters is however remarkably efficient, by providing more accurate results than the 3-D finite-element method on the same test-case with a number of DoF divided by 150 000 and a CPU time divided by 15.

Perspective As a perspective, the realization of new numerical tests using the updated version of the generalized PEEC method (and particularly of the auxiliary numerical toolboxes embedded in the MIPSE project) is proposed. Also, the combination of the generalized PEEC formulation with surface impedance boundary conditions would allow to represent the windings using only tubular meshes corresponding to the conductors skin, with an expected drastic reduction in the computational burden.

Contribution 4

For decreasing the computational burden associated with the 3-D model, **an original $\mathbf{a} - \mathbf{v}$ magnetodynamic finite-element formulation for implementing a strong coupling of conductors modeled via 3-D surface impedance boundary conditions (SIBCs) with an external circuit has been proposed**. Such a technique permits to avoid the conductors volume mesh by removing the conducting domains from the modeling problem, while still embedding the eddy-current effects and the circuit relations in the model. This original method has been validated experimentally by estimating the equivalent parameters of the windings from our experimental test-case with a high accuracy (less than 2 % on the resistance and less than 4 % on the self-inductance). Keeping in mind that this experimental test-case is complex in front of the academic test-cases addressed with the classic finite-element formulation, the improvements in accuracy and in the computational performances (370 000 DoF and 120 seconds of CPU time) is clearly demonstrated. Moreover, the effectiveness of the circuit coupling has been demonstrated by observing the complex frequency splitting phenomenon using the proposed formulation.

Perspective As a perspective, the extension of the proposed formulation to more complex conductors shapes via the consideration of higher-order SIBCs is envisioned.

Contribution 5

In this process leading to exploitable electromagnetic models for the windings involved in RIPT, an **experimental validation of the proposed numerical methods has been pursued**. A comparison with the most accurate analytical formulae available in the current literature has also been presented.

Contribution 6

The integrality of the electromagnetic models developed in this thesis have been gathered in a fully parametrized virtual laboratory. Such an approach required to employ software tools and to develop computer codes enabling adaptability and automatization properties. Destined to be used for the quick, flexible and accurate windings characterization, the proposed tool is particularly well-adapted to an integration in any optimization process.

Perspective As a perspective, the scope of application of the virtual laboratory can be improved by the inclusion of ferrite couplers (provided that an accurate model of ferrite losses in the targeted frequency range is available), and by the support of Litz wire via the integration of corresponding finite-element formulations (*e.g.* homogenized formulations). The library of geometrical models can also be extended (notably in 3-D).

Second objective

The second objective of this thesis aimed at elaborating an optimal control strategy for ensuring a maximum coil-to-coil efficiency despite deviations in the circuit parameters or non-optimal operation conditions. Deviations in the circuit parameters or in the operating conditions have a strong impact on the power efficiency of WPT system. An adequate command is therefore mandatory for practicable domestic and industrial WPT applications, which are subject to windings misalignment and components deterioration.

Contribution 1

In this context, **an original optimal command strategy for bidirectional series-series compensated WPT systems has been proposed**. Based on a resonant dual active bridge (RDAB) topology, the proposed methodology considers proceeding to non-synchronous active rectification for simultaneously and independently controlling the active and the reactive power flows in order to achieve the maximum efficiency despite deviations in the circuit parameters and/or detuning of the LC-circuits. As the proposed methodology is based on a first harmonic analysis (FHA), the beneficial impacts of the methodology have first been illustrated and interpreted in the frequency domain by considering an electric vehicle (EV) test-case. According to the latter study, the proposed system can produce a rated power at the maximum efficiency physically achievable by the transmission windings despite any deviations in the mutual inductance or in the secondary capacitance. The case of a secondary devoid of any resonant capacitor has been also successfully supported by the proposed method. Finally, the time-domain simulation of the power converters controlled according to the proposed command has demonstrated the relevance of the FHA-based methodology despite the enriched harmonic content of the actual converters voltages. Nevertheless, controllability restrictions in case of severe deviations of the secondary capacitance have been raised and associated with the limited AC-side voltage range of the active rectifier.

Perspective As the command presented here has been developed and implemented in open-loop, the establishment of an equivalent closed-loop control scheme is envisioned as an interesting perspective for this contribution.

Contribution 2

For boosting the voltage range of the active rectifier and alleviate the controllability restrictions of the proposed method, the Z-source converter has been investigated and compared to a more conventional solution consisting in adding a DC-DC conversion stage (i.e. a two-quadrant chopper) to the system. Via time-domain simulations, both solutions have demonstrated their equivalent ability to extend the controllability range of the proposed command. To our knowledge, using a Z-source active rectifier had not been proposed before in the framework of WPT. Holistically, in comparison with the cascading of a two-quadrant chopper with a full-bridge converter, the Z-source converter is more interesting as it achieves the combined rectifying and DC-DC conversion functions in a single power stage. Although requiring more passive components, it is also more reliable, as it requires one less active switch component and is intrinsically immune to eventual leg short-circuits. Nevertheless, for achieving a given AC voltage, the Z-source-based solution produces a higher DC-link voltage and requires the switches to withstand a higher voltage. Moreover, a dimensionless analysis has been realized for comparing the losses associated with each solution, as a best-effort approach regarding the high-level of this holistic study. Although needing to be nuanced by more concrete and quantitative investigations, it demonstrates that (with the proposed shoot-through strategy) the Z-source-based solution is mainly interesting for slight extensions of the voltage range, for which its lower conduction losses could balance its higher switching losses. For high extensions of the voltage range, the conventional solution is however recommended, due to higher conduction and switching losses impacting the Z-source converters.

Perspective As an interesting and mandatory perspective, a quantitative and absolute comparison of both solutions should be conducted with respect to their operation range and their respective losses, based on a substantive converters design and on concrete specifications for the associated semiconductors components.

Contribution 3

For extending the range of applicability of the proposed methodology, **the optimal command strategy has been generalized to parallel-parallel, series-parallel and parallel-series compensated bidirectional WPT systems**. By employing cleverly circuit theory principles, common formalism and procedure have been maintained for all the compensation topologies, leading to an harmonization of the proposed methodology.

Perspective The proposed generalized methodology has demonstrated its theoretical ability to operate optimally the system even with a secondary devoid of resonant capacitor, and this regardless of the primary compensation scheme. In this context, the secondary side is not characterized by any self-resonant frequency or any compensation scheme (as it is limited to the sole winding, connected to the active rectifier). Therefore, such a generalization of the method paves the way to the realization of a universal WPT receiver, virtually adapted to any operating frequency and to any compensation scheme presented by the transmitter.

Contribution 4

In order to **validate experimentally the general methodology proposed in this thesis, a successful low-power 20-W experimental proof-of-concept has been realized in laboratory**, based on the implementation of the proposed optimal command on a series-series topology, and on windings designed using our virtual laboratory. The time-domain simulations have been corroborated by experimental measurements. The experimental system has demonstrated its ability to optimize the active power flow (with respect to the mutual inductance value) by operating at the maximum coil-to-coil efficiency while furnishing the rated power to the active rectifier for different positions of the windings. Also, it has evinced its capacity to optimize the reactive power flow by emulating an entire capacitive function in a secondary devoid of resonant capacitor. As the system has been commanded in open-loop using the windings parameters determined via our virtual laboratory, the concordance between simulated and experimental results demonstrates anew its accuracy.

Perspectives The experimental validation of the optimal command methodology for parallel-parallel, series-parallel and parallel-series topologies is envisioned. As an experimental and general perspective, one proposes to benefit from the tools and the strategies elaborated and discussed in the framework of this thesis for driving the development of a high-power experimental prototype, based on concrete specifications. The conception of such prototype would require optimizing the design of the converters, by assessing precisely the losses and the influence of the proposed command methodology on the latter. As a matter of fact, the active rectification as well as the extension of the voltage range of the converters are in practice producing additional losses which must be compared with the efficiency gain provided by the holistic strategy developed here. In other words, the aim would consist in maximizing no longer the local coil-to-coil efficiency, but the global source-to-load efficiency of the system.

BIBLIOGRAPHY

[1] A. W. Green and J. T. Boys, “10 khz inductively coupled power transfer-concept and control,” in *1994 Fifth International Conference on Power Electronics and Variable-Speed Drives*, Oct 1994, pp. 694–699.

[2] A. Kurs, A. Karalis, R. Moffatt, J. D. Joannopoulos, P. Fisher, and M. Soljacic, “Wireless power transfer via strongly coupled magnetic resonances,” *Science*, vol. 317, no. 5834, pp. 83–86, July 2007.

[3] K. V. Schuylenbergh and R. Puers, *Inductive PoweringBasic: Theory and Application to Biomedical Systems*, Springer, Ed., 2009.

[4] A. P. Sample, D. T. Meyer, and J. R. Smith, “Analysis, experimental results, and range adaptation of magnetically coupled resonators for wireless power transfer,” *IEEE Transactions on Industrial Electronics*, vol. 58, no. 2, pp. 544–554, Feb 2011.

[5] S. Y. R. Hui, W. Zhong, and C. K. Lee, “A critical review of recent progress in mid-range wireless power transfer,” *IEEE Transactions on Power Electronics*, vol. 29, no. 9, pp. 4500–4511, Sept 2014.

[6] R. Bosshard and J. W. Kolar, “Inductive power transfer for electric vehicle charging: Technical challenges and tradeoffs,” *IEEE Power Electronics Magazine*, vol. 3, no. 3, pp. 22–30, Sept 2016.

[7] Z. Yang, W. Liu, and E. Basham, “Inductor modeling in wireless links for implantable electronics,” *IEEE Transactions on Magnetics*, vol. 43, no. 10, pp. 3851–3860, Oct 2007.

[8] M. Ghovanloo and S. Atluri, “A wide-band power-efficient inductive wireless link for implantable microelectronic devices using multiple carriers,” *IEEE Transactions on Circuits and Systems I: Regular Papers*, vol. 54, no. 10, pp. 2211–2221, Oct 2007.

[9] D. W. Ferreira, “Topics in design and analysis of transcutaneous energy transfer to ventricular assist devices,” Ph.D. dissertation, University of Sao Paulo, 2013.

[10] H. Alemdar and C. Ersoy, “Wireless sensor networks for healthcare: A survey,” *Computer Networks*, vol. 54, no. 15, pp. 2688 – 2710, 2010. [Online]. Available: http://www.sciencedirect.com/science/article/pii/S1389128610001398

[11] Mao Xingkui, Huang Qisheng, Xiao Yudi, Lan Shifa, Zhang Zhe, and M. A. E. Andersen, “Wireless power supply via coupled magnetic resonance for on-line monitoring wireless sensor of high-voltage electrical equipment,” in *IECON 2016 - 42nd Annual Conference of the IEEE Industrial Electronics Society*, Oct 2016, pp. 4582–4587.

[12] K. A. Kalwar, M. Aamir, and S. Mekhilef, "Inductively coupled power transfer (icpt) for electric vehicle charging – a review," *Renewable and Sustainable Energy Reviews*, vol. 47, pp. 462 – 475, 2015.

[13] "Electrifying insights: How automakers can drive electrified vehicle sales and profitability," https://www.mckinsey.com/industries/automotive-and-assembly/our-insights/electrifying-insights-how-automakers-can-drive-electrified-vehicle-sales-and-profitability, accessed: 30-10-2017.

[14] S. Li and C. C. Mi, "Wireless power transfer for electric vehicle applications," *IEEE Journal of Emerging and Selected Topics in Power Electronics*, vol. 3, no. 1, pp. 4–17, March 2015.

[15] B. Witkamp, "The transition to electric drive," May 2017.

[16] M. P. Kazmierkowski and A. J. Moradewicz, "Unplugged but connected: Review of contactless energy transfer systems," *IEEE Industrial Electronics Magazine*, vol. 6, no. 4, pp. 47–55, Dec 2012.

[17] F. Musavi, M. Edington, and W. Eberle, "Wireless power transfer: A survey of ev battery charging technologies," in *2012 IEEE Energy Conversion Congress and Exposition (ECCE)*, Sep 2012, pp. 1804–1810.

[18] M. Tomar and S. Gupta, "Wireless power transmission: Applications and components," *International Journal of Engineering Research and Technology*, vol. 1, no. 5, Jul 2012.

[19] G. A. Covic and J. T. Boys, "Modern trends in inductive power transfer for transportation applications," *IEEE Journal of Emerging and Selected Topics in Power Electronics*, vol. 1, no. 1, pp. 28–41, March 2013.

[20] C. Qiu, K. T. Chau, C. Liu, and C. C. Chan, "Overview of wireless power transfer for electric vehicle charging," in *2013 World Electric Vehicle Symposium and Exhibition (EVS27)*, Nov 2013, pp. 1–9.

[21] S. D. Barman, A. W. Reza, N. Kumar, M. Karim, and A. B. Munir, "Wireless powering by magnetic resonant coupling: Recent trends in wireless power transfer system and its applications," *Renewable and Sustainable Energy Reviews*, vol. 51, pp. 1525–1552, Aug. 2015.

[22] N. Tesla, *Experiments with alternate currents of very high frequency and their application to methods of artificial illumination experiments with alternate currents of high potential and high frequency*, 1892.

[23] L. P. Wheeler, "Tesla's contribution to high frequency," *Electrical Engineering*, vol. 62, no. 8, pp. 355–357, Aug 1943.

[24] J. Orto, *The Story of Semiconductors*, 1st ed., O. U. Press, Ed., 2004.

[25] T. Burress, "Benchmarking ev and hev technologies," Jun 2015.

[26] M. Chinthavali, O. C. Onar, S. L. Campbell, and L. M. Tolbert, "Integrated charger with wireless charging and boost functions for phev and ev applications," in *2015 IEEE Transportation Electrification Conference and Expo (ITEC)*, June 2015, pp. 1–8.

[27] "M-pec power electronics consulting," http://www.mpec.at/, accessed: 16-11-2017.

[28] "Witricity corp." http://www.witricity.com/, accessed: 08-09-2017.

[29] B. Goeldi, S. Reichert, and J. Tritschler, “Design and dimensioning of a highly efficient 22 kw bidirectional inductive charger for e-mobility,” in *Int. Exhibition Conf. Power Electronics*, 2013, pp. 1496–1503.

[30] R. Bosshard and J. W. Kolar, “Multi-objective optimization of 50 kw/85 khz ipt system for public transport,” *IEEE Journal of Emerging and Selected Topics in Power Electronics*, vol. 4, no. 4, pp. 1370–1382, Dec 2016.

[31] “Primove by bombardier transportation,” http://primove.bombardier.com/, accessed: 16-11-2017.

[32] “Wireless power transfer for light-duty plug-in/electric vehicles and alignment methodology,” http://standards.sae.org/wip/j2954/.

[33] U. K. Madawala and D. J. Thrimawithana, “A bidirectional inductive power interface for electric vehicles in v2g systems,” *IEEE Transactions on Industrial Electronics*, vol. 58, no. 10, pp. 4789–4796, Oct 2011.

[34] X. Lu, P. Wang, D. Niyato, D. I. Kim, and Z. Han, “Wireless charging technologies: Fundamentals, standards, and network applications,” *IEEE Communications Surveys Tutorials*, vol. 18, no. 2, pp. 1413–1452, Secondquarter 2016.

[35] R. Shadid, S. Noghanian, and A. Nejadpak, “A literature survey of wireless power transfer,” in *2016 IEEE International Conference on Electro Information Technology (EIT)*, May 2016, pp. 0782–0787.

[36] M. G. L. Roes, J. L. Duarte, M. A. M. Hendrix, and E. A. Lomonova, “Acoustic energy transfer: A review,” *IEEE Transactions on Industrial Electronics*, vol. 60, no. 1, pp. 242–248, Jan 2013.

[37] A. Sahai and D. Graham, “Optical wireless power transmission at long wavelengths,” in *2011 International Conference on Space Optical Systems and Applications (ICSOS)*, May 2011, pp. 164–170.

[38] J. H. Poynting, “On the transfer of energy in the electromagnetic field,” *Philosophical Transactions of the Royal Society of London*, vol. 175, pp. 343–361, 1884.

[39] P. E. Glaser, “Power from the sun: Its future,” *Science*, vol. 162, no. 3856, pp. 857–861, 1968. [Online]. Available: https://science.sciencemag.org/content/162/3856/857

[40] R. M. Dickinson, “Performance of a high-power, 2.388-ghz receiving array in wireless power transmission over 1.54 km,” in *1976 IEEE-MTT-S International Microwave Symposium*, June 1976, pp. 139–141.

[41] W. C. Brown, “The history of power transmission by radio waves,” *IEEE Transactions on Microwave Theory and Techniques*, vol. 32, no. 9, pp. 1230–1242, Sep 1984.

[42] N. Shinohara, Y. Kubo, and H. Tonomura, “Wireless charging for electric vehicle with microwaves,” in *2013 3rd International Electric Drives Production Conference (EDPC)*, Oct 2013, pp. 1–4.

[43] A. E. Oualkadi and J. Zbitou, *Handbook of Research on Advanced Trends in Microwave and Communication Engineering*, I. Global, Ed., 2016.

[44] M. Kline, I. Izyumin, B. Boser, and S. Sanders, “Capacitive power transfer for contactless charging,” in *2011 Twenty-Sixth Annual IEEE Applied Power Electronics Conference and Exposition (APEC)*, March 2011, pp. 1398–1404.

[45] C. Liu, A. P. Hu, and N. . C. Nair, "Modelling and analysis of a capacitively coupled contactless power transfer system," *IET Power Electronics*, vol. 4, no. 7, pp. 808–815, Aug 2011.

[46] M. P. Theodoridis, "Effective capacitive power transfer," *IEEE Transactions on Power Electronics*, vol. 27, no. 12, pp. 4906–4913, Dec 2012.

[47] C. Mi, "High power capacitive power transfer for electric vehicle charging applications," in *2015 6th International Conference on Power Electronics Systems and Applications (PESA)*, Dec 2015, pp. 1–4.

[48] N. Sakai, D. Itokazu, Y. Suzuki, S. Sakihara, and T. Ohira, "One-kilowatt capacitive power transfer via wheels of a compact electric vehicle," in *2016 IEEE Wireless Power Transfer Conference (WPTC)*, May 2016, pp. 1–3.

[49] D. Rozario, V. K. Pathipati, A. Ram, N. A. Azeez, and S. S. Williamson, "Modified resonant converters for contactless capacitive power transfer systems used in ev charging applications," in *IECON 2016 - 42nd Annual Conference of the IEEE Industrial Electronics Society*, Oct 2016, pp. 4510–4517.

[50] H. Zhang, F. Lu, H. Hofmann, W. Liu, and C. C. Mi, "A four-plate compact capacitive coupler design and lcl-compensated topology for capacitive power transfer in electric vehicle charging application," *IEEE Transactions on Power Electronics*, vol. 31, no. 12, pp. 8541–8551, Dec 2016.

[51] F. Lu, H. Zhang, and C. Mi, "A review on the recent development of capacitive wireless power transfer technology," *Energies*, vol. 10, no. 11, 2017. [Online]. Available: https://www.mdpi.com/1996-1073/10/11/1752

[52] K. W. Klontz, A. Esser, R. R. Bacon, D. M. Divan, D. W. Novotny, and R. D. Lorenz, "An electric vehicle charging system with 'universal' inductive interface," in *Conference Record of the Power Conversion Conference - Yokohama 1993*, April 1993, pp. 227–232.

[53] "Wireless power consortium," http://www.wirelesspowerconsortium.com/, accessed: 08-09-2017.

[54] G. Chateigner, M. Boes, D. Bouix, J. Vaillant, and D. Verkindere, *Manuel de Génie électrique*, Dunod, Ed., 2007.

[55] N. Tesla, "Apparatus for transmission of electrical energy," 1897.

[56] H. A. Haus and W. Huang, "Coupled-mode theory," *Proceedings of the IEEE*, vol. 79, no. 10, pp. 1505–1518, Oct 1991.

[57] "Network research witricity," http://www.asquare.org/networkresearch/2007/witricity, accessed: 19-08-2019.

[58] J. T. Boys, G. A. Covic, and A. W. Green, "Stability and control of inductively coupled power transfer systems," *IEE Proceedings - Electric Power Applications*, vol. 147, no. 1, pp. 37–43, Jan 2000.

[59] C.-S. Wang, O. H. Stielau, and G. A. Covic, "Load models and their application in the design of loosely coupled inductive power transfer systems," in *PowerCon 2000. 2000 International Conference on Power System Technology. Proceedings (Cat. No.00EX409)*, vol. 2, 2000, pp. 1053–1058 vol.2.

[60] C.-S. Wang, G. A. Covic, and O. H. Stielau, "Power transfer capability and bifurcation phenomena of loosely coupled inductive power transfer systems," *IEEE Transactions on Industrial Electronics*, vol. 51, no. 1, pp. 148–157, Feb 2004.

[61] C.-S. Wang, O. H. Stielau, and G. A. Covic, "Design considerations for a contactless electric vehicle battery charger," *IEEE Transactions on Industrial Electronics*, vol. 52, no. 5, pp. 1308–1314, Oct 2005.

[62] H. L. N. Wiegman, D. M. Divan, D. W. Novotny, and R. Mohan, "A zvs dual resonant converter for battery charging applications," in *PESC '91 Record 22nd Annual IEEE Power Electronics Specialists Conference*, June 1991, pp. 202–208.

[63] J. G. Hayes, J. T. Hall, M. C. Egan, and J. M. D. Murphy, "Full-bridge, series-resonant converter supplying the sae j-1773 electric vehicle inductive charging interface," in *PESC Record. 27th Annual IEEE Power Electronics Specialists Conference*, vol. 2, June 1996, pp. 1913–1918 vol.2.

[64] R. Laouamer, M. Brunello, J. P. Ferrieux, O. Normand, and N. Buchheit, "A multi-resonant converter for non-contact charging with electromagnetic coupling," in *Proceedings of the IECON'97 23rd International Conference on Industrial Electronics, Control, and Instrumentation (Cat. No.97CH36066)*, vol. 2, Nov 1997, pp. 792–797 vol.2.

[65] M. Kiani and M. Ghovanloo, "The circuit theory behind coupled-mode magnetic resonance-based wireless power transmission," *IEEE Transactions on Circuits and Systems I: Regular Papers*, vol. 59, no. 9, pp. 2065–2074, Sept 2012.

[66] N. Hagiwara, "Study on the principle of contactless electric power transfer via electromagnetic coupling," *Electrical Engineering in Japan*, vol. 182, no. 2, pp. 53–60, 2013. [Online]. Available: http://dx.doi.org/10.1002/eej.21285

[67] "Guidelines for limiting exposure to time-varying electric, magnetic, and electromagnetic fields (up to 300 ghz)," Int. Commission Non-Ionizing Radiation Protection (ICNIRP), 1998.

[68] "Guidelines for limiting exposure to time-varying electric, magnetic, and electromagnetic fields (1 hz - 100 khz)," Int. Commission Non-Ionizing Radiation Protection (ICNIRP), 2010.

[69] P. Dular, F. Henrotte, and W. Legros, "A general and natural method to define circuit relations associated with magnetic vector potential formulations," *IEEE Transactions on Magnetics*, vol. 35, no. 3, pp. 1630–1633, May 1999.

[70] T. T. Nguyen, G. Meunier, J. M. Guichon, O. Chadebec, and T. S. Nguyen, "An integral formulation for the computation of 3-d eddy current using facet elements," *IEEE Transactions on Magnetics*, vol. 50, no. 2, pp. 549–552, Feb 2014.

[71] S. Yuferev and N. Ida, "Selection of the surface impedance boundary conditions for a given problem," *IEEE Transactions on Magnetics*, vol. 35, no. 3, pp. 1486–1489, May 1999.

[72] S. Yuferev and L. D. Rienzo, "Surface impedance boundary conditions in terms of various formalisms," *IEEE Transactions on Magnetics*, vol. 46, no. 9, pp. 3617–3628, Sept 2010.

[73] S. Yuferev, L. D. Rienzo, and N. Ida, "Surface impedance boundary conditions," *ICS Newsletter*, vol. 21, no. 2, pp. 3–16, Jul 2014.

[74] C. Geuzaine and J.-F. Remacle, "Gmsh: a three-dimensional finite element mesh generator with built-in pre- and post-processing facilities," *International Journal for Numerical Methods in Engineering*, vol. 79, no. 11, pp. 1309–1331, 2009.

[75] P. Dular, C. Geuzaine, F. Henrotte, and W. Legros, "A general environment for the treatment of discrete problems and its application to the finite element method," *IEEE Transactions on Magnetics*, vol. 34, no. 5, pp. 3395–3398, Sep. 1998.

[76] M. Budhia, J. T. Boys, G. A. Covic, and C. Huang, "Development of a single-sided flux magnetic coupler for electric vehicle ipt charging systems," *IEEE Transactions on Industrial Electronics*, vol. 60, no. 1, pp. 318–328, Jan 2013.

[77] F. Y. Lin, G. A. Covic, and J. T. Boys, "Evaluation of magnetic pad sizes and topologies for electric vehicle charging," *IEEE Transactions on Power Electronics*, vol. 30, no. 11, pp. 6391–6407, Nov 2015.

[78] U. M. Jow and M. Ghovanloo, "Design and optimization of printed spiral coils for efficient transcutaneous inductive power transmission," *IEEE Transactions on Biomedical Circuits and Systems*, vol. 1, no. 3, pp. 193–202, Sept 2007.

[79] T. Imura and Y. Hori, "Maximizing air gap and efficiency of magnetic resonant coupling for wireless power transfer using equivalent circuit and neumann formula," *IEEE Transactions on Industrial Electronics*, vol. 58, no. 10, pp. 4746–4752, Oct 2011.

[80] Y. Park, J. Kim, and K.-H. Kim, "Magnetically coupled resonance wireless power transfer (mr-wpt) with multiple self-resonators," in *Wireless Power Transfer*, K. Y. Kim, Ed. Rijeka: IntechOpen, 2012, ch. 3. [Online]. Available: https://doi.org/10.5772/28387

[81] K. Fotopoulou and B. W. Flynn, "Wireless power transfer in loosely coupled links: Coil misalignment model," *IEEE Transactions on Magnetics*, vol. 47, no. 2, pp. 416–430, Feb 2011.

[82] L. Chen, S. Liu, Y. C. Zhou, and T. J. Cui, "An optimizable circuit structure for high-efficiency wireless power transfer," *IEEE Transactions on Industrial Electronics*, vol. 60, no. 1, pp. 339–349, Jan 2013.

[83] B. H. Waters, B. J. Mahoney, G. Lee, and J. R. Smith, "Optimal coil size ratios for wireless power transfer applications," in *2014 IEEE International Symposium on Circuits and Systems (ISCAS)*, June 2014, pp. 2045–2048.

[84] A. M. Urling, V. A. Niemela, G. R. Skutt, and T. G. Wilson, "Characterizing high-frequency effects in transformer windings-a guide to several significant articles," in *Proceedings, Fourth Annual IEEE Applied Power Electronics Conference and Exposition*, March 1989, pp. 373–385.

[85] J. A. Ferreira, "Improved analytical modeling of conductive losses in magnetic components," *IEEE Transactions on Power Electronics*, vol. 9, no. 1, pp. 127–131, Jan 1994.

[86] A. Reatti and M. K. Kazimierczuk, "Comparison of various methods for calculating the ac resistance of inductors," *IEEE Transactions on Magnetics*, vol. 38, no. 3, pp. 1512–1518, May 2002.

[87] M. K. Kazimierczuk, *High-Frequency Magnetic Components*, J. W. . Sons, Ed., 2009.

[88] G. S. Smith, *The proximity effect in systems of parallel conductors*, J. A. Physics, Ed., 1972.

[89] C. M. Zierhofer and E. S. Hochmair, "Geometric approach for coupling enhancement of magnetically coupled coils," *IEEE Transactions on Biomedical Engineering*, vol. 43, no. 7, pp. 708–714, July 1996.

[90] S. Babic, F. Sirois, C. Akyel, and C. Girardi, "Mutual inductance calculation between circular filaments arbitrarily positioned in space: Alternative to grover's formula," *IEEE Transactions on Magnetics*, vol. 46, no. 9, pp. 3591–3600, Sept 2010.

[91] R. Chang, L. Quan, X. Zhu, Z. Zong, and H. Zhou, "Design of a wireless power transfer system for ev application based on finite element analysis and matlab simulation," in *2014 IEEE Conference and Expo Transportation Electrification Asia-Pacific (ITEC Asia-Pacific)*, Aug 2014, pp. 1–4.

[92] Z. Dang and J. A. A. Qahouq, "Modeling and investigation of magnetic resonance coupled wireless power transfer system with lateral misalignment," in *2014 IEEE Applied Power Electronics Conference and Exposition - APEC 2014*, March 2014, pp. 1317–1322.

[93] A. O. Hariri, A. Berzoy, A. A. S. Mohamed, and O. A. Mohammed, "Performance evaluation of a wireless power transfer system using coupled 3d finite element-circuit model," in *2015 IEEE Wireless Power Transfer Conference (WPTC)*, May 2015, pp. 1–4.

[94] A. O. Hariri, T. Youssef, A. Elsayed, and O. Mohammed, "A computational approach for a wireless power transfer link design optimization considering electromagnetic compatibility," *IEEE Transactions on Magnetics*, vol. 52, no. 3, pp. 1–4, March 2016.

[95] R. Bosshard, J. W. Kolar, and B. Wunsch, "Accurate finite-element modeling and experimental verification of inductive power transfer coil design," in *2014 IEEE Applied Power Electronics Conference and Exposition - APEC 2014*, March 2014, pp. 1648–1653.

[96] J. Gyselinck and P. Dular, "Frequency-domain homogenization of bundles of wires in 2-d magnetodynamic fe calculations," *IEEE Transactions on Magnetics*, vol. 41, no. 5, pp. 1416–1419, May 2005.

[97] D. Klis, S. Burgard, O. Farle, and R. Dyczij-Edlinger, "Fast simulation of wireless power transfer systems with varying coil alignment," *IFAC-PapersOnLine*, vol. 48, no. 1, pp. 248 – 253, 2015, 8th Vienna International Conferenceon Mathematical Modelling. [Online]. Available: http://www.sciencedirect.com/science/article/pii/S2405896315001147

[98] D. W. Ferreira, R. V. Sabariego, L. Lebensztajn, L. Krahenbuhl, F. Morel, and C. Vollaire, "Homogenization methods in simulations of transcutaneous energy transmitters," *IEEE Transactions on Magnetics*, vol. 50, no. 2, pp. 1017–1020, Feb 2014.

[99] Z. Badics, S. Bilicz, S. Gyimóthy, and J. Pávó, "Finite-element-integral equation full-wave multisolver for efficient modeling of resonant wireless power transfer," *IEEE Transactions on Magnetics*, vol. 52, no. 3, pp. 1–4, March 2016.

[100] H. Wang, D. Liao, and Z. Nie, "A fast and stable integral equation algorithm for magnetic couplings in low frequency wireless transfers," in *2016 IEEE MTT-S International Conference on Numerical Electromagnetic and Multiphysics Modeling and Optimization (NEMO)*, July 2016, pp. 1–2.

[101] L. Huang, G. Meunier, O. Chadebec, J. Guichon, Y. Li, and Z. He, “General integral formulation of magnetic flux computation and its application to inductive power transfer system,” *IEEE Transactions on Magnetics*, vol. 53, no. 6, pp. 1–4, June 2017.

[102] G. Meunier, *The Finite Element Method for Electromagnetic Modeling*, J. W. . Sons, Ed., 2008.

[103] Z. D. Grève, “Modélisation numérique de composants magnétiques multi-enroulements sollicités à haute fréquence,” Ph.D. dissertation, University of Mons, 2012.

[104] C. Geuzaine and P. Dular, “Modelling and design of electromagnetic systems (teaching slides),” Feb 2016.

[105] J. Lobry and O. Deblecker, *Calcul assisté par ordinateur de systèmes énergétiques (Notes de cours)*, 2005.

[106] P. Dular, A. Nicolet, A. Genon, and W. Legros, “A discrete sequence associated with mixed finite elements and its gauge condition for vector potentials,” *IEEE Transactions on Magnetics*, vol. 31, no. 3, pp. 1356–1359, May 1995.

[107] C. Hoer and C. Love, “Exact inductance equations for rectangular conductors with applications to more complicated geometries,” *Journal of Research National Bureau of Standards, Section C: Engineering and Instrumentation*, vol. 69, no. C, pp. 127–137, Apr 1965.

[108] A. E. Ruehli, “Inductance calculations in a complex integrated circuit environment,” *IBM Journal of Research and Development*, vol. 16, no. 5, pp. 470–481, Sep. 1972.

[109] R. Bellman, “On the approximation of curves by line segments using dynamic programming,” *Commun. ACM*, vol. 4, no. 6, pp. 284–, Jun. 1961. [Online]. Available: http://doi.acm.org/10.1145/366573.366611

[110] H. Stone, “Approximation of curves by line segments,” *Mathematics of Computation*, vol. 15, no. 73, pp. 40–47, 1961. [Online]. Available: http://www.jstor.org/stable/2003089

[111] B. Gluss, “A line segment curve-fitting algorithm related to optimal encoding of information,” *Information and Control*, vol. 5, no. 3, pp. 261 – 267, 1962. [Online]. Available: http://www.sciencedirect.com/science/article/pii/S0019995862905995

[112] G. Meunier, C. Guerin, and Y. L. Floch, “Circuit-coupled $bft_0hbox{-}phi$ formulation with surface impedance condition,” *IEEE Transactions on Magnetics*, vol. 44, no. 6, pp. 730–733, June 2008.

[113] N. Mohan, T. M. Undeland, and W. P. Robbins, *Power Electronics: Converters, Applications, and Design*, J. W. . Sons, Ed., 2003.

[114] D. C. Marian K. Kazimierczuk, *Resonant Power Converters*, 2nd ed. Wiley-IEEE Press, 2011.

[115] O. Deblecker, *Electronique de puissance (Notes de cours)*, 2014.

[116] M. T. Outeiro, G. Buja, and D. Czarkowski, “Resonant power converters: An overview with multiple elements in the resonant tank network,” *IEEE Industrial Electronics Magazine*, vol. 10, no. 2, pp. 21–45, June 2016.

[117] J.-P. Ferrieux and F. Forest, *Alimentation à découpage - Convertisseurs à résonance (3 ème édition)*, Dunod, Ed., 2006.

[118] M. Pinuela, D. C. Yates, S. Lucyszyn, and P. D. Mitcheson, "Maximizing dc-to-load efficiency for inductive power transfer," *IEEE Transactions on Power Electronics*, vol. 28, no. 5, pp. 2437–2447, May 2013.

[119] M. K. Uddin, G. Ramasamy, S. Mekhilef, K. Ramar, and Y. C. Lau, "A review on high frequency resonant inverter technologies for wireless power transfer using magnetic resonance coupling," in *2014 IEEE Conference on Energy Conversion (CENCON)*, Oct 2014, pp. 412–417.

[120] F. Corti, F. Grasso, A. Reatti, A. Ayachit, D. K. Saini, and M. K. Kazimierczuk, "Design of class-e zvs inverter with loosely-coupled transformer at fixed coupling coefficient," in *IECON 2016 - 42nd Annual Conference of the IEEE Industrial Electronics Society*, Oct 2016, pp. 5627–5632.

[121] R. Bosshard, U. Badstübner, J. W. Kolar, and I. Stevanović, "Comparative evaluation of control methods for inductive power transfer," in *2012 International Conference on Renewable Energy Research and Applications (ICRERA)*, Nov 2012, pp. 1–6.

[122] D. Patil, M. Sirico, L. Gu, and B. Fahimi, "Maximum efficiency tracking in wireless power transfer for battery charger: Phase shift and frequency control," in *2016 IEEE Energy Conversion Congress and Exposition (ECCE)*, Sept 2016, pp. 1–8.

[123] T. Murayama, T. Bando, K. Furiya, and T. Nakamura, "Method of designing an impedance matching network for wireless power transfer systems," in *IECON 2016 - 42nd Annual Conference of the IEEE Industrial Electronics Society*, Oct 2016, pp. 4504–4509.

[124] H. Li, J. Li, K. Wang, W. Chen, and X. Yang, "A maximum efficiency point tracking control scheme for wireless power transfer systems using magnetic resonant coupling," *IEEE Transactions on Power Electronics*, vol. 30, no. 7, pp. 3998–4008, July 2015.

[125] W. X. Zhong and S. Y. R. Hui, "Maximum energy efficiency tracking for wireless power transfer systems," *IEEE Transactions on Power Electronics*, vol. 30, no. 7, pp. 4025–4034, July 2015.

[126] C. Zhao, Z. Wang, J. Du, J. Wu, S. Zong, and X. He, "Active resonance wireless power transfer system using phase shift control strategy," in *2014 IEEE Applied Power Electronics Conference and Exposition - APEC 2014*, March 2014, pp. 1336–1341.

[127] A. Berger, M. Agostinelli, S. Vesti, J. . Oliver, J. A. Cobos, and M. Huemer, "Phase-shift and amplitude control for an active rectifier to maximize the efficiency and extracted power of a wireless power transfer system," in *2015 IEEE Applied Power Electronics Conference and Exposition (APEC)*, March 2015, pp. 1620–1624.

[128] A. Berger, M. Agostinelli, S. Vesti, J. A. Oliver, J. A. Cobos, and M. Huemer, "A wireless charging system applying phase-shift and amplitude control to maximize efficiency and extractable power," *IEEE Transactions on Power Electronics*, vol. 30, no. 11, pp. 6338–6348, Nov 2015.

[129] A. K. Swain, M. J. Neath, U. K. Madawala, and D. J. Thrimawithana, "A dynamic multivariable state-space model for bidirectional inductive power transfer systems," *IEEE Transactions on Power Electronics*, vol. 27, no. 11, pp. 4772–4780, Nov 2012.

[130] D. J. Thrimawithana and U. K. Madawala, "A generalized steady-state model for bidirectional ipt systems," *IEEE Transactions on Power Electronics*, vol. 28, no. 10, pp. 4681–4689, Oct 2013.

[131] M. J. Neath, A. K. Swain, U. K. Madawala, and D. J. Thrimawithana, "An optimal pid controller for a bidirectional inductive power transfer system using multiobjective genetic algorithm," *IEEE Transactions on Power Electronics*, vol. 29, no. 3, pp. 1523–1531, March 2014.

[132] J. Y. Lee and B. M. Han, "A bidirectional wireless power transfer ev charger using self-resonant pwm," *IEEE Transactions on Power Electronics*, vol. 30, no. 4, pp. 1784–1787, April 2015.

[133] "Psim software," https://powersimtech.com/products/psim/.

[134] Fang Zheng Peng, "Z-source inverter," *IEEE Transactions on Industry Applications*, vol. 39, no. 2, pp. 504–510, March 2003.

[135] T. Wang, X. Liu, H. Tang, and M. Ali, "Modification of the wireless power transfer system with z-source inverter," *Electronics Letters*, vol. 53, no. 2, pp. 106–108, 2017.

[136] H. Zeng and F. Z. Peng, "Sic-based z-source resonant converter with constant frequency and load regulation for ev wireless charger," *IEEE Transactions on Power Electronics*, vol. 32, no. 11, pp. 8813–8822, Nov 2017.

[137] N. S. González-Santini, H. Zeng, Y. Yu, and F. Z. Peng, "Z-source resonant converter with power factor correction for wireless power transfer applications," *IEEE Transactions on Power Electronics*, vol. 31, no. 11, pp. 7691–7700, Nov 2016.

[138] H. Zeng, X. Wang, and F. Z. Peng, "High power density z-source resonant wireless charger with line frequency sinusoidal charging," *IEEE Transactions on Power Electronics*, vol. 33, no. 12, pp. 10 148–10 156, Dec 2018.

[139] O. Ellabban, J. Van Mierlo, and P. Lataire, "Comparison between different pwm control methods for different z-source inverter topologies," in *2009 13th European Conference on Power Electronics and Applications*, Sep. 2009, pp. 1–11.

[140] S. Patra, N. Kishor, S. R. Mohanty, and P. K. Ray, "Power quality assessment in 3-phi grid connected pv system with single and dual stage circuits," *International Journal of Electrical Power and Energy Systems*, vol. 75, pp. 275 – 288, 2016. [Online]. Available: http://www.sciencedirect.com/science/article/pii/S0142061515003968

[141] Xu Peng Fang, Zhao Ming Qian, and Fang Zheng Peng, "Single-phase z-source pwm ac-ac converters," *IEEE Power Electronics Letters*, vol. 3, no. 4, pp. 121–124, Dec 2005.

[142] Xupeng Fang, "A novel z-source dc-dc converter," in *2008 IEEE International Conference on Industrial Technology*, April 2008, pp. 1–4.

[143] J. Rabkowski, "The bidirectional z-source inverter as an energy storage/grid interface," in *EUROCON 2007 - The International Conference on "Computer as a Tool"*, Sep. 2007, pp. 1629–1635.

APPENDIX
A

LIST OF PUBLICATIONS

A.1 Peer-review journal articles

- A. Desmoort, Z. De Grève, P. Dular, C. Geuzaine and O. Deblecker, "Surface Impedance Boundary Condition With Circuit Coupling for the 3-D Finite-Element Modeling of Wireless Power Transfer," in *IEEE Transactions on Magnetics*, vol. 53, no. 6, pp. 1-4, June 2017, Art no. 7402104.
- A. Desmoort, O. Deblecker and Z. De Grève, "Active Rectification for the Optimal Command of Bidirectional Resonant Wireless Power Transfer Robust to Severe Circuit Parameters Deviations," in reviewing process in *IEEE Transactions in Industry Applications*

A.2 Peer-review conference articles

- A. Desmoort, Z. De Grève and O. Deblecker, "A virtual laboratory for the modeling of Wireless Power Transfer systems," *2015 International Conference on Electromagnetics in Advanced Applications (ICEAA)*, Turin, Italy, 2015, pp. 1353-1356.
- A. Desmoort, Z. De Grève and O. Deblecker, "Multiobjective optimal design of wireless power transfer devices using a Genetic Algorithm and accurate analytical formulae," IECON 2016 - 42nd Annual Conference of the IEEE Industrial Electronics Society, Florence, Italy, 2016, pp. 4518-4522.
- A. Desmoort, J. Siau, G. Meunier, J.-M. Guichon, O. Chadebec, O. Deblecker, "Comparing partial element equivalent circuit and finite element methods for the resonant wireless power transfer 3D modeling," *2016 IEEE Conference on Electromagnetic Field Computation (CEFC)*, Miami, United States, 2016, pp. 1-1.
- A. Desmoort, Z. De Grève, P. Dular, C. Geuzaine and O. Deblecker, "Surface impedance boundary condition with circuit coupling for the 3D finite element modeling of wireless power transfer," *2016 IEEE Conference on Electromagnetic Field Computation (CEFC)*, Miami, United States, 2016, pp. 1-1.
- A. Desmoort, Z. De Grève and O. Deblecker, "Modeling and Optimal Control of Resonant Wireless Power Transfer," *2018 IEEE Young Researcher Symposium Benelux (YRS2018)*, Brussels, Belgium, 2018.

- A. Desmoort, O. Deblecker and Z. De Grève, "Active Rectification for the Optimal Control of Bidirectional Resonant Wireless Power Transfer," *2018 International Symposium on Power Electronics, Electrical Drives, Automation and Motion (SPEEDAM)*, Amalfi, 2018, pp. 756-761.

A.3 Invited article

- A. Desmoort, Z. De Grève and O. Deblecker, "Analytical, Numerical and Experimental Modeling of Resonant Wireless Power Transfer Devices (Research & Development Award)," in *SRBE/KBVE Revue E Tijdschrift*, 132nd year, no. 1-4, 2016.

APPENDIX

B

OPTIMIZATION OF THE POWER EFFICEINCY WITH RESPECT TO THE APPARENT LOAD RESISTANCE AND REACTANCE

The power efficiency of a series-series resonant WPT system can be expressed as

$$\eta(R_L, X_L) = \frac{R_L}{R_p\frac{(R_s+R_L)^2+(X_s+X_L)^2}{\omega^2 M^2} + R_s + R_L} \tag{6.10}$$

and the control strategy proposed in Section 6.2 requires to determine the couple (R_L^{opt}, X_L^{opt}) maximizing the efficiency. This couple of values verifies that

$$\frac{\partial\eta}{\partial R_L}(R_L^{opt}, X_L^{opt}) = 0 \text{ and } \frac{\partial\eta}{\partial X_L}(R_L^{opt}, X_L^{opt}) = 0$$

In accordance with the procedure for the optimization of a two-variable function, let first determine the optimal value for one of the two parameters, *i.e.* the optimal reactance X_L^{opt}. One has

$$\frac{\partial\eta}{\partial X_L}(R_L, X_L) = \frac{-R_L}{\left(R_p\frac{(R_s+R_L)^2+(X_s+X_L)^2}{\omega^2 M^2} + R_s + R_L\right)^2}\frac{2R_p(X_s+X_L)}{\omega^2 M^2} \tag{B.1}$$

and one can observe that the reactance X_L^{opt} cancelling expression (B.1) is independent from the resistance R_L and given by

$$X_L^{opt} = -X_s \tag{B.2}$$

The optimal resistance is finally determined by cancelling the efficiency partial differential with respect to the resistance, when $X_L = X_L^{opt}$. One has

$$\frac{\partial\eta}{\partial R_L}(R_L, X_L^{opt}) = \frac{R_p\frac{(R_s+R_L)^2}{\omega^2 M^2} + R_s + R_L - R_L\left(\frac{2R_p(R_s+R_L)}{\omega^2 M^2} + 1\right)}{\left(R_p\frac{(R_s+R_L)^2}{\omega^2 M^2} + R_s + R_L\right)^2} \tag{B.3}$$

$$= \frac{\frac{R_p(R_s^2-R_L^2)}{\omega^2 M^2} + R_s}{\left(R_p\frac{(R_s+R_L)^2}{\omega^2 M^2} + R_s + R_L\right)^2} \tag{B.4}$$

and the optimal resistance R_L^{opt} cancelling expression (B.4) is given by

$$R_L^{opt} = \sqrt{\frac{\omega^2 M^2 R_s}{R_p} + R_s^2} = R_s\sqrt{1 + \frac{\omega^2 M^2}{R_p R_s}} \tag{B.5}$$

APPENDIX

C

EXTENSIONS OF THE PROPOSED OPTIMAL COMMAND METHODOLOGY TO SERIES-PARALLEL AND PARALLEL-SERIES TOPOLOGIES

C.1 Series-parallel resonant dual active bridge

As announced in the Chapter 8, the proposed methodology is extended to systems presenting a series-parallel compensation scheme. The topology of the corresponding conversion chain is presented in Figure C.1.

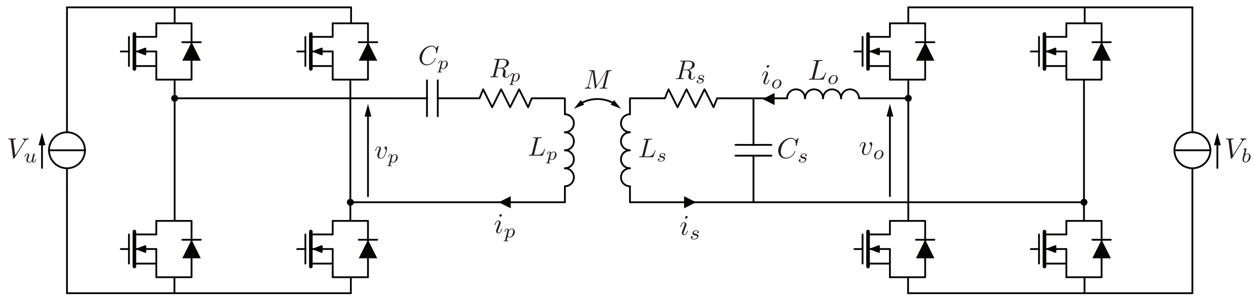

Figure C.1: Proposed series-parallel resonant WPT topology

C.1.1 Equivalent model of the converters

As mentioned previously, the voltage-source converter are controlled via an SVC-based command for producing AC voltage v_p and v_o which are controllable in both module and phase. These converter are therefore assimilable to AC voltage source $\underline{V}_p$ and $\underline{V}_o$, respectively. On the secondary side, the voltage source $\underline{V}_o$ and its series filtering inductance L_o are replaced by an equivalent current source in parallel with the same inductance, thanks to the Thevenin-Norton equivalence. One has

$$\underline{I}_o^N = \frac{\underline{V}_o}{j\omega L_o} \tag{C.1}$$

C.1.2 Equivalent model for the coupled windings

As for the method extension to parallel-parallel compensated systems, the circuit equations are alleviated and formatted analogously to the original series-series case by transforming the equivalent model for the coupled windings. For suiting the series compensation on the primary side and the parallel compensation on the secondary side, the conventional mutual inductance model is converted in an equivalent circuit presenting a resistance in series with an inductance and an electromotive force on the primary side (qualified earlier as impedance-based) and a resistance in parallel with an inductance and a magnetomotive force on the secondary side (qualified earlier as admittance-based).

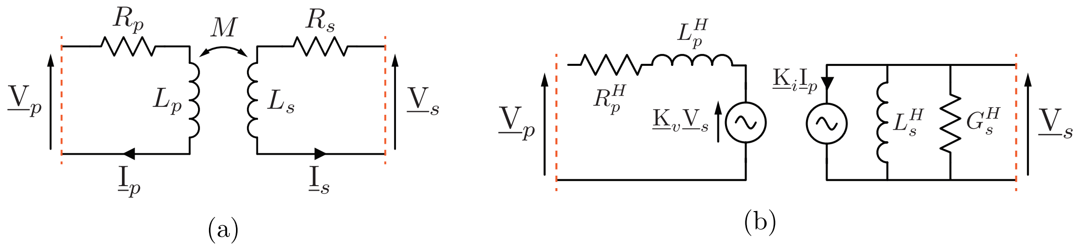

Figure C.2: (a) Impedance- and (b) mixed impedance/admittance-based model for the coupled windings

Once again, for doing so in a simple way, the mutual inductance model can be seen as a two-port network described by its impedance matrix $\mathbf{Z}$, expression the mathematical relation between each side voltage with respect to each side current. One has

$$\begin{bmatrix}\underline{V}_p\\ \underline{V}_s\end{bmatrix} = \mathbf{Z}\begin{bmatrix}\underline{I}_p\\ \underline{I}_s\end{bmatrix} \qquad \text{with } \mathbf{Z} = \begin{bmatrix} R_p + j\omega L_p & j\omega M \\ j\omega M & R_s + j\omega L_s\end{bmatrix} \tag{8.2}$$

In addition to the impedance and admittance matrices, the same two-port network can be described by an hybrid matrix $\mathbf{H}$, expressing the link between the primary current and the secondary current with respect to the secondary voltage and the primary current, *i.e.*

$$\begin{bmatrix}\underline{V}_p\\ \underline{I}_s\end{bmatrix} = \mathbf{H}\begin{bmatrix}\underline{I}_p\\ \underline{V}_s\end{bmatrix} \text{ with } \mathbf{H} = \begin{bmatrix} \frac{(R_p+j\omega L_p)(R_s+j\omega L_s)+\omega^2M^2}{R_s+j\omega L_s} & \frac{j\omega M}{R_s+j\omega L_s} \\ -\frac{j\omega M}{R_s+j\omega L_s} & \frac{1}{R_s+j\omega L_s}\end{bmatrix} \tag{C.2}$$

The latter system of equations can rewritten as

$$\underline{V}_p = (R_p^H + jX_p^H)\underline{I}_p + \underline{K}_v\underline{V}_s \tag{C.3}$$

$$\underline{I}_s = (G_s^H + jB_s^H)\underline{V}_s + \underline{K}_i\underline{I}_p \tag{C.4}$$

where R_p is an equivalent primary resistance, X_p^H is an equivalent primary reactance, $\underline{K}_v$ is an adimensional ratio between the primary and secondary voltages, G_s^H is an equivalent secondary conductance, B_s^H is an equivalent secondary susceptance and $\underline{K}_i$ is an adimensional ratio between the primary and secondary currents, with

$$R_p^H = \mathbf{Re}\left(\frac{(R_p + j\omega L_p)(R_s + j\omega L_s) + \omega^2 M^2}{R_s + j\omega L_s}\right) \qquad X_p^H = \mathbf{Im}\left(\frac{(R_p + j\omega L_p)(R_s + j\omega L_s) + \omega^2 M^2}{R_s + j\omega L_s}\right)$$

$$G_s^H = \mathbf{Re}\left(\frac{1}{R_s + j\omega L_s}\right) \qquad B_s^H = \mathbf{Im}\left(\frac{1}{R_s + j\omega L_s}\right)$$

$$\underline{K}_v = \frac{j\omega M}{R_s + j\omega L_s} \qquad \underline{K}_i = -\frac{j\omega M}{R_s + j\omega L_s}$$

The analytical development of the expression for X_p^H and B_s^H demonstrates that the former is always positive and the latter is always negative, corresponding logically to inductive behaviours. As a consequence, in the equivalent circuit, the reactance X_p and the susceptance B_s^H can be respectively replaced by the inductance L_{pH} and L_s^H, given by

$$L_p^H = \frac{X_p}{\omega} \qquad L_s^H = -\frac{1}{\omega B_s} \tag{C.5}$$

According to the interpretation of this mathematical model, the resultant impedance/admittance-based equivalent circuit for the coupled windings is represented in Figure C.2b.

C.1.3 Equivalent circuit of the complete system

By combining the primary converter equivalent voltage source and the secondary converter Norton equivalent circuit with the hybrid circuit model for the coupled windings, the equivalent circuit for the first-harmonic analysis of a SP-RDAB system is shown in Figure C.3.

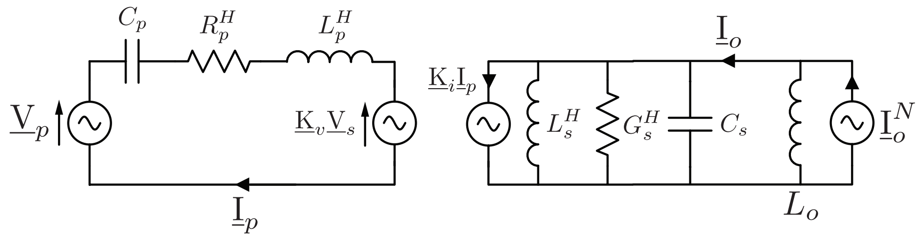

Figure C.3: Equivalent impedance/admittance-based circuit for the first-harmonic analysis

Before addressing the optimal conditions for operating the latter, the primary current and the secondary voltage are solved. By applying the Kirchhoff's current and voltage laws, one has

$$\underline{V}_p = \underline{Z}_p\underline{I}_p + \underline{K}_v\underline{V}_s \tag{C.6}$$

$$\underline{I}_o^N = \underline{Y}_s\underline{V}_s + \underline{K}_i\underline{I}_p \tag{C.7}$$

with the primary circuit impedance $\underline{Z}_p$ and the secondary circuit admittance $\underline{Y}_s$ defined as

$$\underline{Z}_p = R_p^H + j\omega L_p^H + 1/j\omega C_p \tag{C.8}$$

$$\underline{Y}_s = G_s^H + j\omega C_s + 1/j\omega L_s^H + 1/j\omega L_o \tag{C.9}$$

By observing equations (C.6) and (C.7), one can notice the intended analogy between this hybrid formalism and the previous impedance- or admittance-based formalisms. By solving equations (C.6) and (C.7), the expressions for the primary current and the secondary voltage are obtained with

$$\underline{I}_p = \frac{\underline{Y}_s\underline{V}_p - \underline{K}_i\underline{I}_o^N}{\underline{Z}_p\underline{Y}_s - \underline{K}_v\underline{K}_i} \tag{C.10}$$

$$\underline{V}_s = \frac{\underline{Z}_p\underline{I}_o^N - \underline{K}_v\underline{V}_p}{\underline{Z}_p\underline{Y}_s - \underline{K}_v\underline{K}_i} \tag{C.11}$$

The aforementioned analogy allows once again the analogous adaptation of the methodology presented for series-series and parallel-parallel topologies to series-parallel topologies.

C.1.4 Power efficiency and optimal load admittance

For analyzing the power efficiency of this third topology, secondary current source $\underline{I}_o^N$ can be replaced by an equivalent load admittance $\underline{Y}_L = G_L + jB_L$. The power efficiency can be expressed as

$$\eta = \frac{G_L V_s^2}{R_p^H I_p^2 + G_s^H V_s^2 + G_L V_s^2} \tag{C.12}$$

where, as a reminder, I_p and V_s are the RMS values of the primary current and of the secondary voltage, respectively. For developing the expression of the power efficiency, the values I_p and V_s can be related by applying the Kirchhoff's current low on the secondary circuit. One has

$$\begin{aligned}\underline{K}_i\underline{I}_p &= -(G_s^H + \underbrace{j\omega C_s + \frac{1}{j\omega L_s^H} + \frac{1}{j\omega L_o}}_{jB_{tot_s}} + G_L + jB_H)\underline{V}_s \\ &= -(G_s^H + G_L + jB_{tot_s} + jB_L)\underline{V}_s \end{aligned} \tag{C.13}$$

so that the RMS value of the primary voltage V_p can be expressed as

$$I_p = \frac{\sqrt{(G_s^H + G_L)^2 + (B_{tot_s} + B_L)^2}}{K_i} \; V_s \tag{C.14}$$

By introducting (C.14) in the expression (C.12), the efficiency becomes

$$\eta = \frac{G_L}{R_p^H \frac{\sqrt{(G_s^Y + G_L)^2 + (B_{tot_s} + B_L)^2}}{K_i^2} + G_s^H + G_L} \tag{C.15}$$

For taking full advantage of a given transmission circuit, the transfer efficiency can therefore be maximized by imposing the optimal load conductance G_L^{opt} and susceptance B_L^{opt} so that

$$\frac{\partial \eta}{\partial G_L}(G_L^{opt}, B_L^{opt}) = 0 \text{ and } \frac{\partial \eta}{\partial B_L}(G_L^{opt}, B_L^{opt}) = 0 \tag{C.16}$$

Since this problem demonstrates a perfect analogy with the equivalent problem for the series-series and the parallel-parallel compensated systems (see equations (6.10)), their solutions are also analogous and one has

$$G_L^{opt} = G_s^H \sqrt{1 + \frac{K_i^2}{R_p^H G_s^H}} \tag{C.17}$$

$$B_L^{opt} = -B_{tot_s} = \frac{1}{\omega L_s^H} + \frac{1}{\omega L_o} - \omega C_s \tag{C.18}$$

As for the parallel-parallel compensated system, one can observe that the optimal load susceptance B_L^{opt} is different from zero when the secondary LC oscillator is tuned in accordance with the conventional practice (*i.e.*, when $\omega = 1/\sqrt{L_s^H C_s}$).

Ensuring $G_L = G_L^{opt}$ and $B_L = B_L^{opt}$ guarantees to operate the system at its maximum physically achievable efficiency η_{max}, which is imposed by the design of the LC circuits only and given by

$$\eta_{max} = \frac{K_i^2}{R_p^H G_s^H \left(1 + \sqrt{1 + \frac{K_i^2}{R_p^H G_s^H}}\right)^2} \tag{C.19}$$

C.1.5 Methodology for the system optimal command

The methodology consists in determining the source currents $\underline{V}_p$ and $\underline{I}_o^N$ ensuring simultaneously the maximization of the power efficiency and the setting of the output power.

Maximization of the power efficiency

According to the developments above, the system achieves its maximum physical efficiency when the equivalent conductance and susceptance seen from the secondary oscillator terminals are respectively equal to G_L^{opt} and to B_L^{opt}. Therefore, the mathematical condition for the system to achieve the maximum efficiency is written as

$$\underline{I}_o^N = -(G_L^{opt} + jB_L^{opt})\underline{V}_s \tag{C.20}$$

By eliminating the secondary voltage using (C.11) in (C.20), the condition becomes

$$-\underline{K}_v(G_L^{opt} + jB_L^{opt})\underline{V}_p + (\underline{Z}_p\underline{Y}_s - \underline{K}_v\underline{K}_i + G_L^{opt}\underline{Z}_p + jB_L^{opt}\underline{Z}_p)\underline{I}_o^N = 0 \tag{C.21}$$

which is the first equation linking the complex unknowns $\underline{V}_p$ and $\underline{I}_o^N$. However, the definition of another equation is mandatory for creating a solvable system of complex equations allowing to determine these unknowns. As for the series-series compensated system, this additional equation is associated with the setting of the required output power.

Setting of the output power

Achieve a reference output power P_{ref} to the load is accomplished by setting adequately the module of the secondary voltage. Assuming that condition (C.21) is achieved, the real part of the equivalent load admittance is equal to G_L^{opt} so that a power P_{ref} is transmitted to the load when

$$V_s = \sqrt{\frac{P_{ref}}{G_L^{opt}}} \tag{C.22}$$

The secondary voltage $\underline{V}_s$ is chosen as a phase reference and the complex condition for producing a reference output power P_{ref} becomes

$$\underline{V}_s = \sqrt{\frac{P_{ref}}{G_L^{opt}}} \tag{C.23}$$

Using (8.11) and (8.23), this condition is expressed in terms of currents $\underline{V}_p$ and $\underline{I}_o^N$ as

$$-\underline{K}_v\underline{V}_p + \underline{Z}_p\underline{I}_o^N = (\underline{Z}_p\underline{Y}_s - \underline{K}_v\underline{K}_i)\sqrt{\frac{P_{ref}}{G_L^{opt}}} \tag{C.24}$$

which is a second equation linking the pursued currents. Finally, the desired operating point is reached by imposing the current $\underline{V}_p$ and $\underline{I}_o^N$ solving equations (C.21) and (C.24).

C.2 Parallel-series resonant dual active bridge

Finally, the proposed methodology is extended to systems presenting a parallel-series compensation scheme. The topology of the corresponding conversion chain is presented in Figure C.4.

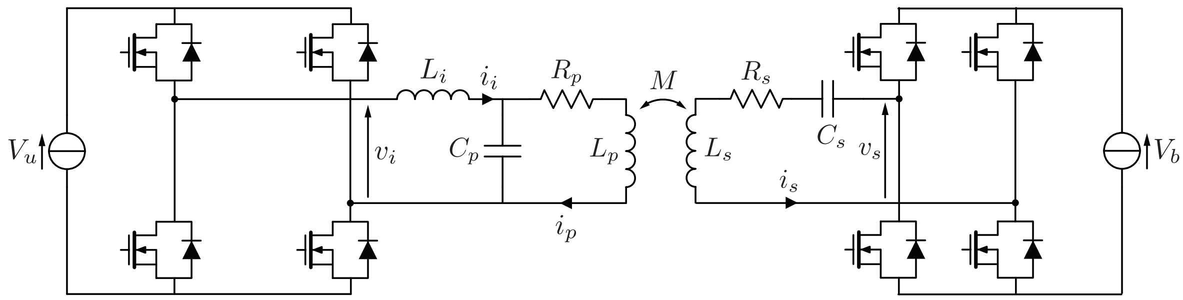

Figure C.4: Proposed parallel-series resonant WPT topology

C.2.1 Equivalent model of the converters

As mentioned previously, the voltage-source converter are controlled via an SVC-based command for producing AC voltage v_i and v_s which are controllable in both module and phase. These converter are therefore assimilable to AC voltage source $\underline{V}_i$ and $\underline{V}_s$, respectively. On the primary side, the voltage source $\underline{V}_i$ and its series filtering inductance L_i are replaced by an equivalent current source in parallel with the same inductance, thanks to the Thevenin-Norton equivalence. One has

$$\underline{I}_i^N = \frac{\underline{V}_i}{j\omega L_i} \tag{C.25}$$

C.2.2 Equivalent model for the coupled windings

As for the method previous extensions, the circuit equations are alleviated and formatted analogously to the original series-series case by transforming the equivalent model for the coupled windings. For suiting the parallel compensation on the primary side and the series compensation on the secondary side, the conventional mutual inductance model is converted in an equivalent circuit presenting a resistance in parallel with an inductance and a magnetomotive force on the secondary side (qualified earlier as admittance-based) and a resistance in series with an inductance and an electromotive force on the primary side (qualified earlier as impedance-based).

The two-port network constituted by the mutual inductance model of the coupled windings can be described by a similar hybrid matrix **H** to the series-parallel case, where the role of the primary and of the secondary windings have been interchanged. The coupled windings can be therefore described by the equations

$$\underline{\mathrm{I}}_p = (G_p^H + jB_p^H)\underline{\mathrm{V}}_p + \underline{\mathrm{K}}_i\underline{\mathrm{I}}_s \tag{C.26}$$

$$\underline{\mathrm{V}}_s = (R_s^H + jX_s^H)\underline{\mathrm{I}}_s + \underline{\mathrm{K}}_v\underline{\mathrm{V}}_p \tag{C.27}$$

where G_p^H is an equivalent primary conductance, B_p^H is an equivalent primary susceptance, $\underline{\mathrm{K}}_v$ is an adimensional ratio between the primary and secondary voltages, R_s^H is an equivalent secondary conductance, X_s^H is an equivalent secondary reactance and $\underline{\mathrm{K}}_i$ is an adimensional ratio between the primary and secondary currents, with

$$G_p^H = \mathbf{Re}\left(\frac{1}{R_p + j\omega L_p}\right) \qquad B_p^H = \mathbf{Im}\left(\frac{1}{R_p + j\omega L_p}\right)$$

$$R_s^H = \mathbf{Re}\left(\frac{(R_p + j\omega L_p)(R_s + j\omega L_s) + \omega^2 M^2}{R_p + j\omega L_p}\right) \qquad X_s^H = \mathbf{Im}\left(\frac{(R_p + j\omega L_p)(R_s + j\omega L_s) + \omega^2 M^2}{R_p + j\omega L_p}\right)$$

$$\underline{\mathrm{K}}_v = \frac{j\omega M}{R_p + j\omega L_p} \qquad \underline{\mathrm{K}}_i = -\frac{j\omega M}{R_p + j\omega L_p}$$

The analytical development of the expression for B_p^H and X_s^H demonstrates that the former is always negative and the latter is always positive, corresponding logically to inductive behaviours. As a consequence, in the equivalent circuit, the susceptance B_p^H and the reactance X_s^H can be respectively replaced by the inductance L_p^H and L_s^H, given by

$$L_p^H = -\frac{1}{\omega B_p^H} \qquad L_s^H = \frac{X_s^H}{\omega} \tag{C.28}$$

C.2.3 Equivalent circuit of the complete system

By combining the primary converter Norton equivalent circuit and the secondary converter equivalent voltage source with the hybrid circuit model for the coupled windings, the equivalent circuit for the first-harmonic analysis of a PS-RDAB system is shown in Figure C.5. Before addressing the optimal conditions for operating the latter, the primary current and the secondary voltage are solved. By applying the Kirchhoff's current and voltage laws, one has

$$\underline{\mathrm{I}}_i^N = \underline{\mathrm{Y}}_p\underline{\mathrm{V}}_p + \underline{\mathrm{K}}_i\underline{\mathrm{I}}_s \tag{C.29}$$

$$\underline{\mathrm{V}}_s = \underline{\mathrm{Z}}_s\underline{\mathrm{I}}_s + \underline{\mathrm{K}}_v\underline{\mathrm{V}}_p \tag{C.30}$$

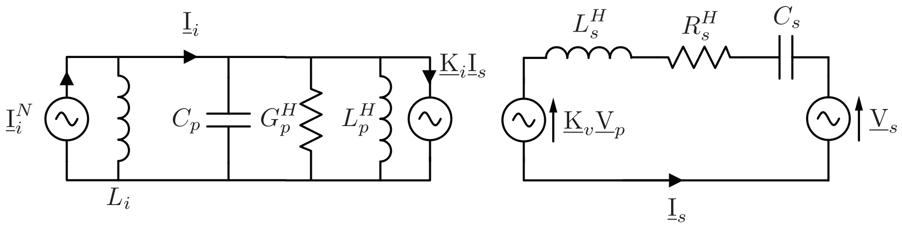

Figure C.5: Equivalent admittance/impedance-based circuit for the first-harmonic analysis

with the primary circuit admittance $\underline{Y}_p$ and the secondary circuit impedance $\underline{Z}_s$ defined as

$$\underline{Y}_p = G_p^H + j\omega C_p + 1/j\omega L_p^H + 1/j\omega L_o \tag{C.31}$$

$$\underline{Z}_s = R_s^H + j\omega L_s^H + 1/j\omega C_s \tag{C.32}$$

By observing equations (C.29) and (C.30), one can notice the intended analogy between this hybrid formalism and the previous impedance- or admittance-based formalisms. By solving equations (C.29) and (C.30), the expressions for the primary voltage and the secondary current are obtained with

$$\underline{V}_p = \frac{\underline{Z}_s\underline{I}_i^N - \underline{K}_v\underline{V}_s}{\underline{Y}_p\underline{Z}_s - \underline{K}_v\underline{K}_i} \tag{C.33}$$

$$\underline{I}_s = \frac{\underline{Y}_p\underline{V}_p - \underline{K}_i\underline{I}_i^N}{\underline{Y}_p\underline{Z}_s - \underline{K}_v\underline{K}_i} \tag{C.34}$$

The aforementioned analogy allows once again the analogous adaptation of the methodology presented for series-series, parallel-parallel and series-parallel topologies to parallel-series topologies.

C.2.4 Power efficiency and optimal load impedance

For analyzing the efficiency, the secondary voltage source $\underline{V}_s$ is replaced by an equivalent load impedance $\underline{Z}_L = R_L + jX_L$. The power efficiency can be expressed as

$$\eta = \frac{R_L I_s^2}{G_p^H V_p^2 + R_s^H I_s^2 + R_L I_s^2} \tag{C.35}$$

where V_p and I_s are the RMS values of the primary voltage and of the secondary current, respectively. The values V_p and I_s can be related by applying the Kirchhoff's voltage law to the secondary circuit mesh. One has

$$\underline{K}_v\underline{V}_p = -(R_s^H + \underbrace{j\omega L_s^H + \frac{1}{j\omega C_s}}_{jX_s} + R_L + jX_L)\ \underline{I}_s = -(R_s^H + R_L + jX_s + jX_L)\ \underline{I}_s$$

so that the RMS value of the primary current I_p can be expressed as

$$V_p = \frac{\sqrt{(R_s^H + R_L)^2 + (X_s + X_L)^2}}{K_v}\ I_s \tag{C.36}$$

By introducing the relation (C.36) in the expression (C.35), the efficiency becomes

$$\eta(R_L, X_L) = \frac{R_L}{G_p^H \frac{(R_s^H + R_L)^2 + (X_s + X_L)^2}{\omega^2 M^2} + R_s^H + R_L} \tag{C.37}$$

For taking full advantage of a given transmission circuit, the transfer efficiency can therefore be maximized by imposing the optimal load resistance R_L^{opt} and reactance X_L^{opt} so that

$$\frac{\partial\eta}{\partial R_L}(R_L^{opt}, X_L^{opt}) = 0 \text{ and } \frac{\partial\eta}{\partial X_L}(R_L^{opt}, X_L^{opt}) = 0 \tag{C.38}$$

Since this problem demonstrates a perfect analogy with the equivalent problem for the other topologies, their solutions are also analogous and one has

$$R_L^{opt} = R_s^H \sqrt{1 + \frac{K_v^2}{G_p^H R_s^H}} \quad \text{(C.39)} \qquad X_L^{opt} = -X_s = \frac{1}{\omega C_s} - \omega L_s^H \quad \text{(C.40)}$$

One can notice that the optimal load reactance X_L^{opt} is null when the secondary LC oscillator is correctly tuned (*i.e.*, when $\omega = 1/\sqrt{L_s^H C_s}$), whereas it ensures the cancellation of the residual reactance in the secondary circuit in the case of a mistuned secondary oscillator.

Ensuring $R_L = R_L^{opt}$ and $X_L = X_L^{opt}$ guarantees to operate the system at its maximum intrinsically (or physically) achievable efficiency η_{max}, which is imposed by the design of the LC circuits only and given by

$$\eta_{max} = \frac{K_v^2}{G_p^H R_s^H \left(1 + \sqrt{1 + \frac{K_v^2}{G_p^H R_s^H}}\right)^2} \tag{C.41}$$

C.2.5 Methodology for the system optimal command

The methodology consists in determining the source current $\underline{I}_i^N$ and voltage $\underline{V}_s$ ensuring simultaneously the maximization of the power efficiency and the setting of the output power.

Maximization of the power efficiency

According to the developments above, the system achieves its maximum intrinsic efficiency when the equivalent resistance and reactance seen from the secondary oscillator terminal are respectively equal to R_L^{opt} and to X_L^{opt}. Therefore, the mathematical condition for the system to achieve the maximum efficiency is written as

$$\underline{V}_s = -(R_L^{opt} + jX_L^{opt})\underline{I}_s \tag{C.42}$$

By eliminating the secondary current using (C.30) in (C.42), the condition becomes

$$-\underline{K}_v(R_L^{opt} + jX_L^{opt})\underline{I}_i^N + (\underline{Y}_p\underline{Z}_s + \underline{K}_v\underline{K}_i + R_L^{opt}\underline{Y}_p + jX_L^{opt}\underline{Y}_p)\underline{V}_s = 0 \tag{C.43}$$

which is a first equation linking the complex unknowns $\underline{I}_i^N$ and $\underline{V}_s$. The definition of another equation is mandatory for creating a solvable system of complex equations. This additional equation is associated with the setting of the required active output power.

Setting of the required output power

Achieving a reference power P_{ref} to the load is accomplished by setting adequately the module of the secondary current. Indeed, assuming that condition (C.43) is achieved, the real part of the load impedance is equal to R_L^{opt} so that a power P_{req} is transmitted to the load when

$$I_s = \sqrt{\frac{P_{ref}}{R_L^{opt}}} \tag{C.44}$$

The secondary current $\underline{I}_s$ is chosen here as a phase reference and the complex condition for achieving an output power P_{ref} becomes

$$\underline{I}_s = \sqrt{\frac{P_{ref}}{R_L^{opt}}} \tag{C.45}$$

Using (C.34) and (C.45), this condition is expressed in terms of current $\underline{\mathrm{I}}_i^N$ and voltage $\underline{\mathrm{V}}_s$ as

$$-\underline{\mathrm{K}}_v\underline{\mathrm{I}}_i^N + \underline{\mathrm{Y}}_p\underline{\mathrm{V}}_s = (\underline{\mathrm{Y}}_p\underline{\mathrm{Z}}_s + \underline{\mathrm{K}}_v\underline{\mathrm{K}}_i)\sqrt{\frac{P_{ref}}{R_L^{opt}}} \tag{C.46}$$

which is a second equation linking the voltages. Finally, the desired operating point is reached by imposing the voltages $\underline{\mathrm{I}}_i^N$ and $\underline{\mathrm{V}}_s$ solving simultaneously equations (C.43) and (C.46).